Understanding the Structure-Composition Relationship in Layered Perovskite-Related Materials

AREESHA ALI

Understanding the Structure - Composition Relationship in Layered Perovskite-Related Materials

Areesha Ali

A Thesis Presented for the Degree of Doctor of Philosophy

Department of Physics

Durham University

United Kingdom

July 2025

Declaration

I declare that this thesis is my own original work and has been composed solely by me, except where otherwise stated by reference or acknowledgement. The research presented here was conducted under the supervision of Dr Emma E. McCabe. This thesis is submitted to Durham University in partial fulfilment of the requirements for the degree of Doctor of Philosophy in Physics. This work has not been submitted for any other degree or qualification at this or any other institution.

Areesha Ali

Signed: Areesha Ali

Date: 29/07/25

Abstract

Complex oxides, particularly ABO_3 perovskite oxides, have garnered the interest of solid-state scientists because of their fascinating physical properties such as ferroelectricity, piezoelectricity, optical properties, and technological applications. The relationship between their structure, composition, and properties has been very well studied. This understanding allows for the precise tailoring of ABO_3 perovskites to meet specific application requirements. The layered perovskite-related materials share many features with the three-dimensional perovskites but are more complex. This thesis focuses on such layered systems - Dion-Jacobson phases, Aurivillius phases and Ruddlesden-Popper phases to understand the relationship between structure and composition to help design property optimised materials.

Chapter one provides an introduction to perovskites and layered perovskite-related materials with particular emphasis on the mechanisms of ferroelectricity within these materials. In chapter two, the experimental and computational methodology used throughout the project are introduced.

The Dion-Jacobson (DJ) phases are known to adopt polar ground states stabilised by either proper or hybrid improper mechanisms. Chapter three investigates the structure-composition-property relationships in the n = 3 $A'A_2B_3O_{10}$ (A' = Rb, Cs; A = Ca, Sr, Ba; B = Nb, Ta) Dion-Jacobson phases, showing how both geometric as well as electronic factors play a role in determining the structures of these materials. This chapter also demonstrates the advantages of neutron powder diffraction and single-crystal diffraction over conventional X-ray diffraction. In addition to their ferroelectric behaviour, these n = 3 DJ phases have recently attracted attention for their optical properties and applications such as photocatalytic activity, X-ray detectors, solar cells, photo detectors. The study shows the dependence of bandgap on the composition of the material.

Chapter four uses both X-ray and neutron diffraction to explore the structure-composition relation in the n = 2 $Bi_2A_{0.5}La_{0.5}B_2O_9$ (A = Na, K; B = Nb, Ta) Aurivillius phases. The study shows how tuning the composition can tune the balance between polar and anti-polar states. Density Functional Theory (DFT) calculations help to validate experimental findings of the Aurivillius phases and to study composition–structure relationship in the n = 2 $Li_2AB_2O_7$ (A = Ca, Sr, Ba; B = Nb, Ta) Ruddlesden–Popper (RP) phases. The findings of this study offer valuable insights into how

composition can be tuned to manipulate the polar behaviour in Aurivillius and Ruddlesden-Popper phases.

Chapter five offers insights into the fluorination of $n = 2$ Ruddlesden-Popper phases. Inserting fluoride ions into RP phases can help modify the tilting and twisting of octahedra. This provides an additional route to break inversion symmetry and stabilise the polar structures in $n = 2$ RP phases.

Chapter six is a preliminary study using X-ray diffraction on *A*-site ordered $A_{0.5}Nd_{0.33}TaO_3$. It shows that the structure undergoes a change when the vacancies in the structure are occupied by $A = Li^+$, Na^+ and K^+. It suggests that the difference between the size of the *A*-cations can influence the structure of perovskites. To complete the study and determine the structure of $A_{0.5}Nd_{0.33}TaO_3$ (*A* = Li, Na, K) neutron powder diffraction, solid-state NMR, DFT calculations are required.

Chapter seven summarises the key conclusions of this thesis and outlines the future work.

Acknowledgements

I would like to express my deepest gratitude to all those who supported me throughout the course of this PhD.

First and foremost, I would like to thank my supervisor, Emma, for her endless patience, kindness, and unwavering support over the past four years. Her mentorship has been a cornerstone of this research, and I have learned and grown so much under her supervision. I deeply admire her professionalism, compassion, and dedication, and I aspire to be like her in my own career.

I would also like to thank everyone who contributed to the research presented in this thesis: Dr Vanessa Cascos for synthesizing the Dion-Jacobson samples, Prof. Maxim Avdeev for performing the neutron diffraction experiments at ANSTO, Dr Jack Woolley and Faith Pritchard for performing SHG measurements, Dr Ivan da Silva for performing the neutron diffraction experiments at ISIS, and Prof. Stewart Clark for his help on the computational side of this thesis. Your expertise and collaboration have been invaluable.

I would especially like to thank Glen for always being patient with me, his willingness to help when I got stuck, and for his constant encouragement. His support has meant a great deal to me throughout my PhD journey. I'm truly grateful for the lasting friendship we've built and of course for all the lifts to the university!

Thank you to my partner, Ben, for helping me adjust to life in the UK - with you by my side, the transition was so much easier. I'm deeply grateful for your emotional support and motivation throughout this journey. I truly can't thank you enough for your love, encouragement, and for always believing in me - especially during the times when I found it hardest to believe in myself.

I couldn't have got to this point without the immense love and unconditional support from my wonderful family. Ammi, Papa, Wareesha and Areeba - thank you for always being there, no matter the distance. Your belief in me has been my strength throughout this journey.

Finally, I am deeply grateful to Allah (SWT) for granting me the strength, patience, and guidance to complete this journey. ٱلْحَمْدُ للهِ. Without His mercy and blessings, none of this would have been possible.

Contents

Chapter 1: Introduction to Layered Perovskite-Related Materials

1.1 Introduction to Perovskites

1.1.1 Historical Background

Perovskite is the name given to the mineral calcium titanate, $CaTiO_3$. It was first discovered by a German minerologist Gustavus Rose (1798-1873) in the Ural Mountains of Russia in 1839. He named the mineral perovskite in honour of the Russian mineralogist and sponsor of his work Lev Alekseyevich von Perovski (1792-1856).[2] Natural perovskites in the form of $MgSiO_3$, make up 50-90% of the Earth's mantle. This makes them the most abundantly available mineral on the planet.

The perovskite structure, as described by Victor Goldschmidt (1888-1947), is anything that has the stoichiometry ABX_3 and shares the same crystallographic structure as the mineral perovskite. This structure is found for numerous materials with diverse properties, including ferroelectricity, superconductivity, and colossal magnetoresistance, making perovskites valuable in various industrial applications.

1.1.2 General Description of Perovskite Structure

As described by Goldschmidt, the simple three-dimensional (3D) perovskites have the general formula ABX_3 where *A* and *B* are cations and *X* is an anion, most commonly oxide, that coordinates both cations. Almost every element on the periodic table, aside from the noble gases, has been incorporated into the perovskite structure. The atomic arrangement of a perovskite can be described as a large cation *A* occupying the corners (12-coordinate site) of a cube, a smaller cation *B* at the centre (6-coordinate site), and anions *X* (oxygen) at the faces of the cube (**Figure 1.1**). The perovskite structure is formed from a network of corner-linked BO_6 octahedra.[3] The ideal perovskite structure adopts a simple cubic lattice with the centrosymmetric $Pm\bar{3}m$ space group,[4] as illustrated in **Figure 1.1**.

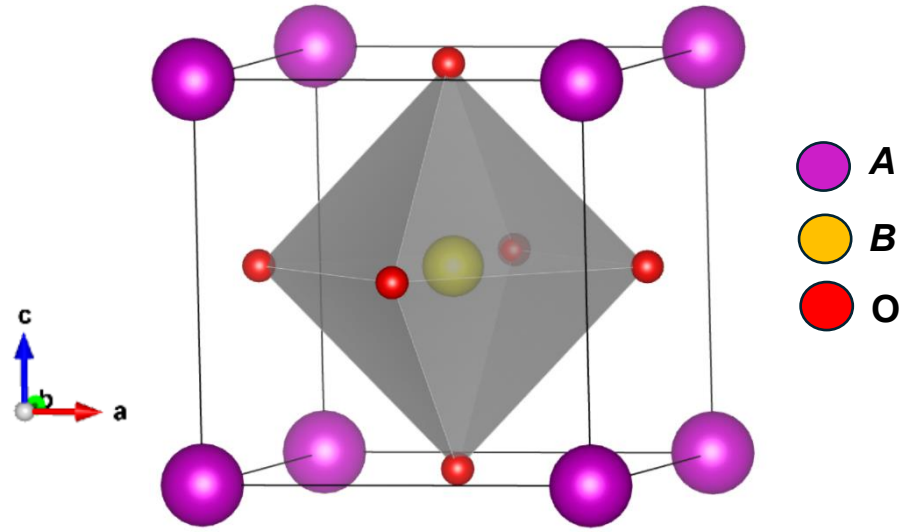

Figure 1.1: Ideal cubic perovskite structure - ABX_3. *A* and *B* cations are shown in pink and yellow respectively, and BO_6 octahedron in grey.

1.1.3 Octahedral Tilting Distortions

Not many perovskites exist in the ideal $Pm\bar{3}m$ cubic phase. Most perovskites undergo symmetry lowering distortions caused by structural frustrations such as ionic size mismatch between the *A*-site and *B*-site cations. The distortions lead to deviations from the high symmetry cubic structure to lower symmetry crystal structures.[5]

Goldschmidt proposed an empirical parameter, tolerance factor (*t*), to assess the stability of ideal perovskite-like structures. It takes into account the size limits of the cations to form a perovskite structure. This parameter is useful for designing and predicting the formation of perovskite-like materials. It is calculated using the ionic radii of the constituent cations in the general formula of a perovskite (ABX_3) and is measured by the equation:

$$t = \frac{r_A + r_x}{\sqrt{2}(r_B + r_x)} \qquad \textbf{(1.1)}$$

where r_A, r_B and r_x are the ionic radii of the cations *A* and *B* and anion *X* (oxygen), respectively.[6]

When $t = 1$, a perfect cubic cell, reflecting the ideal perovskite structure, is formed. For example, at room temperature $SrTiO_3$ with $t = 1.00$ adopts a cubic structure (**Figure 1.2(a)**). As *t* deviates from 1, the perovskite cell gets distorted, and the

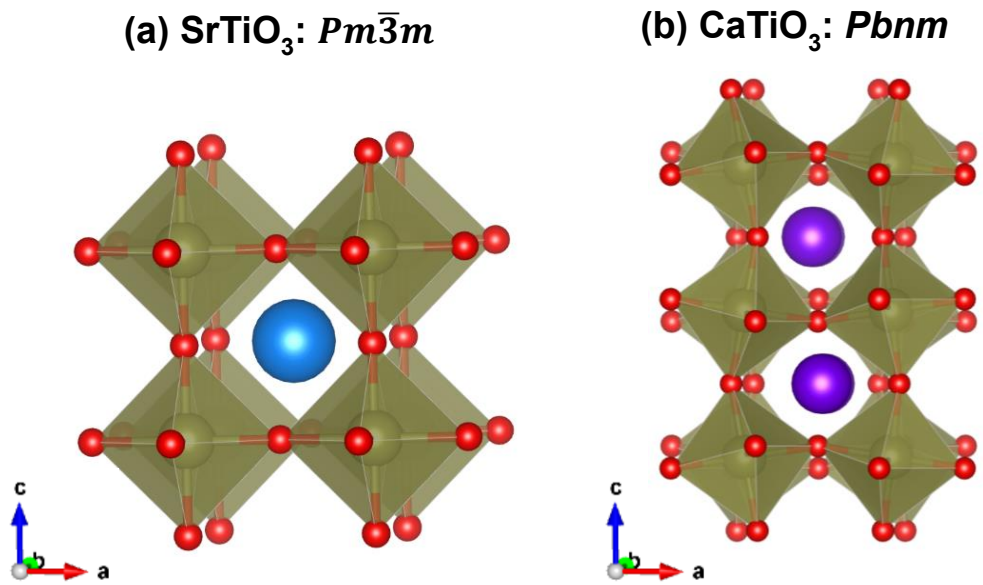

Figure 1.2: Illustration of structures adopted by (a) $SrTiO_3$, (b) $CaTiO_3$ at room temperature. Sr, Ca and Ti cations are shown in blue, purple and golden respectively, and TiO_6 octahedra are in golden.

symmetry is lowered. For example, at room temperature $CaTiO_3$ with t = 0.97 is orthorhombic (**Figure 1.2(b)**). If t is significantly away from 1, then the perovskite is not formed.[7, 8]

The symmetry lowering in perovskites is often due to polar/anti-polar displacements of cations relative to anions, the tilting of the octahedra, or by a combination of both.[9-11] If the ionic radii of the ions at the *A* site are too small to occupy the available volume, the octahedra tilt or the cations and anions are displaced to compensate. Setter et.al. reported that the octahedra tilting depends on factors such as tolerance factor, composition and temperature.[12, 13] This octahedral tilting can occur in-phase or out-of-phase and can be described by the Glazer tilt notation.[10]

Glazer tilt notation is a system used to describe the tilting of octahedra in perovskite structures. The notation is written as $a^x b^y c^z$ where *a*, *b*, and *c* represent the magnitudes of the tilting of octahedra about the crystallographic *x*-, *y*- and *z*- axes of the perovskite cell respectively. The superscripts *x*, *y* and *z* denote the nature of tilting in adjacent layers with respect to the reference layer:

I. 0: No tilt along that axis
II. +: In-phase tilting (neighbouring octahedra rotate in the same direction along the axis)
III. –: Out-of-phase tilting (neighbouring octahedra rotate in opposite directions along the axis).

For example, $a^0a^0a^0$: no tilting along any axis, $a^-a^-c^+$, as observed in $CaTiO_3$: out-of-phase tilting along *x* and *y* axes and in-phase tilting along *z*-axis. There are 23 possible Glazer tilt systems, which provide a comprehensive classification of tilted octahedra in perovskites.[14]

In addition to using Glazer notations, distortions such as tilts or rotations of octahedra and in-plane or out-of-plane polar and antipolar displacements can also be described in terms of the active symmetry modes that drive the transition from a higher-symmetry phase to a lower-symmetry phase.[15] ISODISTORT, a web-based tool, can be used to visualise and analyse these distortion modes.

These distortion modes, classified as irreducible representations (irreps), are described with respect to the high symmetry points of the aristotype structure and labelled using Miller and Love notation. This notation consists of the k-point of the mode, followed by a numeral subscript and a superscript + or -, which indicates whether the distortion mode is even or odd under inversion.

The X-point of $Pm\bar{3}m$ space group corresponds to k = (½,0,0). There are three symmetry-equivalent arms, k = (½,0,0), k = (0,½,0) and k = (0,0,½), which together make up the star of k. A structural distortion transforming as an X-point irrep can have components along one or more of these propagation vectors. Parts of the complete irrep belonging to different k-actives are separated by semi-colons. For example, X_1^+ (a;0;0) denotes that only one k of the star is active. X_1^+ (a;a;a) represents a distortion in which all three ks are active with equal amplitudes, corresponding to a higher-symmetry configuration whereas X_1^+ (a;b;c) denotes that all three ks are active and unconstrained, resulting in the lowest symmetry.

The R-point of $Pm\bar{3}m$ space group corresponds to k = (½,½,½) and has only one possible k-active. In this case, the irrep is multi-dimensional and its components are separated by commas. For example, R_5^+ (a,a,a) is a three-dimensional irrep where the commas separate the individual components of the irrep.

The structural distortions observed in a material can be described by using a single irrep or a combination of two or more irreps. In this thesis, the latter approach is frequently used. In the combination of irreps, the direction of the distortion has a vertical bar "|" within the brackets. This vertical bar "|" separates the parts belonging to different irreps. For example, in X_3^- + X_2^+ (a;0|b;0), (a;0) corresponds to X_3^- and (b;0) corresponds to X_2^+.

Irreducible representations (irreps) are therefore valuable for describing and comparing different symmetry allowed distortion modes in a material.

1.2 Layered Perovskite-Related Materials

In addition to the three-dimensional perovskites described above, layered analogues can also be prepared, in which the perovskite blocks are separated along the stacking direction by different layers. This reduced dimensionality gives them unique physical, chemical, and electronic properties, making these materials highly versatile for a wide range of applications. Examples include the Ruddlesden-Popper phases, Dion-Jacobson phases, and Aurivillius phases, which are the focus of this thesis.

1.2.1 Aurivillius Phases

The Aurivillius phases were first identified by Bengt Aurivillius in the late 1940s.[16] This family of layered perovskites have the general formula $Bi_2A_{n-1}B_nO_{3n+3}$.[16] They consist of blocks of perovskite, n layers thick, with the formula $[A_{n-1}B_nO_{3n+1}]$, separated by a fluorite-like Bi_2O_2 layers (**Figure 1.3**). Unlike the conventional ABO_3 perovskites, where BO_6 octahedra are connected in three dimensions, in Aurivillius

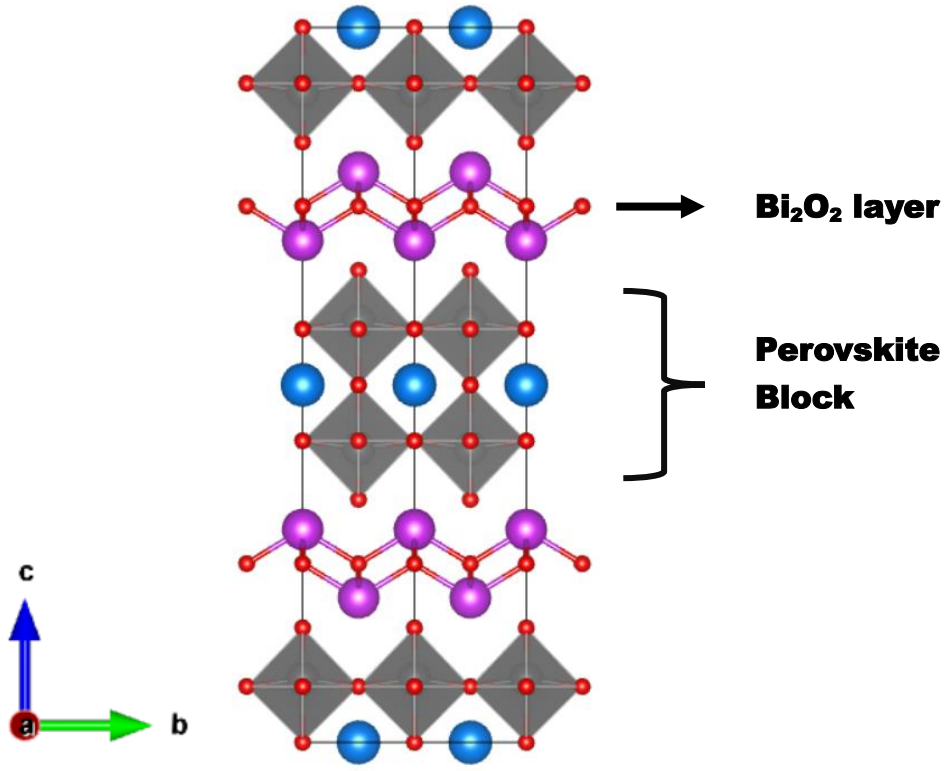

Figure 1.3: Illustration of the parent $n = 2$ Aurivillius Phase described by $I4/mmm$ symmetry. A cation and BO_6 octahedra are shown in blue and grey. Bi_2O_2 layers are shown in pink.

phases, these octahedra are linked only in two dimensions (parallel to the *a* and *b* axes). The *A*-site, which is 12-coordinated, is occupied by mono-, di- or trivalent cations such as Na^{+}, K^{+}, Ca^{2+}, Sr^{2+}, Ba^{2+}, Pb^{2+}, Bi^{3+}, or Ln^{3+}. The 6-coordinated *B*-site is typically occupied by d^{0} tetra-, penta- or hexavalent cations such as Ti^{4+}, Nb^{5+}, Ta^{5+}, W^{6+}.[17-24] Aurivillius phases containing non-d^{0} cations at the *B*-site, such as Fe^{3+}, Ru^{4+}, Cr^{3+}, Ir^{4+} or Mn^{4+}, have been explored for their potential magnetic and multiferroic properties.[25-29] The Bi^{3+} in Bi_2O_2 layers can also be replaced by Pb^{2+}, Sb^{3+} and Te^{4+}.[30-32]

A few well studied Aurivillius phases include:

(I) Odd layered: Bi_2WO_6,[33, 34] $Bi_4Ti_3O_{12}$[35]

(II) Even layered: $Bi_2SrTa_2O_9$,[36-42] $Bi_2AB_2O_9$ (*A* = Ca, Sr, Ba; *B* = Nb, Ta),[37, 43, 44] $Bi_2W_2O_9$[23, 45].

Most of the Aurivillius phases share common structural characteristics. At high temperatures, they crystallize in the tetragonal *I*4/*mmm* space group, which is referred to as the high symmetry parent structure for the entire family. At low temperatures, the majority of the Aurivillius phases undergo octahedral tilting leading to a transition into a lower-symmetry polar orthorhombic ground state, where the *a* and *b* unit cell parameters remain nearly identical.

1.2.2 Dion-Jacobson Phases

The Dion-Jacobson phases were first identified by M. Dion et al. in 1981.[46] These phases have not been extensively investigated however there has been a recent resurgence of interest in them. They have a general formula $A'A_{n-1}B_nO_{3n+1}$, where *n* (> 1) is the number of the BO_6 octahedral layers, and the *A'* cation separates the $A_{n-1}B_nO_{3n+1}$ perovskite-like layers (**Figure 1.4**).[46, 47]

The ideal, aristotype structure is tetragonal of *P*4/*mmm* symmetry. The *n* = 1 member of this family is $A'B^{vii}O_4$ but no single-layer Dion-Jacobson phases have been reported. This is due to the lack of suitable *B*-site cations for this formula that would adopt octahedral symmetry. The 12-coordinated *A*-site is typically occupied by di- or trivalent cations Ca^{2+}, Sr^{2+}, Ba^{2+}, Pb^{2+}, Bi^{3+}, or Ln^{3+}.[48-50] The *B*-site, which is 6-coordinated, is occupied by cations such as Ti^{4+}, Nb^{5+}, or Ta^{5+}.[51-53] The *A'* cation is typically an alkali cation such as Cs^{+}, Rb^{+}, Li^{+}, H^{+}, or Ag^{+}.[54, 55] Oxyfluoride Dion-Jacobson phases have also been investigated.[56-58]

A few well studied Dion-Jacobson phases include:

(I) Odd layered: $KCa_2Nb_3O_{10}$,[59] $A'La_2Ti_2TaO_{10}$ (A' = Cs, Rb),[60] $CsBi_2Ti_2NbO_{10}$.[61]

(II) Even layered: $A'BiNb_2O_7$ (A' = Cs, Rb),[54] $RbLaNb_2O_7$,[62] $KLaNb_2O_7$.[63]

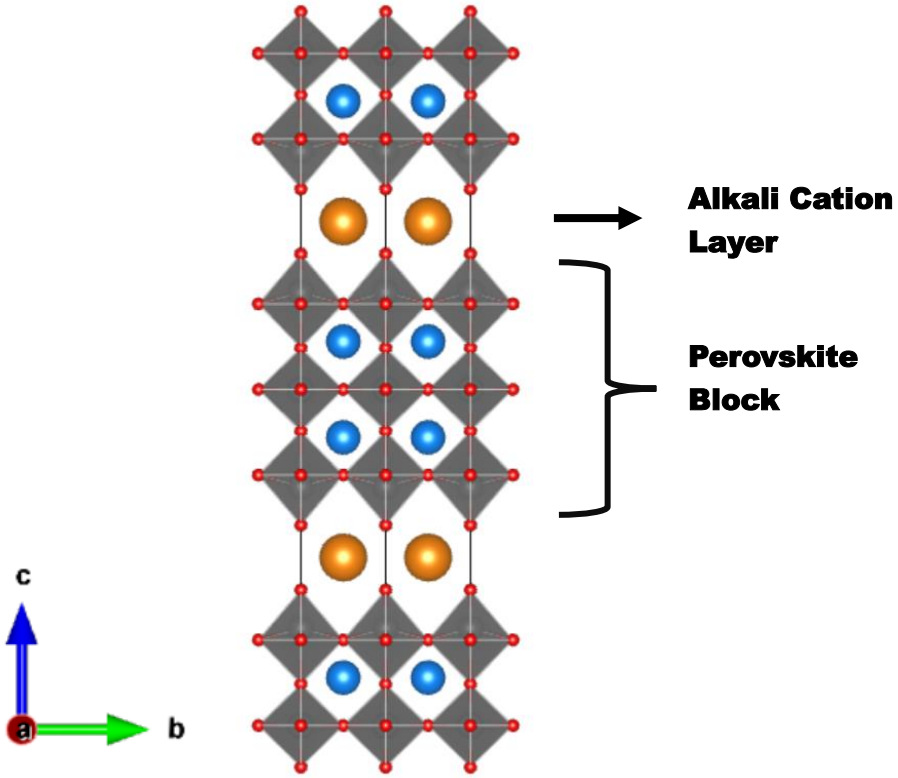

Figure 1.4: Illustration of the parent n = 3 Dion-Jacobson Phase described by $P4/mmm$ symmetry. A' and A cations, and BO_6 octahedra are shown in orange, blue and grey.

1.2.3 Ruddlesden-Popper Phases

The Ruddlesden-Popper phases were first identified through research on K_2NiF_4-type structure compounds which consists of layers of corner-sharing NiF_6 octahedra separated by rocksalt-like interlayers containing potassium.[64] Attempts to develop the oxide analogues resulted in the successful synthesis of compounds such as Sr_2TiO_4, Ca_2MnO_4 and $SrLaAlO_4$.[64] With successful structure determination of $Sr_3Ti_2O_7$, researchers recognized a new family of layered perovskite-related materials with the general formula $A_2[A_{n-1}B_nO_{3n+1}]$, where n represents the number of the BO_6 octahedral layers (**Figure 1.5**).[65]

Similar to the Dion-Jacobson structure, the Ruddlesden-Popper structure consists of perovskite-like slabs separated by AO interlayers. This interlayer region resembles the rocksalt (NaCl) structure. Like Aurivillius phases, at high

temperatures, they also crystallize in the tetragonal *I*4/*mmm* space group, which is referred to as the high symmetry parent structure for the entire family. The *A*-site is typically occupied by cations such as Ca^{2+}, Sr^{2+}, Ba^{2+} and Ln^{3+} while the *B*-site is usually occupied by a transition metal for example Ni^{2+}, Mn^{2+}, Mn^{4+}, Ru^{4+}, Ti^{4+}.[66-69]

A few well studied Ruddlesden-Popper phases include:

(I) Odd layered: $NaLnTiO_4$ (*Ln* = La, Pr, Nd, Sm, Eu, Gd, Y),[70] Sr_2RuO_4,[71] $Ca_4Ti_3O_{10}$,[65] $A_2La_2Ti_3O_{10}$ (*A* = Na, K, Rb).[72]

(II) Even layered: $A_3Ti_2O_7$ (*A* = Ca, Sr),[66] Sr_3FeRuO_7,[73] $LaCa_2Mn_2O_7$.[67]

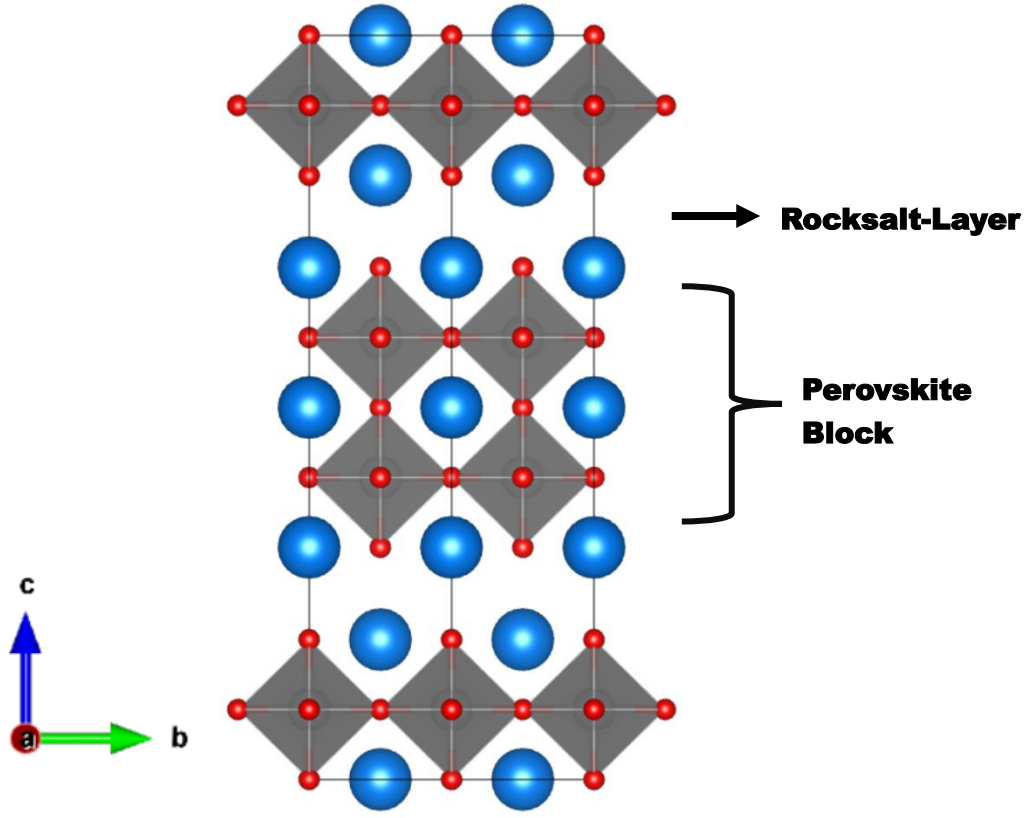

Figure 1.5: Illustration of the parent *n* = 2 Ruddlesden-Popper Phase described by *I*4/*mmm* symmetry. *A* cation, and BO_6 octahedra are shown in blue and grey.

1.3 Understanding Ferroelectricity in Layered Perovskite-Related Materials

Complex oxides, particularly ABO_3 perovskite oxides, have captivated the interest of solid-state scientists because of their fascinating physical properties such as ferroelectricity, piezoelectricity, optical properties, and technological applications.[74-77] In bulk ABO_3 perovskites, second-order Jahn-Teller (SOJT) distortions stabilise the polar structures whereas in the family of layered perovskite-like phases, the

polar and ferroelectric materials can arise from either SOJT distortions or the hybrid improper mechanism. This section provides an overview of the mechanisms of ferroelectricity and antiferroelectricity in layered perovskite-related materials, specifically the Aurivillius, Dion-Jacobson and Ruddlesden-Popper phases with a particular focus on how polar phases can be stabilised in these materials.

1.3.1 Ferroelectric Materials

Ferroelectrics are materials with a polar ground state that exhibit spontaneous polarization in the absence of an applied electric field.[78] This polarization results from a net displacement of cations relative to anions, causing the centres of positive and negative charge to no longer coincide in the material.[79] In order to be classed as a ferroelectric, a material must be able to switch the direction of polarization i.e. the polarisation state can be reversed by applying an external electric field.[3] Most ferroelectric materials undergo a structural phase transition from a high temperature paraelectric (non-ferroelectric) phase to a low temperature ferroelectric phase.

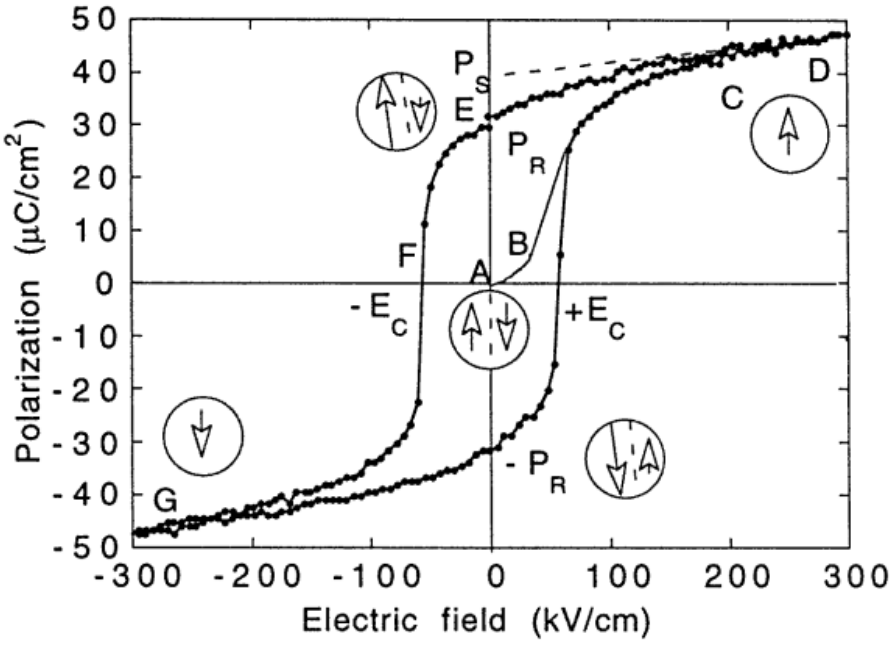

Figure 1.6: The *P-E* hysteresis loop of ferroelectric materials, where circles with arrows illustrate the polarization state of the material at the corresponding electric fields.(reproduced from reference 1)[1]

The symmetry of the ferroelectric phase is always lower than the paraelectric phase. The ferroelectric properties of a material are studied using a *P-E* hysteresis loop. In

dielectric materials, polarization varies linearly with the applied electric field at low fields. However, in ferroelectric materials, this relationship is nonlinear (**Figure 1.6**).

A ferroelectric specimen that has never been subjected to an external electric field is referred to as a virgin ferroelectric specimen. If the virgin ferroelectric specimen is exposed to an external electric field, its polarization initially increases linearly with field strength at small applied field values (segment AB in **Figure 1.6**). As the field strength increases, the domains along the direction of the field grow whilst others shrink, resulting in a nonlinear polarization response (segment BC). Once all domains are aligned (point C), the material starts exhibiting a linear response until saturated (segment CD). When the field is reduced, the domains do not reorientate instantaneously, the polarization lags behind the applied field. This lag arises because the domain reorientation requires the domain walls to overcome energy barriers caused by interactions between dipoles, defects, and lattice pinning. The field must be reversed to point F to bring polarization to zero. This field is called the coercive field, E_C. Further increasing the field strength in the opposite direction realigns dipoles in the opposite direction, reaching saturation (point G). The field strength is then reduced to zero and reversed to complete the cycle. The existence of a hysteresis loop in a material implies that the substance possesses spontaneous polarization, i.e. polarization when the applied field is zero.

1.3.2 Symmetry Requirements for Ferroelectricity

The symmetry of a crystal structure can be described by one of the 32 point groups. According to Neumann's principle, this point group has important consequences for the properties of a material as their symmetry elements must, at least, exhibit the same symmetry as the point group of the crystal.[80]

Point groups are divided into two categories: centrosymmetric and non-centrosymmetric. Centrosymmetric point groups possess an inversion centre, meaning that an any point (*x,y,z*) in the crystal there is a corresponding point (*-x,-y,-z*) which is identical. On the other hand, non-centrosymmetric point groups do not possess an inversion centre, making them potential candidates for certain polar properties. Of the 32 point groups, 11 are centrosymmetric and 21 are non-centrosymmetric.[74] Only 10 of the non-centrosymmetric point groups are polar and therefore are compatible with polar properties such as ferroelectricity.[5] **Table 1** summarizes the crystal systems and point groups that can have ferroelectricity.

Table 1: Crystal systems and crystallographic point groups compatible with describing ferroelectric phases.

Crystal System	Polar Point Groups
Hexagonal	6, 6*mm*
Tetragonal	4, 4*mm*
Trigonal	3, 3*m*
Orthorhombic	*mm*2
Monoclinic	2, *m*
Triclinic	1

1.3.3 Mechanisms of Ferroelectricity in Layered Perovskite-Related Materials

The mechanisms by which the polar phases can be stabilised in layered perovskite related materials are namely, proper and hybrid improper ferroelectricity mechanisms. Before discussing these mechanisms in detail, it is useful to understand Landau theory, which is one of the most useful and successful approaches for understanding different types of ferroelectrics.

1.3.3.1 Landau Theory

Landau theory is phenomenological framework for understanding phase transitions (here ferroelectric phase transitions).[81] In this approach, the Landau free energy F is expressed in powers of the order parameter. An order parameter is a physical quantity that is zero in the high temperature (paraelectric) phase but becomes nonzero below the phase transition temperature T_c. This theory provides a way to describe primary and secondary order parameters (or modes).

I. The primary order parameter (mode) is the main structural distortion that derives the ferroelectric phase transition. As the system approaches the critical transition temperature (T_c), the frequency of this mode decreases and eventually goes to zero at T_c. This phenomenon is called softening of modes. The softening signals that the lattice is becoming unstable with respect to this distortion.

II. The secondary order parameters (modes) are distortions that are not independently unstable and are induced by the condensation of the primary mode. These modes do not independently drive the phase transition.

Landau theory also helps us understand how different order parameters couple to one another. Of particular importance to layered perovskite-related materials is trilinear coupling, where the primary order parameters couple linearly to secondary order parameter. This trilinear coupling can stabilise a polar structure even when polarisation is not the primary order parameter. The difference between primary and secondary order parameters can be established experimentally, for example by monitoring the softening of modes as the transition temperature T_c is approached. The primary mode is identified as the one whose frequency decreases to zero at T_c.

When the order parameter is taken as the polarisation Q_p, the Landau free energy can be written as:

$$F = F_0 + \frac{1}{2}\alpha Q_P^2 + \frac{1}{4}\beta Q_P^4 + \frac{1}{6}\gamma Q_P^6 \qquad \textbf{(1.2)}$$

Where

- F_0 is the free energy when the polarization is zero.
- α is a temperature dependent coefficient, expressed as $\alpha = \alpha_0(T - T_c)$
- β is a temperature-independent coefficient. Its sign indicates the nature of phase transition:
  - i. If $\beta > 0$, the transition is second-order (continuous)
  - ii. If $\beta < 0$, the transition is first-order (discontinuous)
- The coefficient γ must be positive in a stable material.

Landau theory can also be connected to irreducible representations (irreps) discussed in **Section 1.1.3**. Within the framework of this theory, the amplitude of each irrep (distortion mode) can be interpreted as the magnitude of an order parameter. The amplitude of the irrep becomes nonzero below the phase transition temperature T_c. This provides a way of classifying proper and hybrid improper ferroelectrics based on which irreps act as the primary order parameter and which are induced via coupling.

1.3.3.2 Proper Ferroelectricity Mechanism

In proper ferroelectrics, polarisation is the primary Landau order parameter and the paraelectric - ferroelectric phase transition is due to the polar displacement of cations relative to anions.[82] Due to this displacement of cations, inversion symmetry is broken resulting in a net polarization, leading to a non-centrosymmetric polar phase.

The phase transition involves not only atomic displacements but also spontaneous strain, which acts as a secondary order parameter. This strain couples to the polarisation and becomes nonzero only in the presence of it. In this case, the free energy can be written as:

$$F = F_0 + \frac{1}{2}\alpha Q_P^2 + \frac{1}{4}\beta Q_P^4 + \frac{1}{2}\alpha_\epsilon Q_\epsilon^2 + \frac{1}{4}\beta_\epsilon Q_\epsilon^4 + \gamma Q_\epsilon Q_P^2 \qquad \textbf{(1.3)}$$

Here Q_ϵ is the strain and α_ϵ and β_ϵ are coefficients. The additional terms in the equation show that the polarisation and strain are coupled.

In $BaTiO_3$, if only the strain is considered and the atoms are fixed at their high-symmetry positions, the symmetry reduces from cubic $Pm\bar{3}m$ to tetragonal *P*4/*mmm*, which is higher than what is observed experimentally. However, if the atoms are displaced without unit cell deformation, the symmetry lowers to polar *P*4*mm*, consistent with the reported symmetry.[83] This shows that the polarisation induced by the atomic displacements is the primary order parameter while strain is the secondary order parameter which couples linearly to the polarisation and becomes nonzero only in its presence. Thus, $BaTiO_3$ is a proper ferroelectric.

The proper mechanism is commonly observed in materials that contain d^0 or ns^2np^0 (inert pair) cations which favour lower symmetry coordination environments.[74] This mechanism is often attributed to the second-order Jahn-Teller effect (SOJT), in which a structural distortion lowers the symmetry to allow mixing between anion and cation orbitals.

Another example of a proper ferroelectric is perovskite $PbTiO_3$ (which contains d^0 Ti^{4+} ions). In its high temperature paraelectric phase, $PbTiO_3$ adopts a high symmetry cubic $Pm\bar{3}m$ perovskite structure, where Pb^{2+} is a 12-coordinated cation and TiO_6 octahedra are corner linked. Upon cooling below 490°C, it undergoes a displacive phase transition to a tetragonal *P*4*mm* polar, ferroelectric phase in which

the significant polar displacement is from Pb^{2+} ions as compared to the oxide lattice.[84, 85]

1.3.3.3 Hybrid Improper Ferroelectricity Mechanism

Unlike proper ferroelectrics, where polarisation is the primary order parameter, in hybrid improper ferroelectrics the phase transition involves a combination of non-polar distortions, typically rotations or tilts of BO_6 octahedra. These distortions act as the primary order parameter which break the inversion symmetry and couple with the polar distortion, ultimately stabilising the polar structure.[86-88] In this case, polarisation is the secondary order parameter, arising from the coupling rather than from an independent lattice instability. The non-polar structural distortions often arise due to ion size mismatch effects.

For example, $Ca_3Mn_2O_7$ and $Ca_3Ti_2O_7$ undergo a phase transition from tetragonal *I*4/*mmm* to polar *A*2$_1$*am* space group. The in-plane polar Γ_5^- (a,a) displacement is stabilised by a combination of in-plane octahedral tilts (X_3^-(a;0)) and out-of-plane tilts (X_2^+ (a;0)).[87] In this case, the free energy can be written as:

$$F = F_0 + \alpha_{200}Q_P^2 + \alpha_{020}Q_{X_2^+}^2 + \alpha_{002}Q_{X_3^-}^2 + \beta_{400}Q_P^4 + \beta_{040}Q_{X_2^+}^4 + \beta_{040}Q_{X_3^-}^4 + \gamma_{220}Q_P^2Q_{X_2^+}^2 + \gamma_{202}Q_P^2Q_{X_3^-}^2 + \gamma_{022}Q_{X_2^+}^2Q_{X_3^-}^2 + \delta Q_P Q_{X_2^+}Q_{X_3^-} \quad \textbf{(1.4)}$$

Here Q_P is the amplitude of the in-plane Γ_5^- polar mode. Although the Γ_5^- mode can break inversion and produce polarisation, it does not produce the experimentally observed structure of *A*2$_1$*am* symmetry. Instead, the combination of the X_3^- and X_2^+ modes establishes the *A*2$_1$*am* symmetry and makes up a hybrid primary order parameter that drives the transition to the ferroelectric phase. The Γ_5^- mode couples to this hybrid order parameter, enhancing the macroscopic polarisation, but does not itself drive the transition.

Understanding the connection between mechanisms of ferroelectric phase transitions, bonding and crystal chemistry is an extremely powerful strategy for discovering new polar and ferroelectric materials. By understanding how electronic factors (proper mechanism), geometric factors (hybrid improper mechanism) or a combination of both contribute to the stabilisation of polar structures, researchers can better predict and design materials with optimised properties. The following sections discuss these mechanisms in detail in perovskite-related structures.

1.3.4 Ferroelectricity in Aurivillius Phases

The Aurivillius family is well known for its ferroelectric behaviour.[36, 89] In these phases, the primary distortion mode is polar and are often accompanied by rotations of BO_6 octahedra. Hence these materials are classed as proper ferroelectrics.

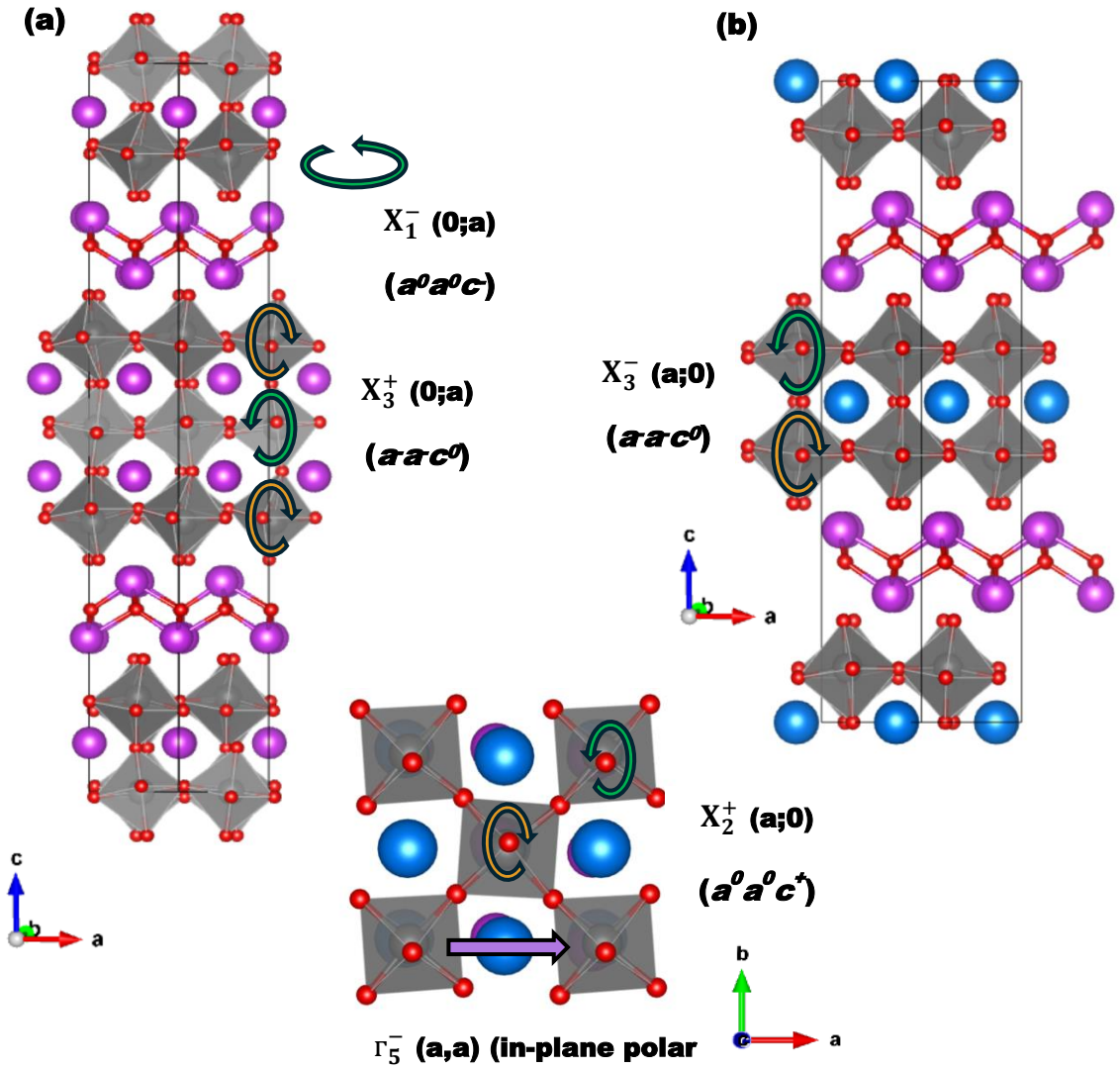

Figure 1.7: The high symmetry reference structure of AP phases is described by *I*4/*mmm* symmetry. Illustration of (a) the polar *B*2*eb* phase of an *n* = 3 Aurivillius phase and (b) polar $A2_1am$ phase of an *n* = 2 Aurivillius phase highlighting rotations of BO_6 octahedra (indicated by green and orange arrows) and in-plane polar displacements (purple arrow). *A*, *B*, Bi and O ions are shown in blue, grey, purple and red, respectively, and BO_6 octahedra are depicted in grey.

The *B*-site cation is almost always a d^0 transition metal cation, such as Ti^{4+}, Nb^{5+}, Ta^{5+}, W^{6+}, which undergoes out-of-centre displacements due to SOJT effect allowing mixing between d^0 and O 2p orbitals and lowering the symmetry to stabilise the polar structure.[90] Similarly, the SOJT can also stabilise displacements of ns^2np^0 cations, such as Bi^{3+} and Pb^{2+}, by allowing mixing between ns^2np^0 and O 2p orbitals. The

$6s^2$ Bi^{3+} cations displace relative to the surrounding anions giving a macroscopic in-plane polarization and lowering the symmetry to stabilise the polar structure.[91]

The polar displacements give larger energy gains than rotations of the BO_6 octahedra in these materials.[92] An important note to make here is that although the way to differentiate between proper and hybrid improper ferroelectrics is to identify which distortion mode softens at T_c, the larger energy gain from polar distortions compared to rotations provides a tentative indication that the mechanism could be proper.

The high symmetry parent structure for the entire family is tetragonal with *I*4/*mmm* space group. Newnham proposed that even layered Aurivillius phases (*n* = 2,4) adopt the polar $A2_1am$ space group.[93] This allows for in-plane polar displacements, described by Γ_5^- (a,a), as well as rotations of BO_6 octahedra about the in-plane axis, described by X_3^- (a;0) (**Figure 1.7(b)**). These distortions together sufficiently lower the symmetry to also allow BO_6 octahedral rotations about the out-of-plane axis, described by X_2^+ (a;0).[94] The interplay between these structural distortions can lead to different phase transition sequences:

(I) A single paraelectric (*I*4/*mmm*) → ferroelectric ($A2_1am$) transition, where Γ_5^- displacements and X_3^- tilts freeze in at the same temperature. This is an avalanche-type transition where multiple modes appear simultaneously making it difficult to identify which mode drives the ferroelectric phase transition. Therefore, this transition cannot be classified as proper or improper.

(II) A two-step transition, where the X_3^- tilt first induces a high-temperature paraelectric (*I*4/*mmm*) → paraelectric (*Amam*) transition, followed by the freezing-in of Γ_5^- displacements coupled with X_2^+ tilts at lower temperatures, leading to the ferroelectric ($A2_1am$) phase.[95] Important to note here is that with respect to the parent *Amam* structure, the two modes Γ_5^- and X_2^+ will transform as the same irrep of Γ^- character. Therefore, with reference to *Amam* parent structure this transition would always be classified as proper.

The in-plane polar Γ_5^- displacement is dominant in odd layered (*n* = 1,3) Aurivillius phases as well which is accompanied by in-plane rotations of the BO_6 octahedra (X_3^+). For *n* = 3 phases, *B*2*eb* symmetry is widely reported, consistent with Newnham.[92] This symmetry allows Γ_5^- (a,a) displacement along with rotations of the octahedra about the in-plane axis (X_3^+ (0;a)) and out-of-plane axis (X_1^- (0;a)).

1.3.5 Ferroelectricity in Dion-Jacobson Phases

Many even layered Dion-Jacobson (DJ) phases have been identified as hybrid-improper ferroelectrics where the non-polar distortions typically the tilting/rotation of BO_6 octahedra are the primary order parameter. In these layered perovskite-related materials, the octahedral rotations and tilts have larger energy gains than the polar distortions.*[87] Therefore, the key difference between the Aurivillius and DJ phases lies in the relative energies of their rotational and polar distortions. The energy gains in the DJ phases are driven more by geometric factors than electronic factors.

Benedek's theoretical work shows that in n = 2 DJ phases, in-plane polar Γ_5^- (a,a) displacements can be stabilised through a combination of in-plane octahedral tilts (M_5^-(a,0)) and out-of-plane tilts (M_2^+ (a)) (**Figure 1.8(a)**).[96] Zhu et al. further explored how cation size influences these tilts in the n = 2 $A'NdB_2O_7$ (A' = Cs, Rb; B = Nb, Ta) DJ phases.[97] Asaki et al. and Chen et al. confirmed the ferroelectric nature of n = 2 DJ phases by demonstrating switchable polarization in them.[98, 99] Vascos et al. study on $CsLn_2Ti_2NbO_{10}$ (Ln = La, Nd) phases showed the existence of hybrid-improper ferroelectricity in n = 3 DJ phases, where a combination of in-plane and out-of-plane octahedral rotations stabilise the polar displacement.[100]

Although the DJ family is better known for its hybrid improper ferroelectricity, having Bi^{3+} cations on A sites has been shown to change the relative energies of distortions in some DJ phases, making these bismuth analogues proper ferroelectrics.† In these cases, the distortion that gives that largest energy gain is the polar Γ_5^- displacement.[61, 96, 101] For example, in the n = 2 $CsBiNb_2O_7$ phase,[94] the combination of in-plane polar Γ_5^- displacement and rotations of NbO_6 octahedra about the in-plane axis, described by M_5^-, sufficiently lowers the symmetry to allow out-of-plane octahedral rotations, described by M_2^+, giving a polar ground state of $P2_1am$ symmetry, where Γ_5^- gives the largest energy gain. Similarly, in n = 3 $A'Bi_2B_3O_{10}$ (A' = Cs, Rb; B = Ti, Nb, Ta)[61, 101] phases, the largest energy gain is the polar Γ_5^- displacement which is indicative that the mechanism could be proper. This suggests that the phase transition from the high symmetry paraelectric phase to lower symmetry ferroelectric phase could be driven by the polar Γ_5^- displacements. These displacements, accompanied by the rotations of BO_6 about the in-plane axis,

* This only provides a tentative indication that the mechanism of ferroelectricity could be hybrid improper.

† It is important to mention here that the presence of Bi^{3+} cations on A sites does not automatically guarantee a proper mechanism of ferroelectricity.

described by A_5^+ (a,0) further allow the out-of-plane octahedral rotations, described by A_1^- (a), give a polar ground state of *Ima*2 symmetry.

The examples above show that within this family of layered perovskite materials, it is possible to tune between proper and hybrid improper mechanisms of ferroelectricity.

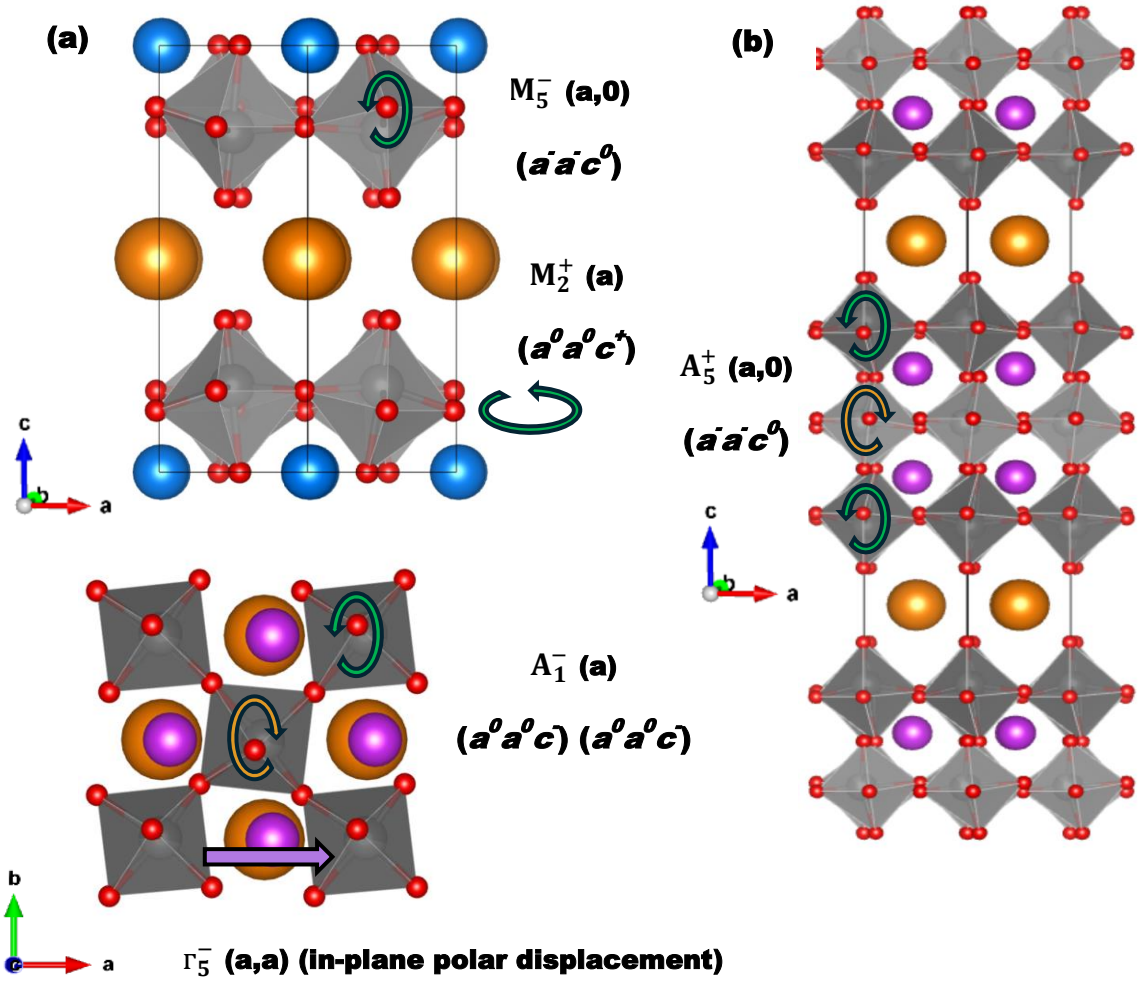

Figure 1.8: The high symmetry reference structure of DJ phases is described by *P*4/*mmm* symmetry. Illustration of (a) the polar $P2_1am$ phase of an n = 2 DJ phase and (b) polar *Ima*2 phase of n = 3 $CsBi_2Ti_2NbO_{10}$ DJ phase highlighting rotations of BO_6 octahedra (indicated by green and orange arrows) and in-plane polar displacements (purple arrow). *A'*, *A*, *B,* Bi and O ions are shown in orange, blue, grey, purple and red, respectively, and BO_6 octahedra are depicted in grey.

1.3.6 Ferroelectricity in Ruddlesden-Popper Phases

The Ruddlesden-Popper phases undergo structural distortions similar to those in Aurivillius phases, as they both adopt an ideal high symmetry paraelectric phase of *I*4/*mmm* symmetry. However, unlike the Aurivillius phases discussed above, which are proper ferroelectrics, the even layered RP phases exhibit hybrid improper ferroelectricity, where octahedral rotations and tilts have larger energy gains and stabilise the polar displacements.* This might be due to the inherently more "geometric" nature of the RP phases as they lack $6s^2$ inert pair cations with a tendency for the SOJT effect, as seen in the Aurivillius phases. Similar to DJ phases, the energy gains in the RP phases are also driven more by geometric factors than electronic factors.

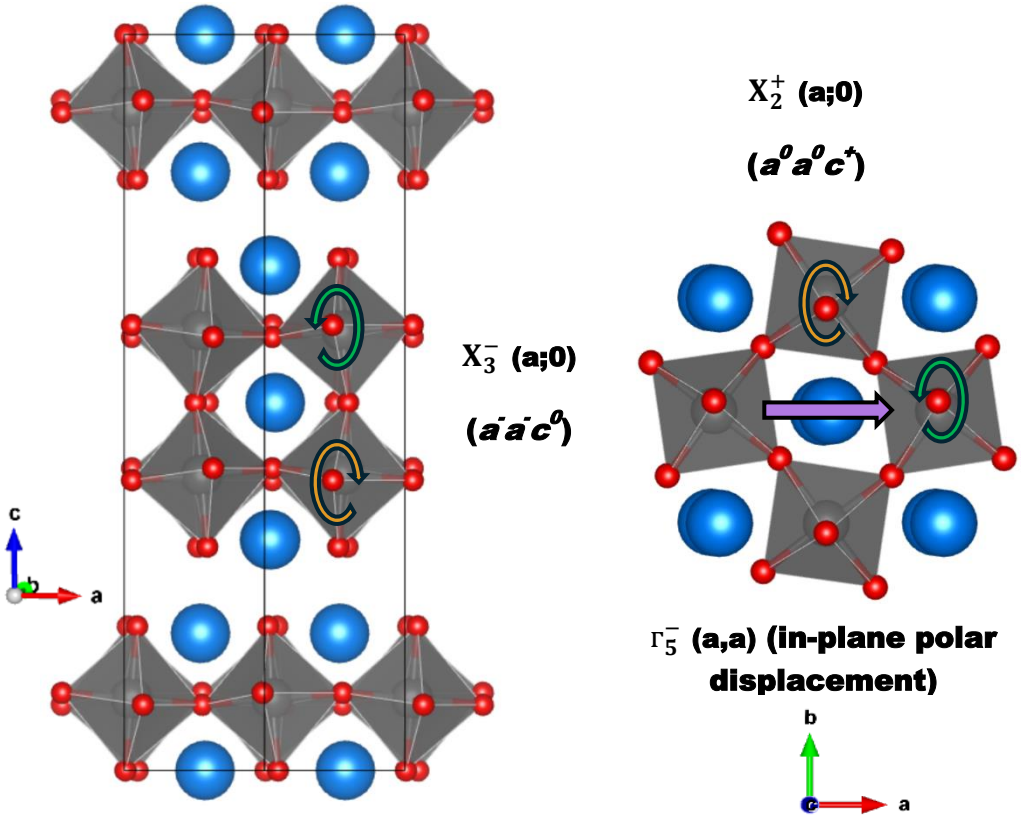

Figure 1.9: The high symmetry reference structure of RP phases is described by *I*4/*mmm* symmetry. An illustration of the polar $A2_1am$ phase of an n = 2 RP phase highlighting rotations of BO_6 octahedra (indicated by green and orange arrows) and in-plane polar displacements (purple arrow). *A*, *B,* and O ions are shown in blue, grey, and red, respectively, and BO_6 octahedra are depicted in grey.

* This only provides a tentative indication that the mechanism of ferroelectricity could be hybrid improper.

Benedek and Fennie's work shows that in *n* = 2 $Ca_3Mn_2O_7$ and $Ca_3Ti_2O_7$ RP phases, in-plane polar Γ_5^- (a,a) displacement can be stabilised through a combination of in-plane octahedral tilts (X_3^-(a;0)) and out-of-plane tilts (X_2^+ (a;0)), giving a polar ground state of $A2_1am$ symmetry (**Figure 1.9**).[87] Another *n* = 2 RP hybrid-improper ferroelectric, $Sr_3Zr_2O_7$, has also been reported to crystalize in $A2_1am$ ground state, though it undergoes a series of phase transitions upon warming.[102] Computational studies suggest that $Sr_3Zr_2O_7$ has a metastable non-polar phase of *Pnab* symmetry that is only slightly higher in energy than its polar ground state, suggesting that the energy landscape of some hybrid-improper ferroelectrics can be quite shallow.[102] This highlights the competition between polar and antipolar structures in these materials.

In the RP ferroelectric $Li_2Sr_{1-x}Ca_x(Nb_{1-x}Ta_x)_2O_7$, reported by Nakano et al.[103] by varying the composition, the authors were able to tune between paraelectric, ferroelectric and antipolar phases. Their study also showed that at low *x*, the SOJT effect predominantly drives the phase transition, whereas for high *x* (>0.5), geometrical instabilities become the dominant factor. This demonstrates the delicate balance between competing electronic and geometric effects in some RP phases and suggests the possibility to tune them by tuning the material's composition.

1.4 Antiferroelectricity

Antiferroelectrics are materials that have a non-polar ground state in which adjacent dipoles are spontaneously ordered in such a way that they are in opposite direction to each other, cancelling out net polarization in the absence of an applied electric field.[104] In addition, these materials have a polar, ferroelectric metastable which is only slightly higher in energy than the non-polar, antiferroelectric ground state. When a sufficiently strong electric field is applied, these materials can undergo a phase transition from the non-polar, antiferroelectric state to the polar, ferroelectric state.[105] A key characteristic of antiferroelectrics is their double hysteresis loop. Dielectric polarization measurements for *P-E* hysteresis loop are a good experimental method to find the presence of an antiferroelectric phase.

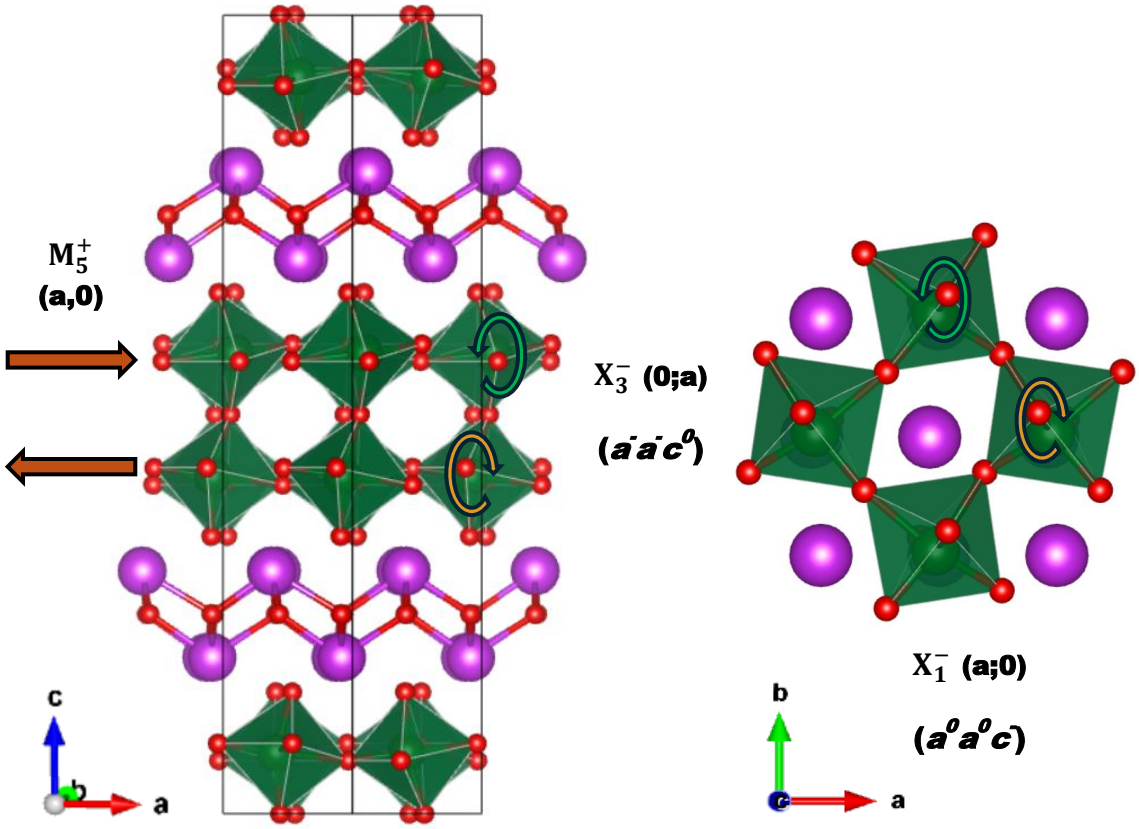

Figure 1.10: The high symmetry reference structure of AP phases is described by *I*4/*mmm* symmetry. An illustration of the antipolar *Pnab* phase of $Bi_2W_2O_9$ highlighting rotations of WO_6 octahedra (indicated by green and orange arrows) and in-plane antipolar displacements of W^{6+} ions (brown arrows). Bi, W and O ions are shown in purple, green, and red, respectively, and WO_6 octahedra are depicted in green.

Most Aurivillius phases crystalize in an orthorhombic polar ground state, however exceptions do exist. For example, the *n* = 2 *A*-site deficient $Bi_2W_2O_9$ Aurivillius phase adopts an antipolar *Pnab* ground state.[23] This space group allows the in-plane antipolar displacements of W^{6+} and Bi^{3+} cations (M_5^+), in-plane octahedral tilts (X_3^-) and out-of-plane octahedral rotations (X_1^-) (**Figure1.10**). The largest energy gains are from the polar/antipolar displacements of W^{6+} cations due to cation's strong tendency of SOJT. The first principles calculations suggest that there exists a polar metastable state of $A2_1am$ symmetry only slightly higher in energy (34 meV/f.u.), above the antipolar ground state in $Bi_2W_2O_9$. However, experimental attempts to access this polar $A2_1am$ phase have been unsuccessful.[23] From calculations it was predicted that a field of about 200 kV/cm could stabilise the polar phase, but experimental measurements up to 250 kV/cm failed to induce the ferroelectric transition. This is possibly due to the underestimation of the switching field or the barrier may be too high.

1.5 Summary

This chapter has introduced the three main families of layered perovskite related materials: Aurivillius phases, Dion-Jacobson phases and Ruddlesden-popper phases. We have discussed how structural distortions in these materials can be described using Glazer notations as well as by symmetry-adapted modes (irreps), which also provides a way of comparing different distortions in the structure.

The two mechanisms of ferroelectricity namely proper ferroelectricity and hybrid improper ferroelectricity have been discussed with examples from each family of the layered perovskites mentioned above. It is important to understand the difference between the two mechanisms as it determines whether the polarisation arises as a primary order parameter (proper) or as a secondary effect induced by coupling to non-polar distortions (hybrid improper).

We have also discussed how the choice of *A*-site and *B*-site cations influences the structure and distortions in layered perovskites. Understanding this particularly important because the aim of this thesis is to investigate how structure-composition relationship in layered perovskite-related materials can be exploited to tune the ground states and the two mechanisms of ferroelectricity.

1. D. Damjanovic, *Reports on progress in physics*, 1998, **61**, 1267.
2. K. Manjunath and C. G. Thimmanna, *Current Nanomaterials*, 2016, **1**, 145-155.
3. K. M. Rabe, M. Dawber, C. Lichtensteiger, C. H. Ahn and J.-M. Triscone, *Modern physics of ferroelectrics: Essential background*, Springer, 2007.
4. P. Ghosez, *Microscopic Properties of Ferroelectric Oxides from First Principles: Selected Topics: Troisième Cycle de la Physique en Suisse Romande, Spring 2002*, Université de Lausanne, 2002.
5. N. A. Spaldin, in *Physics of Ferroelectrics: A Modern Perspective*, Springer, 2007, pp. 175-218.
6. V. Goldschmidt, *Naturwissenschaften*, 1926, **14**, 477-485.
7. E. L. Carranza and R. Cox, *Journal of Physics and Chemistry of Solids*, 1979, **40**, 413-420.
8. N. Wilson, J. Muscat, D. Mkhonto, P. Ngoepe and N. Harrison, *Physical Review B—Condensed Matter and Materials Physics*, 2005, **71**, 075202.
9. H. Megaw, *A working approach, Studies in physics and chemistry*, 1973, **10**.
10. A. M. Glazer, *Acta Crystallographica Section B: Structural Crystallography and Crystal Chemistry*, 1972, **28**, 3384-3392.
11. A. Glazer, *Acta Crystallographica Section A: Crystal Physics, Diffraction, Theoretical and General Crystallography*, 1975, **31**, 756-762.
12. E. Colla, I. Reaney and N. Setter, *Journal of Applied Physics*, 1993, **74**, 3414-3425.
13. I. M. Reaney, E. L. C. E. L. Colla and N. S. N. Setter, *Japanese Journal of Applied Physics*, 1994, **33**, 3984.
14. A. M. Glazer, *Structural Science*, 1972, **28**, 3384-3392.
15. S. Kerman, B. J. Campbell, K. K. Satyavarapu, H. T. Stokes, F. Perselli and J. S. O. Evans, *Foundations of Crystallography*, 2012, 68, 222-234.
16. B. Aurivillius, *Arkiv kemi*, 1949, **1**, 463-480.
17. S. Borg and G. Svensson, *Journal of Solid State Chemistry*, 2001, **157**, 160-165.
18. Y. Idemoto, T. Takahashi, N. Koura and C.-K. Loong, *Japanese journal of applied physics*, 2006, **45**, 5091.
19. S. M. Blake, M. J. Falconer, M. McCreedy and P. Lightfoot, *Journal of Materials Chemistry*, 1997, **7**, 1609-1613.
20. O. A. Fregoso, *J. Appl. Phys*, 1997, **81**, 1387-1391.
21. K. Srinivas and A. James, *Journal of applied physics*, 1999, **86**, 3885-3889.
22. T. Zeng, X. Yu, S. Hui, Z. Zhou and X. Dong, *Materials Research Bulletin*, 2015, **68**, 271-275.
23. H. Djani, E. E. McCabe, W. Zhang, P. S. Halasyamani, A. Feteira, J. Bieder, E. Bousquet and P. Ghosez, *Physical Review B*, 2020, **101**, 134113.
24. B. Ismunandar, *Solid State Ionics*, 1998, **112**, 281-289.
25. N. Sharma, B. J. Kennedy, M. M. Elcombe, Y. Liu and C. D. Ling, *Journal of Physics: Condensed Matter*, 2007, **20**, 025215.
26. Z. Zulhadjri, B. Prijamboedi, A. Nugroho, N. Mufti, A. Fajar and T. Palstra, *Journal of Solid State Chemistry*, 2011, **184**, 1318-1323.
27. F. Yang, P. Su, C. Wei, X. Chen, C. Yang and W. Cao, *Journal of Applied Physics*, 2011, **110**.
28. S. Tinte and M. G. Stachiotti, *Physical Review B—Condensed Matter and Materials Physics*, 2012, **85**, 224112.
29. A. Y. Birenbaum and C. Ederer, *Physical Review B*, 2014, **90**, 214109.
30. A. Castro, P. Millán, M. Martinez-Lope and J. Torrance, *Solid State Ionics*, 1993, **63**, 897-901.
31. P. Millan, A. Ramirez and A. Castro, *Journal of materials science letters*, 1995, **14**, 1657-1660.
32. A. Castro, P. Millan and B. Jimenez, *Journal of materials research*, 1998, **13**, 2565-2571.
33. J. G. Thompson, S. Schmid, R. L. Withers, A. D. Rae and J. D. F. Gerald, *Journal of Solid State Chemistry*, 1992, **101**, 309-321.
34. R. Withers, J. Thompson and A. Rae, *Journal of Solid State Chemistry*, 1991, **94**, 404-417.
35. C. H. Hervoches and P. Lightfoot, *Chemistry of materials*, 1999, **11**, 3359-3364.

36. C. A.-P. de Araujo, J. Cuchiaro, L. McMillan, M. Scott and J. Scott, *Nature*, 1995, **374**, 627-629.
37. Y. Shimakawa, Y. Kubo, Y. Nakagawa, S. Goto, T. Kamiyama, H. Asano and F. Izumi, *Physical Review B*, 2000, **61**, 6559.
38. Y. Ahn and J. Y. Son, *Solid State Sciences*, 2024, **153**, 107558.
39. K. Babooram and Z.-G. Ye, *Chemistry of materials*, 2006, **18**, 532-540.
40. Z. Huang, P. Yang, Y. Chang and J. Chu, *Journal of applied physics*, 1999, **86**, 1771-1773.
41. Z. Huang, H. Chan, K. W. Kwok and C. Choy, *Journal of materials science*, 2000, **35**, 1793-1797.
42. A. D. Rae, J. G. Thompson and R. L. Withers, *Structural Science*, 1992, **48**, 418-428.
43. R. Macquart, B. J. Kennedy and Y. Shimakawa, *Journal of Solid State Chemistry*, 2001, **160**, 174-177.
44. S. Blake, *Journal of Materials Chemistry*, 1997, **7**, 1609-1613.
45. X. Tian, Z. Gao, F. Chen, Q. Wu, C. Li, W. Lu, Y. Sun and X. Tao, *CrystEngComm*, 2018, **20**, 2669-2680.
46. M. Dion, M. Ganne and M. Tournoux, *Materials Research Bulletin*, 1981, **16**, 1429-1435.
47. A. Jacobson, J. W. Johnson and J. Lewandowski, *Inorganic chemistry*, 1985, **24**, 3727-3729.
48. F. Lichtenberg, A. Herrnberger and K. Wiedenmann, *Progress in Solid State Chemistry*, 2008, **36**, 253-387.
49. E. Syrov, O. Krasheninnikova, A. Knyazev, D. Fukina, E. Suleimanov, N. Volkova, A. Gorshkov and S. Smirnov, *Journal of Physics and Chemistry of Solids*, 2021, **156**, 110184.
50. M. Machida, J.-i. Yabunaka and T. Kijima, *Chemistry of Materials*, 2000, **12**, 812-817.
51. Y.-S. Hong, S.-J. Kim, S.-J. Kim and J.-H. Choy, *Journal of Materials Chemistry*, 2000, **10**, 1209-1214.
52. D. Hamada, W. Sugimoto, Y. Sugahara and K. Kuroda, *Journal of the Ceramic Society of Japan*, 1997, **105**, 284-287.
53. M. Machida, J.-i. Yabunaka and T. Kijima, *Chemical Communications*, 1999, 1939-1940.
54. M. Subramanian, J. Gopalakrishnan and A. Sleight, *Materials Research Bulletin*, 1988, **23**, 837-842.
55. M. Machida, T. Mitsuyama, K. Ikeue, S. Matsushima and M. Arai, *The Journal of Physical Chemistry B*, 2005, **109**, 7801-7806.
56. J.-H. Choy, J.-Y. Kim, S.-J. Kim, J.-S. Sohn and O. H. Han, *Chemistry of materials*, 2001, **13**, 906-912.
57. G. Caruntu, L. Spinu and J. B. Wiley, *Materials research bulletin*, 2002, **37**, 133-140.
58. Y. Kobayashi, M. Tian, M. Eguchi and T. E. Mallouk, *Journal of the American Chemical Society*, 2009, **131**, 9849-9855.
59. H. Fukuoka, T. Isami and S. Yamanaka, *Journal of Solid State Chemistry*, 2000, **151**, 40-45.
60. Y.-S. Hong, C.-H. Han and K. Kim, *Journal of Solid State Chemistry*, 2001, **158**, 290-298.
61. E. E. McCabe, E. Bousquet, C. P. Stockdale, C. A. Deacon, T. T. Tran, P. S. Halasyamani, M. C. Stennett and N. C. Hyatt, *Chemistry of Materials*, 2015, **27**, 8298-8309.
62. A. R. Armstrong and P. A. Anderson, *Inorganic Chemistry*, 1994, **33**, 4366-4369.
63. M. Sato, J. Abo, T. Jin and M. Ohta, *Solid State Ionics*, 1992, **51**, 85-89.
64. S. Ruddlesden and P. Popper, *Acta Crystallographica*, 1957, **10**, 538-539.
65. S. Ruddlesden and P. Popper, *Acta Crystallographica*, 1958, **11**, 54-55.
66. M. Elcombe, E. Kisi, K. Hawkins, T. White, P. Goodman and S. Matheson, *Structural Science*, 1991, **47**, 305-314.
67. M. Green and D. Neumann, *Chemistry of materials*, 2000, **12**, 90-97.
68. J. E. Millburn and J. F. Mitchell, *Chemistry of materials*, 2001, **13**, 1957-1966.
69. R. E. Schaak, D. Afzal, J. A. Schottenfeld and T. E. Mallouk, *Chemistry of materials*, 2002, **14**, 442-448.
70. K. Toda, Y. Kameo, S. Kurita and M. Sato, *Journal of alloys and compounds*, 1996, **234**, 19-25.
71. Y. Maeno, H. Hashimoto, K. Yoshida, S. Nishizaki, T. Fujita, J. Bednorz and F. Lichtenberg, *nature*, 1994, **372**, 532-534.

72. S.-H. Byeon and H.-J. Nam, *Chemistry of materials*, 2000, **12**, 1771-1778.
73. P. Battle, S. Bollen and A. Powell, *Journal of Solid State Chemistry*, 1992, **99**, 267-275.
74. P. S. Halasyamani and K. R. Poeppelmeier, *Chemistry of Materials*, 1998, **10**, 2753-2769.
75. J. B. Goodenough, *Reports on Progress in Physics*, 2004, **67**, 1915.
76. M. E. Lines and A. M. Glass, *Principles and applications of ferroelectrics and related materials*, Oxford university press, 2001.
77. S. Rahman, A. Hussain, S. Noreen, N. Bibi, S. Arshad, J. U. Rehman and M. B. Tahir, *Journal of Solid State Chemistry*, 2023, **317**, 123650.
78. J. E. House, *Introduction to Solid State Chemistry*, Elsevier, 2024.
79. G. Burns, A. Glazer and A. A. Maradudin, *Journal*, 1979.
80. H. Klapper and T. Hahn, 2016.
81. P. Chandra, P. B. Littlewood, A Landau Primer for Ferroelectrics in *Physics of Ferroelectrics: A Modern Perspective*, 2007, pp. 69-116.
82. N. A. Benedek, A. T. Mulder and C. J. Fennie, *Journal of Solid State Chemistry*, 2012, **195**, 11-20.
83. H. T. Evans, *Acta Crystallographica*, 1951, 4(4), pp. 377-377.
84. G. Shirane, R. Pepinsky, B. C. Frazer, *Acta Crystallographica 9.2*, pp. 131-140.
85. G. Shirane, J. D. Axe, J. Harada, J. P. Remeika, *Physical Review B*, 1970, 155.
86. I. Etxebarria, J. Perez-Mato and P. Boullay, *Ferroelectrics*, 2010, **401**, 17-23.
87. N. A. Benedek and C. J. Fennie, *Physical review letters*, 2011, **106**, 107204.
88. E. Bousquet, M. Dawber, N. Stucki, C. Lichtensteiger, P. Hermet, S. Gariglio, J.-M. Triscone and P. Ghosez, *Nature*, 2008, **452**, 732-736.
89. P. Fang, C. Robbins and B. Aurivillius, *Physical Review*, 1962, **126**, 892.
90. K. M. Ok, P. S. Halasyamani, D. Casanova, M. Llunell, P. Alemany and S. Alvarez, *Chemistry of materials*, 2006, **18**, 3176-3183.
91. M. W. Stoltzfus, P. M. Woodward, R. Seshadri, J.-H. Klepeis and B. Bursten, *Inorganic chemistry*, 2007, **46**, 3839-3850.
92. J. Perez-Mato, P. Blaha, K. Parlinski, K. Schwarz, M. Aroyo, L. Elcoro and Z. Izaola, *Integrated Ferroelectrics*, 2004, **62**, 183-188.
93. R. Newnham, R. Wolfe and J. Dorrian, *Materials Research Bulletin*, 1971, **6**, 1029-1039.
94. A. Snedden, C. H. Hervoches and P. Lightfoot, *Physical Review B*, 2003, **67**, 092102.
95. A. Giddings, M. Stennett, D. Reid, E. McCabe, C. Greaves and N. Hyatt, *Journal of Solid State Chemistry*, 2011, **184**, 252-263.
96. N. A. Benedek, *Inorganic Chemistry*, 2014, **53**, 3769-3777.
97. T. Zhu, T. Cohen, A. S. Gibbs, W. Zhang, P. S. Halasyamani, M. A. Hayward and N. A. Benedek, *Chemistry of Materials*, 2017, **29**, 9489-9497.
98. C. Chen, H. Ning, S. Lepadatu, M. Cain, H. Yan and M. J. Reece, *Journal of Materials Chemistry C*, 2015, **3**, 19-22.
99. S. Asaki, H. Akamatsu, G. Hasegawa, T. Abe, Y. Nakahira, S. Yoshida, C. Moriyoshi and K. Hayashi, *Japanese Journal of Applied Physics*, 2020, **59**, SPPC04.
100. V. A. Cascos, J. Roberts-Watts, C. Skingle, I. Levin, W. Zhang, P. S. Halasyamani, M. C. Stennett, N. C. Hyatt, E. Bousquet and E. E. McCabe, *Chemistry of Materials*, 2020, **32**, 8700-8712.
101. H. G. Kim, T. T. Tran, W. Choi, T.-S. You, P. S. Halasyamani and K. M. Ok, *Chemistry of Materials*, 2016, **28**, 2424-2432.
102. S. Yoshida, K. Fujita, H. Akamatsu, O. Hernandez, A. Sen Gupta, F. G. Brown, H. Padmanabhan, A. S. Gibbs, T. Kuge and R. Tsuji, *Advanced Functional Materials*, 2018, **28**, 1801856.
103. A. Nakano, H. Shirakuni, T. Nagai, Y. Mochizuki, F. Oba, H. Yokota, S. Kawaguchi, I. Terasaki and H. Taniguchi, *Physical Review Materials*, 2022, **6**, 044412.
104. C. A. Randall, Z. Fan, I. Reaney, L. Q. Chen and S. Trolier-McKinstry, *Journal of the American Ceramic Society*, 2021, **104**, 3775-3810.
105. C. Kittel, *Physical Review*, 1951, **82**, 729.

Chapter 2: Materials Synthesis and Techniques for Analysis

2.1 Synthesis Methods

The most widely used method for preparing polycrystalline powders is the solid-state method in which a mixture of starting materials is heated at high temperatures without the need for a reaction medium. In this thesis, the compounds were synthesised using this method. Small quantities (about a gram) of starting materials were ground together in an agate mortar and pestle, with a small amount of acetone to aid the mixing of the materials. The resulting ground dry powder mixtures were then pressed into pellets using a hydraulic press and subsequently heated in a furnace at high temperatures.

The solid-state reaction is inherently a slow process.[1] Although the reactants may appear to be well mixed, they may be very inhomogeneous at atomic level and require high temperatures to react as the mobility of the reacting materials is too low. To achieve atomic level mixing, counter diffusion of ions between different particles is necessary to bring atoms of different elements together in order to form the desired product in the correct ratio.

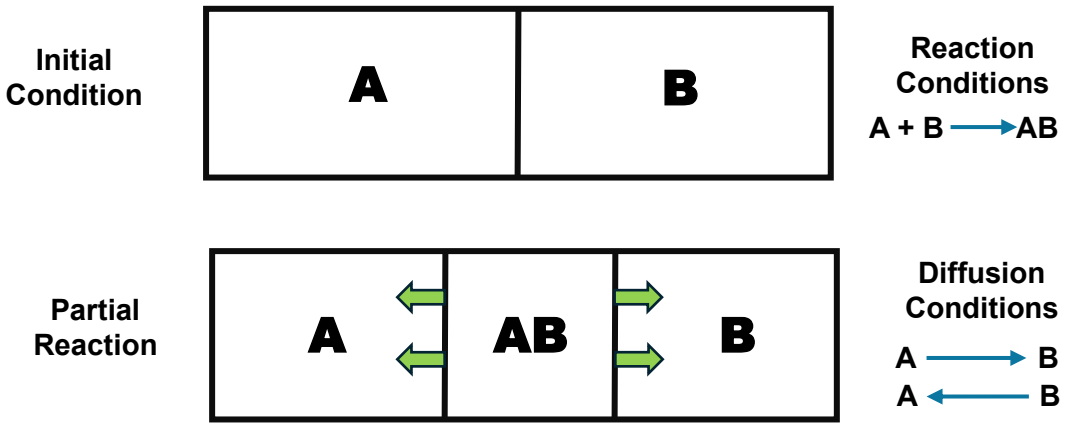

Figure 2.1: Model showing how components react across a phase boundary during the solid-state reaction.

The first step of a solid-state reactions is nucleation i.e., formation of “nucleus” of the product. A nucleus is a point where the atoms or ions have reacted to begin forming the new phase (AB), as shown in **Figure 2.1**.

At least two interfaces are formed between the nucleus/reaction product (AB) and boundary of the reactants A and B (**Figure 2.1**). This AB continues to grow outwards. As the reaction product grows in size, the distance between A and B increases. As a result, the constituent atoms must diffuse across longer distances through the growing AB phase to reach the interface and continue the reaction. Counter diffusion depends on vacant sites. The ions with sufficient thermal energy hop into new empty spaces and travel to their appropriate sites in the crystal structure, enabling continued reaction and growth.[1]

Several factors influence the success of a solid-state reaction. One key factor is the particle size of the reactants: smaller the size of the reactant particles, the faster is the reaction. This is because the reaction occurs at the points of contact between particles and reducing particle size increases the number of contact points, thereby enhancing the reaction rate. Another important factor is the temperature at which the reactants are heated. Higher temperatures accelerate the reaction but depending on the reactants, unintended or entirely different products can be formed at excessively high temperatures. Conversely, if the temperature is too low, the reaction may not proceed at all. A considerable amount of trial and error is involved in finding the perfect balance between the temperature and other reaction variables to achieve the desired product.

Topochemical reactions were used by our collaborators to synthesize desired materials in chapter 5 and chapter 6 of this thesis. It is a clever way of synthesizing new materials where new atoms, called intercalation species or guests**,** can be added into the empty sites or removed from an existing crystalline solid such that the original structure remains the same. The electrons must also be added or removed to preserve charge balance. This type of process is called a topochemical reaction.[1]

2.2 Diffraction

Diffraction is a very powerful technique widely used for identifying and analysing solid-state materials. In this thesis, X-ray powder diffraction (XRPD) is used as the main technique to monitor phase purity. For a more detailed crystallographic characterisation, studies combining X-ray and neutron powder diffraction are carried out.

Neutron powder diffraction was important to provide information about the position of light atoms such as oxygen, which cannot be precisely determined by X-ray data in the presence of heavy atoms.

2.2.1 Bragg's Law

The Bragg approach is to regard crystals as made up of layers or planes that act as semi-transparent mirrors.[1] When X-rays (or neutrons) strike these planes, some are reflected off a plane with the angle of reflection equal to the angle of incidence while the remaining are transmitted to be subsequently reflected by succeeding planes. When the path difference between X-rays scattered from successive planes, $2d\sin\theta$, is equal to an integer number of wavelengths, $n\lambda$, the scattered waves are in-phase, resulting in constructive interference and peaks in a diffraction pattern. The Bragg's law can be written as:

$$2d\sin\theta = n\lambda \tag{2.1}$$

where d is the d-spacing i.e., perpendicular distance between two adjacent planes, θ is the Bragg angle i.e., angle of incidence of the X-ray (or neutron) beam, n is a whole number and λ is the wavelength of the X-ray (or neutron) beam.

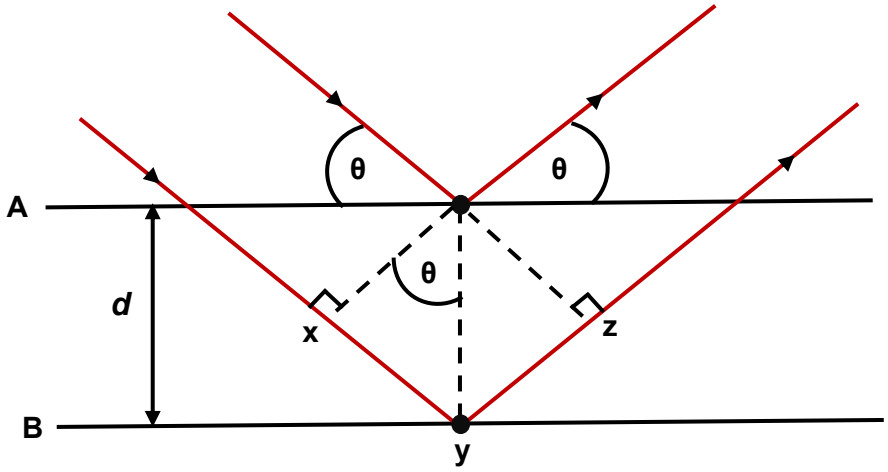

Figure 2.2: Derivation of Bragg's Law. The incident ray is diffracted off two adjacent lattice planes separated by a distance *d*.

Depending on the wavelength, angle, type of incident radiation and the distance between the adjacent planes, the intensity of the diffracted radiation forms a pattern for the crystalline material. Generally, each crystalline solid has its own characteristic pattern, referred to as its 'fingerprint' for its identification. Several

databases of such patterns have been developed for phase identification, among which the Inorganic Crystal Structure Database (ICSD) has been particularly valuable in identifying the phases synthesized and analysed in this thesis.[4]

The intensities in an X-ray diffraction pattern depend on the square of the structure factor, F(hkl), which relates to the crystal structure as described by equation **(2.2):**

$$F(hkl) = \sum_j f_j \exp\left[2\pi i\left(hx_j ky_j lz_j\right)\right] \quad \textbf{(2.2)}$$

where,

- *F(hkl)* is the structure factor, which determines whether a particular atomic arrangement will produce a peak in the X-ray diffraction for the crystal plane labelled by the Miller indices *hkl*.
- f_j is the atomic scattering factor of the j^{th} atom, indicating how strongly that atom scatters X-rays.
- *h*, *k* & *l* are the Miller indices of the *hkl* reflection
- x_j, y_j & z_j are the fractional coordinates of the j^{th} atom.

For neutrons diffraction, the atomic scattering factor f_j is replaced by neutron scattering length b_j, since neutrons interact with nuclei.

2.2.2 X-ray Diffraction

X-ray diffraction (XRD) is a powerful technique used to determine the structure of crystalline solids. X-rays are electromagnetic radiation of wavelength ~1 Å and because their wavelength is comparable to the typical spacing between atoms in a crystal, they are suitable for studying diffraction in crystalline materials.

2.2.2.1 Generation of X-rays

X-rays are generated when a beam of electrons, accelerated by a high voltage, strikes a metal target, often Cu, and ionizes some of the Cu 1*s* (K shell) electrons, as shown in **Figure 2.3**. As a result, an electron from outer orbital (2*p* or 3*p*) immediately drops down to fill the vacant 1*s* site and releases energy in the form of X-rays during the transition.[1]

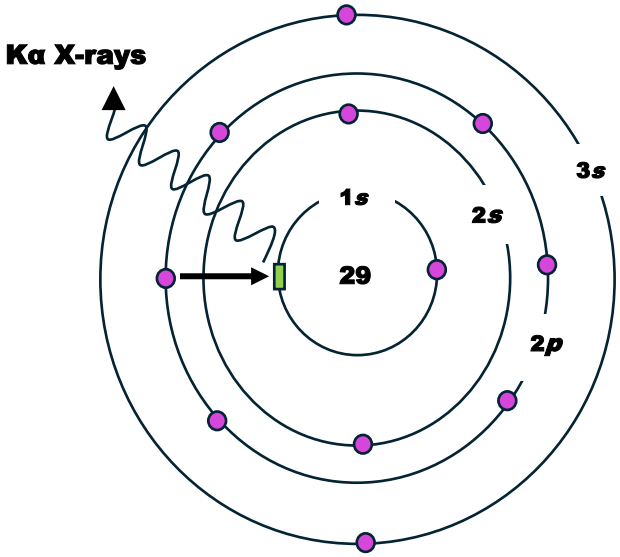

Figure 2.3: Generation of Cu Kα X-rays: A 1*s* electron is ionized, a 2*p* electron falls into the empty 1*s* level and the excess energy is released as X-rays.

The transition energies have fixed values, hence a spectrum of X-rays, as shown in **Figure 2.4**, is emitted. For Cu, the characteristic radiation consists of multiple distinct wavelengths arising from electronic transitions between specific energy levels. These include: $Cu_{K\alpha 1}$ (1.540456 Å) (2*p* – 1*s*), $Cu_{K\alpha 2}$ (1.54439 Å) (2*p* – 1*s*) and $Cu_{K\beta}$ (1.39222 Å) (3*p* – 1*s*).

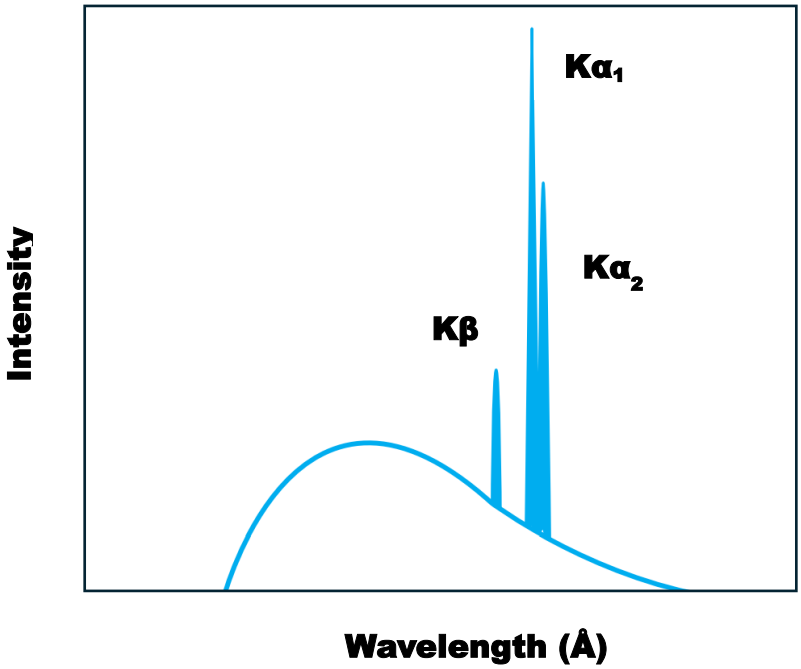

Figure 2.4: X-rays emission spectrum of Cu.[1]

In X-ray diffraction experiments, a monochromatic beam is desired. To achieve this, filters are usually placed right after the source, which absorb most of the unwanted

wavelengths. In **Figure 2.4**, we see that Kα line(s) is most intense in the Cu spectrum. Therefore, all wavelengths except the Kα radiation are needed to be filtered out. A sheet of Ni foil is a very effective filter for Cu radiation. The energy required to ionize 1*s* electrons in Ni correspond to a wavelength of 1.488 Å, which lies between the Cu Kα and Kβ lines. The Ni filter absorbs the majority of the wavelengths, leaving a monochromatic beam of Kα radiation.

2.2.2.2 X-ray Powder Diffraction (XRPD)

Powder diffraction is one of the most important material characterisation methods. XRPD is technique commonly used to assess the crystallinity and phase purity of samples and can also provide information on the unit cell dimensions.[5-9]

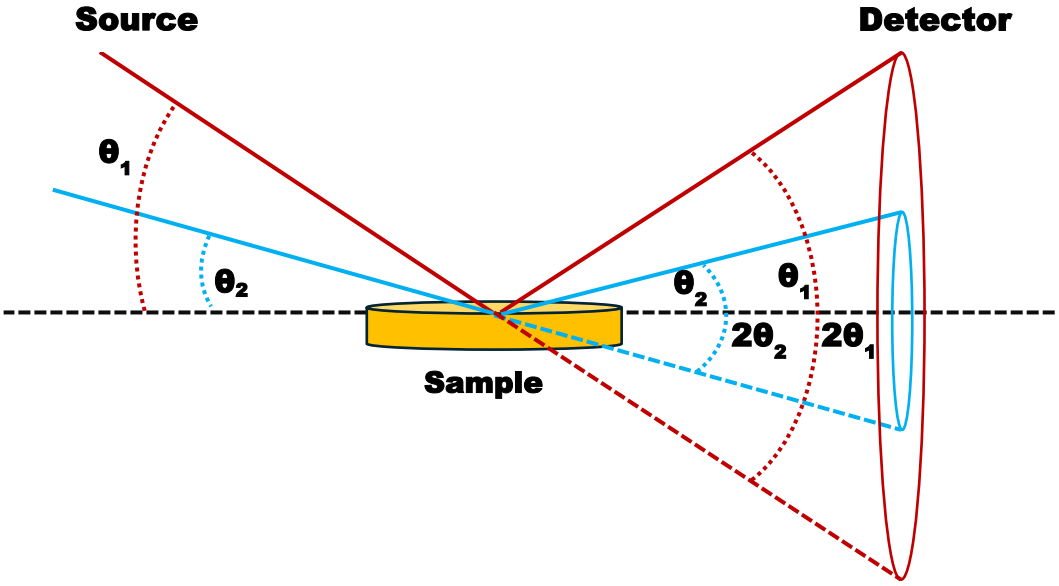

Figure 2.5: A schematic of the Bragg-Brentano geometry.

The Bragg-Brentano geometry, where the sample is loaded on a flat plate with a circular indentation, is the widely used setup in the laboratory-based powder X-ray diffraction instruments.[10] This setup operates on the principle of Bragg's law. In the diffractometer, X-ray beams, generated using a Cu target, strike the stationary, flat sample. Both the sample and the detector move in a coordinated fashion such that the sample is at an angle θ to the plane of the source while the detector is at an angle θ to the plane of the sample and 2θ to the incident radiation, maintaining a precise θ-2θ relationship. When the Bragg's condition is satisfied, constructive interference occurs, and the X-rays diffracted by the crystal planes are detected by a detector. The detector measures the intensity of these diffracted beams and produces a diffraction pattern, which is a plot of intensity versus 2θ.

A Rigaku Miniflex 600, a benchtop XRPD instrument, equipped with D/teX Ultra silicon strip detector in Bragg-Brentano geometry was used to collect the X-ray diffraction data at room temperature presented in this thesis.

Determining the position of lighter elements, such as oxygen, is challenging using XRPD due to their low X-ray scattering power. Therefore, in this thesis, neutron powder diffraction together with XRPD is used to accurately resolve the structure of the materials under investigation.

2.2.3 Neutron Diffraction

Neutron diffraction is similar to X-ray diffraction in that Bragg's law still applies but the cost and size of the neutron diffraction instruments are large compared to the laboratory-based powder X-ray diffraction instruments. Unlike X-rays, which are scattered by interactions with electrons, neutrons are scattered through their interaction with atomic nuclei. Therefore, there is no dependence on the atomic number and information can be obtained on the position of lighter atoms such as oxygen and on the position of two atoms with close atomic numbers (example: N and O). Neutron diffraction data is highly complementary to X-ray diffraction data.

2.2.3.1 Generation of Neutrons

Neutrons used for neutron diffraction are not freely available and are generated artificially by either a nuclear reactor or a pulsed neutron source.[1] These methods are only available in large dedicated science facilities.

In nuclear reactors, neutrons are produced as a by product of ^{235}U fission process. The heavy ^{235}U nuclei split into smaller fragments, producing a continuous source of neutrons for diffraction. In spallation sources, neutrons are generated by bombarding a heavy metal target with protons accelerated by a particle accelerator. The impact causes the target nuclei to release neutrons.

Regardless of the generation method, the initial neutrons produced have high velocity which interact poorly with matter. Moderators are used to slow down these fast-moving neutrons to obtain neutrons suitable for diffraction. The most commonly used moderators are water, hydrogen and methane.[11]

The neutron powder diffraction (NPD) experiments in this thesis were conducted using the Echidna High Resolution Powder Diffractometer (HRPD) at the Australian

Nuclear Science and Technology Organisation (ANSTO) and the General Material Diffractometer (GEM) located at the ISIS Neutron and Muon Source.

2.2.3.2 Echidna – High Resolution Powder Diffractometer (HRPD)

The Echidna HRPD at the Australian Nuclear Science and Technology Organisation (ANSTO) operates using neutrons generated by fission of ^{235}U in the OPAL nuclear research reactor. The generated neutrons are moderated to thermal energies and directed towards the instrument through a neutron guide.[12] A Ge monochromator selects the specific neutron wavelength, between 1-3 Å, and the collimators and slits ensure that the beam is sharp and highly focused. The neutron beam then strikes the powdered sample where diffraction occurs according to Bragg's law. The diffracted neutrons are detected by 128 position sensitive ^{3}He detectors units aligned in an arc of 158.75°.[12, 13] The collected diffraction data provide information about the crystal structure of the material, including the position of the light elements and subtle structural distortions that are often difficult to detect using X-rays.

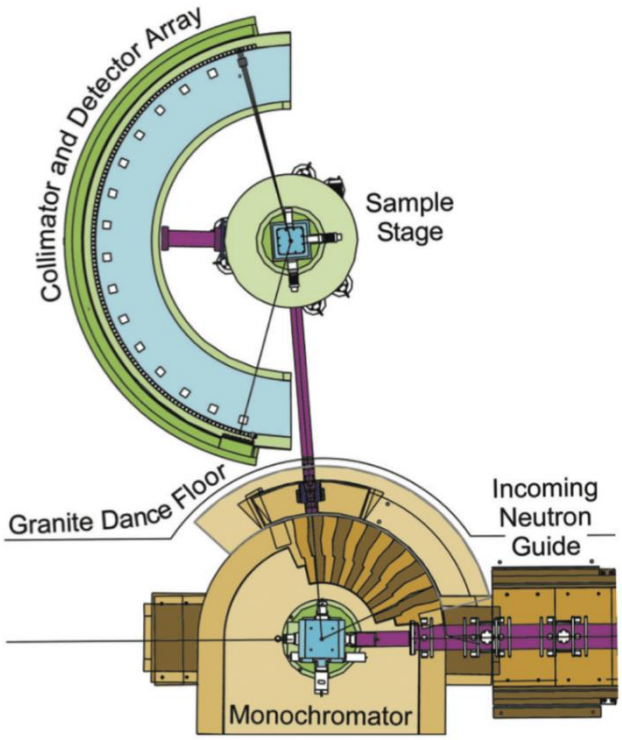

Figure 2.6: Schematic of the high-resolution powder diffractometer Echidna at ANSTO.[2]

2.2.3.3 General Materials Diffractometer (GEM)

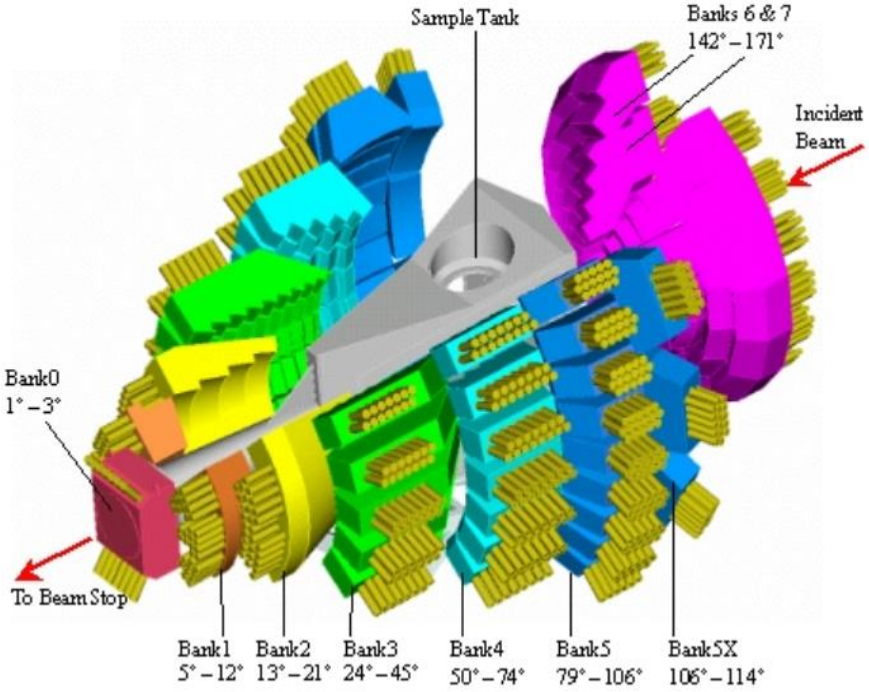

Figure 2.7: Schematic view of the General Materials Diffractometer (GEM) detector banks.[3]

The General Material Diffractometer (GEM) located at the ISIS Neutron and Muon Source is a time-of-flight (tof) neutron diffraction instrument.[14] It uses pulsed neutrons generated by a spallation source, where the high energy proton beam strikes a heavy metal target to generate neutrons.[15] The neutron pulses, travelling through a moderator, are directed towards the sample. After diffraction by the sample, they reach the detector banks, placed at known distance and angle from the sample, and the tof of neutrons is measured. This time-of-flight data is then converted into information about the d-spacing of atomic planes using Bragg's Law.

2.2.4 Rietveld Refinement

The Rietveld method, developed by scientist Hugo Rietveld in 1969, is an extremely valuable method used for detailed structural analysis of crystalline materials from powder diffraction data.[16, 17] It involves the least squares minimisation of the squares of the difference between calculated and observed diffraction patterns such that the calculated data best fits the observed data. This method is not used to determine the structure from scratch, instead it is most effective when a good starting model is already known, but specific details (such as lattice parameters, atomic positions, site occupancies, etc.) need to be refined or confirmed. The caveat of Rietveld

refinement is thus the requirement of a reliable starting structural model**,** from which both structural and instrumental parameters, as well as specimen-related effects, are iteratively refined to fit the whole pattern until the best fit is achieved.[18]

The following fitting statistics are reported after each refinement cycle to determining the quality of the fit:

(I) **Profile R-factor, R_p** that indicates how well our calculated diffraction pattern matches the observed data.

$R_p = \sqrt{\frac{\sum(Y_i^{obs} - Y_i^{cal})^2}{\sum(Y_i^{obs})^2}}$ x 100%, where: $\mathrm{Y}_i^{\mathrm{obs}}$ is observed intensity at data point *i* and $\mathrm{Y}_i^{\mathrm{cal}}$ is calculated intensity at the same point *i*.

(II) **Weighted profile R-factor, R_{wp}** indicates how closely the calculated diffraction pattern matches the observed (experimental) pattern, taking into account the statistical uncertainty of each data point.

$R_{wp} = \sqrt{\frac{\sum w_i(Y_i^{obs} - Y_i^{cal})^2}{\sum w_i(Y_i^{obs})^2}}$ x 100%, where: $\mathrm{Y}_i^{\mathrm{obs}}$ is observed intensity at data point *i*, $\mathrm{Y}_i^{\mathrm{cal}}$ is calculated intensity at the same point *i* and w_i is weight for point *i*.

(III) **Expected R-factor**, R_{exp} represents the ideal R_{wp} value we would get if our calculated pattern perfectly fit the data.

$R_{exp} = \sqrt{\frac{N-P}{\sum w_i(Y_i^{obs})^2}}$ x 100%, where: N is number of data points, P is number of refined parameters and w_i is weight for point *i*.

(IV) $\chi^2 = \frac{R_{wp}}{R_{exp}}$ indicates how well our calculated pattern fits the observed data, considering the quality of the data and the complexity of the model. The lower is the value, the better is the fit. However, the value should never fall below 1.[19]

It is important that the Rietveld refinement is performed in a stepwise manner to avoid falling into a false minimum, which can lead to an incomplete refinement or a structurally unrealistic outcome.

2.2.5 Pawley Refinement

Pawley refinement is a valuable preliminary tool of structure refinement where the crystal structure is not yet known or is only partially understood.[20] In a typical Pawley refinement the unit cell parameters and the space group are provided, on the basis of which allowed reflections are generated. The intensity of the generated reflections is then freely refined in order to fit the calculated diffraction pattern focusing only on fitting the overall lineshape. This approach is very useful for verifying the unit cell parameters, peak shape, assessing the presence of multiple phases and comparing possible unit cell symmetries.

TOPAS Academic (TA) software was used throughout this thesis to perform both Rietveld and Pawley refinements.[19, 21, 22] TA operates by reading user-defined input from plain text files with the extension .inp, which contain all the necessary instructions for the refinement. The text editor jEdit was used to create and edit these input files. jEdit can be easily configured to interact with TA. Once prepared, the .inp files are loaded into TOPAS, where the refinement takes place.

2.3 Symmetry Analysis

ISODISTORT (part of a software suite called ISOTROPY) is a web-based tool used to study how crystal structures change when they lose their parent symmetry via distortion.[23] ISODISTORT helps describe the new distorted structure using the original atomic positions from the parent structure and symmetry-allowed distortion modes that distort the structure as specified by the user.

When a crystal undergoes a phase transition or distortion, its structure can be described as a deviation from a higher-symmetry parent structure. ISODISTORT enables users to input the parent structure and explore possible distorted (child) structures that result from specific symmetry-breaking distortions. Symmetry breaking distortions available in ISODISTORT to model distorted structures are displacive, occupational, strain, rotational and magnetic modes, although in this thesis we apply only displacive and occupational modes.

When a symmetry breaking distortion is applied, ISODISTORT gives a list of possible distortion modes with order parameter direction that can be applied to the high symmetry parent structure. Using this list, we can explore individual distortion

modes or test various combinations to determine which distorted structure best fits our experimental data.

In addition to generating new models, ISODISTORT can also analyse a pre-existing distorted structure by carrying out a mode decomposition of the child structure. This process gives the mode amplitudes that quantify the contribution of each distortion mode.

2.4 Diffuse Reflectance Spectroscopy (DRS)

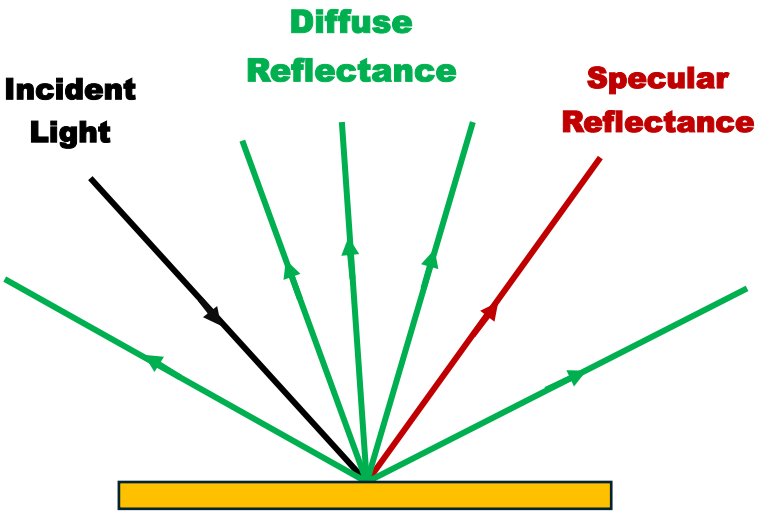

Figure 2.8: Specular and diffuse reflectance components.

Diffuse reflectance spectroscopy (DRS) is an optical technique used to study the bandgap of powdered materials in this thesis. When a beam of light hits a flat, smooth reflective surface like mirror, it is reflected at the angle equal to the angle of incidence, according to the law of reflection. Such a reflection is called specular reflection. But when light strikes a porous or powdered material, it doesn't reflect neatly. Instead, it reflects, refracts, diffracts and finally scatters in many different directions. Some of the light is also absorbed depending on the material. This scattered reflection is called diffuse reflectance. This reflectance is due to the roughness of the surface and variations in particle size and shape.

In a DRS experiment, the light from the source is directed to a hollow spherical chamber with a highly reflective white interior called an integrating sphere. The purpose of the integrating sphere is to exclude specular reflection and allow the diffuse reflectance to be measured. The sample (1% of sample mixed with 99% of

the reference material by weight) is loaded in a cuvette and placed over the hole on the integrating sphere where it is exposed to the incident light. The diffusely reflected light from the sample travels to a spectrometer. The spectrometer measures the intensity of light as a function of wavelength.

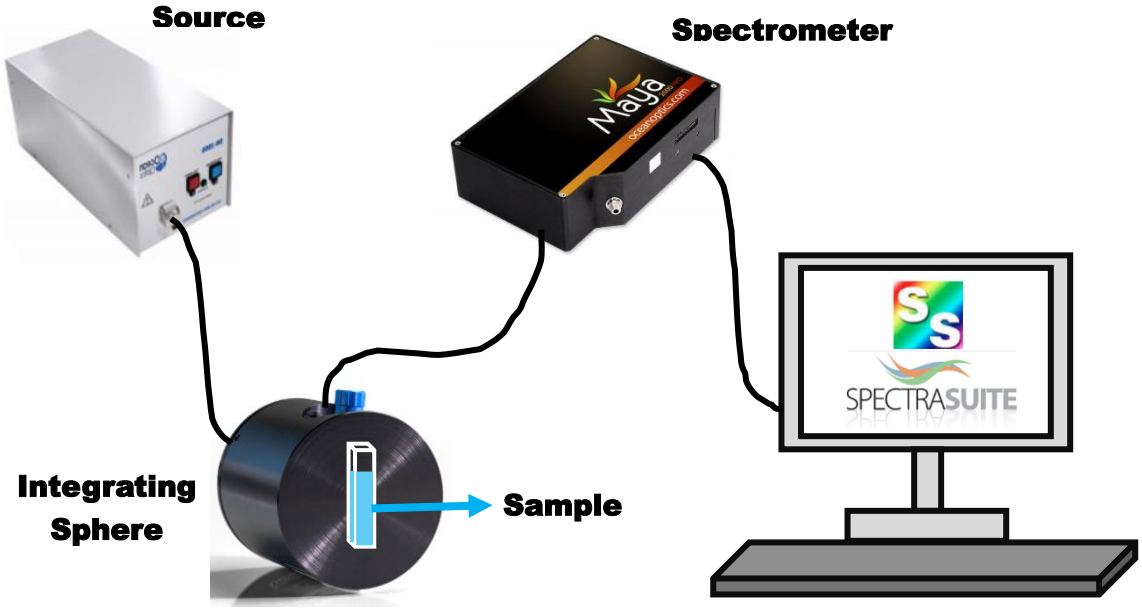

Figure 2.9: The schematic diagram of diffuse reflectance spectroscopy system for bandgap measurements.

The diffuse reflectance data is analysed using the Kubelka-Munk method which is defined as:

$$F(R) = \frac{(1-R)^2}{2R} \tag{2.3}$$

Where *F(R)* is the Kubelka-Munk function and $R = \frac{\mathrm{R_{sample}}}{R_{\mathrm{standard}}}$ is the absolute diffuse reflectance of the sample.

It helps us to convert the reflectance spectrum into data that can be used to find the optical bandgap of a material

2.5 Second Harmonic Generation (SHG)

Second harmonic generation (SHG) is a non-linear optical phenomenon that occurs when light, typically a laser beam, of a certain frequency ω passes through a non-linear crystal. Two photons from the beam combine inside the crystal generating a new beam with twice the frequency (2ω), or half the wavelength, as shown in **Figure 2.10**.[24] This newly generated light is referred to as the second harmonic light.

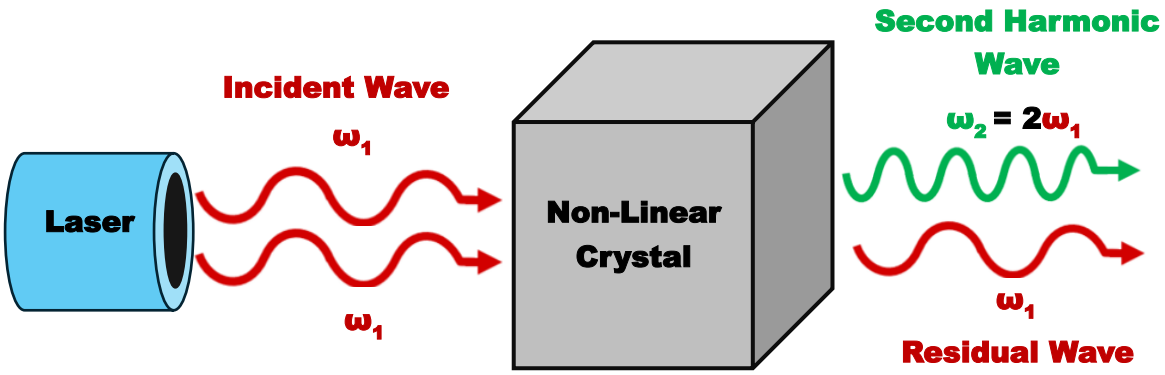

Figure 2.10: The schematic diagram of second harmonic generation.

SHG is a valuable tool that can be used to identify non-centrosymmetric crystal structures as an SHG signal is only generated in materials that lack inversion symmetry.[25] This technique is especially useful in cases where the diffraction data do not clearly distinguish between centrosymmetric and non-centrosymmetric space groups. When a beam passes through a non-centrosymmetric crystal, the combination of two photons from the incoming beam leads to the output of a beam with double frequency (**Figure 2.10**).[24] As a result, an SHG signal is observed.

The SHG measurements in this thesis were conducted at the Department of Chemistry, Durham University and the Department of Physics, University of Warwick.

2.6 Computational Method

The properties of a material depend on its electronic structure. To predict these properties we need to solve the Schrödinger equation but the *N*-electron Schrödinger equation cannot be solved directly due to its complexity. For example: for *N* electrons, the wavefunction is in a space with 3*N* dimensions (three for each electron: x, y, z). This massive dimensionality makes solving the *N*-electron Schrödinger equation directly impractical. Density Functional Theory (DFT) provides a method of determining the ground state electronic structure of a system.[26, 27] It uses electronic charge densities instead of wavefunctions. CASTEP programme was used to perform DFT calculations in this thesis. CASTEP is a quantum mechanical code for performing electronic structure calculations.[28]

2.6.1 Schrodinger Equation

The one-particle Schrodinger equation is:

$$H\psi = E\psi \tag{2.4}$$

where

$$\hat{H} = \hat{T}_e + \hat{T}_n + \hat{V}_{n-e} + \hat{V}_{e-e} + \hat{V}_{n-n} \tag{2.5}$$

$\hat{H}$ is the Hamiltonian operator. It represents the total energy of the system in its eigenstate ψ. $\hat{T}$ is the kinetic energy operator; $\hat{V}$ is the potential energy operator; *n-e*, *e-e* and *n-n* are contributions from nucleus-electron, electron-electron and nucleus-electron respectively. E is the total energy of the system and ψ is the wavefunction.

Compared to electrons, the nuclei are significantly heavier and slower ($m_e << m_p$). From electrons perspective, the positions of the nuclei appear to be static. Conversely, from nuclei perspective, position of electrons changes almost instantaneously. The Born-Oppenheimer approximation allows us to decouple the electronic and the nuclear part. Under this approximation, the positions of the nuclei are fixed and only the electrons are allowed to vary. As the nuclei are fixed, $\hat{T}_n$ = 0. Furthermore, for a given set of nuclei positions, the nuclear-nuclear repulsion does not change, hence $\hat{V}_{n-n}$ is a constant.

Therefore, the electronic Hamiltonian becomes

$$\hat{H} = \hat{T}_e + \hat{V}_{n-e} + \hat{V}_{e-e} \tag{2.6}$$

Using this form of the Hamiltonian (equation **(2.6)**), Schrödinger equation (equation **(2.4)**) becomes:

$$\hat{H}\psi(r_1 \dots r_N) = E\psi(r_1 \dots r_N) \quad \textbf{(2.7)}$$

Here, ψ depends only on the positions of the electrons, r_i.

Equation **(2.7)** is still incredibly complex. For *N* electrons, the wavefunction is in a space with 3*N* dimensions (three for each electron: x, y, z). This massive dimensionality makes solving equation **(2.7)** directly impractical. Moreover, the wavefunction is not experimentally measurable. DFT simplifies this problem. It uses electron density instead of wavefunction. Electron density, *ρ(r)*, is defined as the probability of finding an electron in a specific location around an atom or molecule.

$$\rho(r) = 2\sum_i \psi_i^*(r)\psi_i(r) \quad \textbf{(2.8)}$$

Here the summation is over all the individual electron wave functions that are occupied by electrons. The factor of 2 appears because electrons have spin and according to Pauli exclusion principle each individual electron wave function can be occupied by two separate electrons provided they have different spins.

Unlike the wavefunction, the electron density is measurable and exists in just three dimensions, regardless of the number of electrons in the system. This makes the problem much simpler. In 1964 Hohenberg and Kohn developed a model that laid the foundation for this approach.

2.6.2 Hohenberg-Kohn Theorem

The Hohenberg-Kohn theorem states that the ground state energy, *E*, of a many-electron system can be entirely determined by electron density, *ρ(r)*. This can be proved true by a simple argument that if we know the ground state electron density then we know the ground state energy. There exists a universal functional that maps the electron density to the ground-state energy:

$$E = E[\rho(r)] \quad \textbf{(2.9)}$$

It is possible to determine the energy of a system if the electron density is known. If that density is the ground state density, then the resulting energy is the ground state energy. It is not possible to get an energy lower than the ground state. Therefore,

any electron density that produces this energy must represent the ground state energy.

The Hohenberg-Kohn theorem is powerful. It guarantees that a one-to-one mapping between the ground state wave function and the ground state electron density exists and is true however, it does not provide its explicit form. Hohenberg and Kohn established the theoretical foundation for this mapping but were unable to derive the exact equations that describe it. Another limitation was to find out the kinetic energy in terms of electron density.

2.6.3 Kohn-Sham Equations

The Kohn-Sham equations were introduced to fix the limitations of Hohenberg-Kohn theorem. They proposed a system based on fictitious particles called the Kohn-Sham quasi particles or the non-interacting particles that have the same electron density as the real system. This allows the complex many-body problem to be transformed into *N* simpler single-particle equations. The Kohn-Sham method reduces the problem to solving *N* independent equations, each involving a single 3-D fictitious wavefunctions called Kohn-Sham orbital, that can be used to calculate the kinetic energy of the system.

The Kohn-Sham equations are written as:

$$\left(-\frac{\hbar^2}{2m}\nabla^2 + V(r) + V_H(r) + V_{XC}[\rho](r)\right)\psi_i(r) = \epsilon_i\psi_i(r) \qquad \textbf{(2.10)}$$

where $\psi_i(r)$ is the wavefunction of the *i*th non-interacting electron, ϵ_i is the energy of that wavefunction. $V(r)$ is the potential due to the interaction between an electron and nuclei. $V_H(r)$ is the Hartree potential. It describes the Coulomb repulsion between the electron being considered in one of the Kohn–Sham equations and the total electron density defined by all electrons in the problem. It also involves a Coulomb interaction between the electron and itself. The self-interaction is unphysical. The correction for this along with the exchange term arising from the Pauli exclusion principle, correlation term that accounts how electrons avoid one another in space and time. This correlation term represents the difference between the exact energy and that of the Hartree–Fock approximation and kinetic energy correction. These are some the effects that are lumped together into V_{XC}, the

exchange-correlation potential. It accounts for all the complex many-body interactions not captured by the non-interacting particle approximation.

$$V_{XC}[\rho](r) = \frac{\delta E_{XC}[\rho(r)]}{\delta \rho(r)} \quad \textbf{(2.11)}$$

where E_{XC} is the exchange-correlation interaction energy.

The term V_{XC} is important as it represents the corrections necessary to apply in order to get the exact total energy of the real interacting system. However, its exact form is unknown. Various approximations such as the Local Density Approximation (LDA) or the Generalized Gradient Approximation (GGA) are used for V_{XC}.

2.6.3.1 Exchange-Correlation Functionals

(I) Local Density Approximation (LDA): LDA is the earliest and simplest exchange-correlation functionals used in DFT. It assumes that $E_{XC}[\rho(r)]$ from interactions between the electrons at some point *r* is the same as if the electrons were spread out evenly throughout the system (like a "uniform electron gas" with that same density as at point *r*). It is reasonably effective and a good model for simple systems such as metals, where electron densities are relatively even, but it tends to over-bind atoms resulting in shorter bond lengths, stronger bond strengths and smaller lattice parameters than observed experimentally. This is because in reality electron densities are not uniform, especially near atomic nuclei or in chemical bonds.

(II) Generalized Gradient Approximation (GGA): GGA was developed to fix the limitations of LDA. It extends LDA by including the gradient (change) of the electron density to account for how the density varies in space. There are many GGAs depending on the parametrization of the data such as PW91[29], PBE[30], RPBE[31], WC[32]. The DFT calculations presented in this thesis were performed using the Perdew-Burke-Ernzerhof (PBE) exchange-correlation functional.

2.6.4 Periodicity and Bloch's Theorem

The challenge of solving a set of single-electron Schrödinger (Kohn-Sham) equations is in the large number of electrons – often around 10^{24} in typical solids. However, most crystalline materials can be described by a regular repeating unit cell. By exploiting this periodicity, we can significantly simplify the problem, reducing the complexity of calculations.

The Bloch's theorem states that if the nuclei in a solid are arranged periodically then the measurable properties such as potential and density also exhibit periodicity. The wavefunction is not measurable and hence it is not periodic. Instead, it can be expressed in a quasi-periodic form:

$$\Psi_k(r) = e^{ik.r}\mu_k(r) \tag{2.12}$$

where $\mu_k(r) = \sum_G C_{Gk} e^{iG.r}$ is periodic and $e^{ik.r}$ is an arbitrary phase factor. Therefore, equation **(2.12)** becomes:

$$\Psi_k(r) = \sum_G C_{Gk} e^{i(G+k).r} \tag{2.13}$$

where G are reciprocal lattice vectors and C_{Gk} is are unknown complex coefficients.

Equation **(2.12)** shows that if we go from one unit cell to another, the wavefunctions are related by the phase factor $e^{ik.r}$. The wavefunction changes by acquiring a phase shift of $e^{ik.r}$ in the other unit cell.

Using Bloch's theorem we can solve the Kohn-Sham equations within a single unit cell, exploiting the material's inherent periodicity.

2.6.4.1 *K*-Points

The need for *k*-points comes from Bloch's theorem. From equation **(2.13)** we see that while the magnitude of the wavefunction is periodic, its phase is not periodic.

To determine the electron density, one must integrate over all wavefunctions in the Brillouin zone:

$$\rho(r) = \int |\Psi_k(r)|^2 \, d^3k \tag{2.14}$$

Here, k is continuous in reciprocal space, so the integral is over infinitely many values. In practice, this integral is approximated by discretising and truncating the Brillouin zone into a finite grid of points, known as *k*-points:

$$\approx \sum_{k} |\Psi_k(r)|^2 \qquad \textbf{(2.15)}$$

Thus, instead of integrating over all infinite values of *k*, the calculation is performed over a finite set of *k*-points within the first Brillouin zone. The number of *k*-points required depends on the size of the Brillouin zone. The bigger the real space unit cell is, the smaller is the Brillouin zone and fewer k-points are needed.

2.6.4.2 Basis (Planewaves and Pseudopotentials)

Planewaves (equation **(2.12)**) are the fundamental basis functions used to describe wavefunctions in a periodic crystal structure. They are used to evaluate the total energy and its derivatives.

However, planewaves alone are insufficient in describing the strong variations of the electron density near the nuclei. They are coupled with the pseudopotentials to get a more accurate description of the material's electronic structure.

Pseudopotential approximation gives a simpler way of representing the way the electron interacts with the nucleus. In an atom, electrons are divided into core electrons (those tightly bound to the nucleus) and valence electrons. To accurately model the core electrons, a large number of plane waves are required as they undergo rapid oscillations near the nucleus, making calculations computationally expensive. Pseudopotentials solve this issue by combining the core electrons and the nucleus into a single effective potential. This helps in reducing the number of electrons, allowing calculations to focus only on the valence electrons, as they contribute to the chemical bonding and therefore to most of the properties. As a result, the calculations become much simpler, requiring far fewer plane waves.

2.6.5 Geometry Optimization

Geometry optimization is the process by which positions of atoms in a crystal structure are adjusted iteratively to find a structure with the lowest possible energy. The Hellman-Feynman theorem provides a way to calculate the forces acting on the nuclei. The theorem states that the force acting on a nucleus is simply the negative derivative of the total energy with respect to the nuclear position. This can be calculated using the electron density and the electrostatic potential of the nuclei. There is no need to explicitly calculate the derivative of the total energy with respect to nuclear coordinates. This simplifies the calculations and make them computationally efficient. The calculated forces tell us about the direction in which

the atoms need to move in order to lower the overall energy. Optimisation algorithms such as conjugate gradients, steepest descent or Broyden–Fletcher–Goldfarb–Shanno (BFGS) method can be used to move the atoms. In the steepest descent method, the atomic positions are updated iteratively along the direction of the force until the forces converge to near zero. This is a simple method but can be slow to converge. A more efficient approach is the conjugate gradients method. Here also the forces are calculated to determine the direction of movement, but this method intelligently chooses a new search direction that is "conjugate" (or orthogonal) to the previous search direction. This prevents the algorithm from retracing the steps thereby leading to faster convergence to the minimum energy structure. The BFGS method, which is used in this thesis, is a quasi-Newton algorithm that approximates the Hessian matrix of second derivatives of the energy. It intelligently choses both step direction and step size, leading to very rapid convergence to the minimum energy structure. In the end we get a geometry optimised structure, representing the most stable arrangement of atoms.

1. A. R. West, *Solid state chemistry and its applications*, John Wiley & Sons, 2022.
2. J. M. Hudspeth, 2012.
3. A. C. Hannon, *Nuclear Instruments and Methods in Physics Research Section A: Accelerators, Spectrometers, Detectors and Associated Equipment*, 2005, **551**, 88-107.
4. G. Bergerhoff, I. Brown and F. Allen, *International Union of Crystallography, Chester*, 1987, **360**, 77-95.
5. M. t. Sakata and M. Cooper, *Applied Crystallography*, 1979, **12**, 554-563.
6. L. McCusker, R. Von Dreele, D. Cox, D. Louër and P. Scardi, *Applied Crystallography*, 1999, **32**, 36-50.
7. H. P. Klug and L. E. Alexander, *X-ray diffraction procedures: for polycrystalline and amorphous materials*, 1974.
8. E. J. Mittemeijer and P. Scardi, *Diffraction analysis of the microstructure of materials*, Springer Science & Business Media, 2013.
9. R. Guinebretière, A. Boulle, O. Masson and A. Dauger, *Powder Diffraction*, 2005, **20**, 294-305.
10. E. J. Mittemeijer and U. Welzel, *Modern diffraction methods*, John Wiley & Sons, 2013.
11. D. S. Sivia, *Elementary scattering theory: for X-ray and neutron users*, Oxford University Press, 2011.
12. K.-D. Liss, B. Hunter, M. Hagen, T. Noakes and S. Kennedy, *Physica B: Condensed Matter*, 2006, **385**, 1010-1012.
13. M. Avdeev and J. R. Hester, *Applied Crystallography*, 2018, **51**, 1597-1604.
14. J. Enderby, W. Williams, L. Chapon, A. Hannon, P. Radaelli and A. Soper, *Neutron News*, 2004, **15**, 19-23.
15. W. Williams, R. Ibberson, P. Day and J. Enderby, *Physica B: Condensed Matter*, 1997, **241**, 234-236.
16. H. M. Rietveld, *Applied Crystallography*, 1969, **2**, 65-71.
17. H. Rietveld, *Acta Crystallographica*, 1967, **22**, 151-152.
18. R. A. Young, *The rietveld method*, International union of crystallography, 1993.
19. A. A. Coelho, *Applied Crystallography*, 2018, **51**, 210-218.
20. G. Pawley, *Applied Crystallography*, 1981, **14**, 357-361.
21. A. A. Coelho, *Coelho Software, Brisbane, Australia*, 2007.
22. A. Coelho, *Karlsruhe, Germany*, 2012.
23. B. J. Campbell, H. T. Stokes, D. E. Tanner and D. M. Hatch, *Journal of Applied Crystallography*, 2006, **39**, 607-614.
24. R. W. Boyd, A. L. Gaeta and E. Giese, in *Springer Handbook of Atomic, Molecular, and Optical Physics*, Springer, 2008, pp. 1097-1110.
25. P. S. Halasyamani and K. R. Poeppelmeier, *Chemistry of Materials*, 1998, **10**, 2753-2769.
26. P. Hohenberg and W. Kohn, *Physical review*, 1964, **136**, B864.
27. W. Kohn and L. J. Sham, *Physical review*, 1965, **140**, A1133.
28. S. J. Clark, M. D. Segall, C. J. Pickard, P. J. Hasnip, M. I. Probert, K. Refson and M. C. Payne, *Zeitschrift für kristallographie-crystalline materials*, 2005, **220**, 567-570.
29. J. P. Perdew and Y. Wang, *Physical review B*, 1992, **45**, 13244.
30. J. P. Perdew, K. Burke and M. Ernzerhof, *Physical Review Letters*, 1996, **77**, 3865-3868.
31. B. Hammer, L. B. Hansen and J. K. Nørskov, *Physical Review B*, 1999, **59**, 7413-7421.
32. Z. Wu and R. E. Cohen, *Physical Review B*, 2006, **73**, 235116.

Chapter 3: Structure-Composition-Property Relationships in Dion-Jacobson Phases

3.1 Introduction

Compared with ABO_3 perovskites, layered perovskite-related materials remain comparatively underexplored. A notable family of layered perovskite-related materials is the Dion-Jacobson (DJ) phases. Their general formula is $A'[A_{n-1}B_nO_{3n+1}]$ where A' (e.g., Rb^+, Cs^+) forms the alkali cation layer that separates the perovskite-like layers.[1] The ideal, aristotype structure is tetragonal of $P4/mmm$ symmetry (**Figure 3.1**).

The DJ phases are known to undergo distortions involving rotations of BO_6 octahedra and in-plane polar/antipolar displacements[2] (**Figure 3.2**) and this complex structural behaviour has been shown to give rise to ferroelectricity by either proper or hybrid improper mechanisms.[3-7] More recently these oxides are gaining interest for their optical properties and applications such as photocatalytic activity, x-ray detectors, solar cells, photo detectors.[8-11] Photocatalytic activity in these materials has been reported to be correlated with structural features, including polar

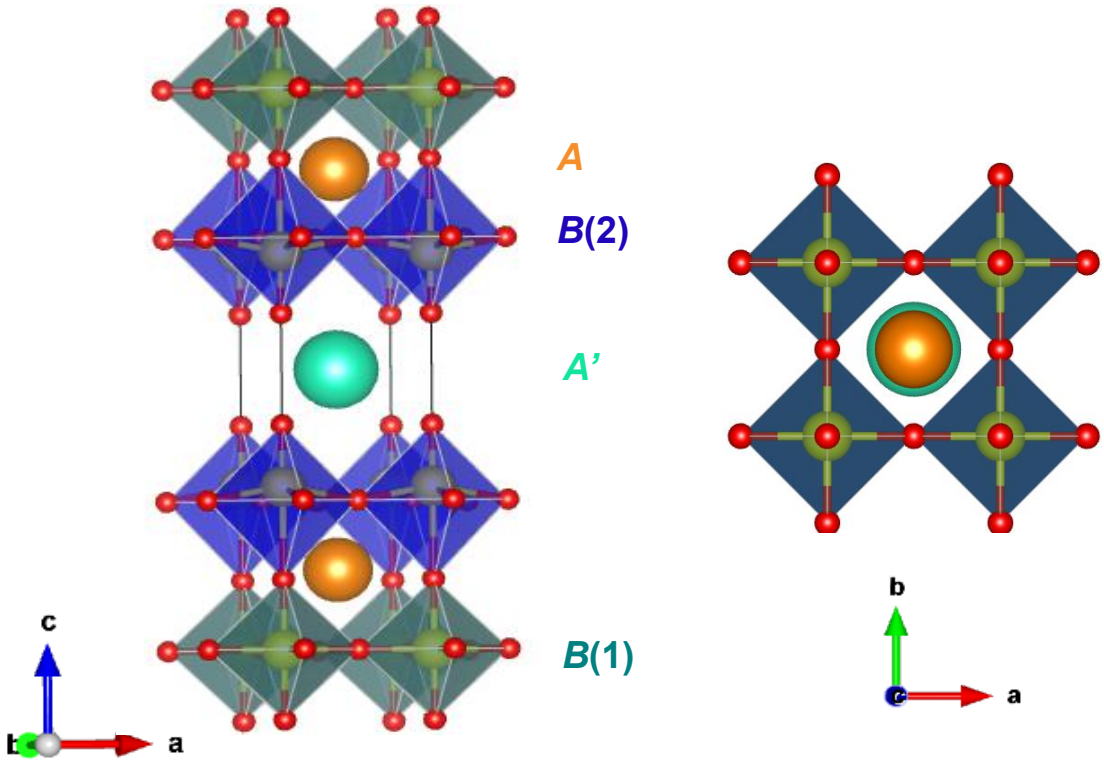

Figure 3.1: Illustration of the parent structure of $A'[A_{n-1}B_nO_{3n+1}]$ described by $P4/mmm$ symmetry, showing A', A, and B cations in orange, green, and pink, respectively, and $B(1)O_6$ and $B(2)O_6$ octahedra in gray and blue.

crystal structures and/or polar cation environments.[12] In addition, the optical band gap is reported to vary with composition.[13, 14] This highlights the need to understand and explore the structural chemistry of these materials, yet there has been relatively little systematic investigation of the structures of the *n* = 3 DJ phases. Many studies rely on characterisation using x-ray powder diffraction and assume the structure as the high symmetry parent structure of *P*4/*mmm* symmetry.[15-17]

The lack of a clear understanding of the crystal structures of these materials makes it difficult to explain the trends in physical properties and makes designing optimized materials and understanding structure-property relationships challenging. In this study, we present a systematic investigation of the *n* = 3 $A'A_2B_3O_{10}$ (where *A'* = Rb, Cs; *A* = Ca, Sr, Ba and *B* = Nb, Ta) DJ phases using a combination of experimental and computational approaches. Our analysis of neutron powder diffraction (NPD) data together with results from density functional theory (DFT) calculations helps in establishing a relationship between structure and composition by addressing how the structure of these materials is influenced by the choice of *A'*, *A* and *B* cations. Factors such as cation size, tolerance factor, stacking strain, and the second order Jahn-Teller effect are explored to understand their roles in determining the degree of distortion and structural symmetry in these phases. Through this study, we aim to provide a comprehensive framework for understanding structure-composition-property relationships in the *n* = 3 DJ phases. This will help us in exploring how optical properties depend on structure and composition by understanding how structure and composition influence the band gap and polarity of a material.

3.2 Methods

3.2.1 Synthesis

Polycrystalline samples of $CsCa_2Nb_3O_{10}$, $CsSr_2Nb_3O_{10}$, $CsBa_2Nb_3O_{10}$, $CsCa_2Ta_3O_{10}$, $RbCa_2Nb_3O_{10}$, and $RbSr_2Nb_3O_{10}$ were synthesised using the conventional solid state reaction method by Dr V.A. Cascos (Centro de Investigaciones Energéticas, Medioambientales y Tecnológicas**)**. The starting materials included Cs_2CO_3 (Alfa Aesar, 99.9%), Rb_2CO_3 (Alfa Aesar, 99.8%), $BaCO_3$ (Alfa Aesar, 99.95%), $SrCO_3$ (Alfa Aesar, 99.99%), $CaCO_3$ (Alfa Aesar, 99.0%), Nb_2O_5 (Alfa Aesar, 99.5%), and Ta_2O_5 (Alfa Aesar, 99.0%). For full description of synthesis please refer to the paper "*Structural chemistry of the n = 3 Dion-Jacobson phases: controlling polarity and band gap*".[18]

3.2.2 Neutron Powder Diffraction

Neutron powder-diffraction (NPD) data were collected on $A'A_2B_3O_{10}$ (where *A'* = Rb, Cs; *A* = Ca, Sr, Ba and *B* = Nb, Ta) at room temperature on the high-resolution powder diffractometer Echidna at ANSTO,[19] with wavelengths of 1.622 Å and 2.435 Å within the 2θ range from 10° to 165° for two hours per scan. Diffraction data were analysed using the Rietveld method[20] in the Topas Academic software.[21, 22]

3.2.3 Symmetry-Adapted Distortion Mode Analysis

The symmetry-adapted distortion mode approach can be used to describe the low symmetry structures in terms of the parent *P*4/*mmm* structure and a number of possible symmetry-adapted distortion mode amplitudes. A description of a hypothetical distorted structure is obtained from ISODISTORT[23] based on the high symmetry *P*4/*mmm* parent structure, with mode amplitudes for all the possible modes allowed by a larger unit cell i.e. lower symmetry structure. The amplitudes of these distortion modes are then refined using simulated annealing to output R_{wp} (and/or χ^2). This helps identify the distortions that give the most significant improvements to the fit. Individual mode amplitudes can be refined to see how each mode influences the fit, or symmetry-defined groups of mode amplitudes can be refined collectively, for example all X_3^+ mode amplitudes.[24] If groups of mode amplitudes are refined, further analysis can determine which specific mode within the group gives the greatest improvement to the fit (e.g. the O(2) X_3^+ modes). In this study, symmetry-adapted distortion mode analysis has been performed using long-wavelength (2.43 Å) neutron powder diffraction (NPD) data.

3.2.4 Geometry Optimization DFT Calculation

Geometry optimisation calculations were performed within Density Functional Theory (DFT) using the pseudo-potential formalism as implemented in the CASTEP code[25] in collaboration with Dr Emma McCabe and Prof. Stewart Clark (Department of Physics, Durham University), who kindly set up all DFT calculations. Electronic wave functions were expanded in a plane wave basis up to a kinetic energy cut-off of ≥ 1000 eV. Electron-ion interactions are described using *ab initio* ultra-soft pseudopotentials based on Vanderbilt's formalism.[26] Integrations of the Brillouin zone were done with a k-point sampling scheme where the *k*-points are spaced at 0.05 $Å^{-1}$. This converges the calculations to ≤0.5 meV/atom. Our standard DFT calculations use the Perdew Burke Ernzerhof (PBE) exchange-correlation functional[27] as it is an all-rounder - computationally efficient and gives reliable

geometries and energies for a wide range of materials. The pseudo-potentials treat certain semicore states as valence, which is essential to obtain accurate electronic structures. In particular, this includes the 5s, 5p and 6s states for Cs; the 4s, 4p and 5s states for Rb; the 3s, 3p and 4s states for Ca; the 4s, 4p and 5s states for Sr; the 5s, 5p and 6s states for Ba; the 4s, 4p, 4d and 5s states for Nb; the 4f, 5s, 5p, 5d and 6s states for Ta, and the 2s and 2p states for O.

3.2.5 Diffuse Reflectance Measurements

To record the diffuse reflectance spectra, finely powdered samples of $A'A_2B_3O_{10}$ (*A'* = Rb, Cs; *A* = Ca, Sr, Ba and *B* = Nb, Ta) (~1% w/w) were ground with dry sodium chloride and then placed in an optical cuvette. The cuvette was then illuminated with an OceanOptics DH-2000 deuterium lamp. Non-specular scattered light was collected using an integrating sphere, and the spectrum was recorded using OceanOptics Maya 2000 Pro spectrometer. A cuvette of ground sodium chloride was used the reference. The data were used to calculate the reflectance spectra *R* and Kubelka-Munk spectra *F(R)*.

$$F(R) = \frac{(1-R)^2}{2R}$$

where, *R* is the ratio of sum of the sample intensities to sum of the reference intensities.

3.2.6 Second-Harmonic-Generation (SHG) Measurements

Preliminary second harmonic generation (SHG) measurements were conducted by Dr Jack Woolley at the Department of Physics, University of Warwick. Hand-ground powders of each sample (of a wide range of particle sizes) were sealed between glass microscope slides and exposed to an 800 nm laser. The resulting SHG signal (400 nm) was detected using a photomultiplier tube (PMT), with filters employed to eliminate the fundamental wavelength.

Additional SHG measurements were performed by Faith Pritchard at the Department of Chemistry, Durham University using the Kurz and Perry powder technique.[28] Powders of each sample were sieved into different particle sizes (38–45, 53–65, 65–75, 75–90, and 90–106 μm) and loaded into NMR tubes. While SHG is highly symmetry-dependent, the I_{SHG} efficiency of powders also depends on the particle size. If the particle size is not optimised, this can lead to false-negative results.

A pulsed carbide laser, producing 1028 nm fundamental light was used to irradiate the samples. The resulting SHG signal (514 nm) was detected using a PMT. SHG efficiencies below 0.5% of the KDP reference typically indicate centrosymmetric materials.

3.3 Results

3.3.1 Symmetry Analysis

Before delving into the results, this section provides an overview of the distortion modes observed in our n = 3 $A'A_2B_3O_{10}$ (A' = Rb, Cs; A = Ca, Sr, Ba and B = Nb, Ta) Dion-Jacobson phases.

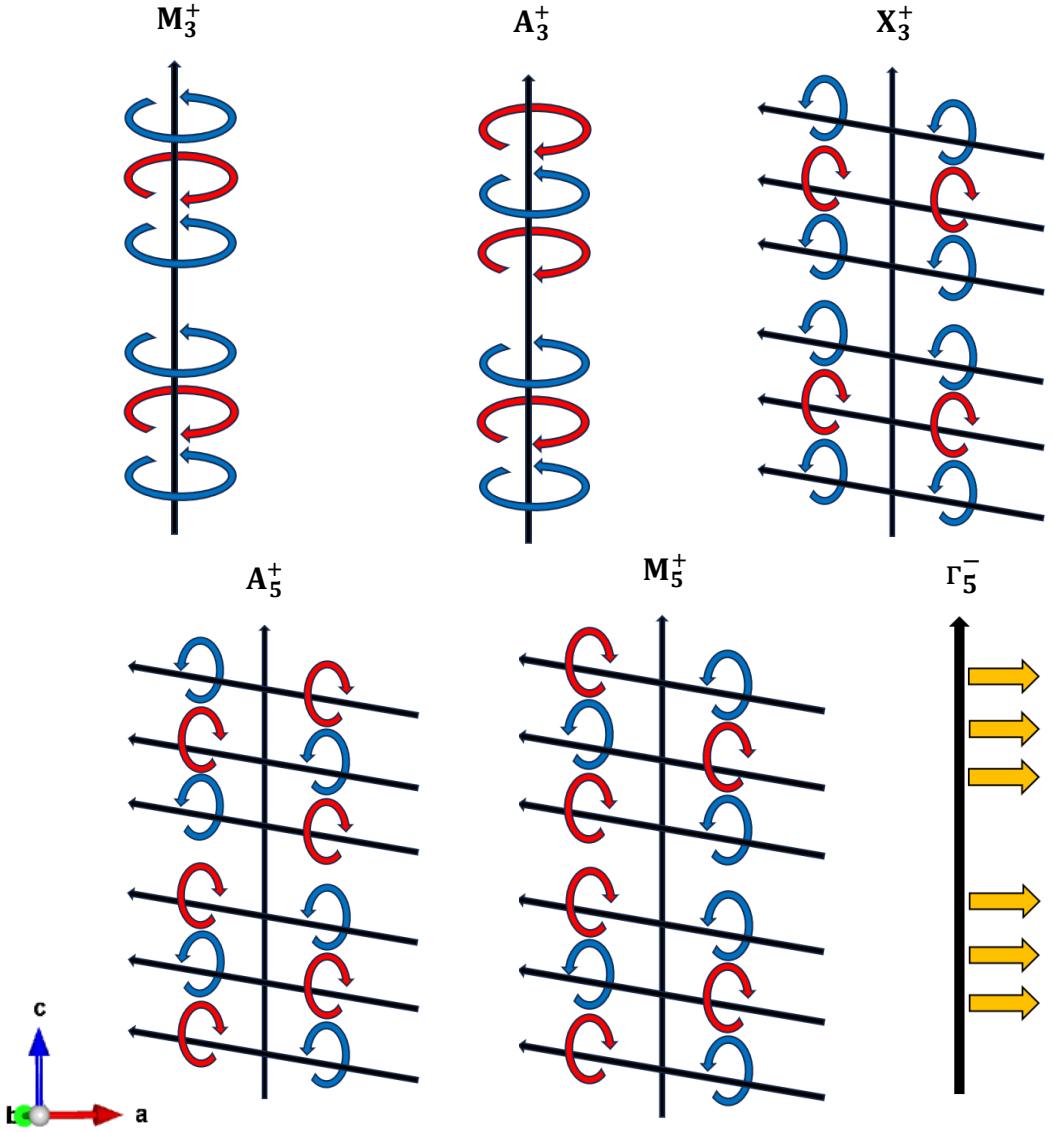

Figure 3.2: Schematic illustration of octahedral rotation modes and polar displacive mode referred to in this chapter.

One of the key octahedral rotations discussed in this chapter is the out-of-phase rotation of BO_6 octahedra about the out-of-plane axis (long axis). The rotations of inner layer octahedra ($B(1)O_6$) and the outer layer octahedra ($B(2)O_6$) within each

block are not constrained to be either in-phase or out-of-phase with respect to each other. This rotation can occur in two patterns:

I. Identical from block to block, described by the M_3^+ mode, which is represented as ($a^0a^0c^-$) *($a^0a^0c^-$)* in Glazer notation.[29] This distortion leads to a unit cell expansion to $\sqrt{2}a_t \times \sqrt{2}a_t \times c$, where a_t and c are lattice constants of the parent *P*4/*mmm* phase, and gives a phase with *P*4/*mbm* symmetry.

II. Alternating in sign from block to block, described by the A_3^+ mode, represented as **(***$a^0a^0c^-$**)**-*($a^0a^0c^-$)* in Glazer notation. This results in unit cell expansion to $\sqrt{2}a_t \times \sqrt{2}a_t \times 2c$ and leads to a phase with *I*4/*mcm* symmetry.

Another significant distortion mode involves in-phase or out-of-phase rotations of BO_6 octahedra about an in-plane axis, which can occur in three patterns:

I. Identical from block to block, described by the X_3^+ mode (in-phase), represented as ($a^+b^+c^0$) *($a^+b^+c^0$)* in Glazer notation, leading to a phase with *Pmmn* symmetry.

II. Alternatively, identical from block to block, described by M_5^+ mode (out-of-phase), represented as ($a^-a^-c^0$) *($a^-a^-c^0$)*, leading to phases with *Pmna* and *Cmma* symmetry.

III. Alternating in sign from block to block, described by the A_5^+ mode (out-of-phase), represented as ($a^-a^-c^0$)-*($a^-a^-c^0$)* in Glazer notation, resulting in a phase with *Imma* symmetry.

Finally, the Γ_5^- mode is an in-plane polar displacement. It corresponds to an in-plane polar displacement of cations relative to anions, which gives rise to phases with *Amm*2 and *Pmm*2 symmetry.

These distortion modes play an important role in determining the structure of our *n* = 3 Dion-Jacobson phases.

3.3.2 Symmetry Determination and Structure Refinement

3.3.2.1 Structural Characterisation of $CsBa_2Nb_3O_{10}$

Multibank Rietveld refinements were carried out to fit the short wavelength (1.6218 Å) and longer wavelength (2.4395 Å) neutron powder diffraction data collected for $CsBa_2Nb_3O_{10}$ with an aristotype *P*4/*mmm* model. Most peaks were indexed by the ~3.9 Å × 3.9 Å × 15.6 Å unit cell of the parent structure *P*4/*mmm* although traces of an impurity phase $Ba_3Nb_5O_{15}$ (9.7(4)% by mass) were found at ~ 63.76°, 70.44°,

and 109.36° 2θ in the 2.43 Å data set (longer wavelength) and at ~ 45° 2θ in 1.62 Å data set (short wavelength) (**Figure 3.3**).

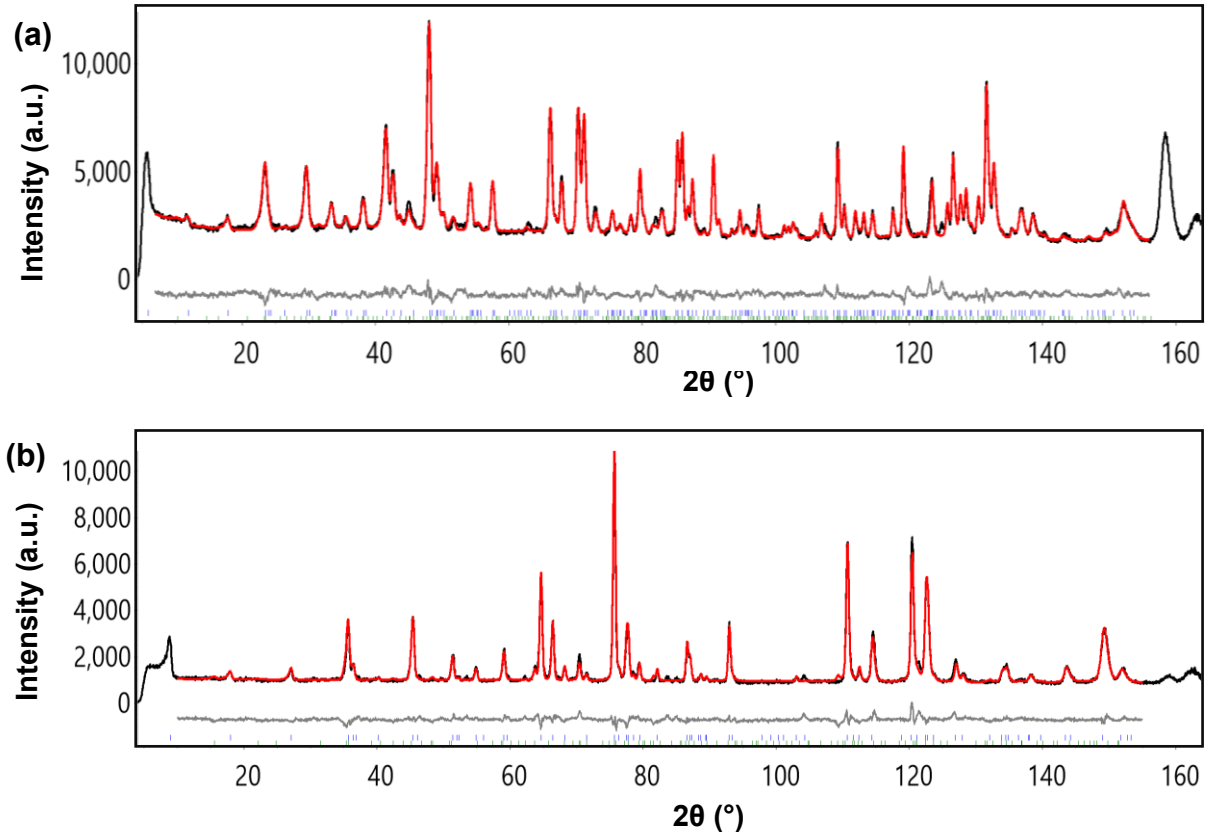

Figure 3.3: Rietveld refinement profiles from combined refinement using room-temperature (a) short wavelength (1.6218 Å) and (b) longer wavelength (2.4395 Å) NPD data for $CsBa_2Nb_3O_{10}$, refined in space group *P*4/*mmm*. The observed, calculated, and difference profiles are shown in black, red, and grey respectively).

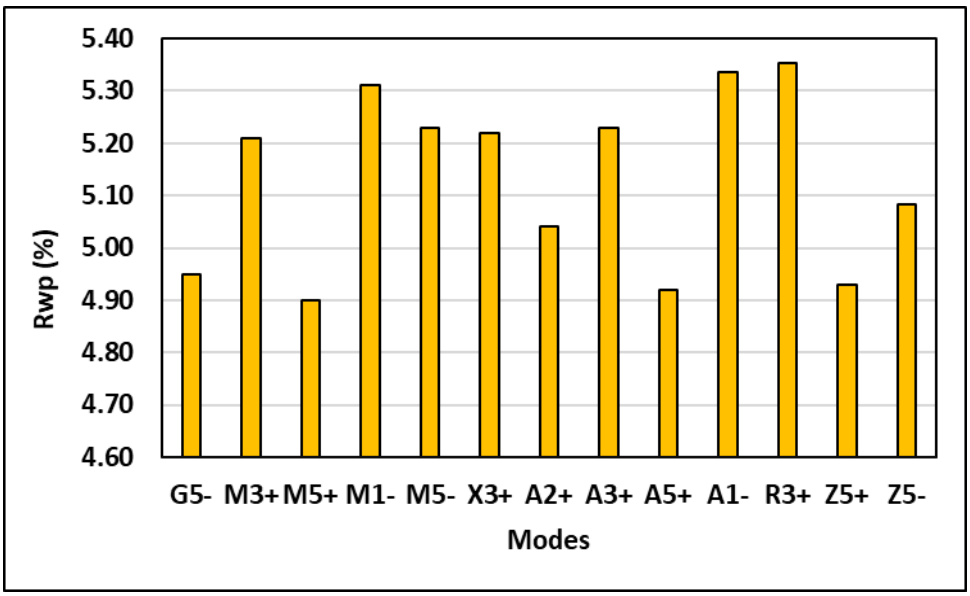

Figure 3.4: Results from mode inclusion analysis showing which mode gives the biggest improvement to the fit on refining for $CsBa_2Nb_3O_{10}$.

To evaluate the impact of lowering symmetry on the fit, lower symmetry models were investigated by using symmetry-adapted distortion mode analysis. It was found that the biggest improvements in R_{wp} in $CsBa_2Nb_3O_{10}$ are either from the in-plane polar/antipolar $\mathrm{r}_5^-/\mathrm{Z}_5^+$ displacements or A_5^+ or M_5^+ modes, representing the rotations of octahedra about an in-plane axis (**Figure 3.4**).

Table 3.1: Summary of R_{wp} values and number of parameters for the lower symmetry models compared with the parent *P*4/*mmm* model for $CsBa_2Nb_3O_{10}$.

Model	R_{wp} (%)	Number of Parameters
Parent *P*4/*mmm*	4.95	56
r_5^- (a,0) *Pmm*2	4.89	63
r_5^- (a,a) *Amm*2	4.89	66
Z_5^+ (a,0) *Cmcm*	4.93	62
Z_5^+ (a,a) *Pmma*	4.95	63
M_5^+ (a,0) *Pmna*	4.90	62
M_5^+ (a,a) *Cmma*	4.90	62
A_5^+ (a,a) *Imma*	4.92	61
A_5^+ (a,a) *Fmmm*	4.94	63

Table 3.1 shows the comparison of R_{wp} value and number of parameters for the lower symmetry models with the parent structure *P*4/*mmm* model. An example showing the Rietveld refinement profiles of lower symmetry r_5^- *Amm*2 model is provided in **Appendix 1**, **Section 1.1**. The lower symmetry models do not give significant improvements in the fit. Hence, we can conclude that the average structure of $CsBa_2Nb_3O_{10}$ is best described by *P*4/*mmm* symmetry (**Figure 3.1**). The *y*-axis range for the plot in **Figure 3.4** is relatively small compared with other plots in this chapter, highlighting the minimal improvement achieved with lower-symmetry models. The refinement details are given in **Table 3.2** and selected bond lengths are given in **Appendix 1**, **Section 1.1, Table 1.1**. Bond valence sum (BVS) calculations are used to validate the experimentally refined structures. BVS is a way to estimate the oxidation state of an atom in a material, based on the lengths of the bonds around it.[30, 31] For an atom, the BVS should roughly be equal the atom's oxidation state. The bond valence sum calculations gave valences of +5.034, +4.735 for Nb(1) and Nb(2), +2.488 for Ba(1), and +0.938 for Cs(1).

Table 3.2: Structural parameters of $CsBa_2Nb_3O_{10}$ from combined refinement using room-temperature (a) short wavelength (1.6218 Å) and (b) longer wavelength (2.4395 Å) NPD data in space group *P*4/*mmm.* All sites are constrained to be fully occupied.

Space group: *P4/mmm* (No. 123). Cell parameters: *a* = 3.97705(6) Å, *c* = 15.5885(3) Å. R_{wp} = 4.95%, R_p = 3.697%, χ^2 = 4.49, 56 parameters.

Atom	Wyckoff Site	*x*	*y*	*z*	U_{iso} x 100 (Å^2)
Cs(1)	1*d*	0.5	0.5	0.5	1.49(10)
Ba(1)	2*h*	0.5	0.5	0.1432(2)	0.37(8)
Nb(1)	1*a*	0	0	0	1.13(8)
Nb(2)	2*g*	0	0	0.2903(1)	0.42(7)
O(1)	2*f*	0	0.5	0	0.44(8)
O(2)	2*g*	0	0	0.1252(2)	0.35(8)
O(3)	4*i*	0	0.5	0.2661(1)	0.46(6)
O(4)	2*g*	0	0	0.4007(2)	0.65(8)

3.3.2.2 Structural Characterisation of $CsSr_2Nb_3O_{10}$

Attempts were made to fit the short wavelength (1.6218 Å) and longer wavelength (2.4395 Å) neutron powder diffraction data collected for $CsSr_2Nb_3O_{10}$ with an aristotype *P*4*/mmm* model. Rietveld refinement profiles from multibank refinement (**Figure 3.5**) show that there is intensity mismatch for this high symmetry model and a few peaks between 80° and 150° 2θ in 1.62 Å data set (short wavelength) and ~ 59.33° and between 120° and 140° 2θ in 2.43 Å data set (longer wavelength) are not fitted by this model.

The *P*4*/mmm* model gave an unreasonably high atomic displacement parameter (ADP) for the central equatorial oxygen site O(1). Allowing anisotropy of this ADP suggested significant displacements in the *ab* plane, suggesting rotation of the BO_6 octahedra about the long axis (**Figure 3.6**). Therefore, lower symmetry models allowing rotations about the out-of-plane axis, described by M_3^+ or A_3^+ modes, were considered to resolve the problems with this site.

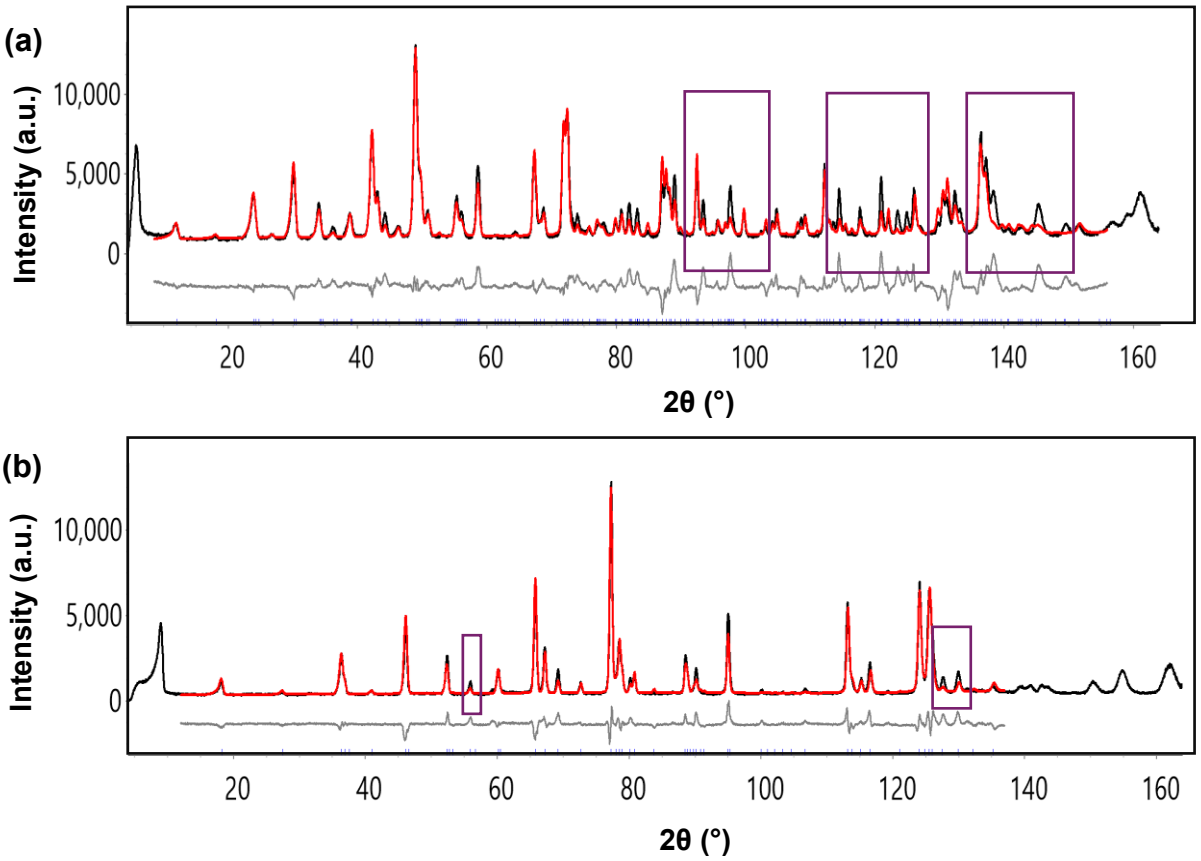

Figure 3.5: Rietveld refinement profiles from combined refinement using room-temperature (a) short wavelength (1.6218 Å) and (b) longer wavelength (2.4395 Å) NPD data for $CsSr_2Nb_3O_{10}$, refined in space group *P*4/*mmm*. The observed, calculated, and difference profiles are shown in black, red, and grey respectively).

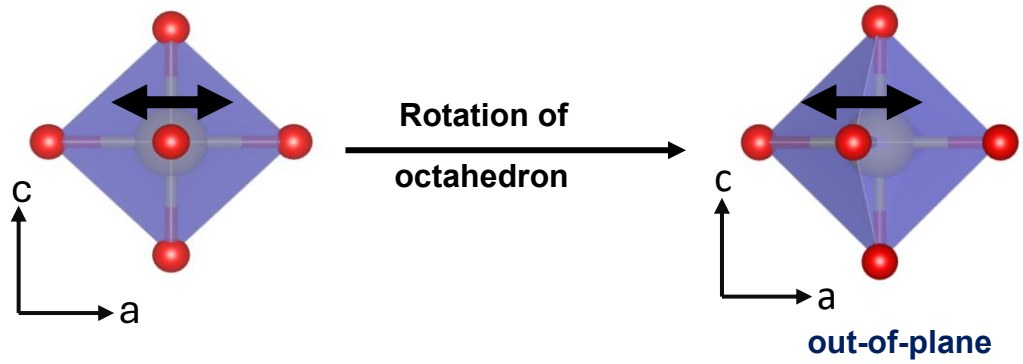

Figure 3.6: Oxygen O(1) site suggesting rotation of octahedra about the long axis (out-of- plane axis).

Additionally, the results from mode inclusion analysis show that the biggest improvements in the R_{wp} value are either from in-plane polar/antipolar r_5^-/Z_5^- displacement or rotations about the out-of-plane axis described by M_3^+ or A_3^+ modes (**Figure 3.7**).

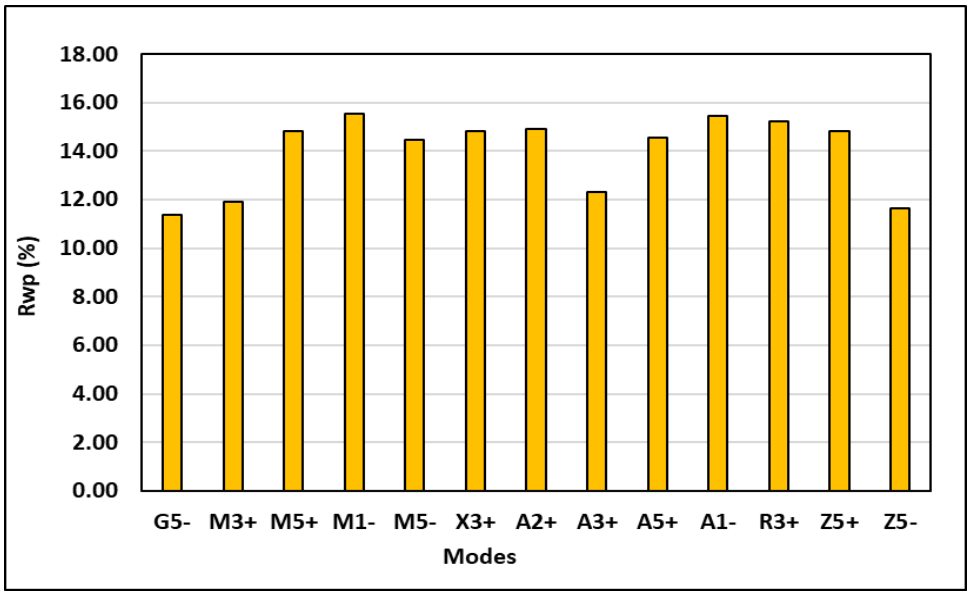

Figure 3.7: Results from mode inclusion analysis showing which modes give the biggest improvement in the R_{wp} value.

Refinement using the $\sqrt{2}a_t \times \sqrt{2}a_t \times c$ model of *P*4/*mbm* symmetry, corresponding to M_3^+ octahedral rotations gave R_{wp} = 6.25% (41 parameters) and using the $\sqrt{2}a_t \times \sqrt{2}a_t \times 2c$ model of *I*4/*mcm* symmetry corresponding to A_3^+ rotations gave R_{wp} = 7.05% (35 parameters). Compared to the ideal *P*4/*mmm* model with R_{wp} =15.80% (33 parameters) both tetragonal models showed a significant improvement in fit. To explore further improvements and check whether $CsSr_2Nb_3O_{10}$ could be polar, the polar r_5^- mode was added to both M_3^+ and A_3^+ modes.

From mode decomposition analysis it was found the mode amplitudes were 0.61 Å for M_3^+ rotations for the *P*4/*mbm* model, and 0.60 and 0.10 Å for M_3^+ rotations and r_5^- polar displacements for the *P*2$_1$*am* model, respectively. This suggests that the average structure is best described by a non-polar model of *P*4/*mbm* symmetry. SHG measurements were performed to confirm this.

Table 3.3 summarizes the R_{wp} values and number of parameters for the lower symmetry models compared with the parent *P*4/*mmm* model. The M_3^+ *P*4/*mbm* model was found to be most suitable for $CsSr_2Nb_3O_{10}$, offering approximately 60% improvement in fit with an increase of only 8 independent parameters. The refinement details are given in **Table 3.4** and selected bond lengths and bond angles are given in **Appendix 1**, **Section 1.2, Table 1.2**. The bond valence sum calculations gave valences of +5.015, +4.887 for Nb(1) and Nb(2), +2.14 for Sr(1), and +1.025 for Cs(1).

Table 3.3: Summary of R_{wp} values and number of parameters for the lower symmetry models compared with the parent *P*4/*mmm* model for $CsSr_2Nb_3O_{10}$.

Model	R_{wp} (%)	Number of Parameters
Parent *P*4/*mmm*	15.80	33
r_5^- (a|0) *Pmm*2	36.93	45
r_5^- (a|a) *Amm*2	6.79	44
M_3^+ *P*4/*mbm*	6.25	41
A_3^+ *I*4/*mcm*	7.05	35
$A_3^+ + r_5^-$ (a|b,0) *Fmm*2	6.74	63
$A_3^+ + r_5^-$ (a|b,b) *Ima*2	6.44	59
$M_3^+ + r_5^-$ (a|b,0) *Amm*2	6.31	63
$M_3^+ + r_5^-$ (a|b,b) *Pmc*2$_1$	6.47	60

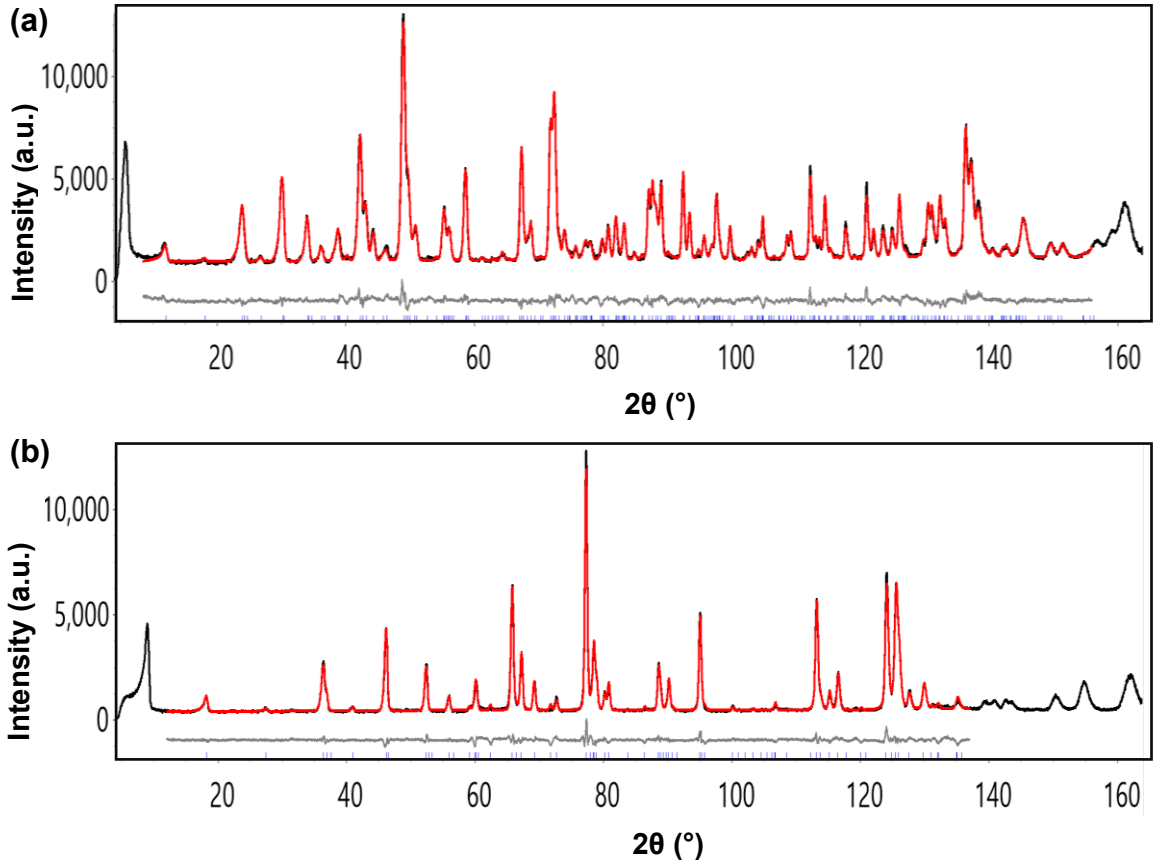

Figure 3.8: Rietveld refinement profiles from combined refinement using room-temperature (a) short wavelength (1.6218 Å) and (b) longer wavelength (2.4395 Å) NPD data for $CsSr_2Nb_3O_{10}$, refined in space group *P*4/*mbm*. The observed, calculated, and difference profiles are shown in black, red, and grey respectively).

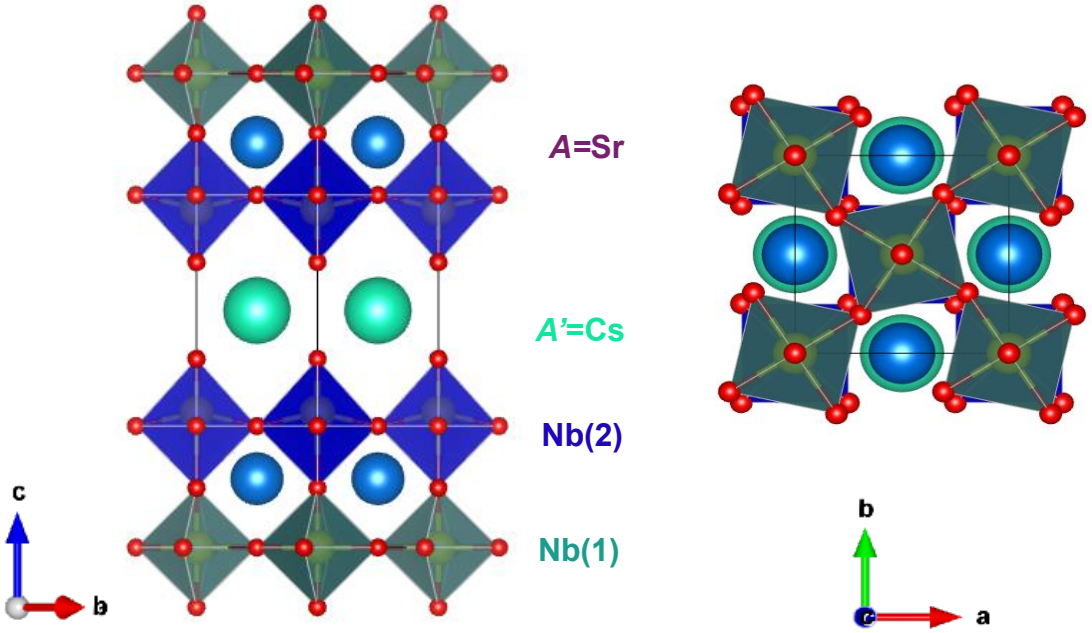

Figure 3.9: Crystal structure of M_3^+ *P4/mbm* model for *n* = 3 DJ phase $CsSr_2Nb_3O_{10}$. Cs, Ca, Sr and O sites are shown in green, blue, yellow, and red, and $Nb(1)O_6$ and $Nb(2)O_6$ octahedra are shown in light and dark blue, respectively.

Table 3.4: Structural parameters of $CsSr_2Nb_3O_{10}$ from combined refinement using room-temperature (a) short wavelength (1.6218 Å) and (b) longer wavelength (2.4395 Å) NPD data in space group *P4/mbm.* All sites are constrained to be fully occupied.

Space group: *P4/mbm* (No. 127). Cell parameters: *a* = 5.52654(7) Å, *c* = 15.4256(2) Å, R_{wp} = 6.25%, R_p = 4.63%, χ^2 = 4.93, 41 parameters.

Atom	Wyckoff Site	*x*	*y*	*z*	U_{iso} x 100 (Å^2)
Cs(1)	*2c*	0	0.5	0.5	1.54(6)
Sr(1)	*4f*	0	0.5	0.1451(1)	0.70(3)
Nb(1)	*2a*	0	0	0	0.27(4)
Nb(2)	4e	0	0	0.2839(1)	0.02(3)
O(11)	4g	0.8048(3)	1.3048(3)	0	1.13(5)
O(21)	4e	0	0	0.1254(1)	0.68(4)
O(31)	8k	0.7513(2)	1.2513(2)	0.7430(1)	0.50(2)
O(41)	4e	0	0	0.3983(1)	1.12(4)

3.3.2.3 Structural Characterisation of $CsCa_2Nb_3O_{10}$

Attempts were made to fit the short wavelength (1.6218 Å) and longer wavelength (2.4395 Å) neutron powder diffraction data collected for $CsCa_2Nb_3O_{10}$ with an aristotype *P4/mmm* model, similar to the approach taken for $CsSr_2Nb_3O_{10}$. Multibank Rietveld refinement profiles (**Figure 3.10**) show that there is intensity mismatch for this high symmetry model and the peaks ~ 38.65°, 41.75°, 46°, 65°, 77°, 82°, 96°, 127° and 145° 2θ in 1.62 Å data set (short wavelength) and ~ 60°, 65°, 69.61°, 72.45°, 107.07°, 132.56°, 133.33°, and 139.06° 2θ in 2.43 Å data set (longer wavelength) are not fitted by this parent structure.

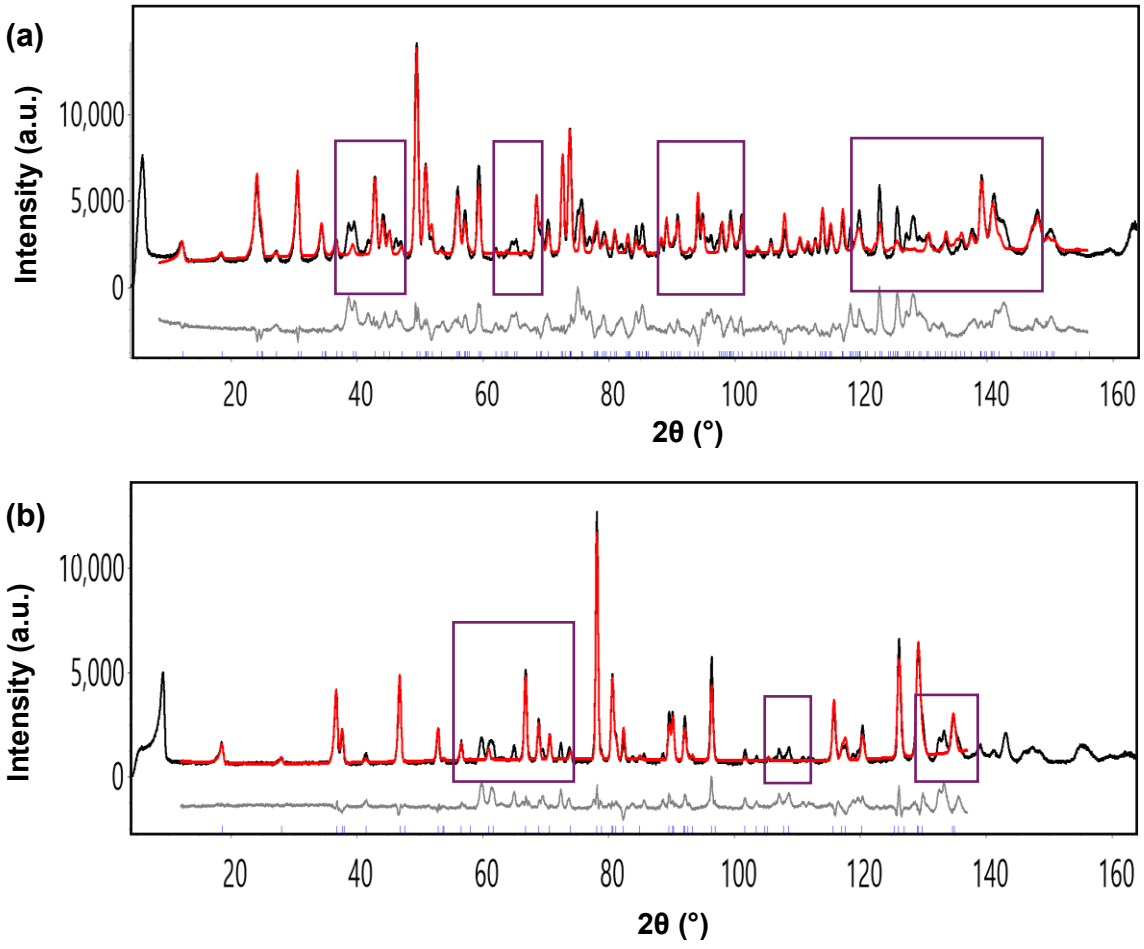

Figure 3.10: Rietveld refinement profiles from combined refinement using room-temperature (a) short wavelength (1.6218 **Å**) and (b) longer wavelength (2.4395 **Å**) NPD data for $CsCa_2Nb_3O_{10}$, refined in space group *P*4/*mmm*. The observed, calculated, and difference profiles are shown in black, red, and grey respectively).

Similar to $CsSr_2Nb_3O_{10}$, the *P4/mmm* model for $CsCa_2Nb_3O_{10}$ also gave an unreasonably high atomic displacement parameter (ADP) for the central equatorial oxygen site O(1). Allowing anisotropy of this ADP suggested significant displacements in the *ab* plane, suggesting rotation of the BO_6 octahedra about the

long axis. The ADP for the apical oxygens was also very high. Allowing anisotropy of this ADP suggested rotation of the BO_6 octahedra about an in-plane axis (**Figure 3.11**). Consequently, models with rotations of octahedra about both the out-of-plane

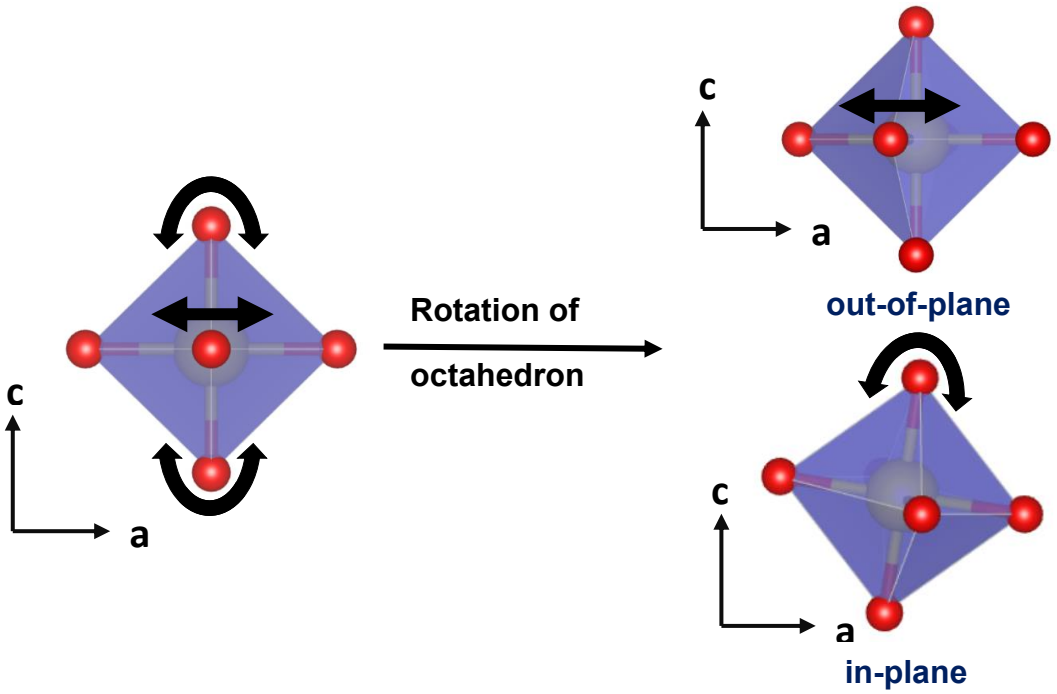

Figure 3.11: Oxygen O(1) site and apical oxygens suggesting rotation of octahedra about the out-of-plane axis and in-plane axis respectively.

axis, described by M_3^+ or A_3^+ modes, and in-plane axis were considered.

Results from mode inclusion analysis show that the biggest improvement in the R_{wp} value are from the rotations about an in-plane axis described by A_5^+ or X_3^+ modes (**Figure 3.12**). Thus, further refinements focused on models with rotations of

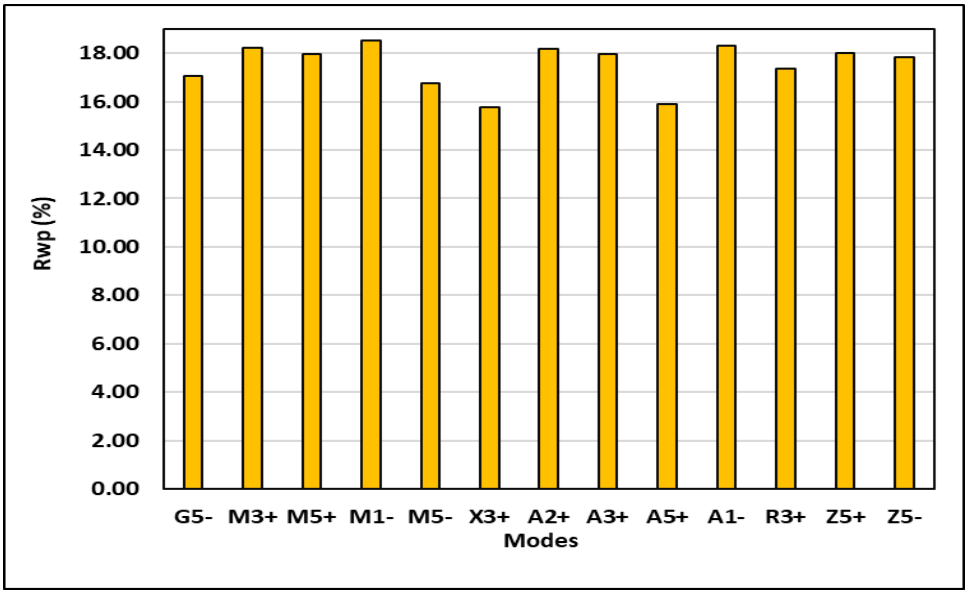

Figure 3.12: Results from first round of mode inclusion analysis showing which modes give the biggest improvement in the R_{wp} value.

octahedra about both the out-of-plane axis, described by M_3^+ or A_3^+ modes, and in-plane axis, described by A_5^+ or X_3^+ modes.

The models that allowed only a single type of rotation about an in-plane axis, either A_5^+ or X_3^+ tilts, failed to account for all the observed peaks. Similarly, models allowing either A_3^+ or M_3^+ tilts combined with a single in-plane tilt also did not index all the peaks. An example showing the Rietveld refinement profiles of M_3^+ + A_5^+ *Pnam* model is provided in **Appendix 1, Section 1.3**. Therefore, more complex models allowing both X_3^+ + A_5^+ tilts about in-plane axes were considered.

Table 3.5: Summary of R_{wp} values and number of parameters for the lower symmetry models compared with the parent *P*4/*mmm* model for $CsCa_2Nb_3O_{10}$.

Model	R_{wp} (%)	Number of Parameters
Parent *P4/mmm*	15.28	39
X_3^+ (a,0) *Pmma*	11.78	49
X_3^+ (a,a) *P4/nmm*	10.94	50
X_3^+ (a,b) *Pmmn*	13.34	60
A_5^+ (a,0) *Imma*	14.79	48
A_5^+ (a,a) *Fmmm*	10.94	48
M_3^+ *P4/mbm*	14.09	41
$X_3^+ + M_3^+$ (a;b|c) *Pmmn*	10.11	61
$A_5^+ + M_3^+$ (a,0|b) *Pnam*	8.84	64
$A_5^+ + M_3^+$ (a,a|b) *Cmcm*	9.36	54
$X_3^+ + A_5^+$ (a;b|c,c) *Pnma*	8.25	90
$X_3^+ + A_5^+ + r_5^-$ (a,0|b;c|d,d) $P2_1cn$	4.46	135
$X_3^+ + A_5^+ + r_5^-$ (a,0|b;c|-d,d) $Pm2_1n$	4.19	146

The X_3^+ + A_5^+ *Pnma* model significantly improved the fit giving a low R_{wp} value. This combination of X_3^+ (a,b) + A_5^+ (c,c) also allows the M_3^+ octahedral rotations. This model is also consistent with the previous studies done by M. Dion et al., using

single crystal x-ray diffraction to determine the structure of $CsCa_2Nb_3O_{10}$.[32] To explore further improvements and check whether $CsCa_2Nb_3O_{10}$ could be polar, the polar Γ_5^- mode was added to the $X_3^+ + A_5^+$ combination. The $X_3^+ + A_5^+ + \Gamma_5^-$ *Pmn*2$_1$ and *Pna*2$_1$ models also allow the M_3^+ octahedral rotations. SHG measurements performed to confirm the polarity gave significant response (Section 3.4.5), hence polar models of *Pna*2$_1$ and *Pmn*2$_1$ symmetries were considered. **Table 3.5** compares the R_{wp} values and number of parameters of the lower symmetry models with the parent *P*4/*mmm* model. Based on these results, the polar $X_3^+ + A_5^+ + \Gamma_5^-$ (+ M_3^+) *Pna*2$_1$ and $X_3^+ + A_5^+ + \Gamma_5^-$ (+ M_3^+) *Pmn*2$_1$ models appear to be the most suitable for $CsCa_2Nb_3O_{10}$. A comparison of bond valence sum (BVS) values for these models is provided in **Appendix 1**, **Section 1.3**. Based on the BVS values, $X_3^+ + A_5^+ + \Gamma_5^-$ (+ M_3^+) *Pmn*2$_1$ was found to be most appropriate for $CsCa_2Nb_3O_{10}$. The space group setting has been changed to *Pm*2$_1$*n* to have long axis along *c*. We will be using the non-standard setting from here on.

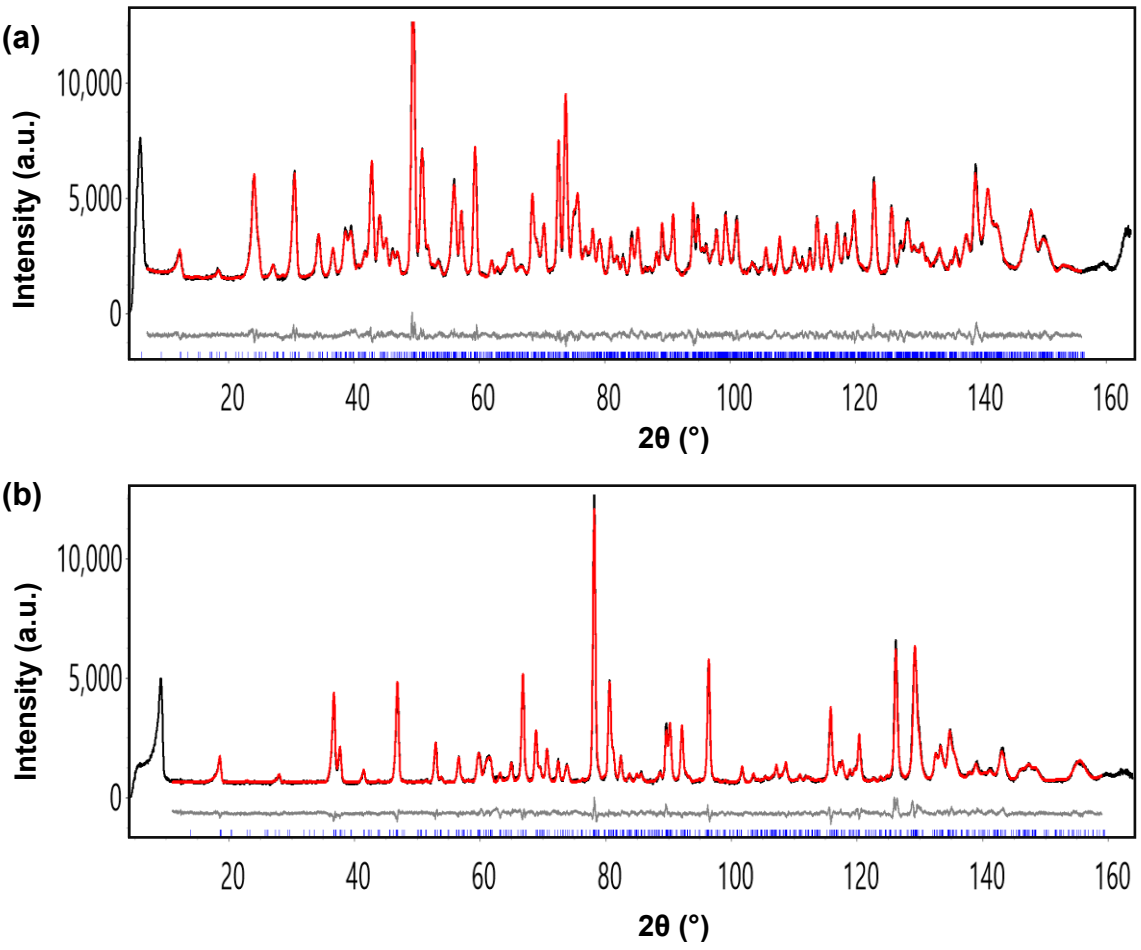

Figure 3.13: Rietveld refinement profiles from combined refinement using room-temperature (a) short wavelength (1.6218 Å) and (b) longer wavelength (2.4395 Å) NPD data for $CsCa_2Nb_3O_{10}$, refined in space group *Pm*2$_1$*n*. The observed, calculated, and difference profiles are shown in black, red, and grey respectively).

The refinement details are given in **Table 3.6** and selected bond lengths and bond angles are given in **Appendix 1, Section 1.3, Table 1.3**. The bond valence sum calculations gave valences of +5.01, +5.059, +4.863, 4.833, +5.29, +5.125 for Nb(11), Nb(12), Nb(21), Nb(22), Nb(23) and Nb(24), +2.299, +2.206, +2.049, +2.342, +1.957, +1.588, +2.053, +2.020 for Ca(11), Ca(12), Ca(13), Ca(14), Ca(15), Ca(16), Ca(17) and Ca(18) and +1.164, +1.212, +1.016, +1.026 for Cs(11), Cs(12), Cs(13) and Cs(14).

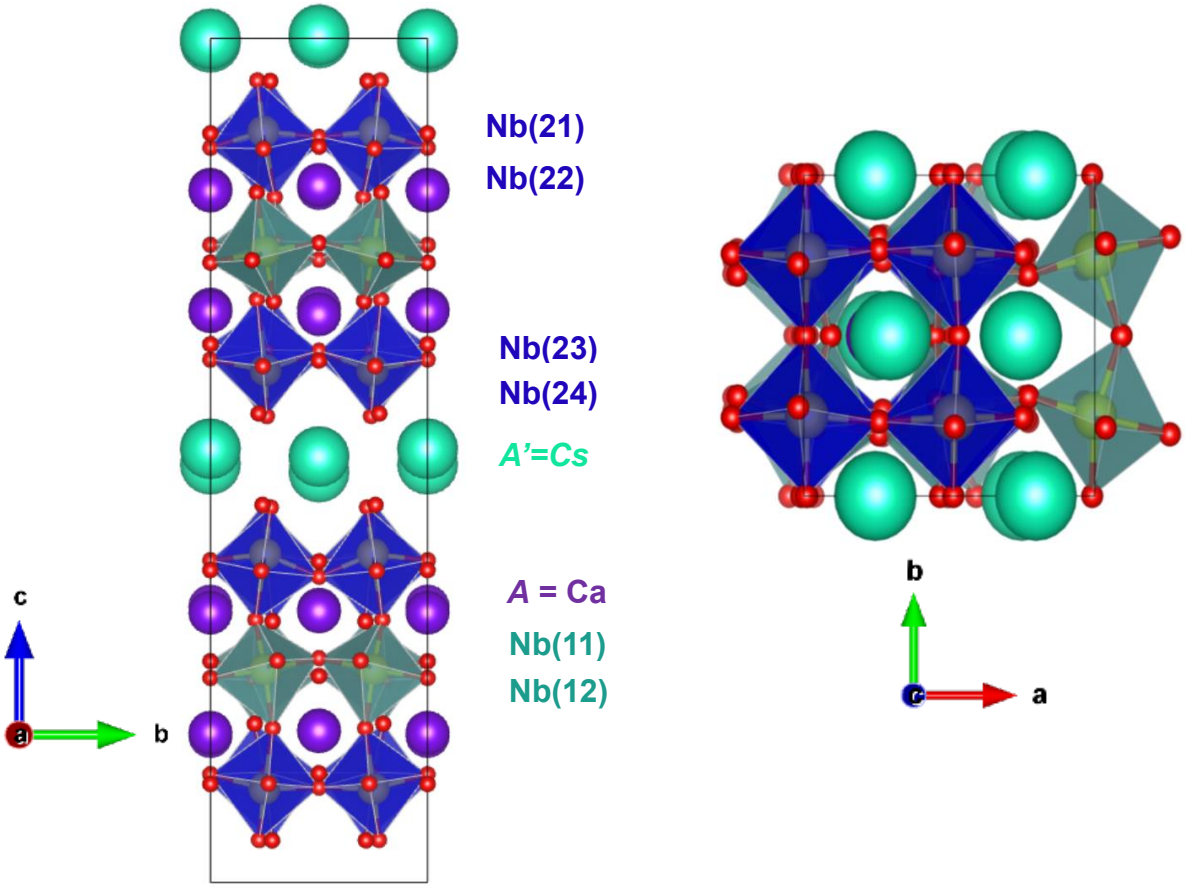

Figure 3.14: Crystal structure of $X_3^+ + A_5^+ + r_5^-$ *Pm*2$_1$*n* model for n=3 DJ phase $CsCa_2Nb_3O_{10}$. Cs, Ca, Nb and O sites are shown in green, purple, yellow, and red, and $Nb(11)O_6$, $Nb(12)O_6$, $Nb(21)O_6$, $Nb(22)O_6$ $Nb(23)O_6$, $Nb(24)O_6$octahedra are shown in light and dark blue respectively.

Table 3.6: Structural parameters of $CsCa_2Nb_3O_{10}$ from combined refinement using room-temperature (a) short wavelength (1.6218 Å) and (b) longer wavelength (2.4395 Å) NPD data in space group *Pm*2_1*n.* All sites are constrained to be fully occupied, and ADP values are constrained to be equal for all sites derived from the same site in the parent structure.

Space group: *Pm*2_1*n* (No. 31). Cell parameters: *a* = 7.7464(1) Å, *b* = 7.7392(1) Å, *c* = 30.2009(4) Å, R_{wp} = 4.19%, R_p = 3.18%, χ^2 = 3.09, 146 parameters.

Atom	Wyckoff Site	*x*	*y*	*z*	U_{iso} x 100 (Å)	Atom	Wyckoff Site	*x*	*y*	*z*	U_{iso} x 100 (Å)
Cs(11)	2*a*	0	0.798(3)	-0.0005(6)	0.3(1)	Nb(12)	4*b*	0.747(2)	0.502(3)	0.7512(5)	0.39(4)
Cs(12)	2*a*	0	0.247(3)	-0.0045(7)	0.3(1)	Nb(21)	4*b*	0.748(1)	0.010(1)	0.8888(4	0.39(4)
Cs(13)	2*a*	0	0.750(3)	0.5139(5)	0.3(1)	Nb(22)	4*b*	0.755(1)	0.517(2)	0.8899(4)	0.39(4)
Cs(14)	2*a*	0	0.244(3)	0.4954(7)	0.3(1)	Nb(23)	4*b*	0.753(1)	0.005(3)	0.3930(4)	0.39(4)
Ca(11)	2*a*	0	0.768(4)	0.1773(1)	0.7(1)	Nb(24)	4*b*	0.747(1)	0.518(2)	0.3890(4)	0.39(4)
Ca(12)	2*a*	0	0.286(3)	0.1734(8)	0.7(1)	O(11)	4*b*	0.808(2)	0.258(3)	0.7373(5)	0.82(9)
Ca(13)	2*a*	0	0.759(5)	0.676(1)	0.7(1)	O(12)	4*b*	0.690(2)	0.772(3)	0.7603(6)	0.82(9)
Ca(14)	2*a*	0	0.272(5)	0.678(1)	0.7(1)	O(13)	2*a*	0	-0.009(3)	0.7344(6)	0.82(9)
Ca(15)	2*a*	0	0.269(4)	0.821(1)	0.7(1)	O(14)	2*a*	0	0.468(3)	0.7554(8)	0.82(9)
Ca(16)	2*a*	0	0.791(5)	0.8198(9)	0.7(1)	O(15)	2*a*	0	-0.050(3)	0.2620(8)	0.82(9)
Ca(17)	2*a*	0	0.234(4)	0.3268(9)	0.7(1)	O(16)	2*a*	0	0.592(3)	0.2422(8)	0.82(9)
Ca(18)	2*a*	0	0.746(4)	0.319(1)	0.7(1)	O(21)	4*b*	0.786(1)	0.037(3)	0.8173(4)	0.32(8)
Nb(11)	4*b*	0.750(2)	0*	0.7479(4)	0.39(4)	O(22)	4*b*	0.704(2)	0.458(3)	0.8120(5)	0.32(8)

* Fixed to define origin of the unit cell along the polar axis.

O(23)	4*b*	0.714(2)	0.045(3)	0.3094(5)	0.32(8)	O(38)	2*a*	0	0.504(3)	0.1281(8)	0.36(5)
O(24)	4*b*	0.792(2)	0.463(3)	0.3112(5)	0.32(8)	O(39)	2*a*	0	0.494(3)	0.3817(8)	0.36(5)
O(31)	4*b*	0.768(2)	0.259(3)	0.8830(4)	0.36(5)	O(310)	2*a*	0	0.013(3)	0.3700(7)	0.36(5)
O(32)	4*b*	0.755(2)	0.752(3)	0.8694(5)	0.36(5)	O(311)	2*a*	0	0.514(3)	0.8706(9)	0.36(5)
O(33)	4*b*	0.741(1)	0.264(3)	0.3882(4)	0.36(5)	O(312)	2*a*	0	0.008(3)	0.8876(7)	0.36(5)
O(34)	4*b*	0.766(2)	0.771(3)	0.3691(6)	0.36(5)	O(41)	4*b*	0.724(2)	-0.019(3)	-0.0502(6)	0.73(9)
O(35)	2*a*	0	0.014(3)	0.6378(6)	0.36(5)	O(42)	4*b*	0.784(2)	0.518(3)	-0.0497(6)	0.73(9)
O(36)	2*a*	0	0.514(4)	0.6196(9)	0.36(5)	O(43)	4*b*	0.760(2)	-0.027(3)	0.4474(5)	0.73(9)
O(37)	2*a*	0	0.033(3)	0.1165(7)	0.36(5)	O(44)	4*b*	0.722(3)	0.521(3)	0.4443(5)	0.73(9)

3.3.2.4 Structural Characterisation of $CsCa_2Ta_3O_{10}$

Rietveld refinement results show that the attempts to fit the longer wavelength (2.4395 Å) neutron powder diffraction data with the aristotype *P*4/*mmm* model were unsuccessful (**Figure 3.15**). Similar to the Nb analogue, extra peaks at 57°, 60°, 62°, 65°, 72.5°, 86°, 89°, 107.34°, and 131° 2θ are not fitted by the parent unit cell.

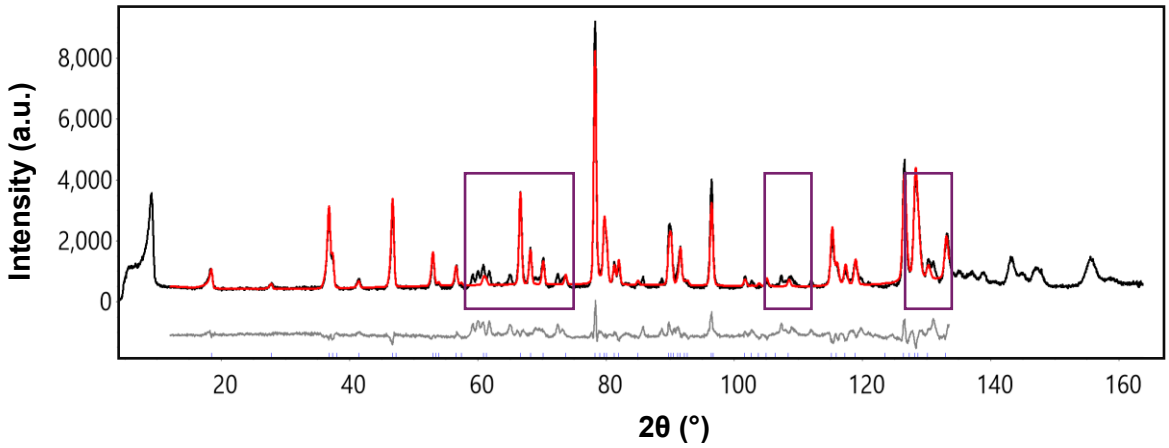

Figure 3.15: Rietveld refinement profile using room-temperature longer wavelength (2.4395 **Å**) NPD data for $CsCa_2Ta_3O_{10}$, refined in space group *P*4/*mmm*. The observed, calculated, and difference profiles are shown in black, red, and grey respectively).

Similar to $CsCa_2Nb_3O_{10}$, the model also gave an unreasonably high atomic displacement parameter (ADP) for the central equatorial oxygen site O(1) and apical oxygens. Allowing anisotropy of these ADPs suggested rotation of the BO_6 octahedra about the out-of-plane axis and in-plane axis. Consequently, models with rotations of octahedra about both the out-of-plane axis, described by M_3^+ or A_3^+ modes, and in-plane axis were considered.

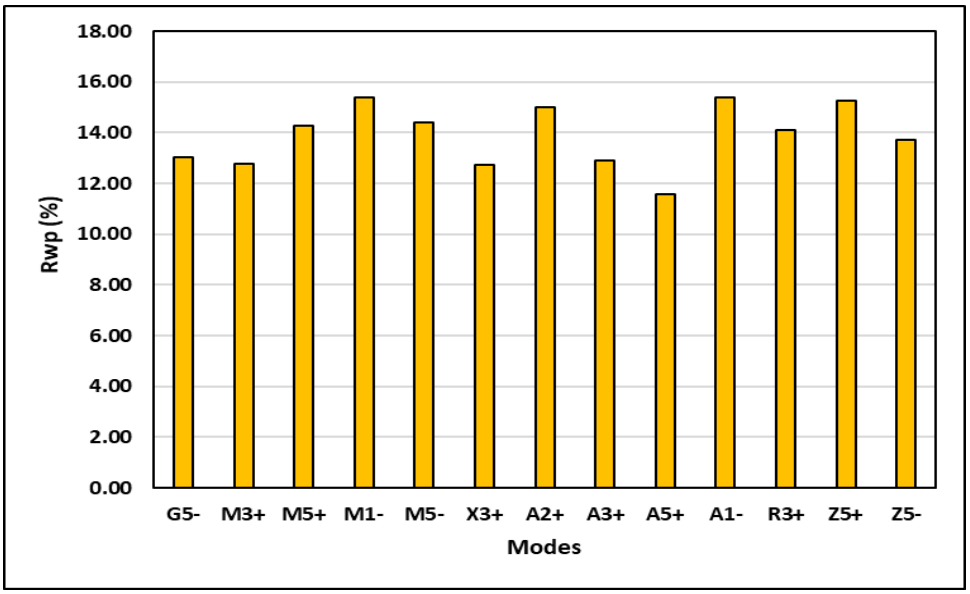

Figure 3.16: Results from first round of mode inclusion analysis showing which modes give the biggest improvement in the R_{wp} value.

Results from mode inclusion analysis show that the biggest improvement in the R_{wp} value are from the rotations about an in-plane axis described by A_5^+ or X_3^+ modes (**Figure 3.16**). Thus, further refinements focused on models with rotations of octahedra about both the out-of-plane axis, described by M_3^+ or A_3^+ modes, and in-plane axis, described by A_5^+ or X_3^+ modes.

Table 3.7: Summary of the R_{wp} values and number of parameters of the lower symmetry models compared with the parent *P*4/*mmm* model for $CsCa_2Ta_3O_{10}$.

Model	R_{wp} (%)	Number of Parameters
Parent *P*4/*mmm*	12.67	27
X_3^+ (a,0) *Pmma*	10.05	38
X_3^+ (a,a) *P*4/*nmm*	9.73	39
X_3^+ (a,b) *Pmmn*	9.19	51
A_5^+ (a,0) *Imma*	9.99	33
A_5^+ (a,a) *Fmmm*	10.26	34
M_3^+ *P*4/*mbm*	11.59	28
$M_3^+ + A_5^+$ (a|b,0) *Pnam*	8.73	38
$M_3^+ + A_5^+$ (a|b,b) *Cmcm*	8.68	40
$X_3^+ + M_3^+$ (a;b|c) *Pmmn*	9.53	48
$X_3^+ + A_5^+$ (a;b|c,c) *Pnma*	6.05	67
$X_3^+ + A_5^+ + \Gamma_5^-$ (a,0|b;c|d,d) *Pna*2_1	6.76	111
$X_3^+ + A_5^+ + \Gamma_5^-$ (a,0|b;c|-d,d) *Pmn*2_1	6.64	123

A similar structural investigation was carried out for $CsCa_2Ta_3O_{10}$. **Table 3.7** compares the R_{wp} values and number of parameters of the lower symmetry models with the parent *P*4/*mmm* model. Here also the polar *Pna*2_1 and *Pmn*2_1 models appear to be most suitable. A comparison of BVS values for these models is provided in **Appendix 1**, **Section 1.3**. The polar X_3^+ + A_5^+ + Γ_5^- (+ M_3^+) *Pmn*2_1 model was found out to be most suitable for $CsCa_2Ta_3O_{10}$, consistent with the findings for $CsCa_2Nb_3O_{10}$. This outcome aligns with expectations, as the ionic radii of Nb^{5+} and Ta^{5+} are similar. The space group setting has been changed to *Pm*2_1*n* to have long

axis along *c*. We will be using the non-standard setting from here on. The refinement details are given in **Table 3.8** and selected bond lengths and bond angles and **Appendix 1**, **Section 1.4, Table 1.4**. The bond valence sum calculations gave valences of +5.160, +5.208, +4.917, +5.011, +4.995, +5.185 for Ta(11), Ta(12), Ta(21), Ta(22), Ta(23) and Ta(24), +1.80, +2.170, +2.675, +2.212, +2.068, +1.519,+1.886, +1.736 for Ca(11), Ca(12), Ca(13), Ca(14), Ca(15), Ca(16), Ca(17) and Ca(18) and +1.174, +1.111, +0.933, +0.999 for Cs(11), Cs(12), Cs(13) and Cs(14).

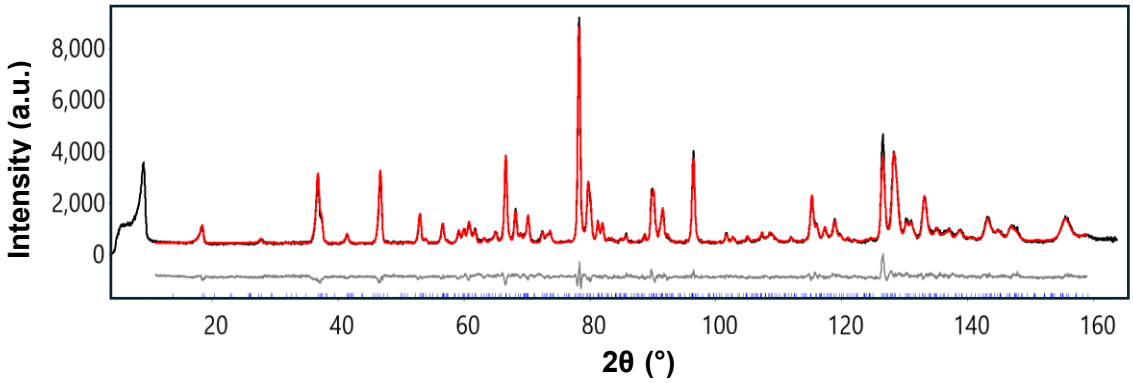

Figure 3.17: Rietveld refinement profile using room-temperature longer wavelength (2.4395 **Å**) NPD data for $CsCa_2Ta_3O_{10}$, refined in space group $Pm2_1n$. The observed, calculated, and difference profiles are shown in black, red, and grey respectively).

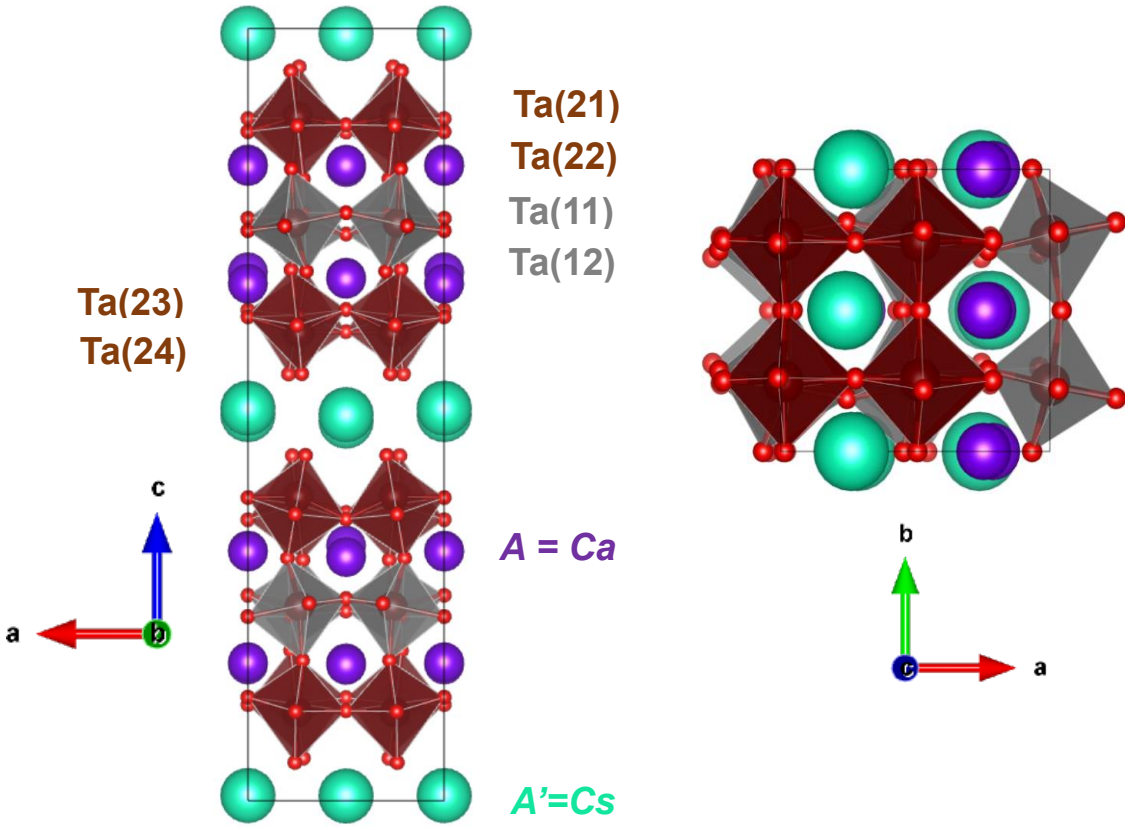

Figure 3.18: Crystal structure $X_3^+ + A_5^+ + r_5^-$ $Pm2_1n$ model for n=3 DJ phase $CsCa_2Ta_3O_{10}$. Cs, Ca, Ta and O sites are shown in green, purple, gray, and red, and $Ta(11)O_6$, $Ta(21)O_6$, $Ta(22)O_6$ $Ta(23)O_6$, $Ta(24)O_6$ octahedra are shown in grey and brown, respectively.

Table 3.8: Structural parameters of $CsCa_2Ta_3O_{10}$ using room-temperature longer wavelength (2.4395 Å) NPD data in space group *Pm*2$_1$*n.* All sites are constrained to be fully occupied All sites are constrained to be fully occupied, and ADP values are constrained to be equal for all sites.

Space group: *Pm*2$_1$*n* (No. 31). Cell parameters: *a*= 7.7322(4) Å, *b* = 7.7290(4) Å, *c* = 30.4660(8) Å, R_{wp} = 5.43%, R_p = 4.26%, χ^2 = 2.28, 123 parameters.

Atom	Wyckoff Site	*x*	*y*	*z*	U_{iso} x 100 (Å)	Atom	Wyckoff Site	*x*	*y*	*z*	U_{iso} x 100 (Å)
Cs(11)	2*a*	0	0.75(1)	0.75(1)	1.24(7)	Ta(12)	4*b*	0.744(7)	0.49(1)	0.751(1)	1.24(7)
Cs(12)	2*a*	0	0.23(1)	0.23(1)	1.24(7)	Ta(21)	4*b*	0.748(8)	0.001(9)	0.891(1)	1.24(7)
Cs(13)	2*a*	0	0.740(9)	0.74(1)	1.24(7)	Ta(22)	4*b*	0.755(8)	0.51(1)	0.890(1)	1.24(7)
Cs(14)	2*a*	0	0.286(7)	0.25(1)	1.24(7)	Ta(23)	4*b*	0.753(8)	0.007(1)	0.386(1)	1.24(7)
Ca(11)	2*a*	0	0.75(1)	0.75(1)	1.24(7)	Ta(24)	4*b*	0.746(9)	0.505(9)	0.389(1)	1.24(7)
Ca(12)	2*a*	0	0.258(9)	0.23(1)	1.24(7)	O(11)	4*b*	0.798(7)	0.24(1)	0.740(1)	1.24(7)
Ca(13)	2*a*	0	0.788(9)	0.77(1)	1.24(7)	O(12)	4*b*	0.681(6)	0.76(1)	0.760(1)	1.24(7)
Ca(14)	2*a*	0	0.285(8)	0.26(1)	1.24(7)	O(13)	2*a*	0	-0.06(1)	0.738(3)	1.24(7)
Ca(15)	2*a*	0	0.297(8)	0.27(1)	1.24(7)	O(14)	2*a*	0	0.44(1)	0.760(3)	1.24(7)
Ca(16)	2*a*	0	0.75(1)	0.75(1)	1.24(7)	O(15)	2*a*	0	-0.05(1)	0.266(3)	1.24(7)
Ca(17)	2*a*	0	0.27(1)	0.25(1)	1.24(7)	O(16)	2*a*	0	0.50(1)	0.243(2)	1.24(7)
Ca(18)	2*a*	0	0.731(9)	0.73(1)	1.24(7)	O(21)	4*b*	0.784(9)	0.02(1)	0.815(1)	1.24(7)
Ta(11)	4*b*	0.749(9)	0*	0.750(2)	1.24(7)	O(22)	4*b*	0.715(8)	0.47(1)	0.812(1)	1.24(7)

* Fixed to define origin of the unit cell along the polar axis.

O(23)	4*b*	0.701(7)	0.056(9)	0.306(1)	1.24(7)	O(38)	2*a*	0	0.49(1)	0.131(3)	1.24(7)
O(24)	4*b*	0.777(9)	0.47(1)	0.313(1)	1.24(7)	O(39)	2*a*	0	0.49(1)	0.384(3)	1.24(7)
O(31)	4*b*	0.744(8)	0.25(1)	0.878(1)	1.24(7)	O(310)	2*a*	0	0.01(1)	0.365(2)	1.24(7)
O(32)	4*b*	0.75(1)	0.75(1)	0.872(1)	1.24(7)	O(311)	2*a*	0	0.50(1)	0.872(3)	1.24(7)
O(33)	4*b*	0.746(8)	0.25(1)	0.387(1)	1.24(7)	O(312)	2*a*	0	-0.01(1)	0.885(3)	1.24(7)
O(34)	4*b*	0.749(9)	0.75(1)	0.370(1)	1.24(7)	O(41)	4*b*	0.712(9)	-0.01(1)	-0.050(1)	1.24(7)
O(35)	2*a*	0	0.005(1)	0.640(2)	1.24(7)	O(42)	4*b*	0.77(1)	0.52(1)	-0.051(2)	1.24(7)
O(36)	2*a*	0	0.49(1)	0.622(3)	1.24(7)	O(43)	4*b*	0.77(1)	-0.01(1)	0.445(1)	1.24(7)
O(37)	2*a*	0	0.008(1)	0.120(3)	1.24(7)	O(44)	4*b*	0.730(9)	0.53(1)	0.446(2)	1.24(7)

3.3.2.5 Structural Characterisation of $RbSr_2Nb_3O_{10}$

Attempts were made to fit the short wavelength (1.6218 Å) and longer wavelength (2.4395 Å) neutron powder diffraction data collected for $RbSr_2Nb_3O_{10}$ with an aristotype *P4/mmm* mode same as we did for the above samples. Multibank Rietveld refinement profiles (**Figure 3.19**) show that there is intensity mismatch in the high symmetry model and the peaks ~ 46.33° and between 110° and 150° in 1.62 Å data set (short wavelength) and ~ 59.49° and 72.52° 2θ in 2.43 Å data set (longer wavelength) are not fitted by the parent unit cell.

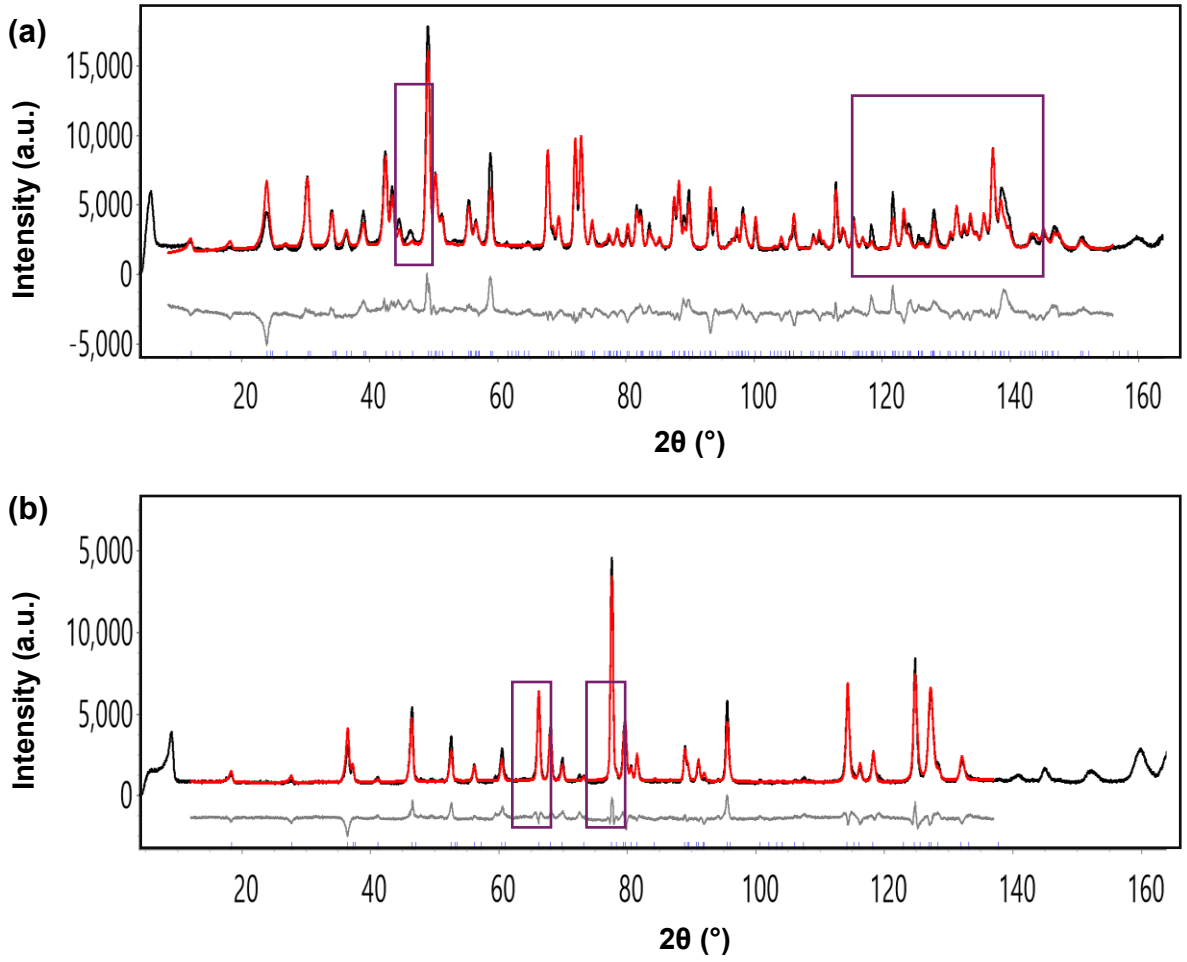

Figure 3.19: Rietveld refinement profiles from combined refinement using room-temperature (a) short wavelength (1.6218 **Å**) and (b) longer wavelength (2.4395 **Å**) NPD data for $RbSr_2Nb_3O_{10}$, refined in space group *P*4/*mmm*. The observed, calculated, and difference profiles are shown in black, red, and grey respectively).

Similar to the Cs-containing materials, refinements using the *P4/mmm* model for $RbSr_2Nb_3O_{10}$ also gave an unreasonably high atomic displacement parameter (ADP) for the central equatorial oxygen site O(1). Allowing anisotropy of this ADP suggested significant displacements in the *ab* plane, suggesting rotation of the BO_6 around the long axis (**Figure 3.6**). Therefore, lower symmetry models allowing

rotations about the out-of-plane axis, described by M_3^+ or A_3^+ modes, were considered to resolve the problems with this site.

Additionally, the results from mode inclusion analysis show that the biggest improvements in the R_{wp} value are either from in-plane polar Γ_5^- displacement or rotations about the out-of-plane axis described by M_3^+ or A_3^+ modes (**Figure 3.20**).

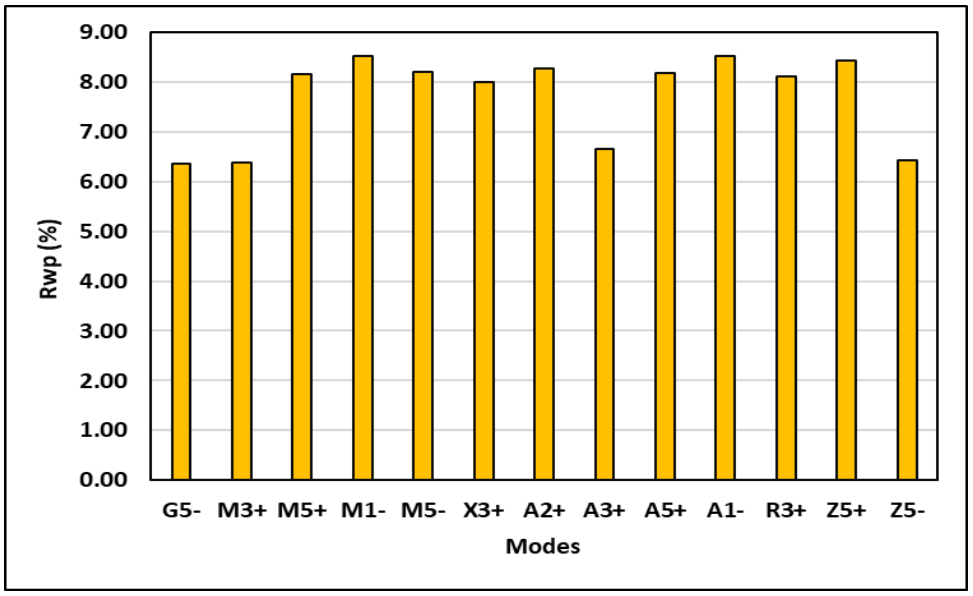

Figure 3.20: Results from first round of mode inclusion analysis showing which modes give the biggest improvement in the R_{wp} value.

Refinement using the $\sqrt{2}a_t \times \sqrt{2}a_t \times c$ model of *P*4/*mbm* symmetry, corresponding to M_3^+ octahedral rotations gave R_{wp} = 6.32% (46 parameters) and using the $\sqrt{2}a_t \times \sqrt{2}a_t \times 2c$ model of *I*4/*mcm* symmetry corresponding to A_3^+ rotations gave R_{wp} = 6.89% (41 parameters). Compared to the ideal *P*4/*mmm* model with R_{wp} =11.03% (33 parameters) both tetragonal models showed a significant improvement in fit. To explore further improvements and check whether $RbSr_2Nb_3O_{10}$ could be polar, the polar Γ_5^- mode was added to both M_3^+ and A_3^+ modes. From mode decomposition analysis it was found the mode amplitudes were 0.63 Å for M_3^+ rotations for the *P*4/*mbm* model, and 0.65 and 0.13 Å for M_3^+ rotations and Γ_5^- polar displacements for the *P*2$_1$*am* model, respectively. This suggests that the average structure is best described by a non-polar model *P*4/*mbm* symmetry. **Table 3.9** summarizes the R_{wp} values and number of parameters for the lower symmetry models compared with the parent *P*4/*mmm* model. The M_3^+ *P*4/*mbm* model was found to be most suitable for $RbSr_2Nb_3O_{10}$, offering approximately 40% improvement in fit with an increase of only 7 independent parameters. The refinement details are given in **Table 3.10** and selected bond lengths and bond angles are given in **Appendix 1**, **Section 1.5, Table**

1.5. The bond valence sum calculations gave valences of + 5.044, + 4.956 for Nb(1) and Nb(2), + 2.149 for Sr(1), and + 0.771 for Rb(1).

Table 3.9: Summary of the R_{wp} values and number of parameters of the lower symmetry models compared with the parent *P*4/*mmm* model for $RbSr_2Nb_3O_{10}$.

Model	R_{wp} (%)	Number of Parameters
Parent *P*4/*mmm*	11.03	39
r_5^- (a,0) *Pmm*2	8.44	44
r_5^- (a|a) *Amm*2	7.73	43
M_3^+ *P*4/*mbm*	6.32	46
A_3^+ *I*4/*mcm*	7.22	41
$M_3^+ + r_5^-$ (a|b,0) *Amm*2	6.89	62
$M_3^+ + r_5^-$ (a|b,b) *Pmc*2$_1$	7.12	60
$A_3^+ + r_5^-$ (a|b,0) *Fmm*2	6.96	62
$A_3^+ + r_5^-$ (a|b,b) *Ima*2	7.14	59

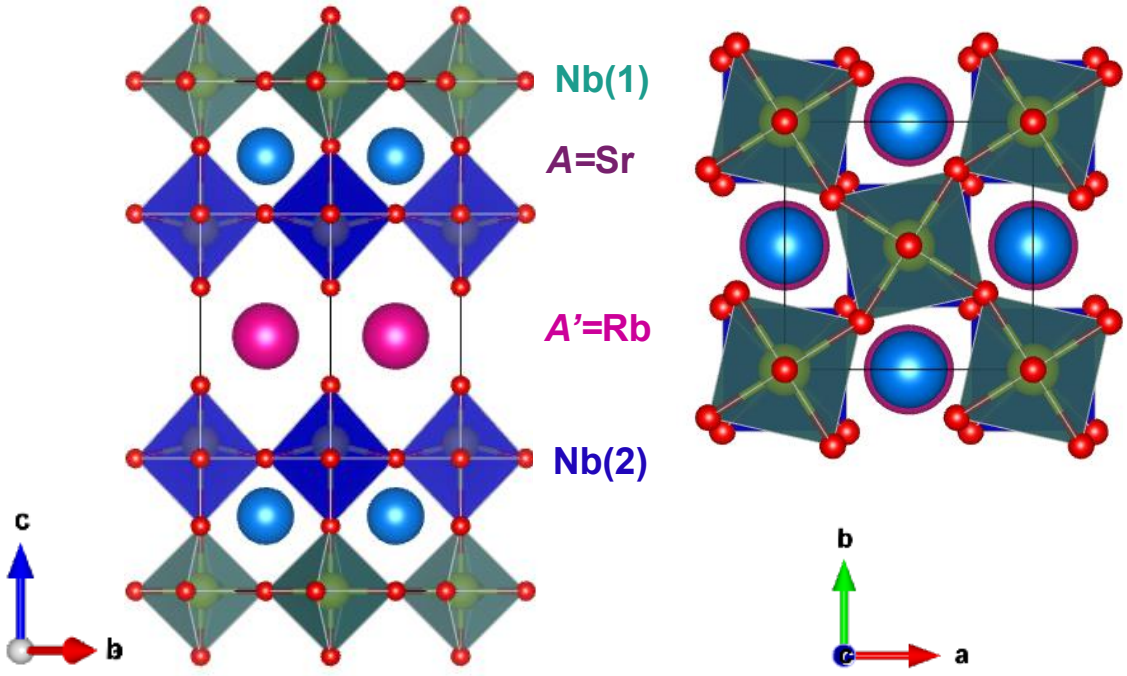

Figure 3.21: Crystal structure M_3^+ *P*4/*mbm* model for n=3 DJ phase $RbSr_2Nb_3O_{10}$. Rb, Sr, Nb and O sites are shown in pink, purple, blue, and red, and Nb(1)O_6 and Nb(2)O_6 octahedra are shown in light and dark blue, respectively.

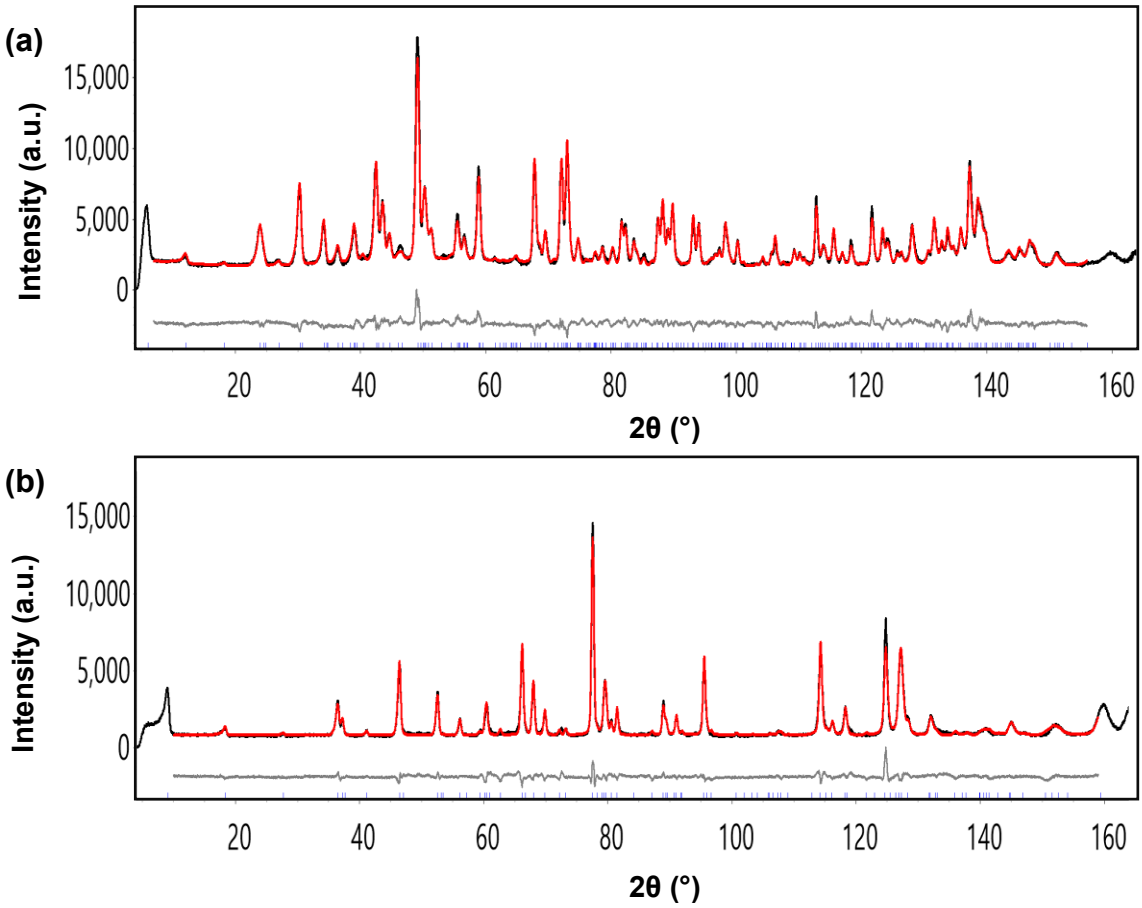

Figure 3.22: Rietveld refinement profiles from combined refinement using room-temperature (a) short wavelength (1.6218 Å) and (b) longer wavelength (2.4395 Å) NPD data for $RbSr_2Nb_3O_{10}$, refined in space group *P4/mbm*. The observed, calculated, and difference profiles are shown in black, red, and grey respectively).

Table 3.10: Structural Parameters of $RbSr_2Nb_3O_{10}$ from combined refinement using room-temperature (a) short wavelength (1.6218 Å) and (b) longer wavelength (2.4395 Å) NPD data in space group *P4/mbm.* All sites are constrained to be fully occupied.

Space group: *P4/mbm* (No. 127). Cell parameters: *a* = 5.50958(9) Å, *c* = 15.2706(3)Å, R_{wp} = 6.31%, R_p = 4.93%, χ^2 = 7.23, 46 parameters.

Atom	Wyckoff Site	*x*	*y*	*z*	U_{iso} x 100 (Å^2)
Rb(1)	2*c*	0	0.5	0.5	2.87(7)
Sr(1)	4*d*	0	0.5	0.1466(1)	0.68(4)
Nb(1)	2*a*	0	0	0	0.58(5)
Nb(2)	4*d*	0	0	0.2875(1)	0.30(3)
O(11)	4*d*	0.8081(4)	1.3081(4)	0	1.19(6)
O(21)	4*d*	0	0	0.1264(1)	0.93(5)
O(31)	8*d*	0.7502(3)	0.2502(3)	0.7390(1)	0.70(3)
O(41)	4*d*	0	0	0.4028(1)	1.74(6)

3.3.2.6 Structural Characterisation of $RbCa_2Nb_3O_{10}$

Rietveld refinement profile shows that the attempts to fit the longer wavelength (2.4395 Å) neutron powder diffraction data with the aristotype *P4/mmm* model were unsuccessful (**Figure 3.23**). Peaks at 60.18°, 73°, 87°, 108°, 111°, and 120.31° 2θ are not fitted by the parent unit cell.

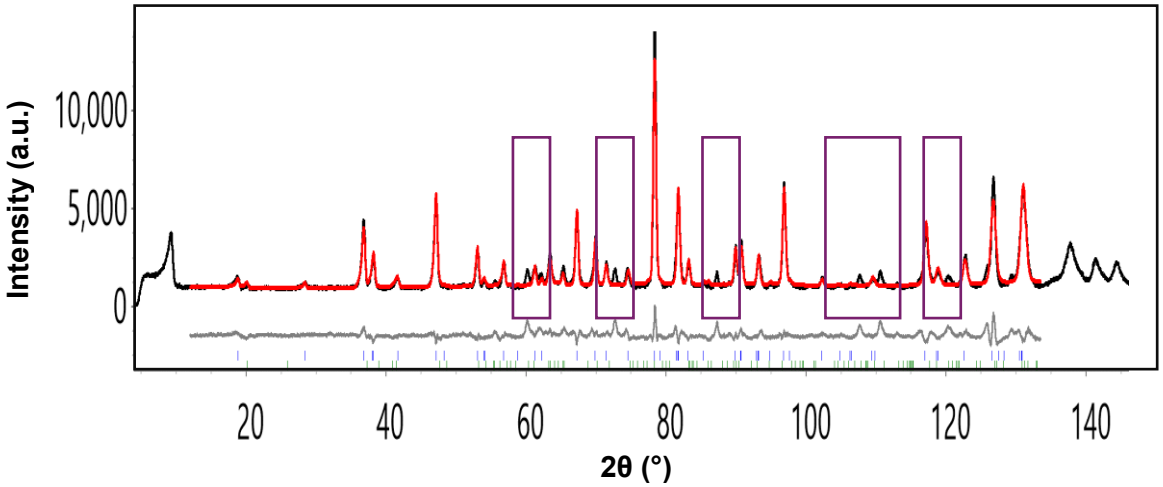

Figure 3.23: Rietveld refinement profile using room-temperature longer wavelength (2.4395 Å) NPD data for $RbCa_2Nb_3O_{10}$, refined in space group *P4/mmm*. The observed, calculated, and difference profiles are shown in black, red, and grey respectively).

Similar to $CsCa_2Nb_3O_{10}$, the *P4/mmm* model for $RbCa_2Nb_3O_{10}$ also gave an unreasonably high ADP for the central equatorial oxygen site O(1). Allowing anisotropy of this ADP suggested significant displacements in the *ab* plane, suggesting rotation of the BO_6 octahedra about the long axis. The ADP for the apical oxygens was also very high. Allowing anisotropy of this ADP suggested rotation of the BO_6 octahedra about in-plane axis (**Figure 3.11**).

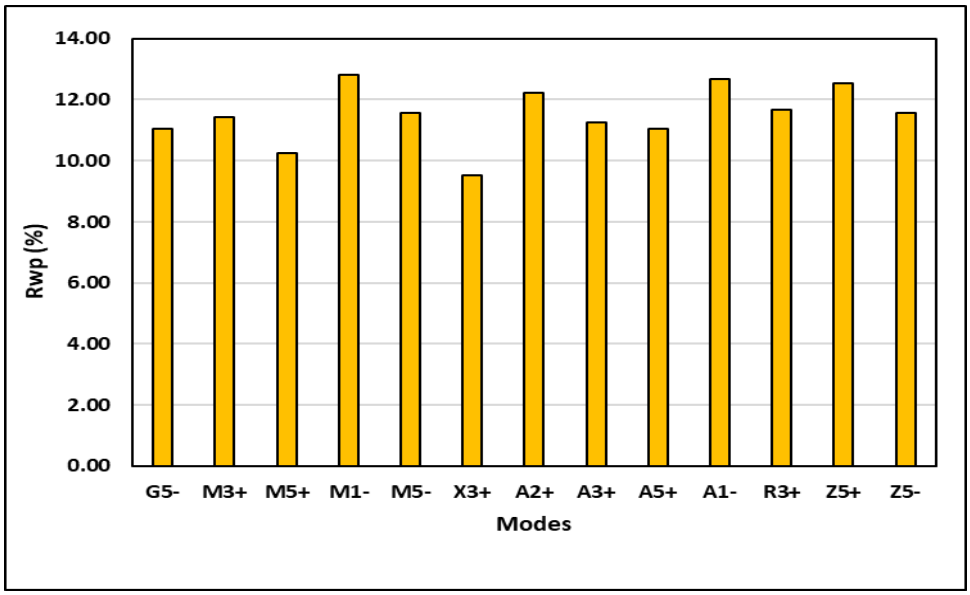

Figure 3.24: Results from first round of mode inclusion analysis showing which modes give the biggest improvement in the R_{wp} value.

Consequently, models with rotations of octahedra about both the out-of-plane axis, described by M_3^+ or A_3^+ modes, and in-plane axis were considered. Results from mode inclusion analysis show that the biggest improvement in the R_{wp} value are from the rotations about an in-plane axis described by X_3^+ or M_5^+ modes (**Figure 3.24)**. Thus, further refinements focused on models with rotations of octahedra about both the out-of-plane axis, described by M_3^+ or A_3^+ modes, and in-plane axis, described by X_3^+ or M_5^+ modes.

Table 3.11: Summary of the R_{wp} values and number of parameters of the lower symmetry models compared with the parent *P*4/*mmm* model for $RbCa_2Nb_3O_{10}$.

Model	R_{wp} (%)	Number of Parameters
Parent *P*4/*mmm*	9.95	33
X_3^+ (a,0) *Pmma*	8.05	38
X_3^+ (a,a) *P*4/*nmm*	6.72	39
X_3^+ (a,b) *Pmmn*	6.30	50
M_5^+ (a,0) *Pnma*	8.78	34
M_5^+ (a,a) *Cmma*	8.85	35
M_3^+ *P*4/*mbm*	9.70	29
$X_3^+ + M_3^+$ (a;b|c) *Pmmn*	7.19	53
$X_3^+ + M_5^+$ (a;0|b,b) *Pbcm*	6.22	47
$X_3^+ + M_5^+$ (a;0|-b,b) *Pmma*	6.95	52
$X_3^+ + M_5^+$ (a;b|c,c) *P*2$_1$/*m*	5.04	70
$X_3^+ + M_5^+$ (a;0|b,c) *P*2/*c*	5.95	67
$X_3^+ + M_5^+ + \Gamma_5^-$ (a,0|b;c|d,d) *P*2$_1$	4.7	119

The X_3^+ + M_5^+ *P*2$_1$/*m* model significantly improved the fit giving a low R_{wp} value. This particular combination of X_3^+ (a,b) + M_5^+ (c,c) also allows M_3^+ rotations. Given the moderate SHG activity measured for $RbCa_2Nb_3O_{10}$ (Section 3.4.5) the polar Γ_5^- mode was added to the X_3^+ + M_5^+ combination. The X_3^+ + M_5^+ + Γ_5^- *P*2$_1$ model also allows the M_3^+ octahedral rotations. **Table 3.11** compares the R_{wp} values and number of parameters of the lower symmetry models with the parent *P*4/*mmm* model. Based on these results, the polar X_3^+ + M_5^+ + Γ_5^- (+ M_3^+) *P*2$_1$ model was found to be the most

suitable for $RbCa_2Nb_3O_{10}$. The refinement details are given in **Table 3.12** and selected bond lengths and bond angles are given in **Appendix 1**, **Section 1.6, Table 1.6**. The bond valence sum calculations gave valences of +5.252, +5.242, +4.915, +5.082, +4.876, +5.219 for Nb(11), Nb(12), Nb(21), Nb(22), Nb(23) and Nb(24), +1.780, +2.100, +1.779, +2.258 for Ca(11), Ca(12), Ca(13), and Ca(14), and + 0.883, +0.944 for Rb(11), and Rb(12).

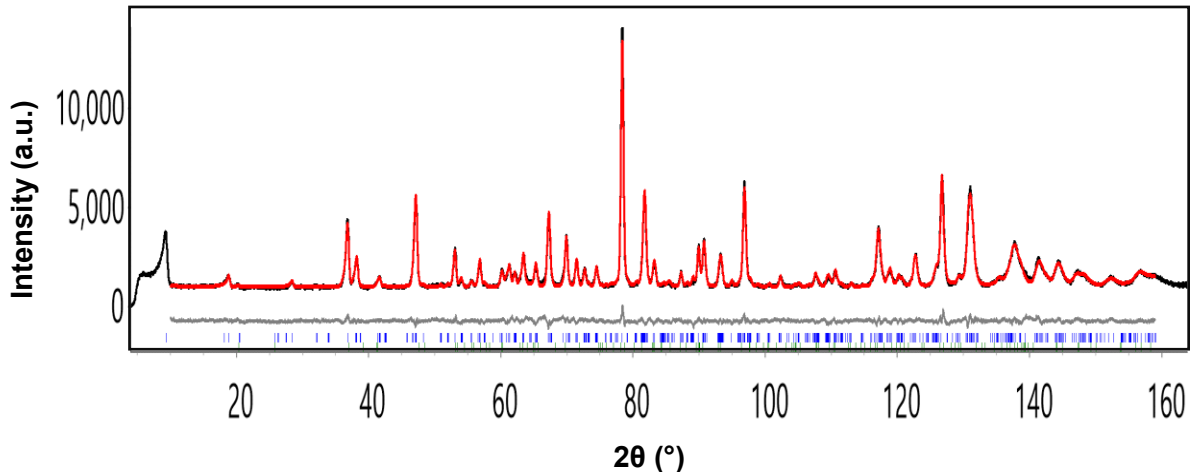

Figure 3.25: Rietveld refinement profile using room-temperature longer wavelength (2.4395 **Å**) NPD data for $RbCa_2Nb_3O_{10}$, refined in space group $P2_1$. The observed, calculated, and difference profiles are shown in black, red, and grey respectively).

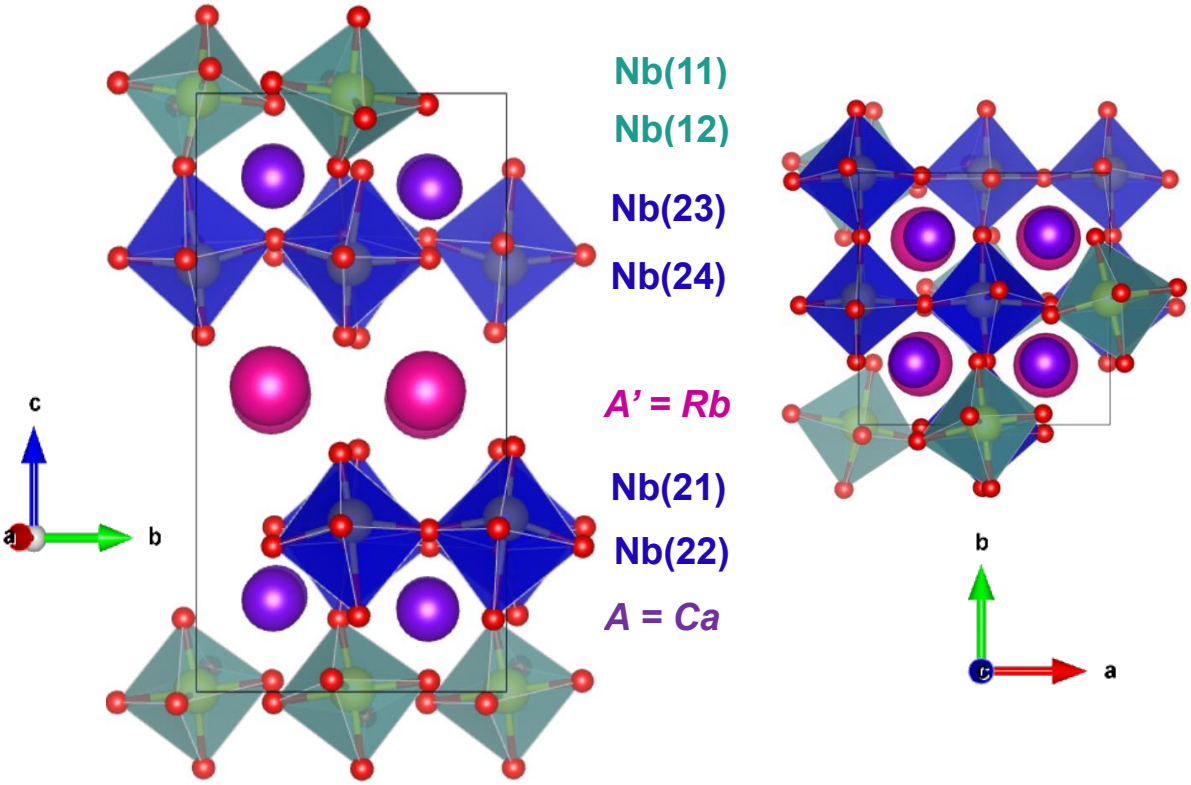

Figure 3.26: Crystal structure of $X_3^+ + M_5^+ + r_5^- P2_1$ model for n=3 DJ phase $RbCa_2Nb_3O_{10}$. Rb, Ca, Nb and O sites are shown in pink, purple, yellow, and red, and $Nb(11)O_6$, $Nb(12)O_6$, and $Nb(21)O_6$, $Nb(22)O_6$, $Nb(23)O_6$, $Nb(24)O_6$ octahedra are shown in light and dark blue, respectively.

Table 3.12: Structural parameters of $RbCa_2Nb_3O_{10}$ using room-temperature longer wavelength (2.4395 Å) NPD data in space group $P2_1$. All sites are constrained to be fully occupied, and ADP values are constrained to be equal for all sites.

Space group: $P2_1$ (No. 4). Cell parameters: a= 7.7226(3) Å, b = 7.7242(3) Å, c = 14.9053(4) Å, β = 90.173(2), R_{wp} = 4.77%, R_p = 3.73%, χ^2 = 3.17, 119 parameters.

Atom	Wyckoff Site	*x*	*y*	*z*	U_{iso} x 100 (Å)	Atom	Wyckoff Site	*x*	*y*	*z*	U_{iso} x 100 (Å)
Rb(11)	2*a*	0.256(4)	0.73(1)	0.488(2)	0.28(6)	Rb(12)	2*a*	0.245(4)	0.24(1)	0.497(2)	0.28(6)
Ca(11)	2*a*	0.260(5)	0.74(1)	0.140(2)	0.28(6)	Ca(13)	2*a*	0.778(5)	0.74(1)	0.136(2)	0.28(6)
Ca(12)	2*a*	0.242(5)	0.25(1)	0.159(2)	0.28(6)	Ca(14)	2*a*	0.721(6)	0.24(1)	0.153(2)	0.28(6)
Nb(11)	2*a*	0.003(7)	0*	0.001(3)	0.28(6)	Nb(22)	2*a*	-0.001(5)	0.49(1)	0.285(3)	0.28(6)
Nb(12)	2*a*	0.498(6)	0.004(1)	-0.003(3)	0.28(6)	Nb(23)	2*a*	0.505(6)	-0.006(1)	0.284(3)	0.28(6)
Nb(21)	2*a*	-0.001(5)	0.00(1)	0.290(3)	0.28(6)	Nb(24)	2*a*	0.503(5)	0.51(1)	0.288(3)	0.28(6)
O(11)	2*a*	0.235(4)	-0.06(1)	-0.020(2)	0.28(6)	O(21)	2*a*	0.014(6)	-0.04(1)	0.122(3)	0.28(6)
O(12)	2*a*	0.267(4)	0.54(1)	-0.041(2)	0.28(6)	O(22)	2*a*	0.044(6)	0.52(1)	0.127(3)	0.28(6)
O(13)	2*a*	0.058(4)	0.24(1)	0.018(3)	0.28(6)	O(23)	2*a*	0.442(6)	0.03(1)	0.129(3)	0.28(6)
O(14)	2*a*	0.474(4)	0.24(1)	-0.018(2)	0.28(6)	O(24)	2*a*	0.473(7)	0.46(1)	0.122(3)	0.28(6)
O(31)	2*a*	0.235(5)	-0.02(1)	0.273(3)	0.28(6)	O(33)	2*a*	0.737(5)	-0.02(1)	0.237(2)	0.28(6)
O(32)	2*a*	0.262(5)	0.46(1)	0.277(2)	0.28(6)	O(34)	2*a*	0.751(6)	0.48(1)	0.251(3)	0.28(6)

* Fixed to define origin of the unit cell along the polar axis.

O(35)	2*a*	-0.009(4)	0.251(1)	0.730(3)	0.28(6)
O(36)	2*a*	0.010(5)	0.746(1)	0.757(2)	0.28(6)
O(37)	2*a*	0.508(4)	0.253(1)	0.756(2)	0.28(6)
O(38)	2*a*	0.492(5)	0.751(1)	0.725(2)	0.28(6)
O(41)	2*a*	-0.030(7)	0.023(1)	0.408(2)	0.28(6)
O(42)	2*a*	-0.010(6)	0.464(1)	0.398(3)	0.28(6)
O(43)	2*a*	0.528(6)	-0.022(1)	0.404(3)	0.28(6)
O(44)	2*a*	0.535(7)	0.522(1)	0.403(3)	0.28(6)

3.3.3 Summary of Results

Table 3.14 summarises the different symmetries and the distortion modes present in each composition studied in this chapter. From the table, it is clear that none of the combinations of the octahedral rotations whether about the in-plane or out-of-plane axes are sufficient to break inversion symmetry on their own and therefore cannot give rise to a polar state. Instead, the in-plane polarisation only arises when the polar Γ_5^- mode is explicitly present, in combination with octahedral rotations. This rules out the possibility of these materials being hybrid improper. Hence, we conclude that the mechanism of ferroelectricity in these materials is proper, with the polar Γ_5^- displacement being the essential distortion responsible for the polar ground state.

Table 3.14: Summary of the different symmetries and the distortion modes present in *A'*$A_2B_3O_{10}$ (*A'* = Rb, Cs; *A* = Ca, Sr, Ba and *B* = Nb, Ta).

Composition	Space Group	Distortion Modes (order parameter direction)
$CsBa_2Nb_3O_{10}$	*P*4/*mmm*	-
$CsSr_2Nb_3O_{10}$	*P*4/*mbm*	M_3^+ (a)
$CsCa_2Nb_3O_{10}$	*Pm*2$_1$*n*	$X_3^+ + A_5^+ + \Gamma_5^- (+M_3^+)$ (a,0|b;c|-d,d)
$CsCa_2Ta_3O_{10}$	*Pm*2$_1$*n*	$X_3^+ + A_5^+ + \Gamma_5^- (+M_3^+)$ (a,0|b;c|-d,d)
$RbSr_2Nb_3O_{10}$	*P*4/*mbm*	M_3^+ (a)
$RbCa_2Nb_3O_{10}$	*P*2$_1$	$X_3^+ + M_5^+ + \Gamma_5^- (+M_3^+)$ (a,0|b;c|d,d)

To understand the structural behaviour of these n = 3 Dion-Jacobson phases, we need to explore their structures in more detail. Orthorhombic strain in layered perovskite related materials refers to the structural distortion that occurs when these materials deviate from their ideal high symmetry structure to adopt an orthorhombic symmetry. Armstrong and Newnham proposed a model for orthorhombic strain, *e*, at room temperature described by the lattice parameter differences *a* and *b*,[33] given by

$$e = \left| \frac{(a-b)}{(a+b)} \right|$$

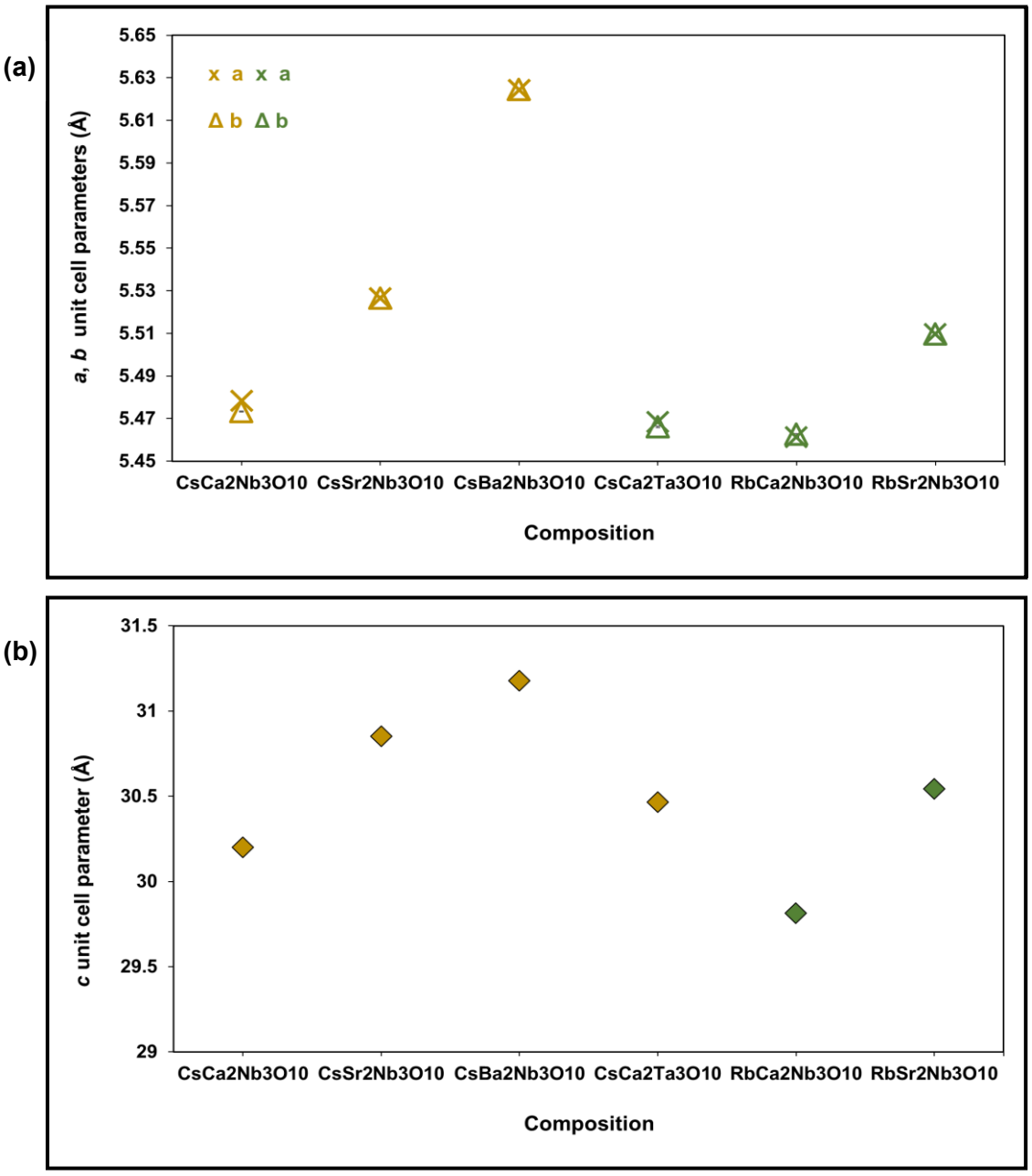

Figure 3.27: (a, b) Refined unit cell parameters *a, b* and *c* for $A'A_2Nb_3O_{10}$ (*A'* = Rb, Cs; *A* = Ca, Sr, Ba) as function of composition.

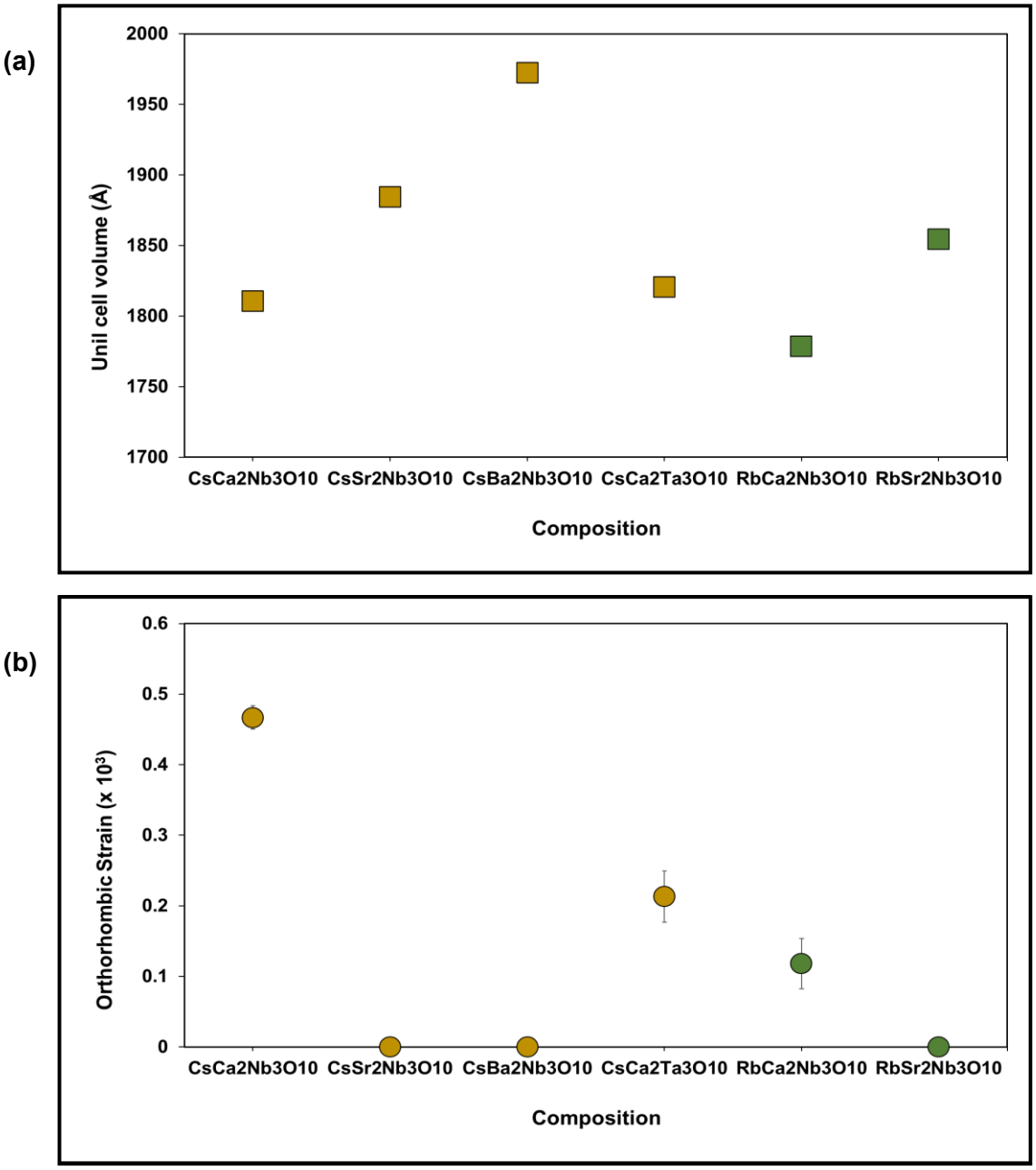

Figure 3.28: (c) Refined unit cell volume and (b) orthorhombic strain for $A'A_2Nb_3O_{10}$ (A' = Rb, Cs; A = Ca, Sr, Ba) as function of composition.

To summarize the results, **Figure 3.27** shows that Rb phases and Cs phases have similar *a* and *b* unit cell parameters but there is a bigger difference in *c* parameter. The Ca-based phases are significantly more complex compared to the Sr- and Ba-based phases. As expected, the unit cell volume increases as the size of the *A* cation increases and the unit cell volume is larger for Cs-based phases compared to Rb-based phases, consistent with their ionic radii (**Figure 3.28)**. Conversely, the orthorhombic strain decreases as the size of the *A* cation increases, with Cs phases generally exhibiting greater orthorhombic strain than Rb samples. Interestingly,

while $CsCa_2Nb_3O_{10}$ and $CsCa_2Ta_3O_{10}$ share the same symmetry crystal structure, the orthorhombic distortion is significantly reduced in the $CsCa_2Ta_3O_{10}$ phase compared to $CsCa_2Nb_3O_{10}$. Moreover, the orthorhombic strain in the *n* = 3 Dion–Jacobson phases is much smaller as compared to the strain in Aurivillius phases, Ruddlesden Popper phases or the *n* = 2 Dion Jacobson phases.

Table 3.15: Comparison of orthorhombic strain in layered perovskite related materials.

Type	Composition	Orthorhombic Strain x 10^3
n = 3 DJ Phases	$CsCa_2Nb_3O_{10}$	0.46(1)
	$CsCa_2Ta_3O_{10}$	0.21(3)
	$RbCa_2Nb_3O_{10}$	0.11(3)
n = 2 DJ Phases[34]	$RbSmNb_2O_7$	3.88(1)
	$LiSmNb_2O_7$	9.05(4)
Ruddlesden-Popper Phase[35, 36]	$Li_2CaTa_2O_7$	4.59(3)
	$Sr_3Sn_2O_7$	2.27(7)
Aurivillius Phase[37, 38]	$Bi_2CaNb_2O_9$	3.75(1)
	$Bi_{2.5}Na_{0.5}Ta_2O_9$	2.61(4)

(a)

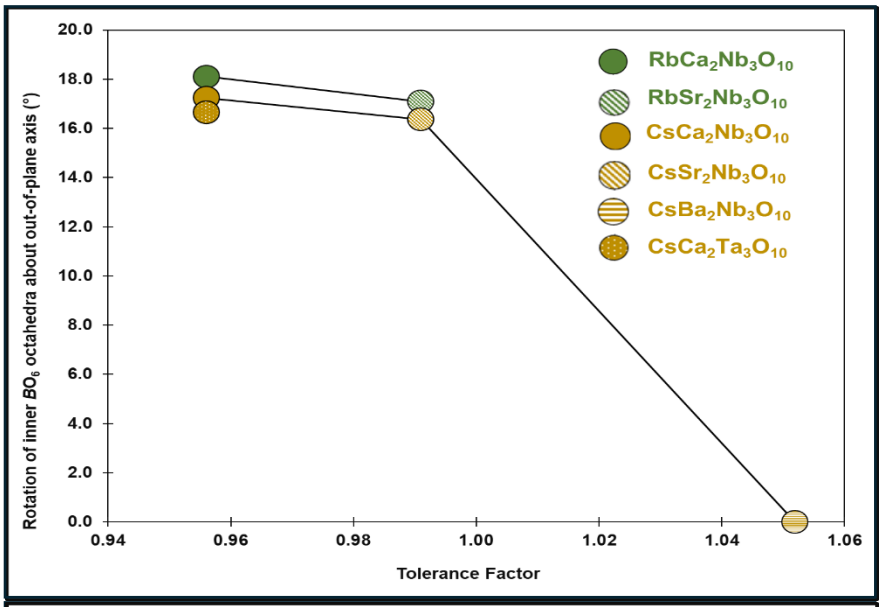

(b)

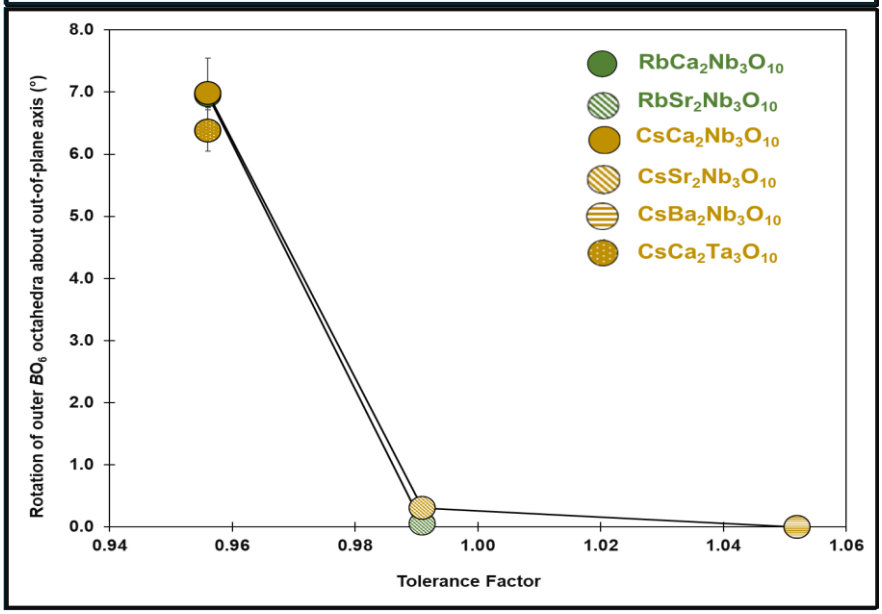

(c)

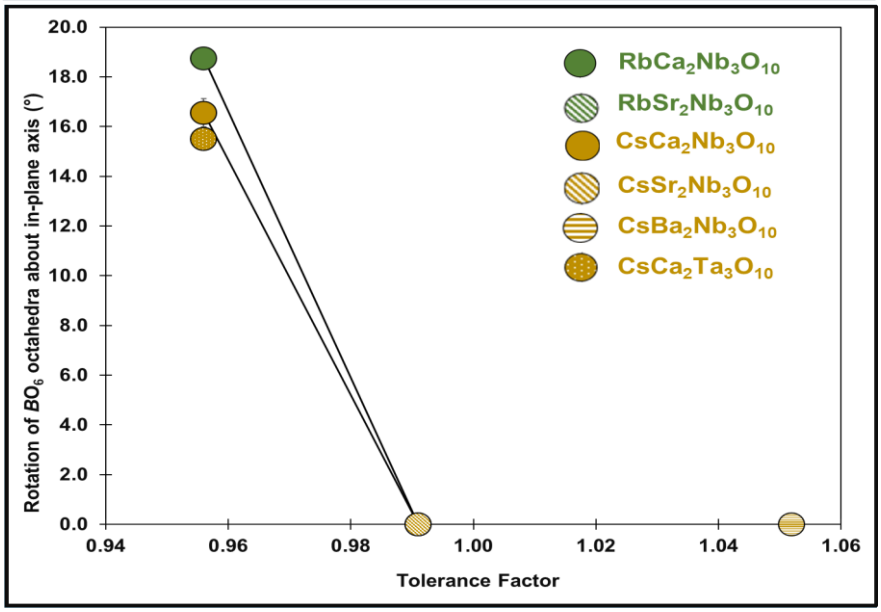

Figure 3.29: Change in the magnitude of octahedral rotation for $A'A_2B_3O_{10}$ (A' = Rb, Cs; A = Ca, Sr, Ba and B = Nb, Ta) about the in-plane and out-of-plane axis as the size of A changes.

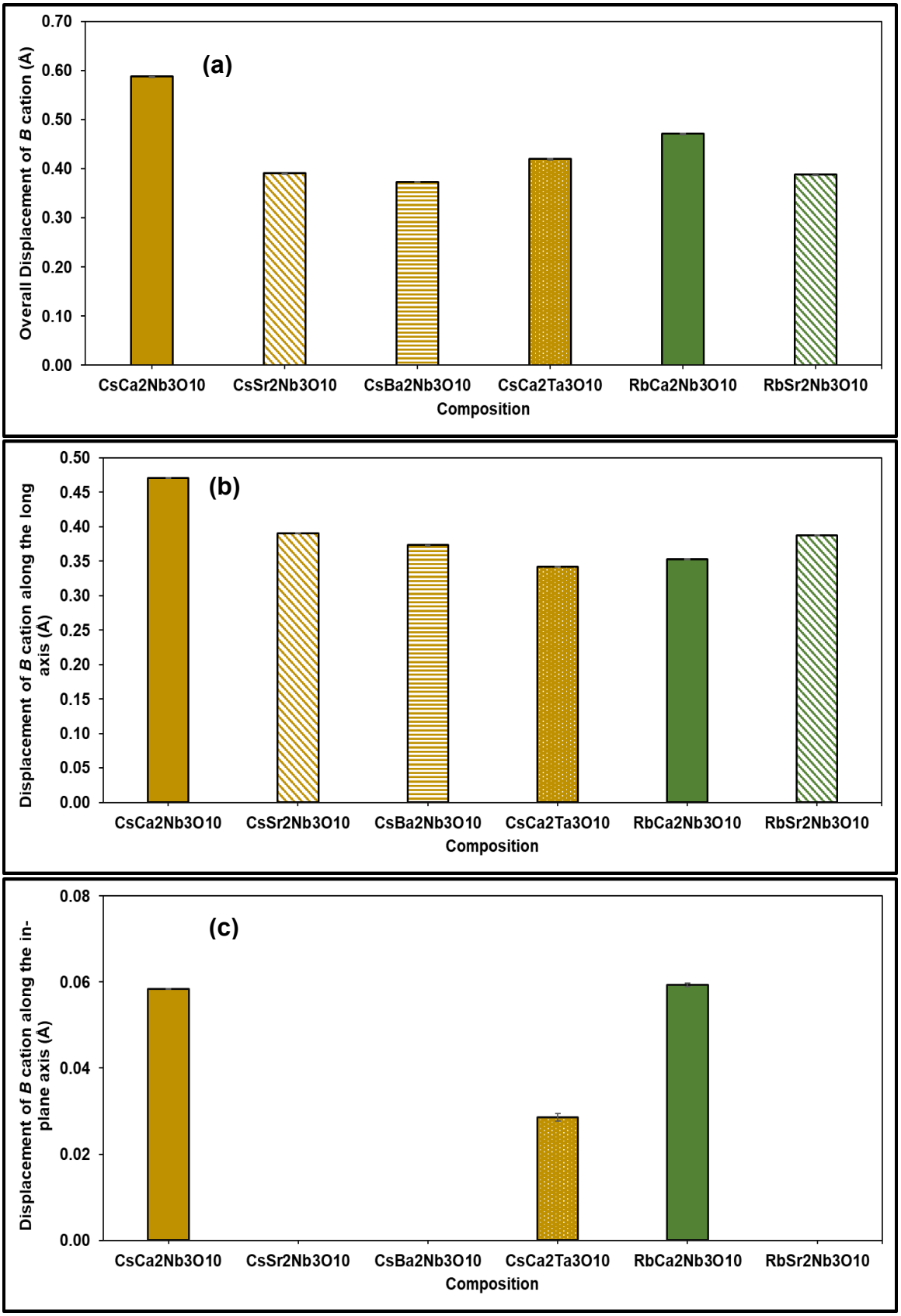

Figure 3.30: (a) Displacement of *B* cation from its centre of mass (b) along the long axis (c) along the in-plane axis as a function of composition.

3.4 Discussion

3.4.1 Perovskite Tolerance Factor

The Goldschmidt tolerance factor, *t,*[39] of the investigated materials can be calculated by neglecting the layered nature of the Dion-Jacobson phases, i.e., approximating the perovskite-like layers as ideal ABO_3 perovskites. This approximation provides an estimate of the degree of distortion but does not indicate the magnitudes or the type of symmetry-lowering distortions (cation displacements, and/or rotations of octahedra) required to optimise the bonding of *A* cation within the perovskite block.[40] The tolerance factors of the hypothetical compositions $ANbO_3$ and $ATaO_3$ (*A* = Ca, Sr, and Ba) are calculated as 0.95, 0.98 and 1.04, respectively since the ionic radii of six-coordinate Nb^{5+} and Ta^{5+} are 0.64 Å.[41] The calculated values suggest that as the size of the A^{2+} ion decreases, the distortions such as rotations of the BO_6 octahedra or polar/antipolar displacements are expected to occur to optimise the bonding of the *A* cations within the perovskite blocks.

This trend is evident in our results for $CsA_2Nb_3O_{10}$ (*A* = Ca, Sr, and Ba) that as the we go from Ba → Sr, attempts to fit the data using the *P4/mmm* model suggest that lower symmetry models that would allow rotations about the out-of-plane axis (described by M_3^+ or A_3^+ modes) might give better fits to the data. Notably, the magnitudes of rotation are different for inner octahedra *B*(1) and the outer octahedra *B*(2) (**Figure 3.29(a)** and **Figure 3.29(b))**. The inner octahedra exhibit greater rotation due to their central position within the perovskite blocks, which allows them to undergo more distortion to optimize bond angles and reduce strain. In contrast, the outer octahedra are constrained by the interlayer cations like Rb^+ or Cs^+, limiting their flexibility. In terms of rotations of octahedra about the in-plane axis, described by X_3^+, A_5^+ and M_5^+ modes, **Figure 3.29(c)** shows that no such rotations are observed for *A* = Sr and Ba.

As we further decrease the size to Ca, attempts to fit the data using the *P4/mmm* model suggest that lower symmetry models accounting for rotations about both the out-of-plane axis (described by M_3^+ or A_3^+ modes) and the in-plane axis (described by X_3^+ or A_5^+ modes) are important to explain the structure of the material.

The **Figures 3.29** illustrates that the tilting/rotation of the octahedra about both the in-plane and out-of-plane axes for $CsA_2Nb_3O_{10}$ (*A* =Ca, Sr, and Ba) and $RbA_2Nb_3O_{10}$ (*A* = Sr, and Ca) decreases as the size of the *A* cation increases. The same trend is

observed in Cs$Ln_2Ti_2NbO_{10}$ (*Ln* = La and Nd) Dion-Jacobson Phases[7] and Aurivillius Phases.[42, 43]

This demonstrates a clear relationship between the tolerance factor and the nature of structural distortions in the *n* = 3 DJ phases, highlighting the important role of the *A* cation size in determining the symmetry and stability of these layered materials. A trend in octahedral rotations is observed: as the size of the *A*-cation decreases from the larger Ba^{2+} to the smaller Sr^{2+}, rotations of the octahedra about the out-of-plane axis, described by M_3^+ distortion, are required to satisfy the bonding requirements within the perovskite block, as seen in *A'*$Sr_2Nb_3O_{10}$ (*A'* =Rb, Cs). As the size of the *A*-cation is further reduced to the even smaller Ca^{2+}, BO_6 octahedral rotations about both out-of-plane and in-plane axes are required, as seen in *A'*$Ca_2B_3O_{10}$ (*A'* =Rb, Cs; *B* = Nb, Ta). This trend highlights the significant role of geometric factors in determining the structure of the *n* = 3 DJ phases and provides a valuable framework for designing these phases with optimised properties.

3.4.2 Layer Mismatch and Stacking Strain

Layered perovskite-related materials are composed of perovskite blocks with interlayers like $[Bi_2O_2]^{2+}$ fluorite layer in Aurivillius phases, *A*'O rock-salt layer in Ruddlesden-Popper phases and *A*' atom layer in Dion-Jacobson phases between them.[44] Size mismatch between the perovskite layer and interlayer can result in strain within the structure which is often relieved by symmetry-lowering distortions. These distortions occur to optimize the bonding within the perovskite blocks as well as between the perovskite blocks and interlayer *A'* region. Mechanisms to relieve strain in layered perovskite-related materials include:

a) Cation disorder between *A* sites in perovskite layers and *A*' interlayer region where the structure retains its original symmetry.[43, 45]
b) Rotation of BO_6 octahedra causing a lowering of the symmetry from tetragonal to orthorhombic or monoclinic.[46]
c) Displacement of cations (*A, A'* or *B*) to optimize bonding.[5, 43]

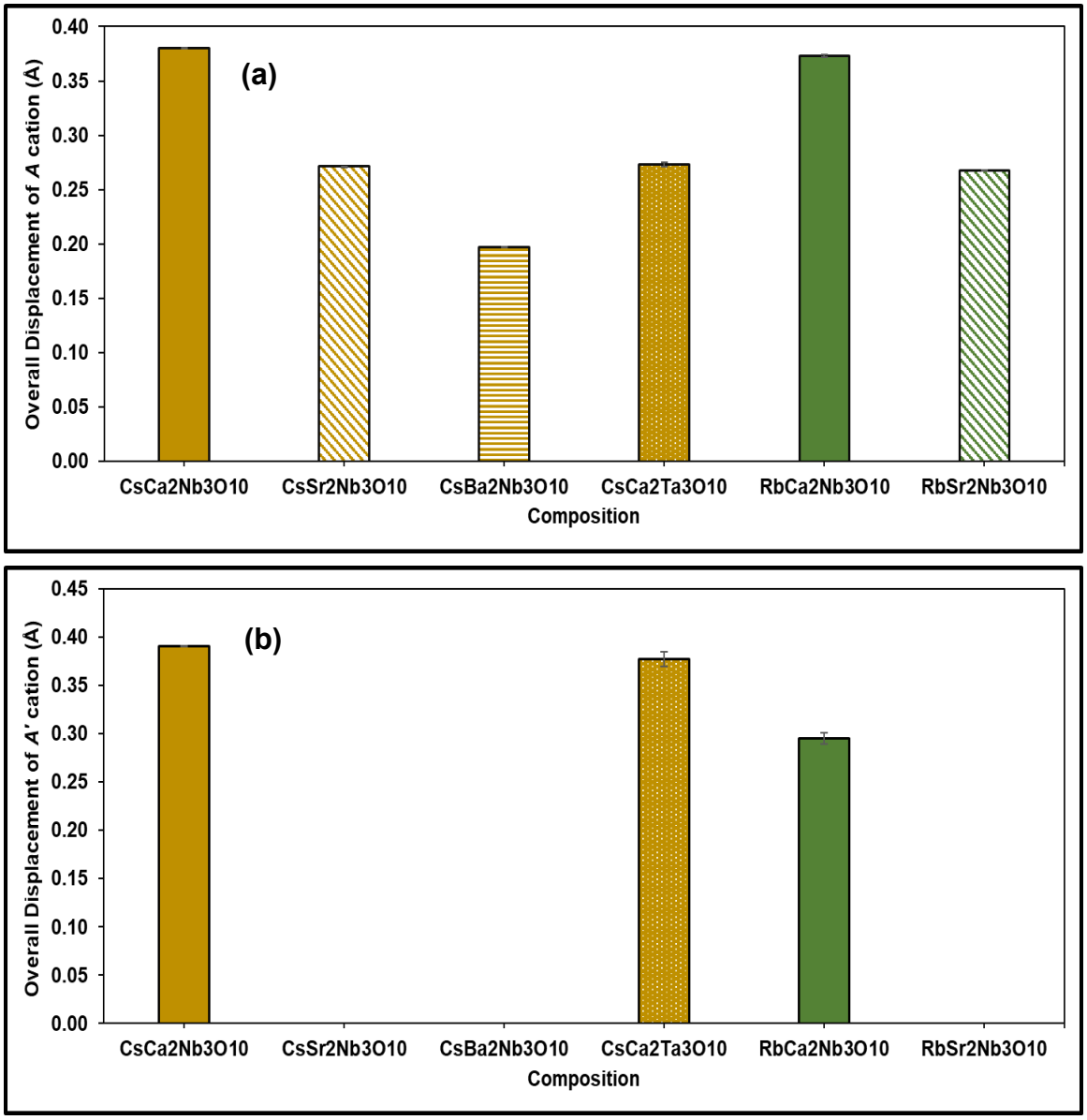

Figure 3.31: Displacement of (a) ***A*** cation (b) *A'* cation from its centre of mass as a function of composition.

Cation disordering is not feasible in Dion-Jacobson phases due to significant size difference between the *A'* and *A* cations (radius of *A'* cations: Rb^{+} = 1.61, Cs^{+} = 1.74 Å; radius of *A* cations: Ca^{+2} = 1.34, Sr^{+2} = 1.44, Ba^{+2} = 1.57). Consequently, rotations of BO_6 octahedra and cation displacements are the primary mechanisms for relieving structural strain in these materials.

The significant size difference between the *A'* and *A* cations creates a mismatch between the interlayer region and the perovskite blocks. This results in the elongation of the interlayer region along the long axis, causing stacking strain in this direction. The rotations of BO_6 octahedra about the in-plane axes are more influenced by this strain because these rotations directly respond to the mismatch between the perovskite blocks and the interlayer region. As shown in **Figure 3.29(c),**

within error, the rotations about the in-plane axes for Cs-based and Rb-based phases are comparable. This suggests that the rotations of BO_6 alone are insufficient to fully optimise the *B*, *A* and *A'* coordination environments when the difference between the size of the *A* and *A'* cations is large. Therefore, it is beneficial to utilize the extra degree of freedom in the *B*, *A* and *A'* cation displacement in order to satisfy the bonding requirements and relieve strain at these sites.

Figure 3.30(a) shows overall displacement of the *B* cation from its centre of mass. This displacement can occur along the long axis or along the in-plane axes and follows the same trend as octahedral rotations i.e. as the size of the *A* cation increases the displacement of the *B* cation decreases. We also notice that the displacement along the long axis is larger than that along the in-plane (polar) axis, raising questions about the true polarity of these materials. The displacement of Ta^{+5} in $CsCa_2Ta_3O_{10}$ along the polar in-plane axis is 0.0285(8) Å whereas the displacement of Nb^{+5} in $CsCa_2Nb_3O_{10}$ is 0.05844(3) Å. This follows the general trend that the displacement of Nb > Ta, as Ta is known to have a weaker second-order Jahn-Teller effect.[47]

Symmetry lowering induced by rotations of BO_6 octahedra and in-plane Γ_5^- polar displacement of the *B* cation gives more degrees of freedom for *A* and *A*' cations (site symmetry 4/*mmm* in parent *P*4/*mmm* to *m* in *Pm*2_1*n* and 1 in *P*2_1). Alongside increased tilts and displacement of the *B* cation, the *A* and *A'* cations are increasingly displaced from their centre of mass (**Figure 3.31**). This optimises the *A* and *A'* site bonding as these ions get increasingly too small for the *A* and *A'* site in an ideal undistorted structure. The displacement of the *A'* cation in $CsCa_2B_3O_{10}$ (*B* = Nb, Ta) is more than that in $RbCa_2Nb_3O_{10}$ due to differences in the size of the *A'* cation and *A* cation (**Figure 3.31(b)**). Cs^+ has a larger ionic radius (1.74 Å) than Rb^+ (1.61 Å),[41] which leads to a more significant elongation of the interlayer region in $CsCa_2Nb_3O_{10}$ (3.29(3) Å) and $CsCa_2Ta_3O_{10}$ (3.23(5) Å) as compared to $RbCa_2Nb_3O_{10}$ (2.94(6) Å). This elongation is evident in the in-plane rotation of the BO_6 octahedra. In $RbCa_2Nb_3O_{10}$ one of the in-plane rotation modes is M_5^+ whereas for $CaCa_2B_3O_{10}$ (*B* = Nb, Ta) one of the in-plane rotation modes is A_5^+ which leads to a doubling of the unit cell along the long axis.

These findings highlight the role of stacking strain, particularly in relation to the *A'* cation size, in determining the structure of layered perovskite-related materials. The

mismatch between the perovskite blocks and the interlayers creates stacking strain, which is relieved by structural distortions.

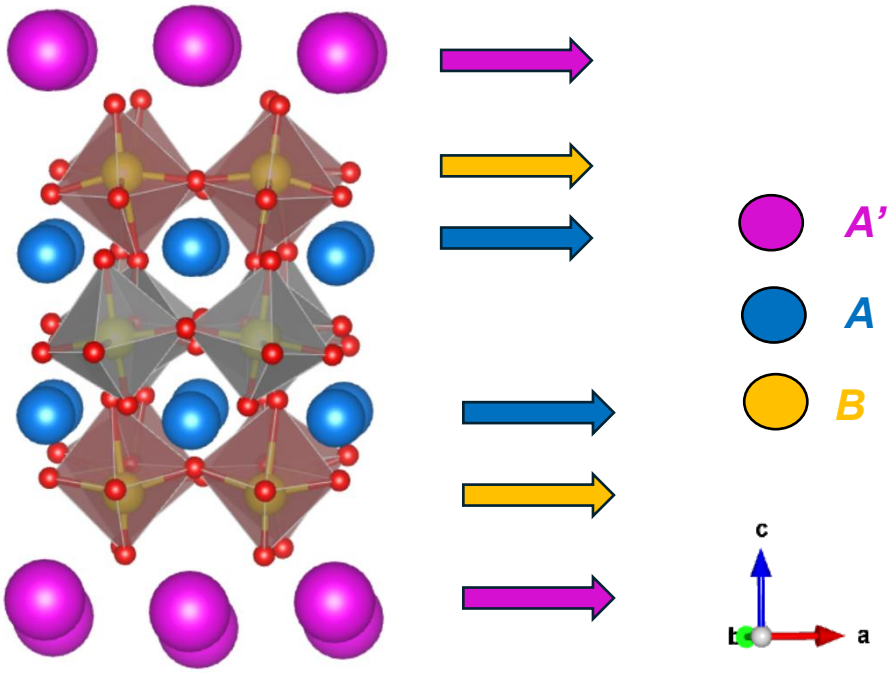

Figure 3.32: Polar displacement of *A'*, *A* and *B* cations in n=3 $A'A_2B_3O_{10}$ (*A'* = Rb, Cs; *A* = Ca and *B* = Nb, Ta) Dion-Jacobson phases.

3.4.3 Cation Displacement

From the structural analysis, it was determined that the structure of $CsCa_2B_3O_{10}$ (*B* = Nb, Ta) and $RbCa_2Nb_3O_{10}$ can be described by the combination of $X_3^+ + A_5^+ + \Gamma_5^-$ and $X_3^+ + M_5^+ + \Gamma_5^-$ respectively. The Γ_5^- mode, being a polar distortion, is always going to give displacements in the same direction in different blocks. Mode decomposition analysis using ISODISTORT[23] suggest that for all three compositions, the displacement of *A'* and *A* cations are in the same direction within the perovskite blocks making the crystal structure non-centrosymmetric and polar.

3.4.4 Computational Studies

To complement our neutron powder diffraction (NPD) data analysis, geometry optimization calculations were performed within the framework of density functional theory (DFT) for $A'A_2B_3O_{10}$ (*A'* = Rb, Cs; *A* = Ca, Sr, Ba and *B* = Nb, Ta).

As mentioned in the introduction, the high symmetry reference structure of Dion-Jacobson phases corresponds to the *P4/mmm* symmetry. The relative energies of various structural distortions were calculated with respect to the undistorted *P4/mmm* parent structures for these compositions.

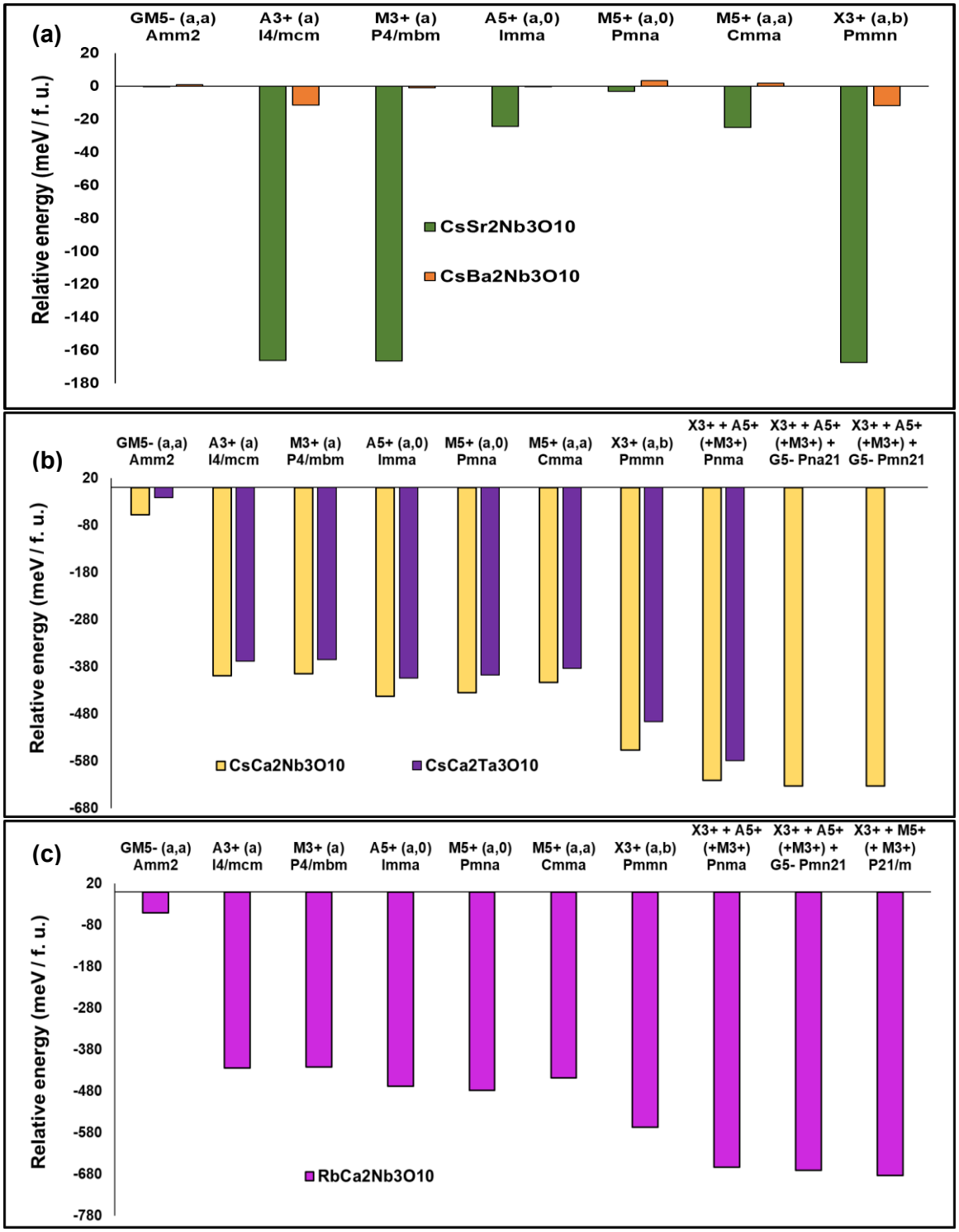

Figure 3.33: Relative energies of distortions with respect to the undistorted *P*4/*mmm* parent structure of $A'A_2B_3O_{10}$ (*A'* = Rb, Cs; *A* = Ca, Sr, Ba and *B* = Nb, Ta).

Figure 3.33(a) shows that the relative energies for lower symmetry models for $CsBa_2Nb_3O_{10}$ are notably small. This observation aligns with our NPD analysis, indicating that the parent *P4/mmm* model is most suitable for $CsBa_2Nb_3O_{10}$.

For $CsSr_2Nb_3O_{10}$ (**Figure 3.33(a)**), the M_3^+ *P*4/*mbm* model (which involves rotations of the octahedra about the out-of-plane axis) results in an energy lowering of -166.29

meV/f.u., while the X_3^+ *Pmmn* model (which involves rotations about the in-plane axis) gives an energy lowering of -167.42 meV/f.u. The difference between these two models is only 0.05 meV/f.u. and lies well within the convergence limit. Moreover, the X_3^+ *Pmmn* model shows no rotations for the Nb(1) octahedra, which is inconsistent with our NPD analysis that suggests models with octahedral rotations about the out-of-plane axis are more appropriate. Hence M_3^+ *P*4/*mbm* was chosen over X_3^+ *Pmmn*. To further investigate, we added the polar Γ_5^- mode to M_3^+ to check for additional energy lowering. This resulted in only a marginal additional energy lowering, again within the convergence limit. Thus, from DFT calculations there is no significant evidence that suggests that the symmetry of $CsSr_2Nb_3O_{10}$ lowers to *Pmc*2$_1$ ($M_3^+ + \Gamma_5^-$) or *Amm*2 ($M_3^+ + \Gamma_5^-$). Therefore, *P*4/*mbm* remains the most suitable choice for $CsSr_2Nb_3O_{10}$. which is consistent with our NPD findings. A similar conclusion is expected for $RbSr_2Nb_3O_{10}$.

Similar approach was applied to $CsCa_2B_3O_{10}$ (*B* = Nb, Ta) as for $CsSr_2Nb_3O_{10}$. From **Figure 3.33(b)** we see that $X_3^+ + A_5^+$ *Pnma* model (which also allows the M_3^+ octahedral rotations), gives the largest energy lowering for non-polar models. To check the energy lowering from the polar models, Γ_5^- mode was added to $X_3^+ + A_5^+$. Both $X_3^+ + A_5^+ + \Gamma_5^-$ *Pna*2$_1$ and $X_3^+ + A_5^+ + \Gamma_5^-$ *Pmn*2$_1$ further reduce the energy by ~12 meV/f.u. for $CsCa_2Nb_3O_{10}$, indicating that the polar structures are energetically favoured in this case. In contrast, for $CsCa_2Ta_3O_{10}$, the energy lowering from the polar models is very small and lies within the convergence limit, suggesting no evidence of transition to polar *Pna*2$_1$ or *Pmn*2$_1$. To draw more definitive conclusions, further DFT analyses such as phonon dispersion calculations would be required. However, at this stage, using the combined evidence from NPD analysis, SHG measurements and bond valence sum comparisons, the *Pmn*2$_1$ model is identified as the most appropriate structural description for $CsCa_2B_3O_{10}$ (*B* = Nb, Ta).

Similarly, for $RbCa_2Nb_3O_{10}$, although the energy lowering from the non-polar $X_3^+ + M_5^+$ *P*2$_1$/*m* model to the polar $X_3^+ + M_5^+ + \Gamma_5^-$ *P*2$_1$ model is only about 5-6 meV/f.u (**Figure 3.33(c)**), the *P*2$_1$ model is identified as the suitable structural description using the combined evidence from NPD analysis and SHG measurements, both of which indicate the presence of polar distortions. However, further DFT investigations such as phonon dispersion calculations are necessary to decisively confirm this assignment.

3.4.4.1 Comparison of Experimental and DFT Results

Table 3.16: Comparison of key structural features from experimentally-refined models and geometry-optimised computational models for $A'A_2B_3O_{10}$ (*A'* = Rb, Cs; *A* = Ca, Sr, Ba and *B* = Nb, Ta).

	Composition	Space Group	Overall M_3^+ mode amplitude (Å)	Average M_3^+ tilt angle for *B*(1)O_6 octahedra (°)	Average M_3^+ tilt angle for *B*(2)O_6 octahedra (°)	Overall A_5^+/M_5^+ mode amplitude (Å)	Average A_5^+ /M_5^+/X_3^+ tilt angle (°)	Overall X_3^+ mode amplitude (Å)	Overall Γ_5^- mode amplitude (Å)	Average magnitude of *B*-cation polar displacement (Å)	Magnitude of *B*-cation displacement along long axis (Å)
Experimental Results	$CsSr_2Nb_3O_{12}$	*P*4/*mbm*	0.61	16.37(1)	0.3 (1)	-	-	-	-		0.39(2)
	$CsCa_2Nb_3O_{12}$	*Pm*2_1*n*	0.49	17.25(1)	6.98(1)	A_5^+: 0.69	22.8(7)	0.75	0.21	0.11(3)	0.47(1)
	$CsCa_2Ta_3O_{12}$	*Pm*2_1*n*	0.45	16.66(7)	6.38(7)	A_5^+: 0.70	21(1)	0.61	0.39	0.07(1)	0.34(2)
	$RbSr_2Nb_3O_{12}$	*P*4/*mbm*	0.63	17.09(1)	0.045(1)	-	-	-	-		0.38(3)
	$RbCa_2Nb_3O_{12}$	*P*2_1	0.53	18.11(1)	6.95(4)	M_5^+: 0.64	27(3)	0.77	0.26	0.11(1)	0.35(5)
Computational Results	$CsSr_2Nb_3O_{12}$	*P*4/*mbm*	0.66	19	1	-	-	-	-	-	0.41
	$CsCa_2Nb_3O_{12}$	*Pm*2_1*n*	0.68	21	7	A_5^+: 0.76	24	0.74	0.13	0.11	0.39
	$CsCa_2Ta_3O_{12}$	*Pm*2_1*n*	0.64	22	6	A_5^+: 0.75	23	0.67	0.02	0.03	0.39
	$RbCa_2Nb_3O_{12}$	*P*2_1	0.70	24	7	M_5^+: 0.85	25	0.70	0.12	0.11	0.40

Table 3.16 compares the key structural features between the experimental and DFT-relaxed structure for *A'A*$_2$*B*$_3$*O*$_{10}$ (*A'* = Rb, Cs; *A* = Ca, Sr, Ba and *B* = Nb, Ta). The distortion mode amplitudes of M_3^+, A_5^+/M_5^+ and X_3^+ which correspond to rotation of the *B*O$_6$ octahedra about both the out-of-plane and in-plane axes as well as the displacement of the *B*-cation along the in-plane polar axis and the long axis show an overall good agreement between the experimentally-refined and geometry-optimised computational models. However, the amplitude of Γ_5^- distortion mode shows larger discrepancies.

In general, the DFT-calculated values are slightly larger than the experimental values. This difference may arise from temperature effects. DFT calculations are performed at 0 K whereas the NPD measurements were collected at room temperature. Another reason could be differences between the experimental and DFT models lattice parameters. Despite the small difference, the overall agreement between the experimental and computational results reinforces the reliability of our results. However, further validation through phonon dispersion calculations is recommended, particularly for CsCa$_2$Ta$_3$O$_{10}$ and RbCa$_2$Nb$_3$O$_{10}$.

3.4.5 Second-Harmonic Generation (SHG)

From Rietveld refinement in **Section 3.3.2** we observed that the polar displacements of *B* cations were very small. Therefore, second-harmonic generation (SHG) measurements were performed to support the assignment of polar space group to RbCa$_2$Nb$_3$O$_{10}$, CsCa$_2$Nb$_3$O$_{10}$ and CsCa$_2$Ta$_3$O$_{10}$. A necessary condition for a material to be polar is that it must exhibit noncentrosymmetricity.[48] Therefore, SHG measurements were conducted to verify the noncentrosymmetric nature of our materials.

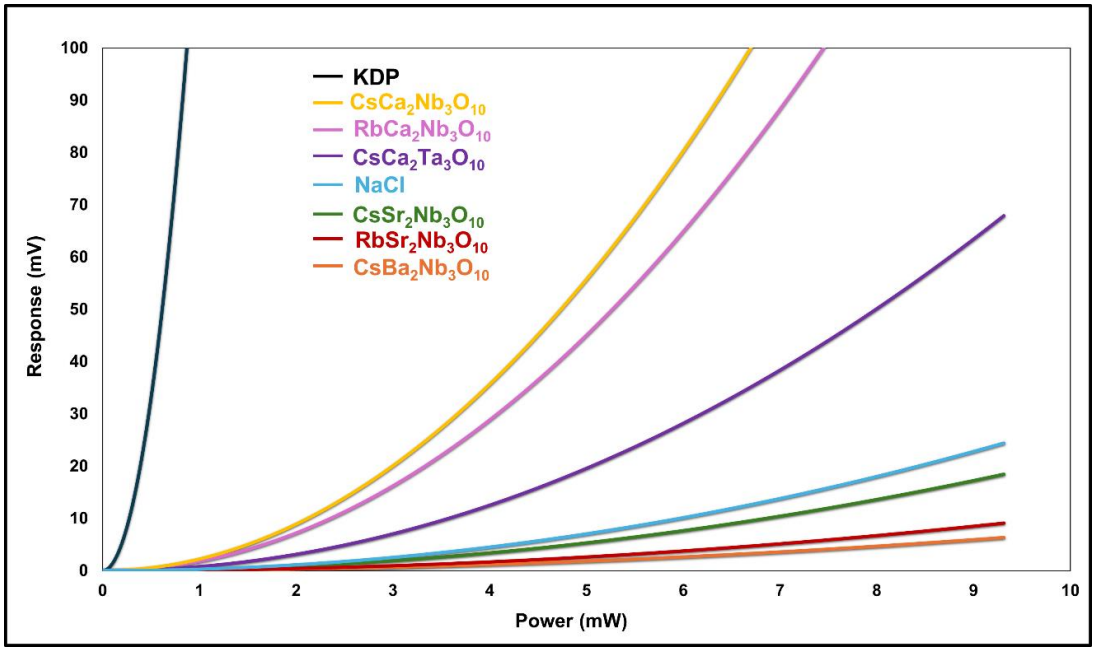

Figure 3.34: SHG signal for $A'A_2B_3O_{10}$ (A' = Rb, Cs; A = Ca, Sr, Ba and B = Nb, Ta) compared to KDP

Potassium dihydrogen phosphate (KDP) a well-known SHG-active material was used as a reference to compare the SHG activity of our samples. A threshold of <0.5% of the KDP signal was adopted, below which the SHG response is considered negative. This cutoff is justified as it aligns with previous reports on related perovskite materials,[49] where small signals of this magnitude are typically due to the surface contributions rather than genuine non-centrosymmetry. Furthermore, our own measurements on NaCl, an SHG-inactive material, gave signals <0.5% of KDP, justifying the threshold. Based on this criterion, we see that there is moderate SHG activity for $CsCa_2Nb_3O_{10}$, weak SHG activity for $RbCa_2Nb_3O_{10}$ and $CsCa_2Ta_3O_{10}$ and are therefore classified as SHG-active (**Figure 3.34**). In contrast $CsSr_2Nb_3O_{10}$, $RbSr_2Nb_3O_{10}$ and $CsBa_2Nb_3O_{10}$ give negligible SHG activity, comparable to NaCl, and are therefore taken to be SHG-inactive.

3.4.6 Diffuse Reflectance

Accurate determination of band gap energy is crucial as it helps us in understanding the photocatalytic properties of a material.[13] Measurement of diffuse reflectance spectra with UV-visible spectrometer is a technique used to determine the band gap energy of materials.[50] The optical bandgap energy E_g determined from **Figure 3.35** after the Kubelka-Munk transformation are tabulated below in **Table 3.17**. Data for $CsCa_2Ta_3O_{10}$ are very noisy $CsCa_2Ta_3O_{10}$ are very noisy but suggest a slightly larger gap than for $CsCa_2Nb_3O_{10}$ (**Appendix 1**, **Section 1.7)**.

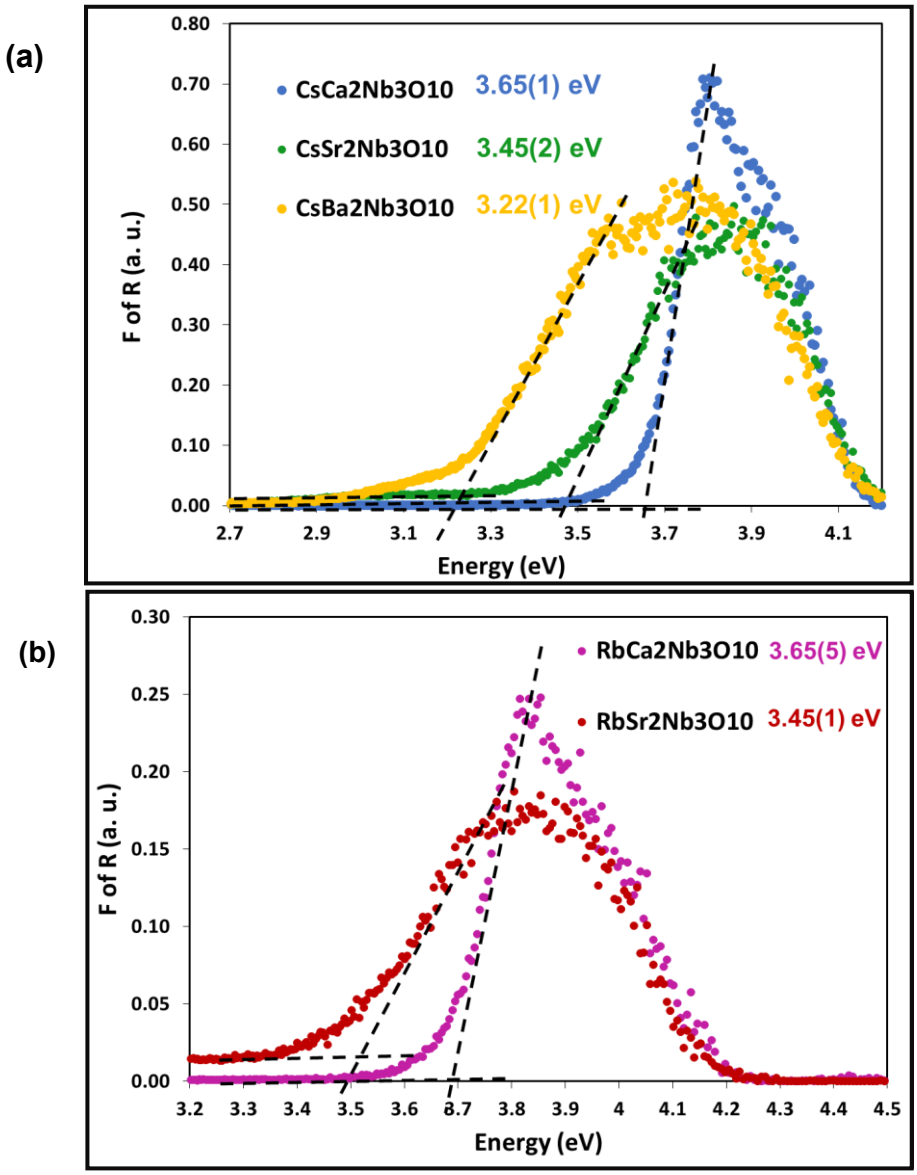

Figure 3.35: Diffuse reflectance spectra for (a) $CsA_2Nb_3O_{10}$ (*A* = Cs, Sr, Ba), (b) $CsCa_2B_3O_{10}$ (*B* = Nb, Ta) and (c) $RbA_2Nb_3O_{10}$ (*A* = Cs, Sr). The dotted lines indicate the band gap of the synthesized compounds.

Table 3.17: Optical bandgap energy (E_g) of $A'A_2Nb_3O_{10}$ (*A'* = Rb, Cs; *A* = Ca, Sr, Ba).

Composition	Bandgap Energy, E_g (eV)
$CsBa_2Nb_3O_{10}$	3.20(1)
$CsSr_2Nb_3O_{10}$	3.45(2)
$CsCa_2Nb_3O_{10}$	3.65(1)
$RbSr_2Nb_3O_{10}$	3.45(1)
$RbCa_2Nb_3O_{10}$	3.65(5)

The bandgap energy for all the compounds is greater than 3 eV which means that they can be used as photocatalyst under UV irradiation but not visible light. From the table above we see that as the size of the *A* cation increases the optical bandgap energy decreases. The same trend is reported by Kurnosenko et al and Kulischow et al.[13, 51] The difference in bandgap among these compounds is mainly due to structural distortion, specifically changes in the *B*-O-*B* (*B* = Nb, Ta) bond angle (θ) due to rotations of the BO_6 octahedra.

Previous studies done on Dion-Jacobson type oxides[14] and oxyfluorides[52] showed a linear correlation between E_g and changes in the Nb-O(F)-Nb bond angle (θ). The degree of distortion can be represented as 180°- *θ*, where *θ* is the Nb-O-Nb angle. The average *θ* values are 153.76 for $CsCa_2Nb_3O_{10}$, 162.23 $CsSr_2Nb_3O_{10}$, 172.08 for $CsBa_2Nb_3O_{10}$, 154.31 for $RbCa_2Nb_3O_{10}$, and 161.93 for $RbSr_2Nb_3O_{10}$. As the Nb-O-Nb deviates from 180°, the band gap increases (**Figure 3.35**). This increase in the band gap is caused by a reduction in bandwidth. In $A'A_2Nb_3O_{10}$ (*A'* = Rb, Cs; *A* = Ca, Sr, Ba) the valence band is mainly composed of equatorial O 2p orbitals, which are hybridised with transition metal Nb 5d orbitals, and the conduction band is mainly composed of Nb d-orbitals.[12, 17] The bandwidth decreases because overlap between the d-orbitals of niobium and the p-orbitals of oxygen becomes less effective when the bond angle deviates from 180° (more octahedral tilting).

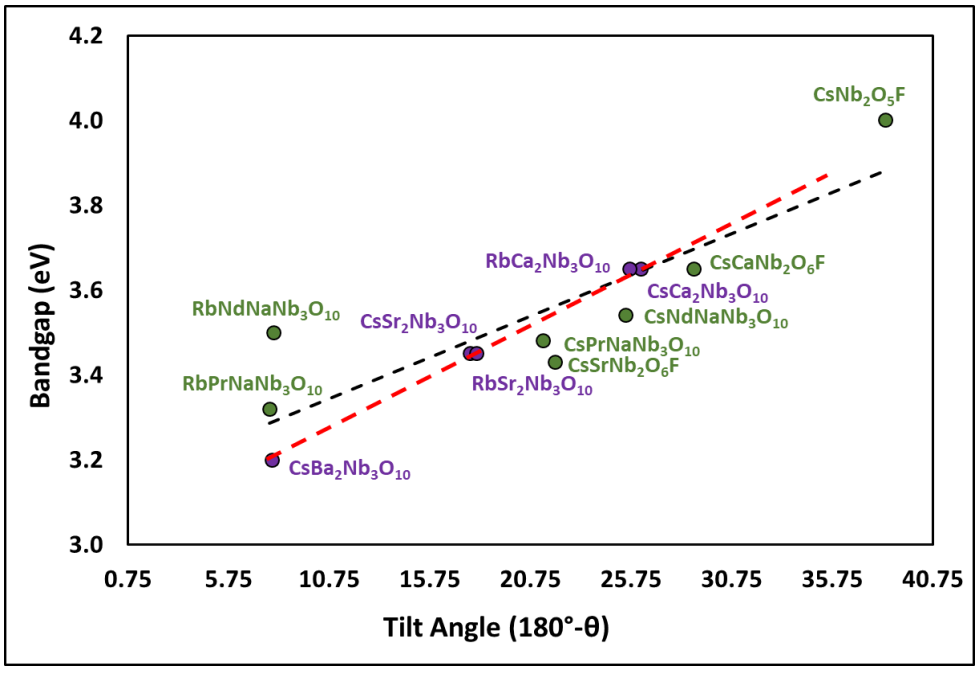

Figure 3.36: Correlation between bandgap energy and Nb – O(F) – Nb bonding angle for some complex oxides and oxyfluorides. Materials reported in literature are shown in green whereas $A'A_2Nb_3O_{10}$ (*A'* = Rb, Cs; *A* = Ca, Sr, Ba) are shown in purple. Black dash line marks linear fit for all experimental points, red dash line for all points except $RbNdNaNb_3O_{10}$ and $CsNb_2O_5F$.

Figure 3.36 shows the relation between E_g and tilt angle (180°- θ) for our materials and for data from the literature. Except for $RbNdNaNb_3O_{10}$ and $CsNb_2O_5F$ there's a close to linear relationship between band gap and tilt angle. This linear relationship between E_g and 180°- θ suggests that the octahedral tilting angle is the main factor influencing the bandgap in these materials.

3.4.7 Effect of Polar Cation Environment on Photocatalytic Activity

E. Zahedi et al. reported the correlation between polar cation environment and photocatalytic activity, highlighting that a polar cation environment leads to enhanced photocatalytic performance of a material. The displacement of *B* cation along the long axis can lower the *B*-site symmetry giving rise to a polar cation environment (example: $m\bar{3}m$ to 4*mm* symmetry). In this work, we attempted to explore how *B*, *A* and *A'* cations may influence photocatalytic behaviour by comparing the reported photocatalytic activities of various materials with their corresponding polar cation environments and octahedral rotations with the aim of gaining preliminary insights into potential structure–property relationships in the *n* = 3 Dion-Jacobson phases. However, these observations are based on reported data and requires more systematic study to confirm and clarify the nature of these correlations.

Table 3.18: Correlation between photocatalytic activity and polar cation environment in layered perovskite related materials.

Compound	Crystal Structure	Cation Choice	Rate of Hydrogen/Oxygen Evolution (μmol/h)		Polar cation environment (Displacement of *B* cation along the long axis) (Å)
			H_2	O_2	
$KCa_2Nb_3O_{10}$	*P*2$_1$/*m*	Nb^{5+}	~1015	-	0.3260(2)
$RbCa_2Nb_3O_{10}$	*P*2$_1$	Nb^{5+}	~1062	-	0.3527(5)
$CsBa_2Nb_3O_{10}$	*P*4/*mmm*	Nb^{5+}	~562	-	0.37340(3)
$RbSr_2Nb_3O_{10}$	*P*4/*mbm*	Nb^{5+}	~1250	-	0.387768(3)
$CsSr_2Nb_3O_{10}$	*P*4/*mbm*	Nb^{5+}	~968	-	0.39093(2)
$CsCa_2Nb_3O_{10}$	*Pm*2$_1$*n*	Nb^{5+}	~1437	-	0.4706(1)
$CsCa_2Ta_3O_{10}$	*Pm*2$_1$*n*	Ta^{5+}	89	53	0.3422(2)
$RbLaTa_2O_7$	*P*4/*mmm*	Ta^{5+}	1.2	0.6	0.34204(3)
$RbNdTa_2O_7$	*P*4/*mmm*	Ta^{5+}	47	25.3	0.37251(2)
$CaLa_4Ti_4O_{15}$	*P*-3*c*1	Ti^{5+}	593	276	0.07820(1)
$BaLa_4Ti_4O_{15}$	*P*-3*c*1	Ti^{5+}	2300	1154	0.10872(1)

Table 3.18 summarizes the photocatalytic activity and polar cation environment of the materials. From the data, the following trends and possible structure–property relationships can be suggested:

I. Effect of *B* Cation: The displacement of the *B* cation along the long axis is greater for Nb compared to Ta. Consequently, $CsCa_2Nb_3O_{10}$ exhibits better photocatalytic performance than $CsCa_2Ta_3O_{10}$.[12, 51, 53]

II. Effect of *A* Cation: The influence of the *A* cation on photocatalytic activity depends on two factors: (1) the displacement of the *B* cation and (2) the rotations of octahedra. As the size of the *A* cation increases, the displacement of the *B* cation along the long axis decreases, and the octahedral rotations also reduce. This leads to a less polar environment and, consequently, lower photocatalytic activity.

   For example, in $CsA_2Nb_3O_{10}$ (*A* = Ca, Sr, Ba), both displacement and octahedral rotation contribute to photocatalytic activity, following the trend Ca > Sr > Ba. A similar trend was reported by N. Kulischow et al., with an exception for $RbSr_2Nb_3O_{10}$.[51] From the table above we can see that the displacement of *B* cation along the axis is greater for $RbSr_2Nb_3O_{10}$ than for $RbCa_2Nb_3O_{10}$. This explains the higher photocatalytic activity of $RbSr_2Nb_3O_{10}$.

   In contrast, for $RbATa_2O_7$ (*A* = Nd, La), only displacement of *B* cation affects photocatalytic activity, as these compounds retain the *P*4*/mmm* parent structure. Here, the trend in photocatalytic activity is Nd > La.[54]

III. Effect of *A*' Cation: As the size of the *A'* cation increases, the displacement of *B* cation along the long axis increases, enhancing the photocatalytic activity.[51] For example: the trend in photocatalytic activity is Cs > Rb > K when *A* = Ca and *B* = Nb. A similar trend was observed by Miseki et.al. in different type of layered perovskite like materials $A'La_4Ti_4O_{15}$.[55] However, $RbSr_2Nb_3O_{10}$ does not follow this general trend, exhibiting an activity order of Rb > Cs > K. This anomalous behaviour warrants further investigation.

These observations suggest a potentially critical role of cation selection in influencing the photocatalytic activity of Dion-Jacobson phases. While these trends may offer useful guidance for the design the *n* = 3 DJ phases with enhanced photocatalytic activity, comprehensive and systematic studies are required to validate these relationships.

3.5 Conclusion

In conclusion, this comprehensive experimental and computational investigation on the n = 3 $A'A_2B_3O_{10}$ (A' = Rb, Cs; A = Ca, Sr, Ba and B = Nb, Ta) DJ phases establishes the intricate relationship between structure, composition, and properties. Our findings show how the structure of these materials changes with the choice of A', A and B cations, with both geometric and electronic factors playing important roles.

First and foremost, one of the key findings of our study is that none of the combinations of the octahedral rotations whether about the in-plane or out-of-plane axes are sufficient to break inversion symmetry on their own. A polar state is stabilised only upon the addition of the in-plane polar r_5^- mode. Hence, we can conclude that ferroelectricity in these materials arises from the proper mechanism rather than the hybrid improper mechanism.

Geometric factors, such as cation size and tolerance factor, were shown to be important in driving structural distortions. As the size of the A cation decreases from Ba to Sr to Ca, the tolerance factor decreases, leading to deviations from the high-symmetry parent $P4/mmm$ structure. As we go from a Ba cation to Sr cation, the rotations of the BO_6 octahedra about the out-of-plane axis become necessary to optimise the bonding of A cation within the perovskite block. As we further decrease the size to Ca, the rotations of BO_6 octahedra about both out-of-plane and in-plane axis are important to satisfy the bonding requirements within the perovskite block.

Not only the geometric but electronic factors also play an important role. There is more distortion in $CsCa_2Nb_3O_{10}$ as compared to $CsCa_2Ta_3O_{10}$. This highlights the role of second order Jahn-Teller (SOJT) distortion. Ta is known to show a weaker SOJT distortion.

The mismatch between the perovskite blocks and the interlayers creates stacking strain, which is relieved by the rotation of octahedra and displacement of B, A and A' cations.

This study establishes role of cation size, tolerance factor, stacking strain, and the second order Jahn-Teller effect in shaping the structural landscape of DJ phases. These insights deepened our understanding of the structure-composition relationship in these materials which helped us in exploring how optical properties depend on structure and composition.

The estimated band gap energies of the compounds show a clear dependence on the ionic radii of the *A* cation. As the size of the *A* cation increased the band gap energy decreased. This variation arises primarily from structural distortion, specifically changes in the *B*-O-*B* (*B* = Nb, Ta) bond angle (θ) due to rotations of the BO_6 octahedra. Furthermore, the narrower band gap observed in $CsCa_2Nb_3O_{10}$ compared to $CsCa_2Ta_3O_{10}$ can be attributed to the inherent electronic and bonding properties of Nb versus Ta. The 4d orbitals of Nb are closer in energy to the oxygen 2p orbitals than the 5d orbitals of Ta, hence the orbital overlap is stronger in $CsCa_2Nb_3O_{10}$ than $CsCa_2Ta_3O_{10}$. The Nb-O bonds in $CsCa_2Nb_3O_{10}$ are slightly shorter as compared to Ta-O bonds in $CsCa_2Ta_3O_{10}$. This shorter bond length enhances the orbital overlap. These two factors raise the valence band closer to the conduction band in $CsCa_2Nb_3O_{10}$ thus reducing the band gap.

The photocatalytic behaviour of these materials has been suggested to be influenced by the polar cation environment, specifically the displacement of the *B* cation along the long axis. As the size of *A* cation increased, the displacement of *B* cation decreased, leading to a reduction in photocatalytic activity, as observed in the trend Ca > Sr > Ba. Similarly, as the size of the *A'* cation increased, the displacement of the *B* cation also increased, enhancing the photocatalytic activity in the order Cs > Rb > K, with an exception for $RbSr_2Nb_3O_{10}$. Between $CsCa_2Nb_3O_{10}$ and $CsCa_2Ta_3O_{10}$, the Nb-containing phase shows higher a photocatalytic activity due to greater displacement of the *B* cation along the long axis.

This study provides a detailed understanding of the role geometric and electronic factors in determining the structure-composition-property relationships in the *n* = 3 DJ phases. These insights not only highlight the potential of these materials for photocatalytic applications but also pave the way for designing and optimizing DJ phases with tailored properties for specific technological applications.

1. A. Jacobson, J. W. Johnson and J. Lewandowski, *Inorganic chemistry*, 1985, **24**, 3727-3729.
2. K. Aleksandrov, *Crystallography Reports*, 1995, **40**.
3. N. A. Benedek and C. J. Fennie, *Physical review letters*, 2011, **106**, 107204.
4. E. E. McCabe, E. Bousquet, C. P. Stockdale, C. A. Deacon, T. T. Tran, P. S. Halasyamani, M. C. Stennett and N. C. Hyatt, *Chemistry of Materials*, 2015, **27**, 8298-8309.
5. T. Zhu, T. Cohen, A. S. Gibbs, W. Zhang, P. S. Halasyamani, M. A. Hayward and N. A. Benedek, *Chemistry of Materials*, 2017, **29**, 9489-9497.
6. N. A. Benedek, *Inorganic Chemistry*, 2014, **53**, 3769-3777.
7. V. A. Cascos, J. Roberts-Watts, C. Skingle, I. Levin, W. Zhang, P. S. Halasyamani, M. C. Stennett, N. C. Hyatt, E. Bousquet and E. E. McCabe, *Chemistry of Materials*, 2020, **32**, 8700-8712.
8. T. Oshima, T. Yokoi, M. Eguchi and K. Maeda, *Dalton Transactions*, 2017, **46**, 10594-10601.
9. W. Guo, H. Xu, Q. Fan, P. Zhu, Y. Ma, Y. Liu, X. Zeng, J. Luo and Z. Sun, *Advanced Optical Materials*, 2024, 2303291.
10. L. Wu, G. Li, K. Prashanthan, A. Musiienko, J. Li, T. W. Gries, H. Zhang, H. Köbler, P. Janasik and A. N. Appiah, *Advanced Materials*, 2023, **35**, 2304150.
11. H. Ye, Y. Peng, X. Shang, L. Li, Y. Yao, X. Zhang, T. Zhu, X. Liu, X. Chen and J. Luo, *Advanced Functional Materials*, 2022, **32**, 2200223.
12. E. Zahedi, M. Hojamberdiev and M. F. Bekheet, *Rsc Advances*, 2015, **5**, 88725-88735.
13. S. Kurnosenko, O. Silyukov, I. Rodionov, Y. Biryukov, A. Burov and I. Zvereva, *Russian Journal of Inorganic Chemistry*, 2023, **68**, 1903-1912.
14. E. Syrov, O. Krasheninnikova, A. Knyazev, D. Fukina, E. Suleimanov, N. Volkova, A. Gorshkov and S. Smirnov, *Journal of Physics and Chemistry of Solids*, 2021, **156**, 110184.
15. V. Thangadurai, P. Schmid-Beurmann and W. Weppner, *Journal of Solid State Chemistry*, 2001, **158**, 279-289.
16. Z.-H. Liang, K.-B. Tang, Q.-W. Chen and H.-G. Zheng, *Acta Crystallographica Section E: Structure Reports Online*, 2009, **65**, i44-i44.
17. M. Machida, T. Mitsuyama, K. Ikeue, S. Matsushima and M. Arai, *The Journal of Physical Chemistry B*, 2005, **109**, 7801-7806.
18. A. Ali, V. Cascos, F. G. Pritchard, J. R. Verlet, N. R. Sutherland, J. Woolley, J. Lloyd-Hughes, M. Avdeev, A. Beeby, S. J. Clark, E. E. McCabe, *Journal of Materials Chemistry A*, 2025, 28, 23073-23086.
19. M. Avdeev and J. R. Hester, *Applied Crystallography*, 2018, **51**, 1597-1604.
20. H. M. Rietveld, *Applied Crystallography*, 1969, **2**, 65-71.
21. A. A. Coelho, *Coelho Software, Brisbane, Australia*, 2007.
22. A. Coelho, *Karlsruhe, Germany*, 2012.
23. B. J. Campbell, H. T. Stokes, D. E. Tanner and D. M. Hatch, *Journal of Applied Crystallography*, 2006, **39**, 607-614.
24. E. E. McCabe, A. S. Wills, L. Chapon, P. Manuel and J. S. Evans, *Physical Review B*, 2014, **90**, 165111.
25. S. J. Clark, M. D. Segall, C. J. Pickard, P. J. Hasnip, M. I. Probert, K. Refson and M. C. Payne, *Zeitschrift für kristallographie-crystalline materials*, 2005, **220**, 567-570.
26. D. Vanderbilt, *Physical review B*, 1990, **41**, 7892.
27. J. P. Perdew, K. Burke and M. Ernzerhof, *Physical review letters*, 1996, **77**, 3865.
28. S. Kurtz and T. Perry, *Journal of applied physics*, 1968, **39**, 3798-3813.
29. A. M. Glazer, *Acta Crystallographica Section B: Structural Crystallography and Crystal Chemistry*, 1972, **28**, 3384-3392.
30. N. Brese and M. O'keeffe, *Acta Crystallographica Section B: Structural Science*, 1991, **47**, 192-197.
31. I. Brown and D. Altermatt, *Acta Crystallographica Section B: Structural Science*, 1985, **41**, 244-247.
32. M. Dion, M. Ganne and M. Tournoux, *Revue de chimie minérale*, 1984, **21**, 92-103.
33. R. Armstrong and R. Newnham, *Materials Research Bulletin*, 1972, **7**, 1025-1034.

34. O. Krasheninnikova, E. Syrov, I. Sorokin, S. Smirnov and D. Titaev, *European Journal of Inorganic Chemistry*, 2024, **27**, e202400563.
35. Z. Liang, K. Tang, Q. Shao, G. Li, S. Zeng and H. Zheng, *Journal of Solid State Chemistry*, 2008, **181**, 964-970.
36. M. Green, K. Prassides, P. Day and D. Neumann, *International Journal of Inorganic Materials*, 2000, **2**, 35-41.
37. S. M. Blake, M. J. Falconer, M. McCreedy and P. Lightfoot, *Journal of Materials Chemistry*, 1997, **7**, 1609-1613.
38. H. Djani, E. E. McCabe, W. Zhang, P. S. Halasyamani, A. Feteira, J. Bieder, E. Bousquet and P. Ghosez, *Physical Review B*, 2020, **101**, 134113.
39. V. M. Goldschmidt, *Naturwissenschaften*, 1926, **14**, 477-485.
40. J. Y. Lee, S. Ling, S. P. Argent, M. S. Senn, L. Cañadillas-Delgado and M. J. Cliffe, *Chemical Science*, 2021, **12**, 3516-3525.
41. R. D. Shannon, *Acta crystallographica section A: crystal physics, diffraction, theoretical and general crystallography*, 1976, **32**, 751-767.
42. S. Blake, *Journal of Materials Chemistry*, 1997, **7**, 1609-1613.
43. S. Borg and G. Svensson, *Journal of Solid State Chemistry*, 2001, **157**, 160-165.
44. N. A. Benedek, J. M. Rondinelli, H. Djani, P. Ghosez and P. Lightfoot, *Dalton Transactions*, 2015, **44**, 10543-10558.
45. C. H. Hervoches and P. Lightfoot, *Journal of Solid State Chemistry*, 2000, **153**, 66-73.
46. C. H. Hervoches, A. Snedden, R. Riggs, S. H. Kilcoyne, P. Manuel and P. Lightfoot, *Journal of Solid State Chemistry*, 2002, **164**, 280-291.
47. T. Nagai, Y. Mochizuki, H. Shirakuni, A. Nakano, F. Oba, I. Terasaki and H. Taniguchi, *Chemistry of Materials*, 2020, **32**, 744-750.
48. P. S. Halasyamani and K. R. Poeppelmeier, *Chemistry of Materials*, 1998, **10**, 2753-2769.
49. T. Wu, B. Yin, Z. Bian, Y. Gao, J. Gu and D. Wang, *Inorg. Chem. Front.,* 2023, 10(9), 2689–2696.
50. B. Karvaly and I. Hevesi, *Z. Naturforsch. A*, 1971, **26**, 245-249.
51. N. Kulischow, C. Ladasiu and R. Marschall, *Catalysis Today*, 2017, **287**, 65-69.
52. C.-Y. Yoo, J. Kim, S.-C. Kim and S.-J. Kim, *Journal of Solid State Chemistry*, 2018, **267**, 146-152.
53. T. Mitsuyama, A. Tsutsumi, T. Hata, K. Ikeue and M. Machida, *Bulletin of the Chemical Society of Japan*, 2008, **81**, 401-406.
54. M. Machida, J.-i. Yabunaka and T. Kijima, *Chemistry of Materials*, 2000, **12**, 812-817.
55. Y. Miseki, H. Kato and A. Kudo, *Energy & Environmental Science*, 2009, **2**, 306-314.

Chapter 4: Tuning Between Ground States and Instabilities in Aurivillius Materials

4.1 Introduction

Layered perovskite related materials exhibiting ferroelectric properties are the focus of extensive research, owing both to their technological importance and for the intriguing interplay between competing structural instabilities that can lead to complex phase transitions.[1] One prominent family within this class is the Aurivillius materials, in which the perovskite blocks [$A_{n-1}B_nO_{3n+1}$] are separated by the fluorite-like Bi_2O_2 layers, with n being the number of layers of BO_6 octahedra in the

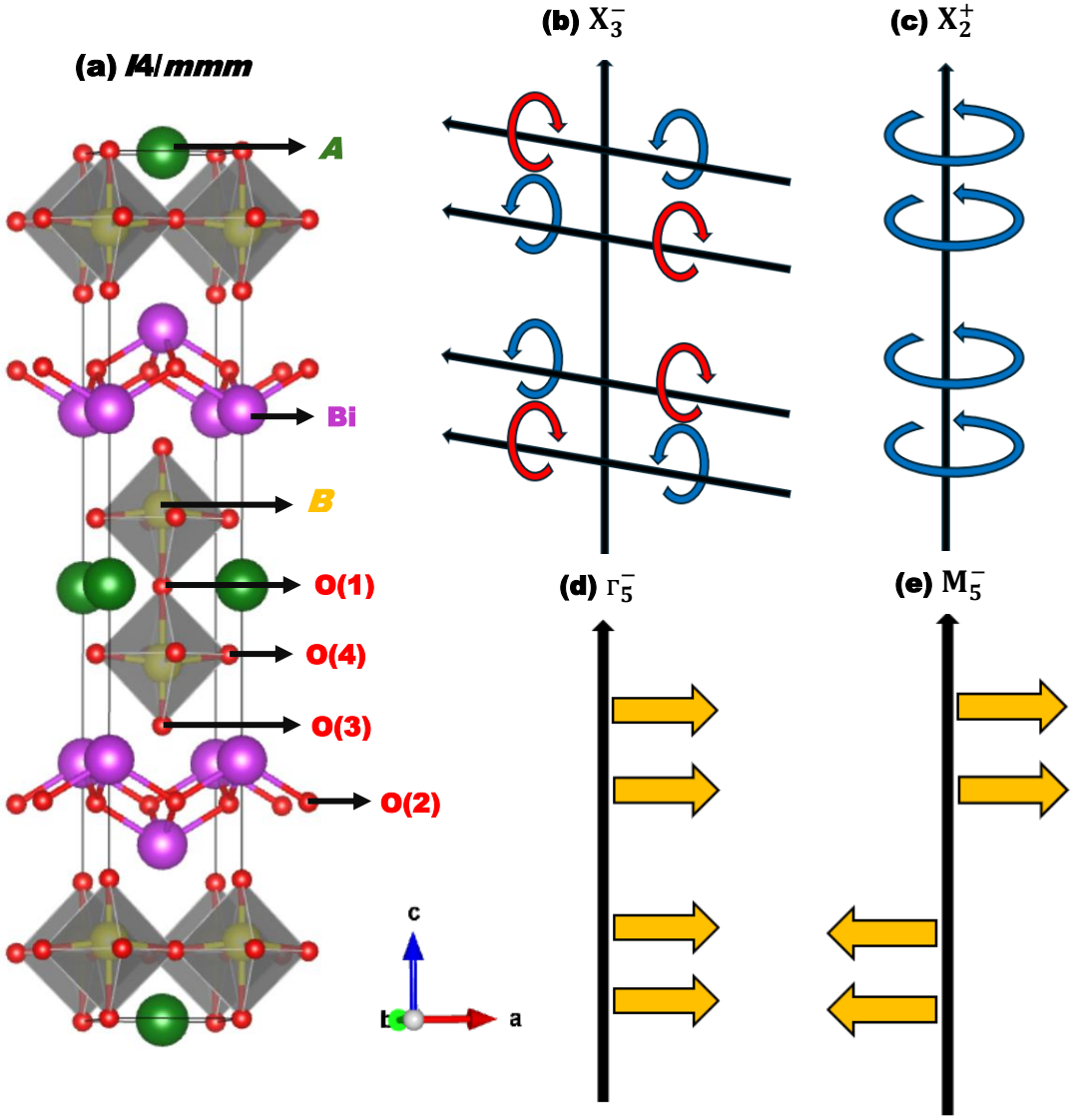

Figure 4.1: (a) High-symmetry tetragonal *I*4/*mmm* crystal structure of n = 2 Aurivillius phases. Schematic illustration of (b) X_3^- octahedral rotation mode, (c) X_2^+ octahedral rotation mode, (d) polar Γ_5^- displacive mode and (e) antipolar M_5^- displacive mode referred to in this chapter.

perovskite block. The ideal, high temperature aristotype structure of these materials is tetragonal of *I*4/*mmm* symmetry, shown in **Figure 4.1(a)**.

The Aurivillius phases are well known as proper ferroelectrics for which the primary distortion mode is polar.[2-6] In this work, we present a combined neutron powder diffraction (NPD) and first-principles density functional theory (DFT) study to determine the ground state of the *n* = 2 $Bi_2A_{0.5}La_{0.5}B_2O_9$ (*A* = Na, K; *B* = Nb, Ta). Our study shows that these compounds adopt a polar $A2_1am$ ground state involving only in-plane polar displacements (**Figure 4.1(d)**), along with both in-plane (**Figure 4.1(b)**) and out-of-plane (**Figure 4.1(c)**) octahedral tilts. DFT calculations also indicate the presence of a metastable antipolar *Pnam* phase only slightly higher in energy than the polar ground state. In contrast, for the *n* = 2 $Li_2AB_2O_7$ (*A* = Ca, Sr, Ba; *B* = Nb, Ta) Ruddlesden-Popper phases, we find that the *Pnam* phase is the ground state and $A2_1am$ is the metastable phase, consistent with the previous reports.[7]

4.1.1 Symmetry Analysis for *n* = 2 Aurivillius and Ruddlesden-Popper phases

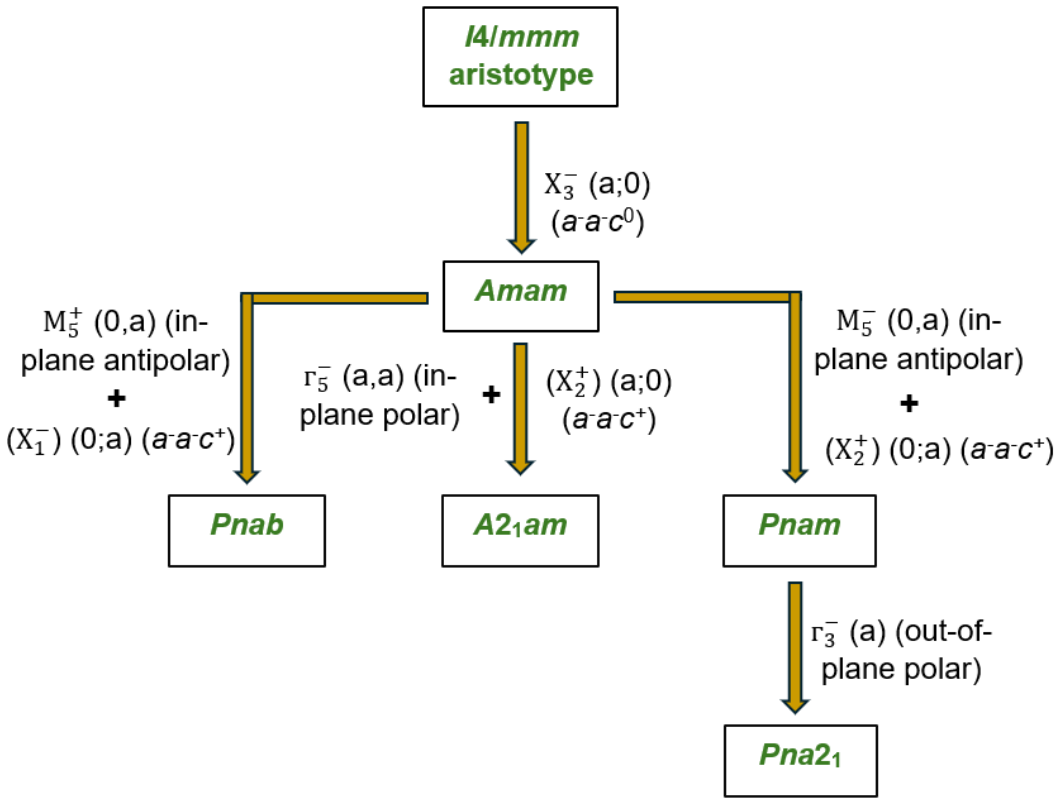

Figure 4.2: Schematic illustrating the symmetry lowering due to possible combinations of distortions expected for *n* = 2 Aurivillius phases.

Upon cooling, the *n* = 2 Aurivillius materials under investigation can undergo structural phase transitions via two possible pathways, as discussed in **Section 1.3.4**:

(I) A direct avalanche-type transition from *I*4/*mmm* to the polar *A*2$_1$*am* or the antipolar *Pnam* or *Pnab* structure, where all three structural distortions condense together. In this case, it difficult to identify which mode as the primary order parameter driving the phase transition. Therefore, such a transition cannot be classified as proper or improper. For example: *n* = 2 Aurivillius $Bi_2SrNb_2O_9$ undergoes a direct avalanche-type transition.[4, 6]

(II) A sequence of two-phase transition: First the X_3^- octahedral rotation condenses leading to an intermediate structure with *Amam* symmetry. This is followed by the condensation of the polar or antipolar (Γ_5^-, M_5^- or M_5^+) and X_2^+ distortions to establish the polar *A*2$_1$*am* or the antipolar *Pnam* or *Pnab* structure. With respect to the parent *Amam* structure, the two modes Γ_5^- and X_2^+ will transform as the same irrep of Γ^- character to give *A*2$_1$*am*. Therefore, this transition would always be classified as proper. For example: *n* = 2 $Bi_2SrTa_2O_9$ Aurivillius phase undergoes a two-step transition.[4, 5]

The *A*2$_1$*am* and *Pnam* structures are closely related as they both exhibit the same X_3^- and X_2^+ octahedral rotations.[8] ISODISTORT, a web-based tool, can be used to explore these distortions.[9] In *A*2$_1$*am* structure, the rotations of BO_6 about the out-of-plane, described by X_2^+, are in the same direction across successive perovskite slabs. In contrast, in *Pnam*, the X_2^+ octahedral rotations alternate in direction between adjacent perovskite slabs. This results in a trilinear coupling between the octahedral rotations and the interblock antipolar M_5^- distortion (**Figure 4.2**). If two *A*2$_1$*am* domains with opposite polarization direction are stacked along the long axis, *c*, the antipolar *Pnam* structure is expected to emerge naturally at their interface.

The polar *Pna*2$_1$ phase is a subgroup of *Pnam*, with inclusion of an additional polar Γ_3^- distortion along the long axis, in combination with X_3^-, X_2^+ and M_5^- modes.

4.2 Methods

4.2.1 Synthesis

Polycrystalline samples of $Bi_2A_{0.5}La_{0.5}B_2O_9$ (*A* = Na, K; *B* = Nb, Ta) were synthesised using the conventional solid state reaction method. The starting materials included Bi_2O_3 (Alfa Aesar, 99.9%), La_2O_3 (Alfa Aesar, 99.9%), Na_2CO_3 (Alfa Aesar, 99.5%),

K_2CO_3 (Alfa Aesar, 99.5%) Nb_2O_5 (Alfa Aesar, 99.5%), and Ta_2O_5 (Alfa Aesar, 99.0%).

For synthesis, stoichiometric quantities of the precursors were thoroughly ground in an agate mortar with acetone, and the resulting mixtures were pressed into pellets (10 mm in diameter). The pellets were placed in an alumina crucible and were covered with sacrificial powder of the same composition during heating to reduce loss of volatile reagents. An initial controlled decomposition stage was required where the pellets were heated in air at 400°C and 600°C for 12 hours in a Carbolite Gero chamber furnace.

The pellets underwent subsequent heating in air at 900°C for 12 hours. After cooling to room temperature in the furnace, the samples were reground with acetone and reheated under the same conditions. This process was repeated twice to ensure homogeneity and phase purity.

4.2.2 Structural Characterisation

Powder X-ray (XRPD) data were collected at room temperature for all samples to monitor synthesis reactions using a Rigaku Miniflex 600 bench-top powder X-ray diffractometer with Cu Kα radiation (with Ni filter), a D/tex Ultra2 detector and step of 0.01°. Neutron powder diffraction (NPD) data were collected on GEM at the ISIS spallation source.[10] A ~5 g sample was loaded into a cylindrical vanadium can, and data were collected at room temperature for 30 minutes across all 6 detector banks. Diffraction data were analysed using the Rietveld method[11] in the Topas Academic software.[12, 13]

4.2.3 Geometry Optimization DFT Calculations

Geometry optimisation calculations were performed within Density Functional Theory (DFT) using the pseudo-potential formalism as implemented in the CASTEP code[14] in collaboration with Prof. Stewart Clark (Department of Physics, Durham University), who kindly set-up all DFT calculations. To address the mixed occupancy of $(Na/K)_{0.5}La_{0.5}$ in the *A*-site, the calculations were carried out assuming complete ordering of (Na/K)/La and Bi. However, to account for the mixed nature of the *A*-site occupancy, supercells with a checkerboard ordering of Na/K and La over the *A*-sites were employed. **Table 4.1** summarises the symmetries resulting from distortion modes as well as those resulting from (Na/K)/La ordered supercell used for DFT

calculations. For simplicity, the symmetries resulting from the distortion modes are used throughout this chapter.

Table 4.1: Symmetries from distortion modes and (Na/K)/La ordered supercells used in DFT calculations.

Distortion Mode (order parameter direction)	**Symmetry resulting from distortion (non-standard settings of space groups are used to give the long axis along *c*)**	**Symmetry of (Na/K)/La ordered supercell used for DFT calculations**
Γ_5^- (a,a)	*F2mm*	*B2mm*
Γ_3^- (a)	*I4mm*	*Amm2*
M_5^- (a;0)	*Cmcm*	*Pmcm*
M_5^+ (a;0)	*Cmca*	*Pcma*
X_3^- (a;0)	*Amam*	*Pnmm*
X_2^+ (a;0)	*Acam*	*Pcnm*
X_1^- (a;0)	*Acaa*	*Pncb*
X_3^-+X_1^-+ M_5^+ (a;0|0;b|0,-c)	*Pnab*	*P2na*
X_3^-+X_2^++Γ_5^- (a;0|b;0|c,c)	*A2$_1$am*	*Cm*
X_3^-+X_2^++M_5^- (a;0|0;b|0,-c)	*Pnam*	*P2$_1$/m*
X_3^-+X_2^++ Γ_3^- (a;0|0;b|c)	*Pna2$_1$*	*P2$_1$*

Electronic wave functions were expanded in a plane wave basis up to a kinetic energy cut-off of ≥ 950 eV. Converging calculations to ~1 meV/atom. Brillouin zone sampling was chosen to give a similar level of convergence. Integrations of the Brillouin zone were done with a k-point sampling scheme where the *k*-points are spaced at 0.05 Å^{-1}. Electron-ion interactions are described using *ab initio* ultra-soft pseudopotentials based on Vanderbilt's formalism.[15] The pseudo-potentials treat certain semicore states as valence, which is essential to obtain accurate electronic structures. In particular, this includes the 5d, 6s, and 6p states for Bi; the 1s and 2s states for Li; the 2s, 2p, and 3s states for Na; the 3s, 3p, and 4s states for K; the 3s, 3p, and 4s states for Ca; the 4s, 4p, and 5s states for Sr; the 5s, 5p and 6s states

for Ba, the 4s, 4p, 4d and 5s states for Nb; the 4f, 5s, 5p, 5d and 6s states for Ta, and the 2s and 2p states for O. Our standard DFT calculations use the Perdew Burke Ernzerhof (PBE) exchange-correlation functional[16] as it is an all-rounder - computationally efficient and gives reliable geometries and energies for a wide range of materials.

4.3 Results

4.3.1 Symmetry Determination and Structure Refinement

4.3.1.1 Structural Characterisation of $Bi_2Na_{0.5}La_{0.5}Nb_2O_9$

Multibank Rietveld refinements were carried out to fit the six banks of data for $Bi_2Na_{0.5}La_{0.5}Nb_2O_9$ with an aristotype *I4/mmm* model. Rietveld refinement profile for bank 6, the highest resolution bank, shows that the peaks at 9860, 10140, 12080, 14380, and 16200 μs are not fitted by the high symmetry model (**Figure 4.3**).

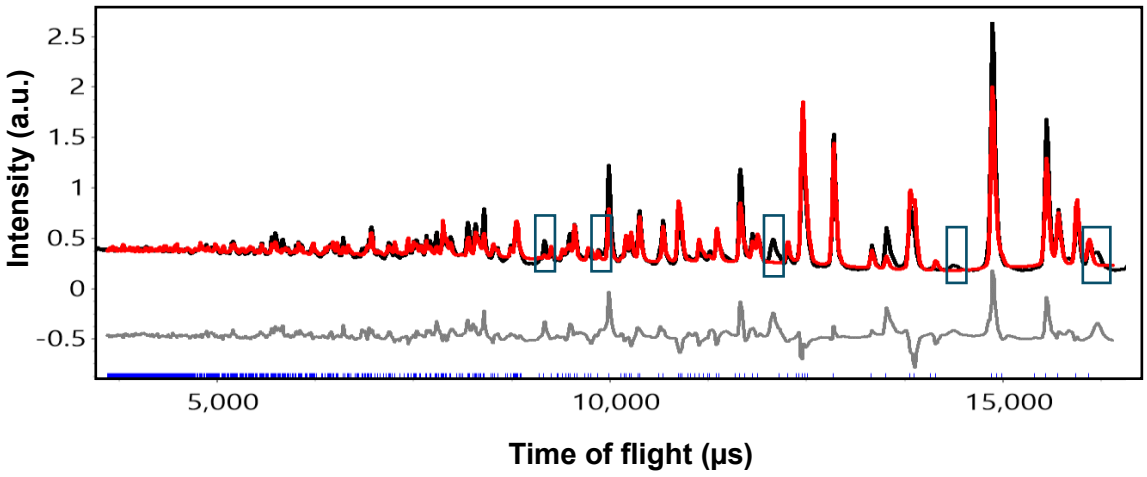

Figure 4.3: Rietveld refinement profile for highest resolution bank 6 data for $Bi_2Na_{0.5}La_{0.5}Nb_2O_9$, refined in space group *I*4/*mmm*. The observed, calculated, and difference profiles are shown in black, red, and grey respectively).

The *I4/mmm* model for $Bi_2Na_{0.5}La_{0.5}Nb_2O_9$ gave an unreasonably high atomic displacement parameter (ADP) for the central equatorial oxygen site O(4). Allowing anisotropy of this ADP suggested significant displacements in the *ab* plane, suggesting rotation of the BO_6 octahedra about the long axis. The ADP for the apical oxygens was also very high. Allowing anisotropy of this ADP suggested rotation of the BO_6 octahedra about an in-plane axis (**Figure 4.4**).

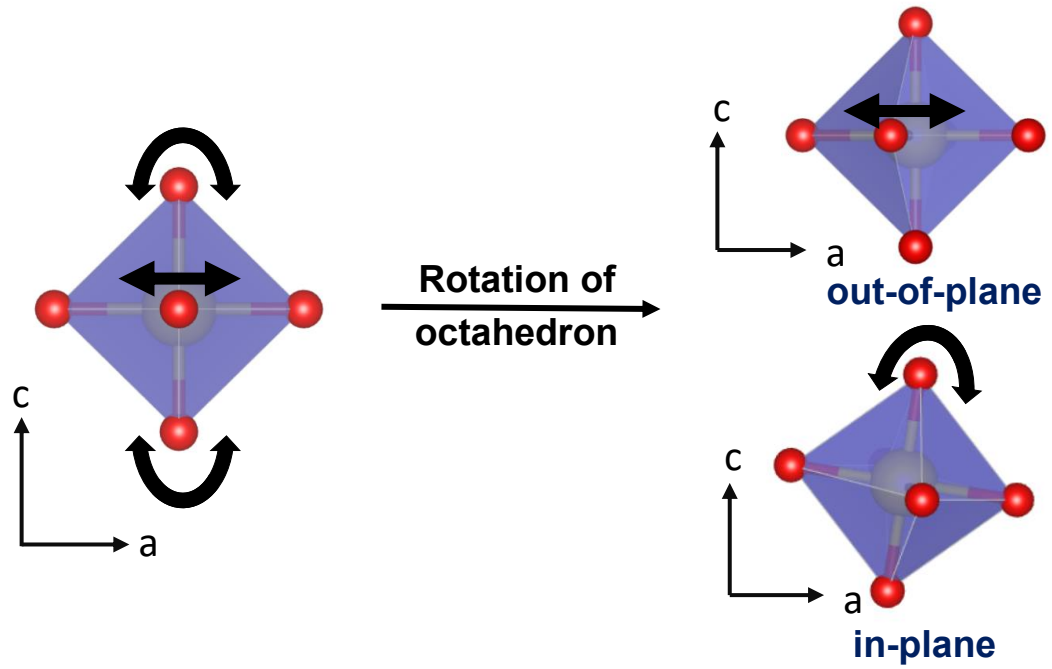

Figure 4.4: Oxygen O(4) site and apical oxygens suggesting rotation of octahedra about the out-of-plane axis and in-plane axis respectively.

Therefore, models that allow the rotation of the octahedra about both the out-of-plane axis, described by X_1^- and X_2^+ modes, and in-plane axis, described by X_3^- mode, were considered. The lower symmetry models considered were *A*2$_1$*am* (X_3^- + Γ_5^- + X_2^+), *Pnam* (X_3^- + M_5^- + X_2^+), *Pnab* (X_3^- + M_5^+ + X_1^-), and *Pna*2$_1$ (X_3^- + X_2^+ + Γ_3^-). The space group setting for *Cmc*2$_1$, *Pnma* and *Pbcn* have been changed to *A*2$_1$*am, Pnam* and *Pnab* respectively to have long axis along *c*. We will be using these non-standard settings from here on.

Table 4.2 compares the R_{wp} values and number of parameters of the lower symmetry models with the parent *I*4/*mmm* model. Based on the data, the *Pna*2$_1$ model has the lowest R_{wp}; however, compared to *A*2$_1$*am*, the reduction in R_{wp} is only 0.1%, while the number of parameters increases by 14. Moreover, the *Pna*2$_1$ model predicts extra intensity that is not observed experimentally, such as additional peaks at 1.11 Å (~10100 μs for bank 6) and 1.16 Å (~10600 μs for bank 6) (Rietveld refinement profile of *Pna*2$_1$ is provided in **Appendix 2, Section 2.1**). Also, the mode amplitude for Γ_3^- is 0.29 Å, which is smaller than Γ_5^- mode amplitude (0.58 Å). Therefore, the polar X_3^- + Γ_5^- + X_2^+ *A*2$_1$*am* model is found to be most suitable for $Bi_2Na_{0.5}La_{0.5}Nb_2O_9$. Mode decomposition analysis gives the following mode amplitudes: 0.58 Å for Γ_5^- mode, 0.64 Å for X_3^- mode and 0.52 Å for X_2^+ mode.

Table 4.2: Summary of R_{wp} values and number of parameters for the lower symmetry models compared with the parent *I*4/*mmm* model for $Bi_2Na_{0.5}La_{0.5}Nb_2O_9$.

Model	R_{wp} (%)	Number of Parameters
Parent *I4/mmm*	10.64	108
X_3^- (a,0) *Amam*	6.48	119
X_3^- + Γ_5^- + X_2^+ (a,a|b;0) *A*2$_1$*am*	4.18	130
X_3^- + M_5^- + X_2^+ (a,0|0;b) *Pnam*	4.29	130
X_3^- + M_5^+ + X_1^- (a;0|0;b) *Pnab*	4.95	128
X_3^- + X_2^+ + Γ_3^- (a|b;0|0;c) *Pna*2$_1$	4.08	144

Two models of *A*2$_1$*am* structure were tested: one assuming no disorder between the Bi_2O_2 layer and *A*-site cations, and another allowing disorder between these sites. In the ordered model, the Bi_2O_2 layer was fully occupied by bismuth (Bi) while the *A*-site was half occupied by sodium (Na) and lanthanum (La).

In the disordered mode, Bi, La, and Na were allowed to mix across both the Bi_2O_2 layer (8*b*) and *A*-site (4*a*). Neutron scattering lengths are Na = 3.63(2) fm, La = 8.24(4) fm, and Bi = 8.532(2) fm.[17] Since neutrons have similar scattering lengths for La and Bi, neutron powder diffraction (NPD) data will not be very sensitive to the distribution of Bi and La over the two sites. However, with Na having a much lower neutron scattering length, NPD data was used to determine its distribution across the two sites. Refinement results suggested a Na distribution of 0.045(2) in the Bi_2O_2 layer (8*b*) and 0.411(4) on *A*-site (4*a*). These values indicate a low disorder. Additionally, the parameter R_{wp} for the two models: ordered and disordered are 4.18 and 4.20 respectively, suggesting that the ordered model provides a better fit. Rietveld refinement profile for bank 6 in shown in **Figure 4.5**. Refinement profiles for banks 1 through 5 are provided in **Appendix 2, Section 2.1**. The distortion modes amplitudes, refinement details, and selected bond lengths are given in **Table 4.3**, **Table 4.4** and **Table 4.5**. Bond valence sum (BVS) calculations are used to validate the experimental refined structures. BVS is a way to estimate the oxidation state of an atom in a material, based on the lengths of the bonds around it. [18, 19] For an atom, the BVS should roughly be equal the atom's oxidation state.

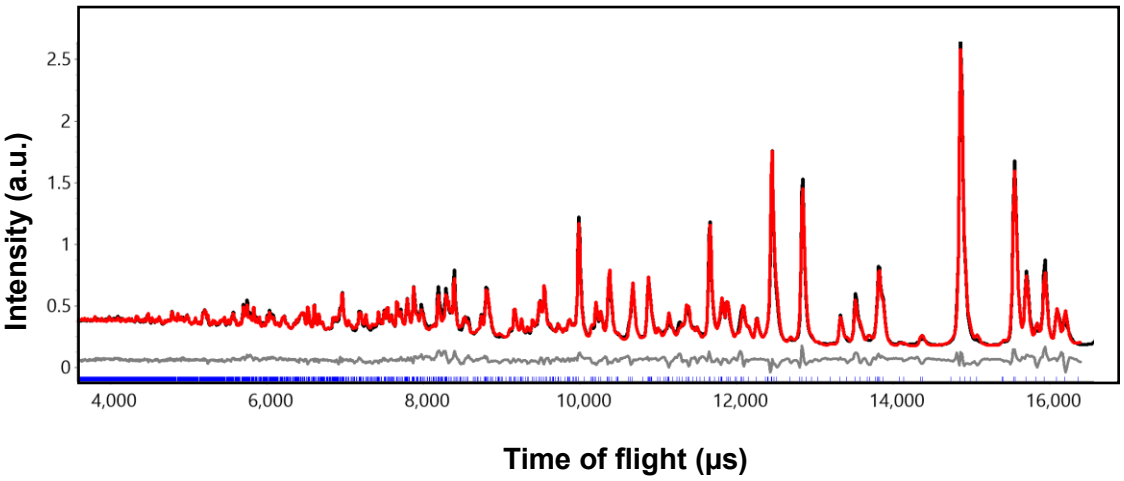

Figure 4.5: Rietveld refinement profile for highest resolution bank 6 data for $Bi_2Na_{0.5}La_{0.5}Nb_2O_9$, refined in space group $A2_1am$. The observed, calculated, and difference profiles are shown in black, red, and grey respectively).

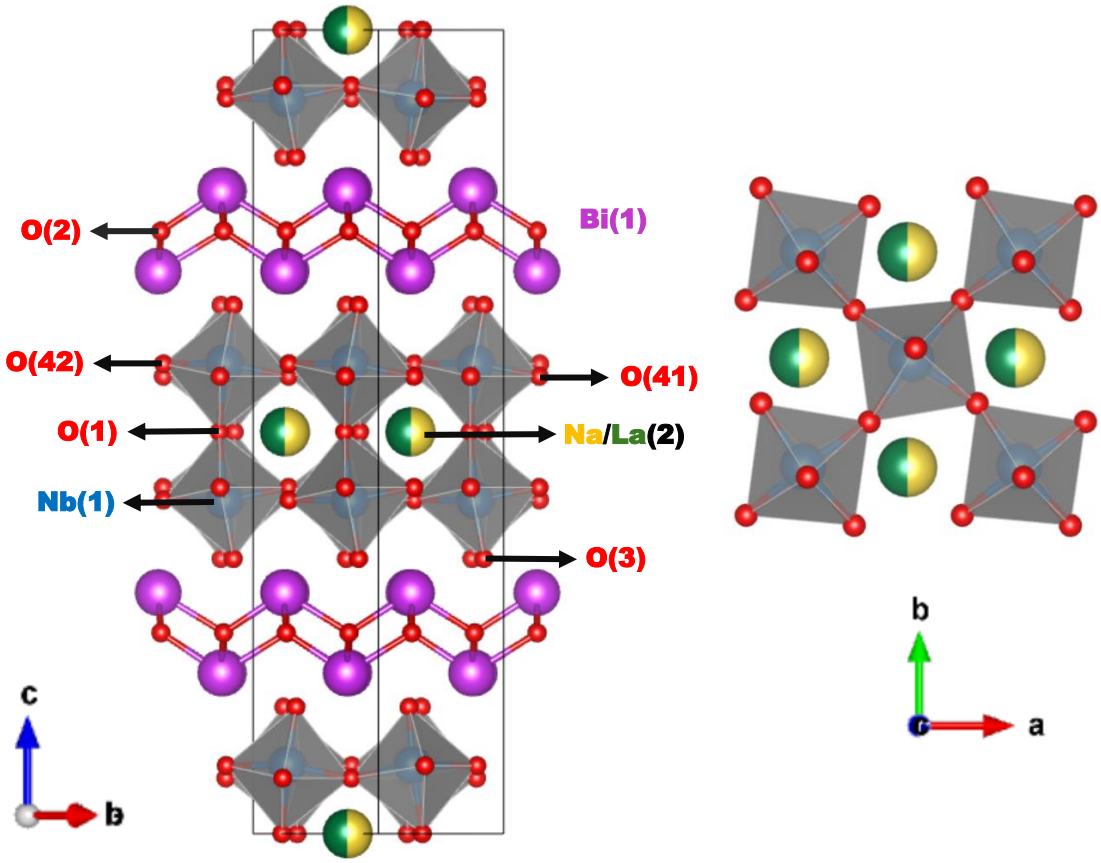

Figure 4.6: Crystal structure of $X_3^- + r_5^- + (X_2^+)$ $A2_1am$ model for $Bi_2Na_{0.5}La_{0.5}Nb_2O_9$. Bi, Na, La, Nb and O sites are shown in purple, yellow, green, blue, and red. NbO_6 are shown in grey.

Table 4.3: Decomposition of $A2_1am$ structure of $Bi_2Na_{0.5}La_{0.5}Nb_2O_9$. $O4_\perp$ and $O4_\parallel$ refer to O4 displacements parallel and perpendicular to the *B*-O4 bond, respectively, and $O4_z$ are displacements along [001]. The distortion amplitudes are reported in Å.

Atom	$Bi_2Na_{0.5}La_{0.5}Nb_2O_9$		
	Γ_5^-	X_3^-	X_2^+
Bi	-0.01	-0.08	
Na/La	0	-0.02	
Nb	0.14	0.00	
O1	0.19	-0.33	
O2	0.08	-0.01	-0.01
O3	0.29	0.38	
$O4_\perp$	0.23		0.01
$O4_\parallel$	0.37		0.52
$O4_z$		0.39	
Total	0.58	0.64	0.52

Table 4.4: Structural parameters of $Bi_2Na_{0.5}La_{0.5}Nb_2O_9$ from time-of-flight NPD data in space group $A2_1am$.

Space group: $A2_1am$ (No. 36). Cell parameters: a = 5.4886 (1) Å, b = 5.4874 (1) Å, c = 24.8416 (3) Å. R_{wp} = 4.18%, R_p = 2.96%, χ^2 = 18.92, 130 parameters.

Atom	Wyckoff Site	*x*	*y*	*z*	Occupancy	U_{iso} x 100 (Å^2)
Bi(1)	8*b*	0.5038(4)	0.2398(3)	0.7001(3)	1	2.04(2)
Na/La(2)	4*a*	0.5*	0.7461(5)	0	0.5/0.5	1.03(3)
Nb(1)	8*b*	0.5233(4)	0.2499(4)	0.0852(3)	1	0.53(1)
O(1)	4*a*	0.0408(8)	0.8100(5)	0	1	1.40(6)
O(2)	8*b*	0.7656(6)	0.0016(4)	0.2498(8)	1	0.81(2)
O(3)	8*b*	0.5434(6)	0.2991(4)	0.1576(5)	1	1.99(4)
O(41)	8*b*	0.2598(4)	-0.0233(5)	0.5691(5)	1	1.62(2)
O(42)	8*b*	0.8288(3)	0.0422(5)	0.0847(6)	1	1.59(4)

* Fixed to define origin of the unit cell along the polar axis.

Table 4.5: Selected bond lengths and bond angles for $Bi_2Na_{0.5}La_{0.5}Nb_2O_9$ from time-of-flight NPD data in space group *A*2$_1$*am*.

Bond	Bond Length (Å)/Bond Angle (°)	Bond	Bond Length (Å)/Bond Angle (°)
Nb(1)-O(11)	2.143(1)	Na/La(2)-O(42)	2.592(3), 3.196(4)
Nb(1)-O(31)	1.824(1)	Bi(1)-O(21)	2.239(4), 2.291(4), 2.307(4), 2.378(4)
Nb(1)-O(41)	1.949(4), 2.024(4)	Bi(1)-O(31)	2.647(3),2.746(4), 3.151(4), 3.252(3), 3.557(1)
Nb(1)-O(42)	1.926(4), 2.027(4)	Bi(1)-O(42)	3.251(3) Å
Na/La(2)-O(11)	2.444(4), 2.575(6), 2.959(6), 3.058(4)	O(42)-O(41)-O(42)	161.01(9)
Na/La(2)-O(41)	2.528(4), 2.637(4)	O(31)-O(11)-O(31)	162.83(1)

The bond valence sum calculations[18, 19] gave valences: $Na(2)_{100\%}$ = +1.154, $La(2)_{100\%}$ = +3.128, Nb(1) = +5.130 and Bi(1) = +2.848. $Na/La(2)_{100\%}$ is apparent valence of the *A*-site assuming full occupation by Na/La.

4.3.1.2 Structural Characterisation of $Bi_2Na_{0.5}La_{0.5}Ta_2O_9$

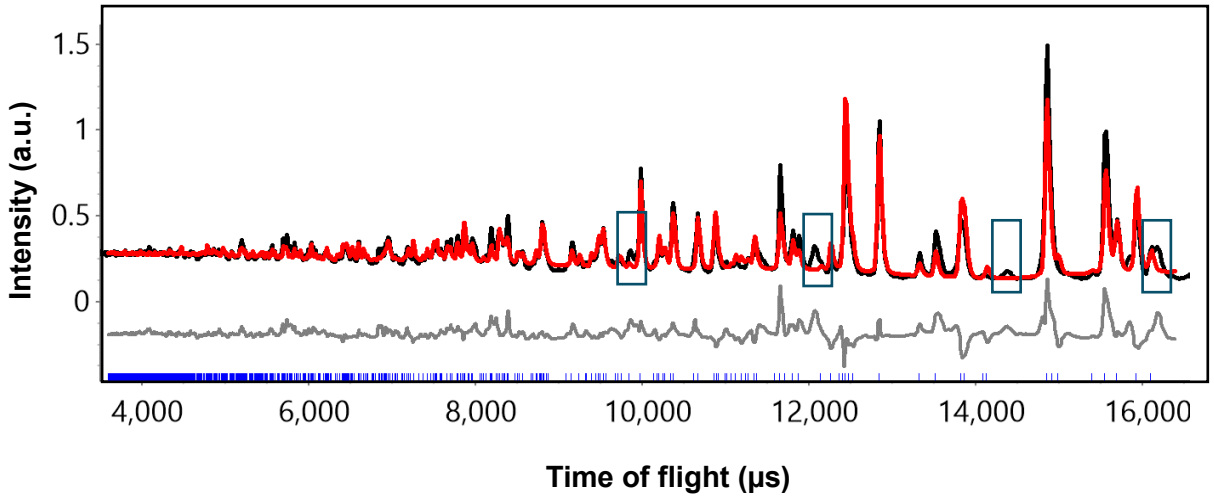

Figure 4.7: Rietveld refinement profile for highest resolution bank 6 data for $Bi_2Na_{0.5}La_{0.5}Ta_2O_9$, refined in space group *I*4/*mmm*. The observed, calculated, and difference profiles are shown in black, red, and grey respectively).

Multibank Rietveld refinements were carried out to fit the six banks of data for $Bi_2Na_{0.5}La_{0.5}Nb_2O_9$ with an aristotype *I*4*/mmm* model. Rietveld refinement profile for bank 6 again showed the peaks at 9850, 12100, 14375, and 16200 μs are not fitted by the high symmetry model (**Figure 4.7**).

Similar to $Bi_2Na_{0.5}La_{0.5}Nb_2O_9$, the *I*4*/mmm* model for $Bi_2Na_{0.5}La_{0.5}Ta_2O_9$ also gave an unreasonably high ADP for the oxygen sites within the perovskite block, consistent with the rotations of BO_6 octahedra about both in-plane and out-of-plane axes (**Figure 4.4**).

Therefore, models that allow the rotation of the rotations of octahedra about both the out-of-plane axis, described by X_2^+ mode, and in-plane axis, described by X_3^- mode, were considered. The lower symmetry models considered were *A*2$_1$*am* ($X_3^- + \Gamma_5^- + X_2^+$), *Pnam* ($X_3^- + M_5^- + X_2^+$), *Pnab* ($X_3^- + M_5^+ + X_1^-$), and *Pna*2$_1$ ($X_3^- + X_2^+ + \Gamma_3^-$).

Table 4.6: Summary of R_{wp} values and number of parameters for the lower symmetry models compared with the parent *I*4/*mmm* model for $Bi_2Na_{0.5}La_{0.5}Ta_2O_9$.

Model	R_{wp} (%)	Number of Parameters
Parent *I*4*/mmm*	10.58	108
X_3^- (a,0) *Amam*	5.50	119
$X_3^- + \Gamma_5^- + X_2^+$ (a,a|b;0) *A*2$_1$*am*	3.60	130
$X_3^- + M_5^- + X_2^+$ (a,0|0;b) *Pnam*	3.79	130
$X_3^- + M_5^+ + X_1^-$ (a;0|0;b) *Pnab*	4.40	128
$X_3^- + X_2^+ + \Gamma_3^-$ (a|b;0|0;c) *Pna*2$_1$	3.59	144

Table 4.6 compares the R_{wp} values and number of parameters of the lower symmetry models with the parent *I*4/*mmm* model. The *Pna*2$_1$ model predicts extra intensity that is not observed experimentally, such as additional peaks at 1.11 Å (~10100 μs for bank 6) and 1.16 Å (~10600 μs for bank 6) (the Rietveld refinement profile of *Pna*2$_1$ is provided in **Appendix 2, Section 2.2**). Also, the mode amplitude for Γ_3^- is 0.24 Å, which is smaller than Γ_5^- mode amplitude (0.36 Å). Therefore, the polar $X_3^- + \Gamma_5^-$ ($+ X_2^+$) *A*2$_1$*am* model is found to be most suitable for $Bi_2Na_{0.5}La_{0.5}Ta_2O_9$, consistent with the findings for $Bi_2Na_{0.5}La_{0.5}Nb_2O_9$. This outcome aligns with expectations, as the ionic radii of Nb^{5+} and Ta^{5+} are similar. From mode

decomposition the mode amplitudes were found out to be 0.36 Å for r_5^- mode, 0.68 Å for X_3^- mode and 0.48 Å for X_2^+ mode.

Here also two models of *A*2$_1$*am* structure were tested: one assuming no disorder between the Bi_2O_2 layer (8*b*) and *A*-site (4*a*), and another allowing disorder between these sites. The disordered model suggested a Na distribution of 0.016(1) in Bi_2O_2 layer (8*b*) and 0.467(4) on *A*-site (4*a*). These values indicate a very small disorder. Additionally, the parameter R_{wp} for the two models: ordered and disordered are 3.60 and 3.62 respectively, suggesting that the ordered model provides a better fit. Rietveld refinement profile for bank 6 in shown in **Figure 4.8**. Refinement profiles for banks 1 through 5 are provided in **Appendix 2, Section 2.2**. The distortion modes amplitudes, refinement details, and selected bond lengths are given in **Table 4.7**, **Table 4.8** and **Table 4.9**.

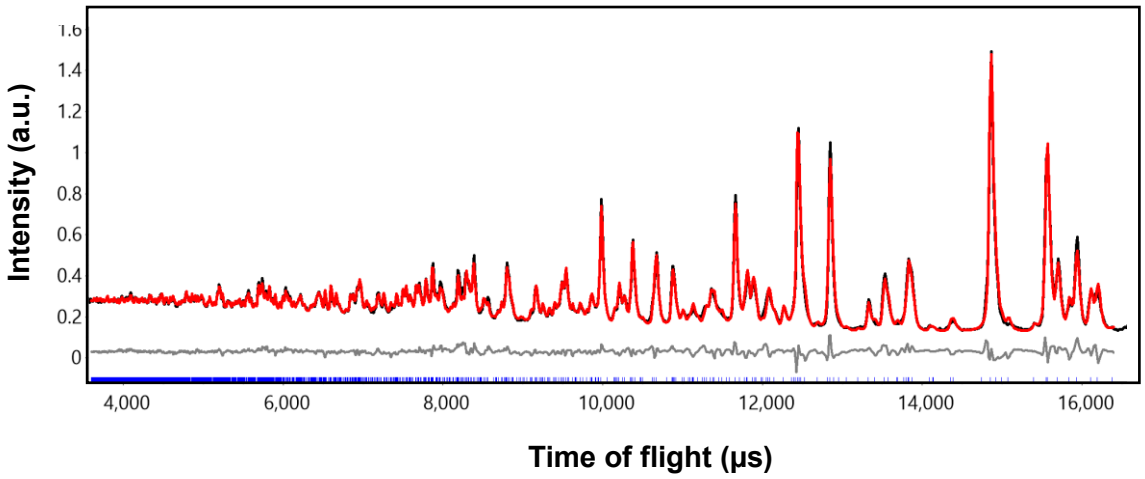

Figure 4.8: Rietveld refinement profile for highest resolution bank 6 data for $Bi_2Na_{0.5}La_{0.5}Nb_2O_9$, refined in space group *A*2$_1$*am*. The observed, calculated, and difference profiles are shown in black, red, and grey respectively).

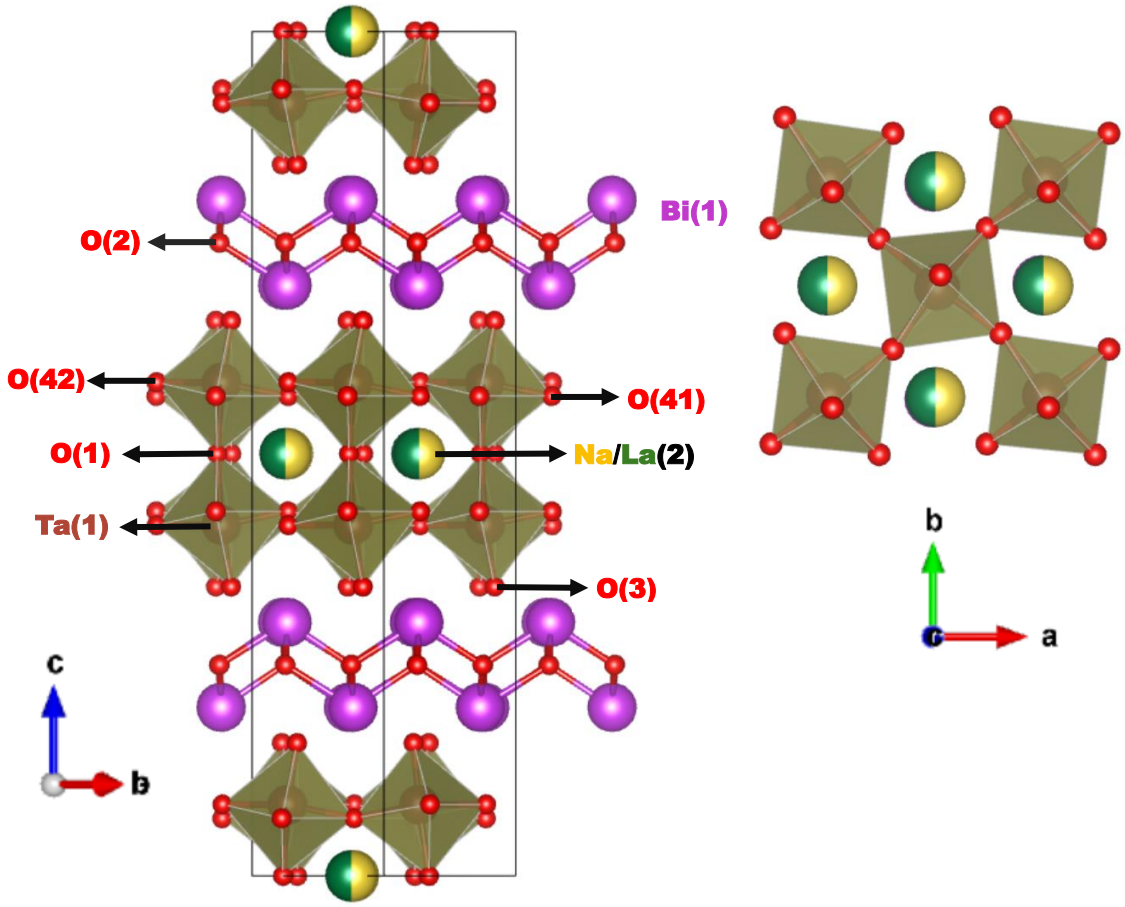

Figure 4.9: Crystal structure of X_3^- + Γ_5^- + (X_2^+) *A*2$_1$*am* model for $Bi_2Na_{0.5}La_{0.5}Ta_2O_9$. Bi, Na, La, Ta and O sites are shown in purple, yellow, green, brown, and red. TaO_6 are shown in golden.

Table 4.7: Decomposition of *A*2$_1$*am* structure of $Bi_2Na_{0.5}La_{0.5}Ta_2O_9$. $O4_\perp$ and $O4_\parallel$ refer to O4 displacements parallel and perpendicular to the *B*-O4 bond, respectively, and $O4_z$ are displacements along [001]. The distortion amplitudes are reported in Å.

Atom	**$Bi_2Na_{0.5}La_{0.5}Ta_2O_9$**		
	Γ_5^-	X_3^-	X_2^+
Bi	-0.09	-0.13	
Na/La	0.00	-0.04	
Ta	0.06	0.00	
O1	0.16	-0.29	
O2	-0.07	-0.01	-0.03
O3	0.18	0.45	
$O4_\perp$	0.12		0.01
$O4_\parallel$	0.21		0.48
$O4_z$		0.41	
Total	0.36	0.69	0.48

Table 4.8: Structural parameters of $Bi_2Na_{0.5}La_{0.5}Ta_2O_9$ from time-of-flight NPD data in space group $A2_1am$.

Space group: $A2_1am$ (No. 36). Cell parameters: a = 5.4860 (1) Å, b = 5.4858 (1) Å, c = 24.8650 (3) Å. R_{wp} = 3.60%, R_p = 2.72%, χ^2 = 10.11, 130 parameters.

Atom	Wyckoff Site	*x*	*y*	*z*	Occupancy	U_{iso} x 100 (Å^2)
Bi(1)	8*b*	0.4983(4)	0.2330(3)	0.6997(3)	1	2.04(2)
Na/La(2)	4*a*	0.5*	0.7420(4)	0	0.5/0.5	1.14(2)
Ta(1)	8*b*	0.5171(4)	0.2504(4)	0.0843(3)	1	0.36(1)
O(1)	4*a*	0.0386(7)	0.8039(5)	0	1	0.72(4)
O(2)	8*b*	0.7508(5)	0.0033(4)	0.2497(7)	1	0.66(2)
O(3)	8*b*	0.5330(6)	0.3074(4)	0.1574(5)	1	1.92(4)
O(41)	8*b*	0.2490(4)	-0.0246(5)	0.5683(5)	1	1.30(2)
O(42)	8*b*	0.8123(3)	0.0365(5)	0.0847(5)	1	1.30(2)

Table 4.9: Selected bond lengths and bond angles for $Bi_2Na_{0.5}La_{0.5}Ta_2O_9$ from time-of-flight NPD data in space group $A2_1am$.

Bond	Bond Length (Å)/Bond Angle (°)	Bond	Bond Length (Å)/Bond Angle (°)
Nb(1)-O(11)	2.119(1)	Na/La(2)-O(42)	2.662(3), 3.132(4)
Nb(1)-O(31)	1.846(1)	Bi(1)-O(21)	2.255(3), 2.259(3), 2.342(3), 2.380(3)
Nb(1)-O(41)	1.961(4), 2.010(4)	Bi(1)-O(31)	2.568(3),2.770(4), 3.124(4), 3.328(3), 3.582(1)
Nb(1)-O(42)	1.934(4), 2.00(4)	Bi(1)-O(42)	3.251(3)
Na/La(2)-O(11)	2.496(4), 2.606(6), 2.922(6), 2.999(4)	O(42)-O(41)-O(42)	161.48(8)
Na/La(2)-O(41)	2.456(4), 2.658(4)	O(31)-O(11)-O(31)	161.96(1)

The bond valence sum calculations gave valences: $Na(2)_{100\%}$ = +1.147, $La(2)_{100\%}$ = +3.112, Ta(1) = +5.252 and Bi(1) = +2.852

* Fixed to define origin of the unit cell along the polar axis.

4.3.1.3 Structural Characterisation of $Bi_2K_{0.5}La_{0.5}Nb_2O_9$

Multibank Rietveld refinements were carried out to fit the six banks of data for $Bi_2K_{0.5}La_{0.5}Nb_2O_9$ with an aristotype *I*4/*mmm* model. The Rietveld refinement profile for bank 6, shows an intensity mismatch and some small peaks are not fitted by the high symmetry model (**Figure 4.10**).

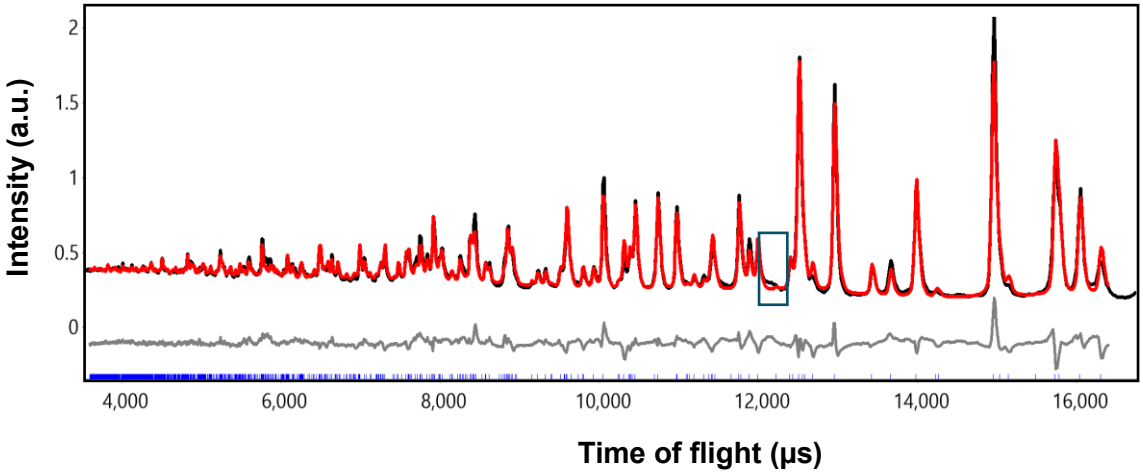

Figure 4.10: Rietveld refinement profile for highest resolution bank 6 data for $Bi_2K_{0.5}La_{0.5}Nb_2O_9$, refined in space group *I*4/*mmm*. The observed, calculated, and difference profiles are shown in black, red, and grey respectively).

Similar to $Bi_2Na_{0.5}La_{0.5}B_2O_9$ (*B* = Nb, Ta), the *I*4/*mmm* model for $Bi_2K_{0.5}La_{0.5}Nb_2O_9$ also gave an unreasonably high ADP for the oxygen sites within the perovskite block, consistent with the rotations of BO_6 octahedra about both in-plane and out-of-plane axes (**Figure 4.2**). Therefore, lower symmetry models, as described previously were considered.

Table 4.10 compares the R_{wp} values and number of parameters of the lower symmetry models with the parent *I*4/*mmm* model. Based on the data, the polar *A*2$_1$*am* and antipolar *Pnam* give comparable fits, but some extra peaks are predicted in *Pnam* which are not allowed for the A-centred model (Rietveld refinement profile of *Pnam* is provided in **Appendix 2, Section 2.3**). The displacements are in the same direction in adjacent perovskite slabs in Γ_5^- polar distortion (yielding a net polarization), whereas they are in opposite directions in the M_5^- antipolar distortion. The amplitude of Γ_5^- in *A*2$_1$*am* (0.29 Å) is slightly more than the M_5^- amplitude in *Pnam* (0.23 Å). Therefore, the polar *A*2$_1$*am* model is chosen over *Pnam*.

The *Pna*2$_1$ model has the lowest R_{wp}; however, compared to *A*2$_1$*am*, the reduction in R_{wp} is only 0.2 %, while the number of parameters increases by 14. Similar to *Pnam*, the *Pna*2$_1$ model also predicts extra intensity that is not observed

experimentally, such as additional peaks at 1.05 Å (~9576 μs for bank 6) and 1.18 Å (~10750 μs for bank 6) (the Rietveld refinement profile of *Pna*2_1 is provided in **Appendix 2, Section 2.3**). Also, the mode amplitude for r_3^- is 0.26 Å, which is slightly smaller than r_5^- mode amplitude (0.29 Å). Therefore, the polar X_3^- + r_5^- (+ X_2^+) *A*2_1*am* model is found to be most suitable for $Bi_2K_{0.5}La_{0.5}Nb_2O_9$.

Table 4.10: Summary of R_{wp} values and number of parameters for the lower symmetry models compared with the parent *I*4/*mmm* model for $Bi_2K_{0.5}La_{0.5}Nb_2O_9$.

Model	R_{wp} (%)	Number of Parameters
Parent *I*4/*mmm*	5.75	108
X_3^- (a,0) *Amam*	4.89	119
X_3^- + r_5^- + X_2^+ (a,a|b;0) *A*2_1*am*	4.65	130
X_3^- + M_5^- + X_2^+ (a,0|0;b) *Pnam*	4.63	130
X_3^- + M_5^+ + X_1^- (a;0|0;b) *Pnab*	4.70	128
X_3^- + X_2^+ + r_3^- (a|b;0|0;c) *Pna*2_1	4.42	144

Here also two models of *A*2_1*am* structure were tested: one assuming no disorder between the Bi_2O_2 layer (8*b*) and *A*-site (4*a*), and another allowing disorder between these sites. Neutron scattering lengths for K = 3.67(2) fm, La = 8.24(4) fm, and Bi = 8.532(2) fm.[17] Since neutrons have similar scattering lengths for La and Bi, neutron powder diffraction (NPD) data will not be sensitive enough to the distribution of Bi and La over the two sites. However, with K having a much lower neutron scattering length, NPD data was used to determine its distribution across the two sites.

The disordered model suggested a K distribution of 0.100(3) in Bi_2O_2 layer (8*b*) and 0.299(6) on *A*-site (4*a*). These values indicate higher disorder and the R_{wp} decreases from 5.45 to 5.21 when disorder was introduced, improving the fit. The K occupancy was then fixed.

X-ray powder diffraction (XRPD) data were used to determine the distribution of Bi and La across the two sites. The disordered model with K/Bi/La occupancy of 0.100(3)/0.900(4)/0.001(4) in Bi_2O_2 layer (8*b*) and 0.299(6)/0.202(8)/0.499(8) on *A*-site (4*a*) with R_{wp} 4.61% most accurately represents the structure of $Bi_2K_{0.5}La_{0.5}Nb_2O_9$. Rietveld refinement profile for bank 6 in shown in **Figure 4.11**.

Refinement profiles for banks 1 through 5 are provided in **Appendix 2, Section 2.3**. The distortion modes amplitudes, refinement details, and selected bond lengths are given in **Table 4.11**, **Table 4.12** and **Table 4.13**.

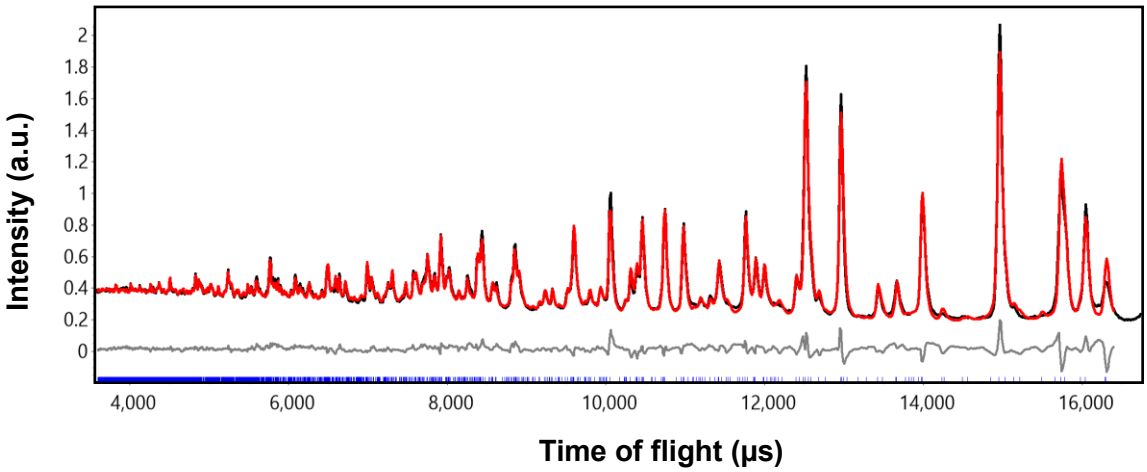

Figure 4.11: Rietveld refinement profile for highest resolution bank 6 data for $Bi_2K_{0.5}La_{0.5}Nb_2O_9$, refined in space group $A2_1am$. The observed, calculated, and difference profiles are shown in black, red, and grey respectively).

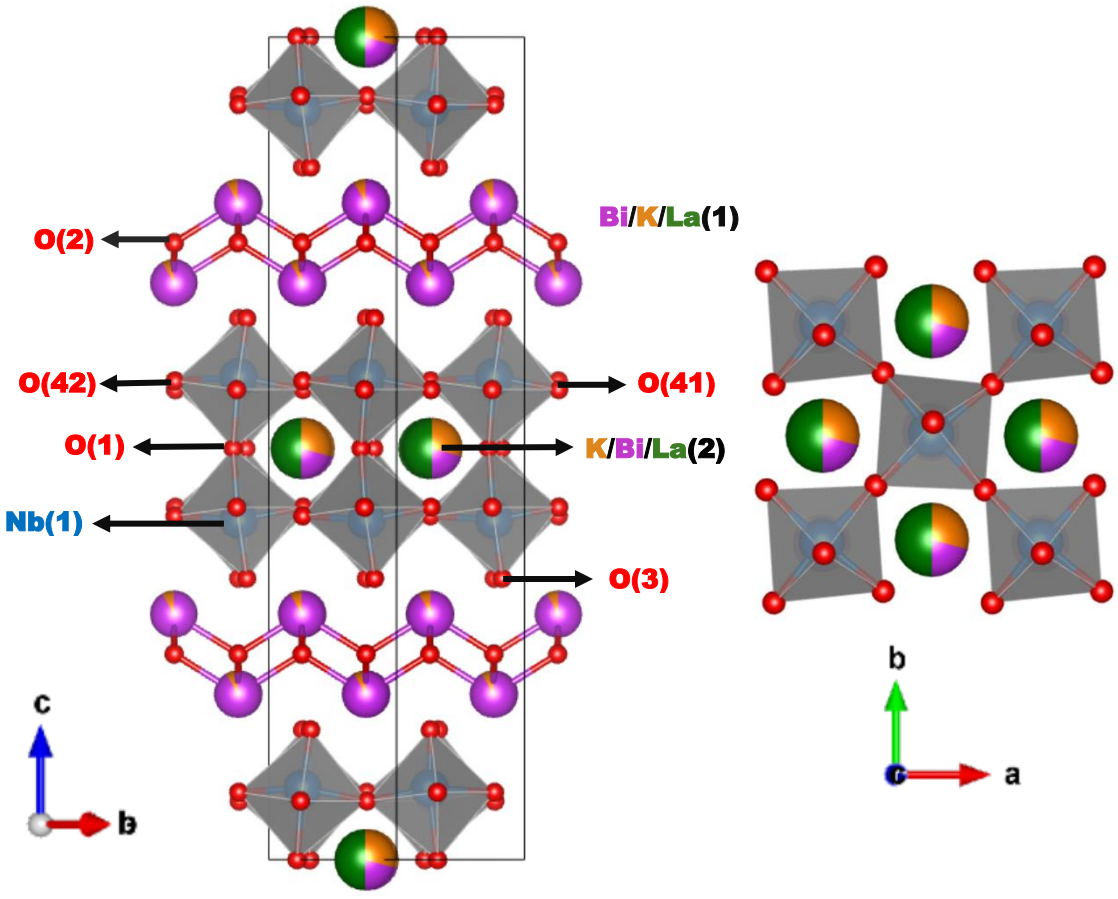

Figure 4.12: Crystal structure of $X_3^- + r_5^- + (X_2^+)$ $A2_1am$ model for $Bi_2K_{0.5}La_{0.5}Nb_2O_9$. Bi, K, La, Nb and O sites are shown in purple, orange, green, blue, and red. NbO_6 are shown in grey.

Table 4.11: Decomposition of *A*2$_1$*am* structure of $Bi_2K_{0.5}La_{0.5}Nb_2O_9$. $O4_\perp$ and $O4_\parallel$ refer to O4 displacements parallel and perpendicular to the *B*-O4 bond, respectively, and $O4_z$ are displacements along [001]. The distortion amplitudes are reported in Å.

Atom	$Bi_2K_{0.5}La_{0.5}Nb_2O_9$ – A21am		
	Γ_5^-	X_3^-	X_2^+
Bi/K/La	-0.03	-0.03	
K/La/Bi	0.00	-0.06	
Nb	-0.02	0.02	
O1	0.04	-0.27	
O2	-0.03	-0.01	0.01
O3	0.25	0.24	
$O4_\perp$	0.02		-0.01
$O4_\parallel$	0.15		0.27
$O4_z$		0.26	
Total	0.29	0.46	0.27

Table 4.12: Structural parameters of $Bi_2K_{0.5}La_{0.5}Nb_2O_9$ from time-of-flight NPD data in space group *A*2$_1$*am.*

Space group: *A*2$_1$*am* (No. 36). Cell parameters: *a* = 5.5172(4) Å, *b* = 5.5175(4) Å, *c* = 25.1685(4) Å. R_{wp} = 4.61%, R_p = 3.28%, χ^2 = 23.52, 131 parameters.

Atom	Wyckoff Site	*x*	*y*	*z*	Occupancy	U_{iso} x 100 (Å^2)
Bi/K/La (1)	8*b*	0.5111(8)	0.2456(5)	0.7014(4)	0.900(4)/ 0.100(3)/0.00	2.00(3)
K/Bi/La (2)	4*a*	0.5*	0.7381(9)	0	0.299(6)/0.20 2(8)/0.499(8)	1.73(4)
Nb(1)	8*b*	0.5113(7)	0.2529(6)	0.0869(4)	1	0.27(1)
O(11)	4*a*	0.021(1)	0.8000(8)	0	1	2.22(9)
O(21)	8*b*	0.759(1)	-0.0011(9)	0.2498(1)	1	0.94(3)
O(31)	8*b*	0.5456(7)	0.2815(8)	0.1579(6)	1	2.22(6)
O(41)	8*b*	0.2587(8)	-0.010(1)	0.57145(7)	1	1.65(5)
O(42)	8*b*	0.7920(7)	0.026(1)	0.0820(8)	1	1.64(6)

* Fixed to define origin of the unit cell along the polar axis.

Table 4.13: Selected bond lengths and bond angles for $Bi_2K_{0.5}La_{0.5}Nb_2O_9$ from time-of-flight NPD data in space group $A2_1am$.

Bond	Bond Length (Å)/Bond Angle (°)	Bond	Bond Length (Å)/Bond Angle (°)
Nb(1)-O(11)	2.206(1)	K/Bi/La(2)-O(42)	2.732(6), 3.022(7)
Nb(1)-O(31)	1.806(2)	Bi/K/La(1)-O(21)	2.291(7), 2.292(7), 2.307(7), 2.323(7)
Nb(1)-O(41)	1.950(7), 2.007(7)	Bi/K/La(1)-O(31)	2.791(5), 2.795(6), 3.158(5), 3.149(6)
Nb(1)-O(42)	1.963(7), 1.994(6)	O(42)-O(41)-O(42)	168.86(1)
K/Bi/La(2)-O(11)	2.549(7), 2.73(1), 2.81(1), 2.969(7)		
K/Bi/La(2)-O(41)	2.574(7), 2.666(7)	O(31)-O(11)-O(31)	166.48(1)

The bond valence sum calculations gave valences: $K(2)_{100\%}$ = +2.432, $La(2)_{100\%}$ = +2.709, $Bi(2)_{100\%}$ = +2.194, Nb(1) = +5.252, $Bi(1)_{100\%}$ = +2.689, $K(1)_{100\%}$ = +2.879 and $La(1)_{100\%}$ = +3.321.

4.3.1.4 Structural Characterisation of $Bi_2K_{0.5}La_{0.5}Ta_2O_9$

Similar to $Bi_2K_{0.5}La_{0.5}Nb_2O_9$, multibank Rietveld refinements were performed to fit the six banks of data for $Bi_2K_{0.5}La_{0.5}Ta_2O_9$ with an aristotype *I*4/*mmm* model.

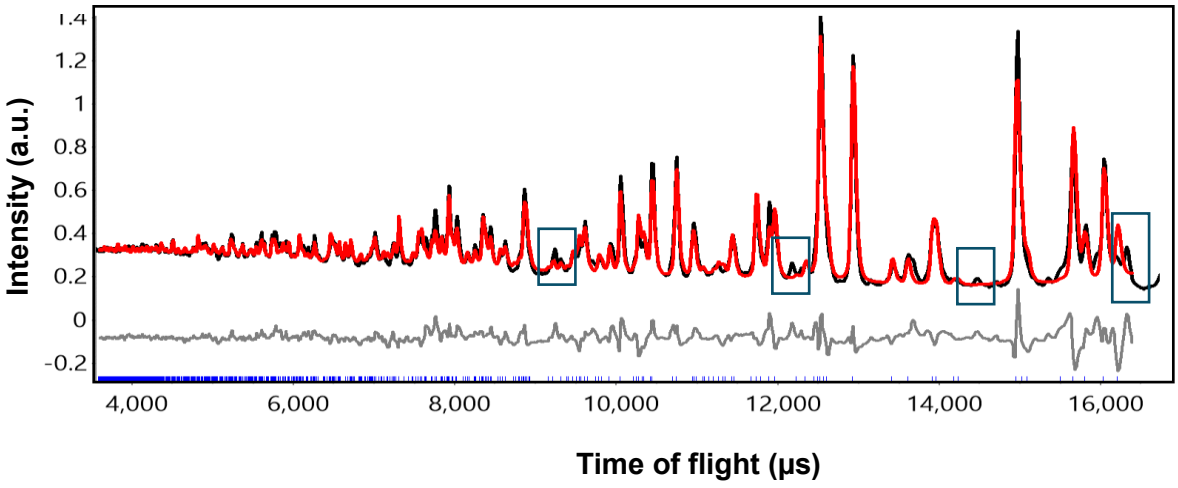

Figure 4.13: Rietveld refinement profile for highest resolution bank 6 data for $Bi_2K_{0.5}La_{0.5}Ta_2O_9$, refined in space group *I*4/*mmm*. The observed, calculated, and difference profiles are shown in black, red, and grey respectively).

The Rietveld refinement profile for bank 6 shows an intensity mismatch and the peaks at 9750, 12175, 14450, and 16350 μs are not fitted by the high symmetry model (**Figure 4.13**).

The *I*4*/mmm* model for $Bi_2K_{0.5}La_{0.5}Ta_2O_9$ also gave an unreasonably high ADP for the oxygen sites within the perovskite block, consistent with the rotations of BO_6 octahedra about both in-plane and out-of-plane axes (**Figure 4.2**). Therefore, lower symmetry models, as described previously were considered.

Table 4.14: Summary of R_{wp} values and number of parameters for the lower symmetry models compared with the parent *I*4/*mmm* model for $Bi_2K_{0.5}La_{0.5}Ta_2O_9$.

Model	R_{wp} (%)	Number of Parameters
Parent *I*4/*mmm*	7.80	108
X_3^- (a,0) *Amam*	6.23	119
X_3^- + Γ_5^- + X_2^+ (a,a|b;0) *A*2$_1$*am*	6.08	130
X_3^- + M_5^- + X_2^+ (a,0|0;b) *Pnam*	6.12	130
X_3^- + M_5^+ + X_1^- (a;0|0;b) *Pnab*	6.15	128
X_3^- + X_2^+ + Γ_3^- (a|b;0|0;c) *Pna*2$_1$	5.98	144

Table 4.14 compares the R_{wp} values and number of parameters of the lower symmetry models with the parent *I*4/*mmm* model. Based on the data, the polar *A*2$_1$*am* and antipolar *Pnam* give comparable fits, but some extra peaks are predicted in *Pnam* which are not allowed for the A-centred model, similar to $Bi_2K_{0.5}La_{0.5}Nb_2O_9$ (Rietveld refinement profile of *Pnam* is provided in **Appendix 2, Section 2.4**). Moreover, the amplitude of Γ_5^- in *A*2$_1$*am* (0.29 Å) is slightly more than the M_5^- amplitude in *Pnam* (0.25 Å). Therefore, the polar *A*2$_1$*am* model is chosen over *Pnam*.

The *Pna*2$_1$ model has the lowest R_{wp}; however, compared *A*2$_1$*am*, the reduction in R_{wp} is only 0.15 %, while the number of parameters increases by 14. Additional peaks, for example: at 1.12 Å (~10175 μs for bank 6) and 1.17 Å (~10650 μs for bank 6) are also predicted by this model (Rietveld refinement profile of *Pna*2$_1$ is provided in **Appendix 2, Section 2.4**). Also, the mode amplitude for Γ_3^- is 0.24 Å, which is slightly smaller than Γ_5^- mode amplitude (0.29 Å). Therefore, the polar X_3^-+

r_5^- (+ X_2^+) *A*2$_1$*am* model is found to be most suitable for $Bi_2K_{0.5}La_{0.5}Ta_2O_9$, consistent with the findings for $Bi_2K_{0.5}La_{0.5}Nb_2O_9$.

Here also two *A*2$_1$*am* models were tested: one assuming no disorder between the Bi_2O_2 layer (8*b*) and *A*-site (4*a*), and another allowing disorder between these sites. The disordered model suggested a K distribution of 0.060(3) in Bi_2O_2 layer (8*b*) and 0.379(6) on *A*-site (4*a*). These values indicate a high disorder and the R_{wp} decreases from 6.78 to 6.69 when disorder was introduced, improving the fit. The K occupancy was then fixed, and X-ray powder diffraction (XRPD) data used to determine the distribution of Bi and La across the two sites. The disordered model with K/Bi/La occupancy of 0.060(3)/0.841(7)/0.099(7) in Bi_2O_2 layer (8*b*) and 0.379(6)/0.32(1)/ 0.30(1) on *A*-site (4*a*) with R_{wp} 6.09% most accurately represents the structure of $Bi_2K_{0.5}La_{0.5}Ta_2O_9$. Rietveld refinement profile for bank 6 in shown in **Figure 4.14**. Refinement profiles for banks 1 through 5 are provided in **Appendix 2, Section 2.4**. The distortion modes amplitudes, refinement details, and selected bond lengths are given in **Table 4.15**, **Table 4.16** and **Table 4.17**.

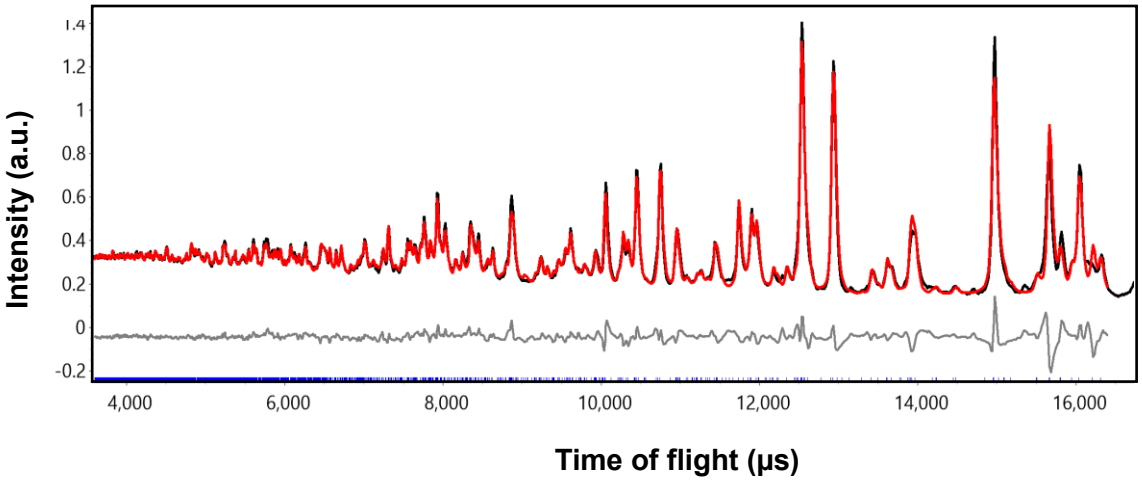

Figure 4.14: Rietveld refinement profile for highest resolution bank 6 data for $Bi_2K_{0.5}La_{0.5}Ta_2O_9$, refined in space group *A*2$_1$*am*. The observed, calculated, and difference profiles are shown in black, red, and grey respectively).

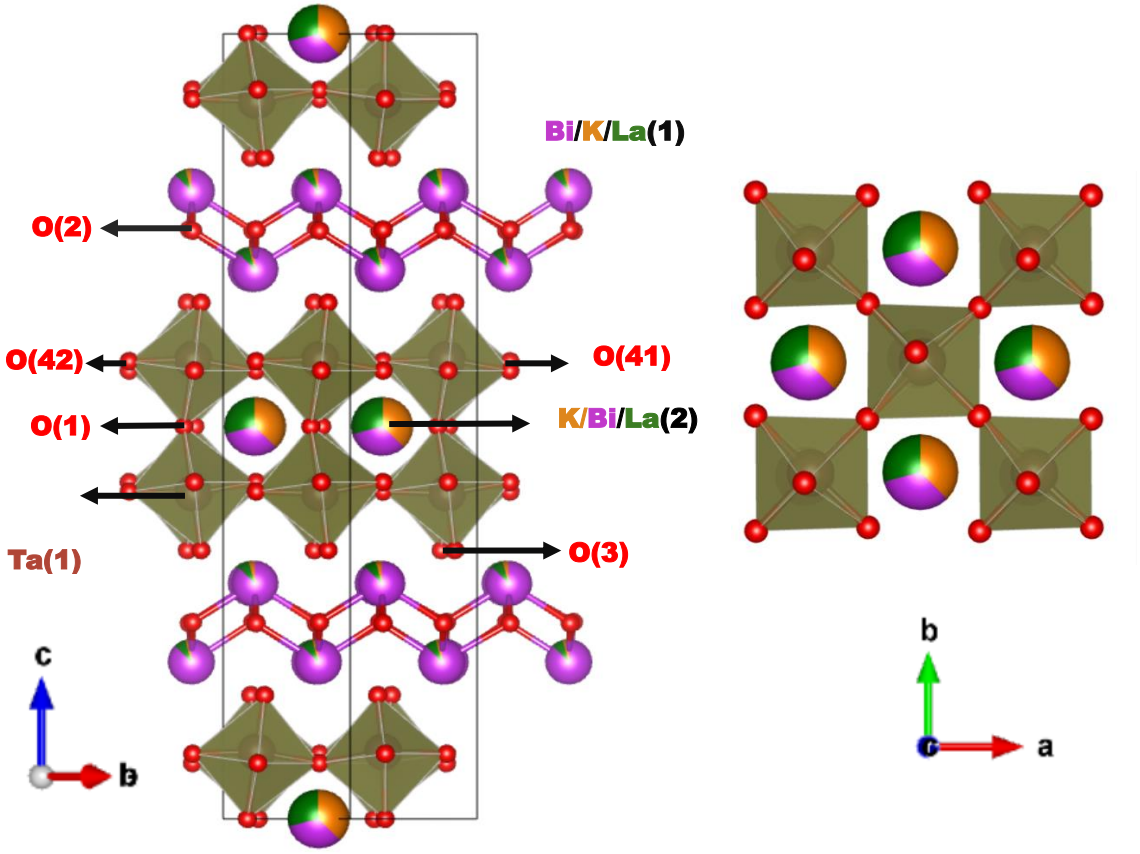

Figure 4.15: Crystal structure of X_3^- + Γ_5^- + (X_2^+) *A*2$_1$*am* model for $Bi_2K_{0.5}La_{0.5}Ta_2O_9$. Bi, K, La, Nb and O sites are shown in purple, orange, green, brown, and red. TaO_6 are shown in golden.

Table 4.15: Decomposition of *A*2$_1$*am* structure of $Bi_2K_{0.5}La_{0.5}Ta_2O_9$. $O4_\perp$ and $O4_\parallel$ refer to O4 displacements parallel and perpendicular to the *B*-O4 bond, respectively, and $O4_z$ are displacements along [001]. The distortion amplitudes are reported in Å.

Atom	**$Bi_2K_{0.5}La_{0.5}Ta_2O_9$**		
	Γ_5^-	X_3^-	X_2^+
Bi/K/La	-0.13	-0.10	
K/La/Bi	0.00	-0.03	
Nb	0.07	0.01	
O1	-0.10	-0.24	
O2	-0.04	-0.03	-0.10
O3	0.15	0.42	
$O4_\perp$	0.06		0.00
$O4_\parallel$	0.17		0.02
$O4_z$		0.29	
Total	0.28	0.58	0.10

Table 4.16: Structural parameters of $Bi_2K_{0.5}La_{0.5}Ta_2O_9$ from time-of-flight NPD data in space group *A*2$_1$*am.*

Space group: *A*2$_1$*am* (No. 36). Cell parameters: *a* = 5.5235(3) Å, *b* = 5.5269(4) Å, *c* = 25.0290(5) Å. R_{wp} = 6.09%, R_p = 4.18%, χ^2 = 32.49, 131 parameters.

Atom	Wyckoff Site	*x*	*y*	*z*	Occupancy	U_{iso} x 100 (Å^2)
Bi/K/La (1)	8*b*	0.4857(8)	0.2365(6)	0.70014(6)	0.841(7)/0.060(3)/0.099(7)	2.48(5)
K/Bi/La (2)	4*a*	0.5*	0.7449(9)	0	0.379(6)/0.32(1)/ 0.30(1)	1.34(4)
Ta(1)	8*b*	0.5113(8)	0.2517(7)	0.0853(6)	1	0.30(2)
O(11)	4*a*	-0.016(1)	0.792(1)	0	1	1.22(9)
O(21)	8*b*	0.7468(9)	0.013(1)	0.2492(1)	1	0.65(4)
O(31)	8*b*	0.521(1)	0.3041(8)	0.1576(9)	1	2.26(7)
O(41)	8*b*	0.265(1)	0.006(1)	0.5710(8)	1	0.70(5)
O(42)	8*b*	0.768(1)	0.008(1)	0.0829(9)	1	0.91(5)

Table 4.17: Selected bond lengths and bond angles for $Bi_2K_{0.5}La_{0.5}Nb_2O_9$ from time-of-flight NPD data in space group *A*2$_1$*am.*

Bond	Bond Length (Å)/Bond Angle (°)	Bond	Bond Length (Å)/Bond Angle (°)
Ta(1)-O(11)	2.155(1)	K/Bi/La(2)-O(42)	2.800(7), 2.931(7)
Ta(1)-O(31)	1.833(3)	Bi/K/La(1)-O(21)	2.436(7), 2.273(7), 2.282(7), 2.292(7)
Ta(1)-O(41)	1.971(8), 1.989(8)	Bi/K/La(1)-O(31)	2.624(6), 2.786(7), 3.153(7), 3.319(6)
Ta(1)-O(42)	1.957(9), 1.967(9)	O(42)-O(41)-O(42)	171.27(9)
K/Bi/La(2)-O(11)	2.557(8), 2.67(1), 2.87(1), 2.974(8)		
K/Bi/La(2)-O(41)	2.569(7), 2.686(7)	O(31)-O(11)-O(31)	163.40(3)

* Fixed to define origin of the unit cell along the polar axis.

The bond valence sum calculations gave valences: $K(2)_{100\%}$ = +2.406, $La(2)_{100\%}$ = +2.681, $Bi(2)_{100\%}$ = +2.171, Ta(1) = +5.211, $Bi(1)_{100\%}$ = +2.689, $K(1)_{100\%}$ = +2.977 and $La(1)_{100\%}$ = +3.317.

Tables 4.3, 4.7 4.11 and **4.15** present the mode amplitudes for the experimentally determined $A2_1am$ structural models for $Bi_2A_{0.5}La_{0.5}B_2O_9$ (*A* = Na, K; *B* = Nb, Ta), revealing the amplitudes of the Γ_5^-, X_3^- and X_2^+ distortions. Among these, the X_3^- distortion (octahedral rotations about an in-plane axis) has the largest amplitude across all four compositions. The majority of the amplitude is primarily due to the displacement of both apical and equatorial BO_6 octahedra oxygens (O4, O3 and O1). The second largest amplitude is of polar Γ_5^- distortion, arising from the displacement of the same BO_6 octahedra oxygens (O4, O3 and O1) relative to the Na/K and Nb/Ta cations. Finally, the smallest amplitude is from the X_2^+ distortion (out-of-plane octahedral rotations) with contributions from the equatorial octahedra oxygens (O4) displacements parallel to the *B*-O4 bond.

4.3.2 First-Principles Calculations for $Bi_2A_{0.5}La_{0.5}B_2O_9$ (*A* = Na, K; *B* = Nb, Ta)

To complement the neutron powder diffraction (NPD) data analysis, geometry optimization calculations were performed within the framework of density functional theory (DFT) for $Bi_2A_{0.5}La_{0.5}B_2O_9$ (*A* = Na, K; *B* = Nb, Ta). The relative energies of

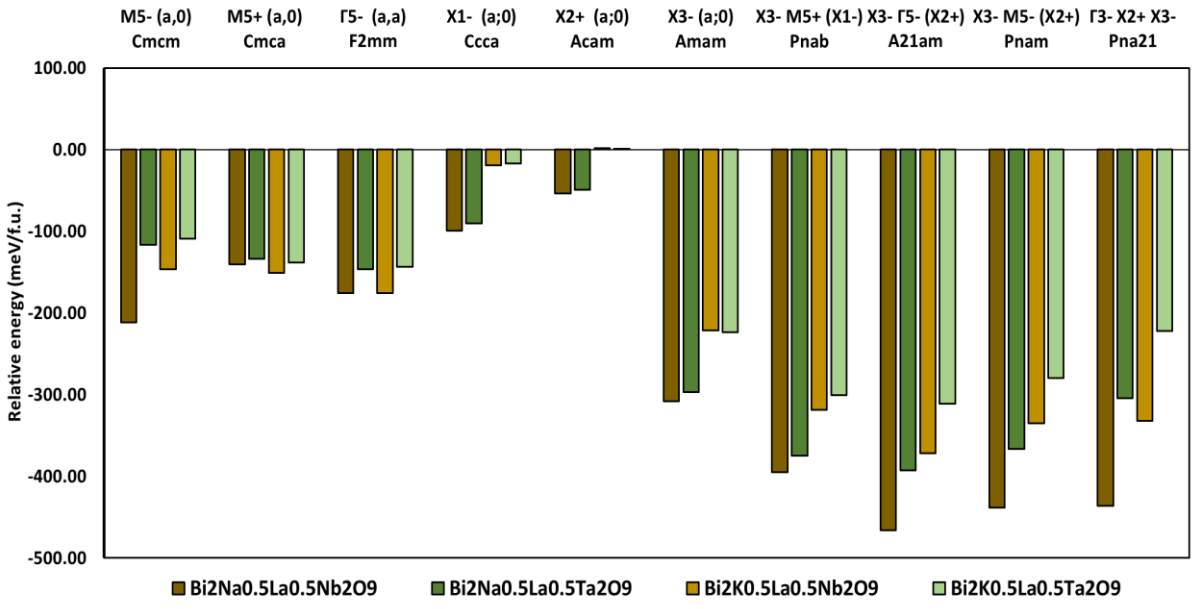

Figure 4.16: Summary of the calculated energies of lower symmetry structures for $Bi_2A_{0.5}La_{0.5}B_2O_9$ (*A* = Na, K; *B* = Nb, Ta) compositions relative to the ideal *I*4/*mmm* structures.

various structural distortions were calculated with respect to the undistorted *I*4/*mmm* parent structures for these compositions (**Figure 4.16**).

The figure above shows that the structures calculated to be low in energy are in good agreement with those determined experimentally from NPD analysis. X_3^- (*Amam*) that describes rotations about an in-plane axis is the single distortion that gives the biggest stabilisation for all compositions. Structures with a combination of a polar/anti-polar distortion with octahedral rotations and tilts about the in-plane and out-of-plane axis, such as Γ_5^- + X_3^- + X_2^+ *A*2$_1$*am*, M_5^- + X_3^- + X_2^+ *Pnam*, M_5^+ + X_3^- + X_1^- *Pnab* and X_3^- + X_2^+ + Γ_3^- *Pna*2$_1$ were found to be the lowest energy models with the energy difference between them being ≤ 35 meV/f.u. These findings highlight the delicate balance between competing polar and antipolar structures in these materials, with *A*2$_1$*am* consistently identified as the calculated ground state.

For $Bi_2Na_{0.5}La_{0.5}B_2O_9$ (*B* = Nb, Ta), the combination of Γ_5^- + X_3^- + X_2^+ gives the largest energy lowering, consistent with the experimental *A*2$_1$*am* model which gives the lowest R_{wp} value. This is also consistent with the space group suggested by Newnham for polar, even-layered Aurivillius phases.[20] A similar *n* = 2 Aurivillius phase $Bi_{2.5}Na_{0.5}B_2O_9$ (*B* = Nb, Ta) with 50/50 occupancy of Bi and Na on *A*- site has also been reported in the same *A*2$_1$*am* space group.[21, 22]

For $Bi_2K_{0.5}La_{0.5}B_2O_9$ (*B* = Nb, Ta), the combination of Γ_5^- + X_3^- + X_2^+ *A*2$_1$*am* gives the largest energy lowering (**Figure 4.16**). From NPD analysis, the antipolar *Pnam* and *A*2$_1$*am* models give comparable fits but in the absence of peaks breaking A-centring (for reflection to be observed, *k* + *l* = 2*n*), the *A*2$_1$*am* experimental model seems more reasonable, consistent with DFT results. The difference in relative energy between *A*2$_1$*am* and *Pnam* models is 36.05 meV/f.u. for $Bi_2K_{0.5}La_{0.5}Nb_2O_9$ and 30.95 meV/f.u. for $Bi_2K_{0.5}La_{0.5}Ta_2O_9$ indicating that *A*2$_1$*am* model is energetically more favourable in both cases. These findings align with the mode decomposition analysis for $Bi_2K_{0.5}La_{0.5}B_2O_9$ (*B* = Nb, Ta). To further validate the results from NPD and DFT analysis and confirm polarity of the room temperature structures of these materials, additional investigations such as variable temperature XRPD and second harmonic generation (SHG) measurements are recommended. Moreover, it would be interesting to explore how substituting larger Rb^+ into the structure can help tune the balance of energies between Γ_5^- or M_5^- displacements and octahedral tilts.

The combination of stronger X_3^- and polar instabilities breaks sufficient symmetry elements to also allow X_2^+ rotations about out-of-plane axis making these phases

proper ferroelectrics. The relative energy of the X_1^- rotation is greater than the X_2^+ rotation across all compositions yet all phases favour the *A*2$_1$*am* symmetry which does not involve the X_1^- distortion because the presence of the X_2^+ distortion appears to be induced by the combined action of the X_3^- and r_5^- distortions. This shows that the stability of the polar *A*2$_1$*am* phase of the investigated materials is due to the coupling of the X_2^+, X_3^- and r_5^- distortion modes.

4.3.3 First-Principles Calculations for $Li_2AB_2O_7$ (*A* = Ca, Sr, Ba; *B* = Nb, Ta)

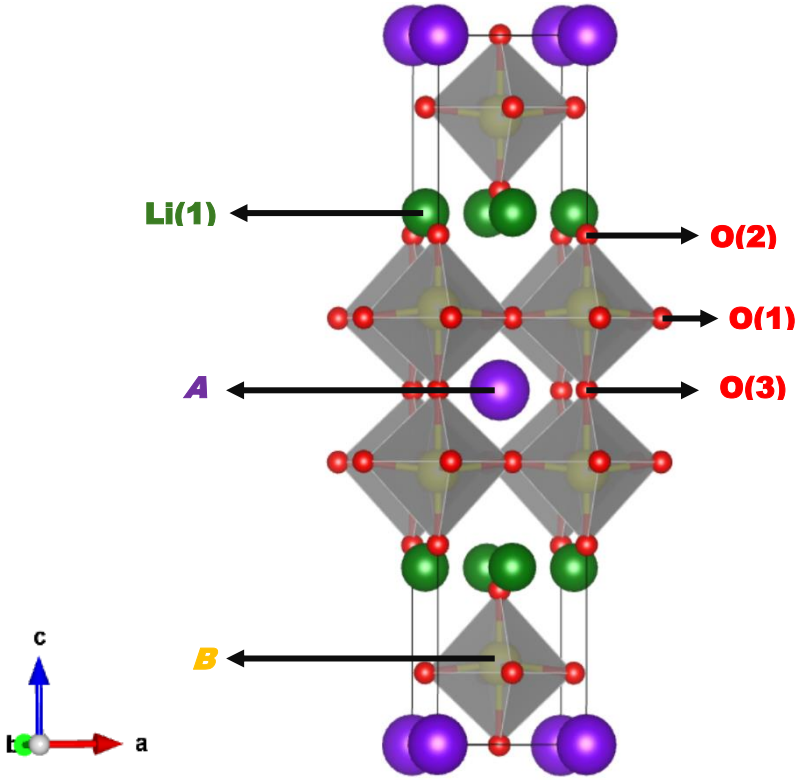

Figure 4.17: High-symmetry tetragonal I4/mmm crystal structure of *n* = 2 $Li_2AB_2O_7$ (*A* = Ca, Sr, Ba; *B* = Nb, Ta) Ruddlesden-Popper phases.

The $Li_2AB_2O_7$ (*A* = Ca, Sr, Ba; *B* = Nb, Ta) are a type of Ruddlesden-Popper (RP) phases characterised by a crystal structure consisting of two ABO_3 perovskite slabs alternating with Li_2O layers. Unlike the thick rock-salt layer found in the conventional *n* = 2 RP phases, the Li_2O layers in these materials are significantly thinner. For this reason, they have also been referred to as pseudo *n* = 2 RP-type structures.[23]

The Li_2O layers is similar to the Bi_2O_2 layers in Aurivillius phases. Both Aurivillius and RP phases adopt an ideal high symmetry paraelectric phase of *I*4/*mmm* symmetry (**Figure 4.17)** suggesting that they are likely to undergo similar structural distortions.[8]

Similar to the Aurivillius Phases, geometry optimization calculations were performed within the framework of density functional theory (DFT) for $Li_2AB_2O_7$ (*A* = Ca, Sr, Ba; *B* = Nb, Ta). The relative energies of various structural distortions were calculated with respect to the undistorted *I4/mmm* parent structures for these compositions (**Figure 4.18**).

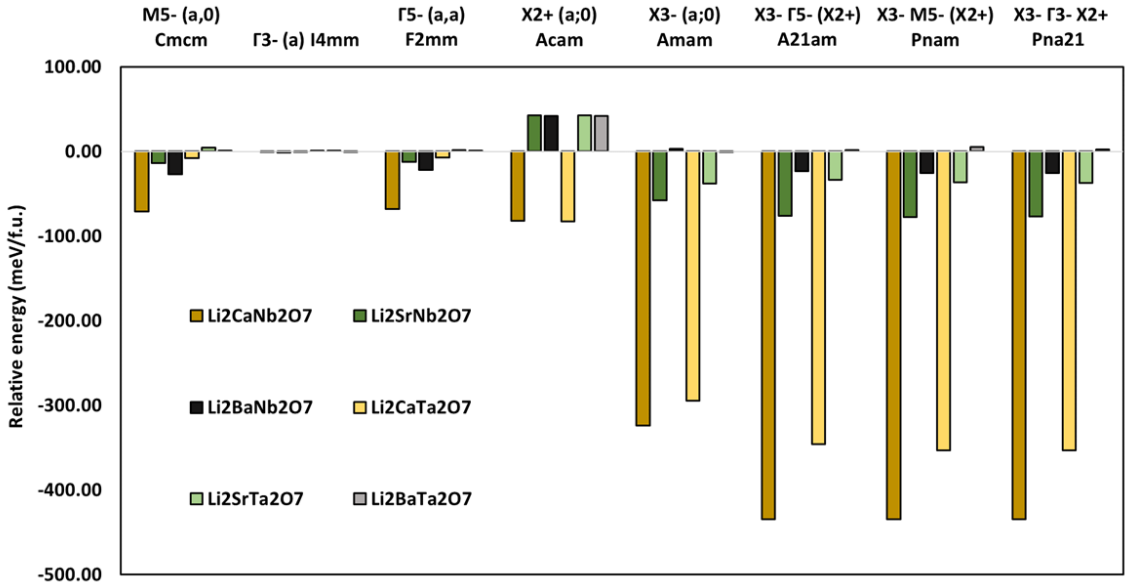

Figure 4.18: Summary of the calculated energies of lower symmetry structures for $Li_2AB_2O_7$ (*A* = Ca, Sr, Ba; *B* = Nb, Ta) compositions relative to the ideal *I*4/*mmm* structures.

Our results are broadly consistent with those reported by K.E. Hasin and E.A. Nowadnick at the end of 2023,[7] although our calculations had already been initiated prior to the release of their study. **Figure 4.18** shows that the relative energies for lower symmetry models for $Li_2BaB_2O_7$ (*B* = Nb, Ta) are notably very small compared to $Li_2AB_2O_7$ (*A* = Ca, Sr; *B* = Nb, Ta). For $Li_2BaNb_2O_7$, the largest energy lowering (~27 meV/f.u.) is for M_5^- *Cmcm* model, suggesting that this is the most appropriate ground state. In contrast, for $Li_2BaTa_2O_7$, the energy lowering from distortions are marginal and within the convergence limit, suggesting it adopts the tetragonal parent *I*4/*mmm* structure.

Similar to the Aurivillius $Bi_2A_{0.5}La_{0.5}B_2O_9$ (*A* = Na, K; *B* = Nb, Ta) phases, our DFT calculations for $Li_2AB_2O_7$ (*A* = Ca, Sr; *B* = Nb, Ta) family show that the single X_3^- (*Amam*) distortion gives the biggest stabilisation. However, structures with a combination of a polar/anti-polar distortion with octahedral rotations and tilts about the in-plane and out-of-plane axis are the lowest energy models, suggesting a close

competition between the polar and antipolar structures in the $Li_2SrNb_2O_7$, $Li_2CaNb_2O_7$ and $Li_2CaTa_2O_7$.

The room-temperature structure of $Li_2SrNb_2O_7$ remains debated in the literature with considerable inconsistency in reported room temperature structures: *A*2$_1$*am*, *Cmcm* and more recently *Pna*2$_1$ (Γ_3^- + X_3^- + X_2^+) space group.[23-26] Our DFT results (**Figure 4.18**), suggest a close competition between the polar *A*2$_1$*am* and antipolar *Pnam* structures, with *Pnam* being 1.48 meV/f.u. lower in energy but within the level of convergence. From mode decomposition we found that the amplitude of M_5^- in *Pnam* (0.38 Å) is larger than Γ_5^- amplitude in *A*2$_1$*am* (0.26 Å), supporting *Pnam* as the more favourable structure for $Li_2SrNb_2O_7$. These findings align with the work of K. Hasin and E. Nowadnick.[7]

Substituting the *A*-site or *B*-site in $Li_2SrNb_2O_7$ can help understand how the balance between the geometric and electronic factors in stabilising the polar ground state can be tuned in this family of Ruddlesden-Popper phases. Ta is known to have a weaker second order Jahn-Teller (SOJT) effect as compared to Nb.[27,28] In $Li_2SrTa_2O_7$, the largest energy lowering is from X_3^- *Amam*, indicating that Ta suppresses in-plane (polar) displacements. The amplitude of M_5^- in *Pnam* is 0.04 Å and Γ_5^- amplitude in *A*2$_1$*am* is 0.01 Å, further supporting that X_3^- *Amam* is the most suitable structure - consistent with previously reports.[7, 27, 29]

Substituting Sr with Ca reduces the perovskite tolerance factor, enhancing both in-plane and out-of-plane rotations of BO_6, as well as polar/antipolar distortions. As shown in **Figure 4.18**, the energy lowerings for $Li_2CaNb_2O_7$ are more significant than those for $Li_2SrNb_2O_7$. Similar to $Li_2SrNb_2O_7$, $Li_2CaNb_2O_7$ also shows a close competition between *A*2$_1$*am* and *Pnam* structures, with *Pnam* again slightly lower in energy (1.13 meV/f.u.) but within the level of convergence. The amplitude of M_5^- in *Pnam* (0.56 Å) is larger than Γ_5^- amplitude in *A*2$_1$*am* (0.44 Å), further supporting *Pnam* as the more favourable structure for $Li_2CaNb_2O_7$. This is also consistent with a previous report.[7] The X_3^- and X_2^+ mode amplitudes are 0.96 Å and 0.56 Å respectively compared to X_3^- and X_2^+ mode amplitudes of 0.66 Å and 0.13 Å in $Li_2SrNb_2O_7$. This demonstrate that the in-plane and out-of-plane rotations of BO_6 and polar/anti distortions increase as the tolerance factor increases i.e., as the size of the *A* cation decreases.

$Li_2CaTa_2O_7$ also demonstrate a close competition *A*2$_1$*am* and *Pnam* structures, with *Pnam* being 7.15 meV/f.u. lower in energy. The amplitude of M_5^- in *Pnam* (0.33 Å) is slightly larger than Γ_5^- amplitude in *A*2$_1$*am* (0.31 Å), once again supporting *Pnam* as the more favourable structure for $Li_2CaTa_2O_7$.

Interestingly, all three compositions - $Li_2SrNb_2O_7$, $Li_2CaNb_2O_7$ and $Li_2CaTa_2O_7$ have been previously reported in *Pna*2$_1$ symmetry.[23, 25, 26, 30-32] From our results, we find that *Pna*2$_1$ is 0.52 meV/f.u., 0.30 meV/f.u. and 0.20 meV/f.u. lower in energy than *Pnam* for $Li_2SrNb_2O_7$, $Li_2CaNb_2O_7$ and $Li_2CaTa_2O_7$ respectively. Mode decomposition analysis shows that the amplitude of the Γ_3^- distortion is very small (~ 0.01 Å) across all three compositions. This suggests that *Pna*2$_1$ may not be the correct ground state model for these compositions.

Finally, we notice from **Figure 4.18,** in $Li_2SrNb_2O_7$ the X_3^- and M_5^-/Γ_5^- distortions couple to induce the X_2^+ distortion which is not intrinsically unstable.[7] In contrast, in $Li_2CaB_2O_7$ (*B* = Nb, Ta) the X_3^- and X_2^+ distortions couple to induce the unstable M_5^-/Γ_5^- distortion. This is due to Ca^{2+} being smaller in size than Sr^{2+} which reduces the perovskite tolerance factor and increases mismatch between the perovskite blocks and the interlayer, introducing greater strain into the system. As a result, stronger octahedral rotations, including both X_3^- and X_2^+, are required to satisfy the bonding within the perovskite blocks and relieve the strain in $Li_2CaB_2O_7$ (*B* = Nb, Ta). Whereas in $Li_2SrNb_2O_7$, the larger *A*-site cation satisfies the bonding requirements through M_5^-/Γ_5^- displacements and X_3^- rotations alone, without necessitating an unstable X_2^+ mode.

This structural distinction suggests that the origin of antiferroelectricity/ferroelectricity in $Li_2SrNb_2O_7$ might be due to the proper mechanism whereas in $Li_2CaB_2O_7$ (*B* = Nb, Ta) it might arise from the hybrid improper mechanism. This can be verified experimentally by monitoring the softening of modes as the transition temperature T_c is approached.

4.3.4 Comparison of Experimental and DFT Results

Table 4.18: Comparison of lattice parameters and distortion mode amplitudes from experimentally-refined models and geometry-optimised computational models for $Bi_2A_{0.5}La_{0.5}B_2O_9$ (*A* = Na, K; *B* = Nb, Ta).

Composition	Symmetry resulting from distortion	Lattice Parameters			Distortion Mode (order parameter direction)	Mode Amplitudes (Å)		
			Exp	DFT			Exp	DFT
$Bi_2Na_{0.5}La_{0.5}Nb_2O_9$	*A*2$_1$*am*	*a*	5.48(1)	5.68	$X_3^- + X_2^+ + \Gamma_5^-$ (a;0|b;0|c,c)	X_3^-	0.64	0.94
		b	5.48(1)	5.63		X_2^+	0.52	0.41
		c	24.84(3)	25.50		Γ_5^-	0.58	0.96
$Bi_2Na_{0.5}La_{0.5}Ta_2O_9$	*A*2$_1$*am*	*a*	5.49(1)	5.63	$X_3^- + X_2^+ + \Gamma_5^-$ (a;0|b;0|c,c)	X_3^-	0.69	0.82
		b	5.48(1)	5.60		X_2^+	0.48	0.32
		c	24.86(3)	25.79		Γ_5^-	0.36	0.63
$Bi_2K_{0.5}La_{0.5}Nb_2O_9$	*A*2$_1$*am*	*a*	5.52(4)	5.72	$X_3^- + X_2^+ + \Gamma_5^-$ (a;0|b;0|c,c)	X_3^-	0.46	0.83
		b	5.51(4)	5.67		X_2^+	0.27	0.25
		c	25.16(4)	25.53		Γ_5^-	0.29	0.87
$Bi_2K_{0.5}La_{0.5}Ta_2O_9$	*A*2$_1$*am*	*a*	5.53(3)	5.66	$X_3^- + X_2^+ + \Gamma_5^-$ (a;0|b;0|c,c)	X_3^-	0.58	0.80
		b	5.52(4)	5.63		X_2^+	0.10	0.14
		c	25.02	25.77		Γ_5^-	0.28	0.86

Table 4.18 compares the lattice parameters and distortion mode amplitudes between the experimental and DFT-relaxed structure for $Bi_2A_{0.5}La_{0.5}B_2O_9$ (*A* = Na, K; *B* = Nb, Ta). The distortion mode amplitude of X_2^+ which correspond to rotation of the BO_6 octahedra about the out-of-plane axis shows an overall good agreement between the experimentally refined and geometry-optimised computational models. However, the amplitude of X_3^- and r_5^- distortion modes which correspond to rotation of the BO_6 octahedra about the in-plane axis and in-plane polar displacement respectively show larger discrepancies. These differences may arise from several factors. First, the DFT calculations are performed on fully ordered models, whereas in the experimental NPD refinements there is disorder between Bi and *A*-site cations across the Bi_2O_2 layer and *A*-cation site. Second, the DFT calculations are performed at 0 K whereas the NPD measurements were collected at room temperature. Finally, the mismatch between the experimental and DFT lattice parameters can influence the calculated amplitudes. The octahedral rotation and polar distortion modes are strongly coupled to strain in the Aurivillius phases. Strain can modify the lattice parameters and interlayer spacing, which in turn influences the octahedral tilts and the in-plane polar displacements thereby altering the mode amplitudes of X_3^- and r_5^- modes. In the table above, the DFT-relaxed structures show larger lattice parameters compared to the experimental values, suggesting a higher strain in the computational models. This enhanced strain leads to increased amplitudes of the X_3^- and r_5^- distortion modes, highlighting the sensitivity of these modes to strain and the strong coupling between structural distortions and strain in these layered oxides.

4.4 Discussion

4.4.1 Investigating the role of the *B*-site cation

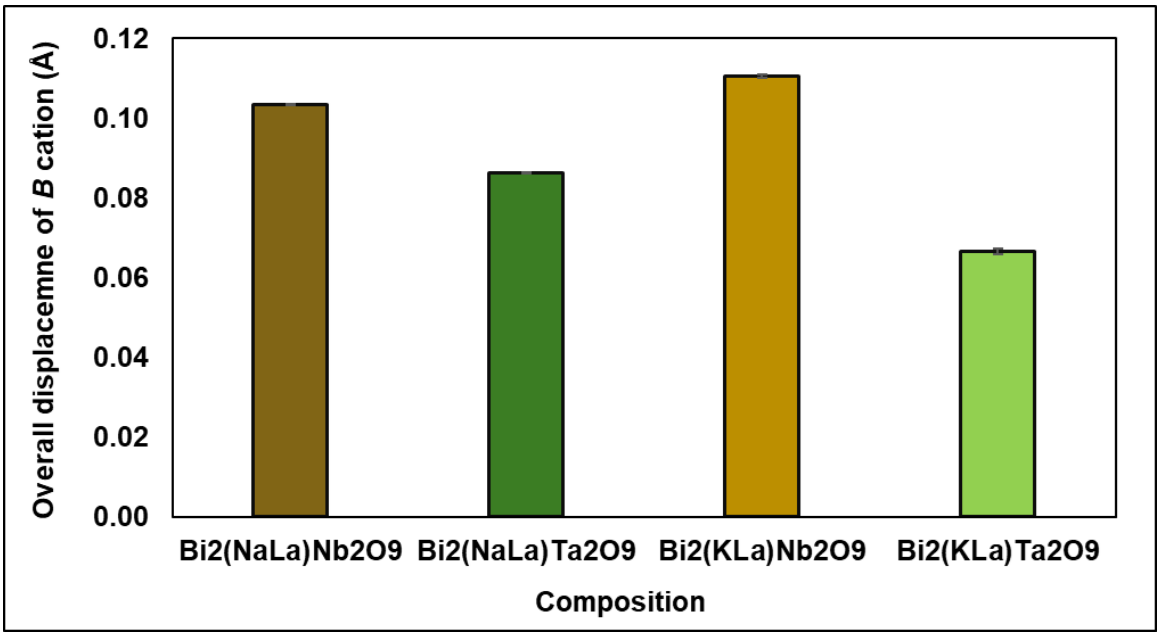

Figure 4.19: Overall displacement of *B* cation from its centre of mass.

Figure 4.19 shows overall displacement of *B* cation from its centre of mass. This displacement can occur along the long axis or along the in-plane axes. The displacement of Nb^{+5} in $Bi_2A_{0.5}La_{0.5}Nb_2O_9$ (*A* = Na, K) from its centre of mass is larger than that of Ta^{+5} in $Bi_2A_{0.5}La_{0.5}Ta_2O_9$ (*A* = Na, K). This follows the general trend that the displacement of Nb > Ta, as Ta is known to have a weaker SOJT effect.[27] It is important to note that the majority of the polar displacement in $Bi_2A_{0.5}La_{0.5}B_2O_9$ (*A* = Na, K; *B* = Nb, Ta) phases is primarily due to the displacement of both apical and equatorial BO_6 octahedra oxygens (O4, O3 and O1) relative to the Na/K and Nb/Ta cations. The difference between the Nb and Ta analogues illustrates the electronic contribution to stabilising the polar ground state.

The geometry optimization calculations can provide insights into the role of second order Jahn-Teller (SOJT) effect on the *B*-site in the *n* = 2 $Bi_2A_{0.5}La_{0.5}B_2O_9$ (*A* = Na, K; *B* = Nb, Ta) phases. From the DFT calculations we see that the relative energies of the Γ_5^- polar motions, M_5^- interblock antipolar motions and M_5^+ intrablock antipolar motions are greater for niobate phases compared to the tantalates, consistent with results from NPD analysis. This is consistent with Nb^{5+} cations having a stronger tendency for SOJT effect than Ta^{5+} cations.[27]

Another notable observation is the shallower energy landscape for Ta-based materials compared to Nb-based and W-based materials.[33] The relative energies of the $A2_1am$, *Pnam* and *Pnab* space groups are closer in the tantalate phases. This suggests that the energy landscape in the $n = 2$ Aurivillius phases can be tuned by selecting the *B*-site cation based on its SOJT tendency - cations with a weaker SOJT effect result in a shallower energy landscape.

4.4.2 Investigating the role of the *A*-site cation

From NPD analysis we find that in $Bi_2K_{0.5}La_{0.5}B_2O_9$ (*B* = Nb, Ta) there is more disorder between the *A*-site and the Bi_2O_2 layer compared to $Bi_2Na_{0.5}La_{0.5}B_2O_9$ (*B* = Nb, Ta). This increased disorder arises from a larger size mismatch between the Bi_2O_2 layer and perovskite layers, which induces strain in the structure. In Aurivillius phases, the perovskite block layer is wider than the Bi_2O_2 layer, and this mismatch becomes more pronounced when a larger cation such as K^+ occupies the *A*-site. Cation disorder helps reduce this mismatch thereby reducing strain. In contrast, smaller cations like Na^+ result in less mismatch and, consequently, less disorder. This is similar to the behaviour seen in $Bi_2ANb_2O_9$ (*A* = Ba, Sr and Ca) and $Bi_{2-x}Sr_{2+x}Ti_{1-x}Nb_{2+x}O_{12}$.[34, 35] Therefore, size mismatch leads to greater cation disorder in the K-containing compounds.

The Goldschmidt tolerance factor, *t*,[36] of the investigated materials can be calculated by neglecting the layered nature of the Aurivillius phases, i.e., approximating the perovskite-like layers as ideal ABO_3 perovskites. This approximation provides an estimate of the degree of distortion but does not indicate the magnitudes or the type of symmetry-lowering distortions (cation displacements, and/or rotations of octahedra) required to optimise the bonding of *A* cation within the perovskite block.[37]

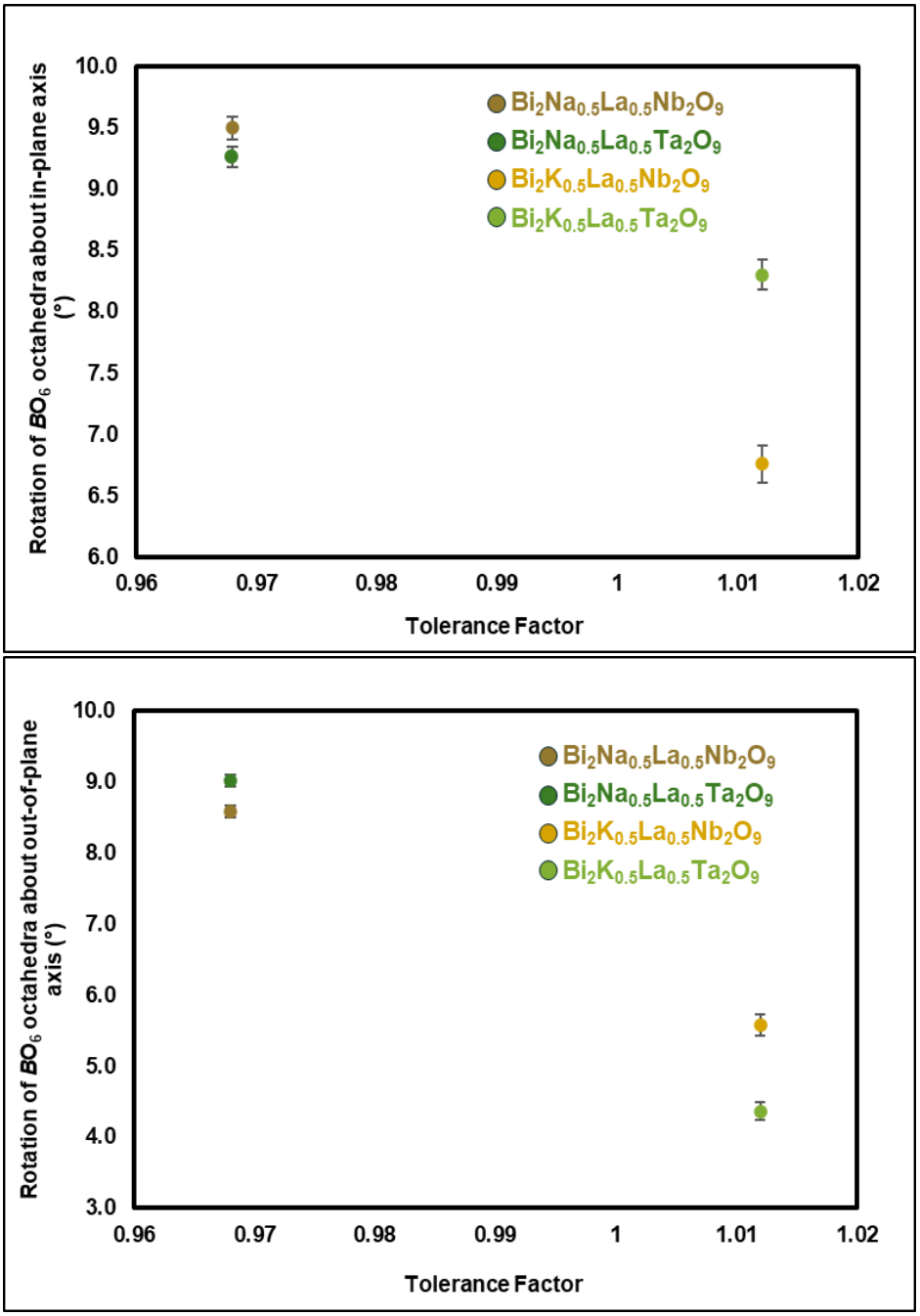

Figure 4.20: Change in the magnitude of octahedral rotation for $Bi_2A_{0.5}La_{0.5}B_2O_9$ (*A* = Na, K; *B* = Nb, Ta) about the in-plane and out-of-plane axis as the size of *A* changes.

The tolerance factors of the hypothetical compositions Na(Nb,Ta)O_3 and K(Nb,Ta)O_3 are calculated as 0.967 and 1.012 respectively since the ionic radii of six-coordinate Nb^{5+} and Ta^{5+} are 0.64 Å.[38] The calculated values suggest that as the size of the A^{2+} ion decreases, the distortions such as rotations of the BO_6 octahedra or polar/antipolar displacements are expected to occur to optimise the bonding of *A* cation within the perovskite blocks.

This trend is evident in our results. The attempts to fit the data using the parent *I*4/*mmm* model suggest that lower symmetry models that would allow rotations about both the in-plane axis (described by X_3^- mode) and the out-of-plane axis (described by X_2^+ mode) are important to explain the structure of the material. The **Figures 4.20** illustrates that tilting/rotation of the octahedra about both the in-plane and out-of-plane axes increases as the size of *A* cation decreases.

The DFT calculations can also be useful in investigating the role of *A*-site cation, helping to understand the role of tolerance factor in $Bi_2A_{0.5}La_{0.5}B_2O_9$ (*A* = Na, K; *B* = Nb, Ta) phases. The results in **Figure 4.12** show that the relative energies of the tilt modes X_3^-, X_2^+ and X_1^- are greater for Na-based materials compared to K-based materials. This is in agreement with tolerance factor values and our experimental analysis, as smaller *A*-site cations require greater octahedral tilting/rotation to optimize bonding within the perovskite blocks. This indicates that geometric factors also play a significant role in stabilising these materials.

The shallowest energy landscape is observed for $Bi_2Na_{0.5}La_{0.5}Ta_2O_9$, which combines the smallest *A*-site cation with the *B*-site cation that has the weakest SOJT effect. This suggests that by carefully considering both geometric and electronic factors, the energy landscapes of the *n* = 2 Aurivillius phases might be tuned. This also suggests that it is perhaps easier to tune between the ground states of $Bi_2Na_{0.5}La_{0.5}Ta_2O_9$ by tuning its composition, compared to the other investigated materials.

4.4.3 Comparison with Ruddlesden-Popper Phases

Aurivillius phases undergo structural distortions similar to those observed in Ruddlesden-Popper phases, as they both adopt an ideal high symmetry paraelectric phase of *I*4/*mmm* symmetry.[8] However, Ruddlesden-Popper phases are well known to be hybrid improper ferroelectrics where octahedral rotations/tilts are the primary distortions and couple with polar/antipolar displacements to stabilise the polar/antipolar structures.[39] Given these similarities, it is natural to draw comparisons between the *n* = 2 Aurivillius phases and the *n* = 2 Ruddlesden-Popper $Li_2AB_2O_7$ (*A* = Ca, Sr, Ba; *B* = Nb, Ta) phases.

In both *n* = 2 Aurivillius phases and Ruddlesden-Popper phases, there exists a close competition between the polar $A2_1am$ and antipolar *Pnam* phases. While the polar $A2_1am$ phase is the ground state and *Pnam* is the metastable state in the Aurivillius

compounds, our DFT results indicate that the antipolar *Pnam* phase is energetically favoured in the Ruddlesden–Popper analogues and $A2_1am$ is the metastable state (as $Li_2SrTa_2O_7$ crystallizes in the nonpolar *Amam* phase, it is excluded from this comparison[7, 27, 29]).

Another key difference is in the energy gains of the individual structural distortions in the two families. In Aurivillius phases, the X_3^- and r_5^-/M_5^- distortions give larger energy gains than the X_2^+ distortion. In contrast, in $Li_2CaB_2O_7$ (*B* = Nb, Ta) Ruddlesden-Popper phases, the X_3^- and X_2^+ distortions give larger energy gains than the r_5^-/M_5^- distortions. This suggets that the appearance of polarization in $Bi_2A_{0.5}La_{0.5}B_2O_9$ (*A* = Na, K; *B* = Nb, Ta) phases is proper whereas it is hybrid improper in $Li_2CaB_2O_7$ (*B* = Nb, Ta) phases.

We also observe trends between the two families of layered perovskites families. As the size of the *A* cation decreases, the amplitude of BO_6 octahedral rotations about both in-plane and out-of-plane axis increases due to decrease in the tolerance factor. The trend of octahedral rotations is: $Li_2CaB_2O_7$ > $Bi_2Na_{0.5}La_{0.5}B_2O_9$ > $Li_2SrB_2O_7$ > $Bi_2K_{0.5}La_{0.5}B_2O_9$ (*B* = Nb, Ta). Another notable trend is in the in-plane displacement of cations relative to anions. In Aurivillius phases, these in-plane displacements are larger than those in Ruddlesden-Popper phases. This is due to greater mismatch between the perovskite blocks and the interlayer in Aurivillius phases, which results in greater strain. To relieve this strain, larger in-plane displacements are required to maintain structural stability.

4.5 Conclusion

This study establishes the role of second order Jahn-Teller (SOJT) effect, cation size and tolerance factor in shaping the structural landscape of the *n* = 2 $Bi_2A_{0.5}La_{0.5}B_2O_9$ (*A* = Na, K; *B* = Nb, Ta) Aurivillius phases and compares them with the *n* = 2 Ruddlesden-Popper $Li_2AB_2O_7$ (*A* = Ca, Sr, Ba; *B* = Nb, Ta) analogues. Through a combined experimental and computational investigation, we report that the Aurivillius phases crystallize in the polar $A2_1am$ structure whereas DFT study on Ruddlesden-Popper phases indicate that the antipolar *Pnam* is more favourable in this family.

Through DFT calculations, we showed that the choice of *B*-site cation influences the energy landscape of these materials such that the cations with weaker SOJT effect result in a shallower energy landscape – Ta^{5+} promotes shallower energy wells than

Nb^{5+}. Similarly, geometric factors, such as cation size and tolerance factor affect the degree of rotations of the BO_6 octahedra about both in-plane and out-of-plane axes. As the *A*-site cation changes from bigger K to smaller Na, the BO_6 octahedral rotations are enhanced. This shows that both electronic and geometric factors play an important role in stabilising the $n = 2$ Aurivillius phases under study.

Among the investigated Aurivillius compounds, $Bi_2Na_{0.5}La_{0.5}Ta_2O_9$ has the shallowest energy landscape. This suggests that by carefully considering both geometric and electronic factors, the energy landscapes of the $n = 2$ Aurivillius phases can be tuned.

We also identified trends in octahedral rotation amplitudes and in-plane cation displacements in the $n = 2$ Aurivillius phases and Ruddlesden-Popper phases. Aurivillius phases, with greater mismatch between the perovskite block and Bi_2O_2 layer, exhibit larger in-plane displacements to relieve internal strain. These trends show how geometric and electronic factors can effectively control the balance of structural instabilities and polarization mechanisms in layered perovskite related materials.

This study provides a detailed understanding of the role geometric and electronic factors in determining the structure-composition relationship in the $n = 2$ Aurivillius phases. These insights pave the way for designing property optimised $n = 2$ Aurivillius phases for ferroelectric and photocatalytic applications.

1. N. A. Benedek, J. M. Rondinelli, H. Djani, P. Ghosez and P. Lightfoot, *Dalton Transactions*, 2015, **44**, 10543-10558.
2. C. H. Hervoches and P. Lightfoot, *Chemistry of materials*, 1999, **11**, 3359-3364.
3. N. C. Hyatt, I. M. Reaney and K. S. Knight, *Physical Review B—Condensed Matter and Materials Physics*, 2005, **71**, 024119.
4. P. Boullay, J. Tellier, D. Mercurio, M. Manier, F. J. Zúñiga and J. Perez-Mato, *Solid state sciences*, 2012, **14**, 1367-1371.
5. A. O. A. Onodera, T. K. T. Kubo, K. Y. K. Yoshio, S. K. S. Kojima, H. Y. H. Yamashita and T. T. T. Takama, *Japanese Journal of Applied Physics*, 2000, **39**, 5711.
6. A. Snedden, C. H. Hervoches and P. Lightfoot, *Physical Review B*, 2003, **67**, 092102.
7. K.-E. Hasin and E. A. Nowadnick, *Physical Review Materials*, 2023, **7**, 124402.
8. K. Aleksandrov and J. Bartolome, *Journal of Physics: Condensed Matter*, 1994, **6**, 8219.
9. B. J. Campbell, H. T. Stokes, D. E. Tanner and D. M. Hatch, *Journal of Applied Crystallography*, 2006, **39**, 607-614.
10. W. Williams, R. Ibberson, P. Day and J. Enderby, *Physica B: Condensed Matter*, 1997, **241**, 234-236.
11. H. M. Rietveld, *Applied Crystallography*, 1969, **2**, 65-71.
12. A. A. Coelho, *Coelho Software, Brisbane, Australia*, 2007.
13. A. Coelho, *Karlsruhe, Germany*, 2012.
14. S. J. Clark, M. D. Segall, C. J. Pickard, P. J. Hasnip, M. I. Probert, K. Refson and M. C. Payne, *Zeitschrift für kristallographie-crystalline materials*, 2005, **220**, 567-570.
15. D. Vanderbilt, *Physical review B*, 1990, **41**, 7892.
16. J. P. Perdew, K. Burke and M. Ernzerhof, *Physical review letters*, 1996, **77**, 3865.
17. V. F. Sears, *Neutron news*, 1992, **3**, 26-37.
18. N. Brese and M. O'keeffe, *Acta Crystallographica Section B: Structural Science*, 1991, **47**, 192-197.
19. I. D. Brown and D. Altermatt, *Acta Crystallographica Section B: Structural Science*, 1985, **41**, 244-247.
20. R. Newnham, R. Wolfe and J. Dorrian, *Materials Research Bulletin*, 1971, **6**, 1029-1039.
21. S. Borg and G. Svensson, *Journal of Solid State Chemistry*, 2001, **157**, 160-165.
22. S. Borg, G. Svensson and J.-O. Bovin, *Journal of solid state chemistry*, 2002, **167**, 86-96.
23. Y. Mochizuki, T. Nagai, H. Shirakuni, A. Nakano, F. Oba, I. Terasaki and H. Taniguchi, *Chemistry of Materials*, 2021, **33**, 1257-1264.
24. R. Uppuluri, H. Akamatsu, A. Sen Gupta, H. Wang, C. M. Brown, K. E. Agueda Lopez, N. Alem, V. Gopalan and T. E. Mallouk, *Chemistry of Materials*, 2019, **31**, 4418-4425.
25. T. Nagai, H. Shirakuni, A. Nakano, H. Sawa, H. Moriwake, I. Terasaki and H. Taniguchi, *Chemistry of Materials*, 2019, **31**, 6257-6261.
26. X. Xu, F. T. Huang, K. Du and S. W. Cheong, *Advanced Materials*, 2022, **34**, 2206022.
27. T. Nagai, Y. Mochizuki, H. Shirakuni, A. Nakano, F. Oba, I. Terasaki and H. Taniguchi, *Chemistry of Materials*, 2020, **32**, 744-750.
28. P. M. Woodward, P. Karen, J. S. Evans and T. Vogt, *Solid state materials chemistry*, Cambridge University Press, 2021.
29. T. Pagnier, N. Rosman, C. Galven, E. Suard, J. Fourquet, F. Le Berre and M.-P. Crosnier-Lopez, *Journal of Solid State Chemistry*, 2009, **182**, 317-326.
30. C. Galven, D. Mounier, B. Bouchevreau, E. Suard, A. Bulou, M.-P. Crosnier-Lopez and F. o. L. Berre, *Inorganic Chemistry*, 2016, **55**, 2309-2323.
31. A. Nakano, H. Shirakuni, T. Nagai, Y. Mochizuki, F. Oba, H. Yokota, S. Kawaguchi, I. Terasaki and H. Taniguchi, *Physical Review Materials*, 2022, **6**, 044412.
32. B. Zhang, Z. Hu, B. Chen, X. Liu and X. Chen, *Journal of Materiomics*, 2020, **6**, 593-599.
33. H. Djani, E. E. McCabe, W. Zhang, P. S. Halasyamani, A. Feteira, J. Bieder, E. Bousquet and P. Ghosez, *Physical Review B*, 2020, **101**, 134113.
34. S. M. Blake, M. J. Falconer, M. McCreedy and P. Lightfoot, *Journal of Materials Chemistry*, 1997, **7**, 1609-1613.
35. C. H. Hervoches and P. Lightfoot, *Journal of Solid State Chemistry*, 2000, **153**, 66-73.

36. V. M. Goldschmidt, *Naturwissenschaften*, 1926, **14**, 477-485.
37. J. Y. Lee, S. Ling, S. P. Argent, M. S. Senn, L. Cañadillas-Delgado and M. J. Cliffe, *Chemical Science*, 2021, **12**, 3516-3525.
38. R. D. Shannon, *Acta crystallographica section A: crystal physics, diffraction, theoretical and general crystallography*, 1976, **32**, 751-767.
39. N. A. Benedek and C. J. Fennie, *Physical review letters*, 2011, **106**, 107204.

Chapter 5: Tuning Octahedral Tilts in Ruddlesden–Popper Phases via Fluorination

5.1 Introduction

Fluoride ions can be inserted into Ruddlesden-Popper (RP) phases by insertion into interstitial sites which is accompanied by oxidation of the metal lattice.[1, 2] In materials where the cations are more reluctant to oxidation, or if less oxidising reagents are used, substitution reactions, where one O^{2-} ion is replaced by two F^- ions occur, with one of the fluoride ions occupying an interstitial position.[3] Fluorination can be achieved using agents such as polyvinylidene fluoride (PVDF), CuF_2 and F_2(g). F_2(g) and CuF_2 are powerful oxidising agents which lead to fluoride ion insertion by oxidising the cations in the solid precursor.[4, 5] Adding extra anions to the interstitial sites in the rocksalt layers results in the formation of a fluorite-like layer, analogous to the $[Bi_2O_2]^{2+}$ layer in the Aurivillius phases discussed in the previous chapter.

In Ruddlesden-Popper phases, as discussed in **Section 1.3.6**, cooperative tilting distortions can be used to break the inversion symmetry and induce ferroelectric behaviour. However, the stabilisation of the desired $A2_1am$ ($a^-a^-c^+/a^-a^-c^+$) phase is limited to compositions with very small tolerance factors, limiting the scope of this symmetry breaking approach.[6]

Fluorination of RP phases offers a means to modify the twisting of octahedra, particularly around the long crystallographic axis. R. Zhang et.al. used this approach to show that by converting $La_3Ni_2O_7$ to $La_3Ni_2O_{5.5}F_{3.5}$, the tilt pattern changes from ($a^-a^-c^0/a^-a^-c^0$) to ($a^-a^-c^+/a^-a^-$-(c^+). Although this locally breaks inversion symmetry, the resulting structure is antipolar with *Pnma* symmetry.[7] While this did not achieve the desired result, it validates the underlying concept and motivates further investigation into the fluorination of other RP compounds to explore the potential stabilisation of a polar ground state.

This chapter investigates the effect of fluorination on the n = 2 $La_2SrFe_2O_7$ Ruddlesden-Popper phases. $La_2SrFe_2O_7$ has been reported to crystallise in $I4/mmm$ space group.[8, 9] As mentioned above, inserting fluoride can help induce tilting of the octahedra which can help in breaking the inversion symmetry and potentially stabilising a polar ground state. Through this study, we aim to understand

how fluorination influences the structure of $La_2SrFe_2O_7$ and evaluate its potential for polar behaviour.

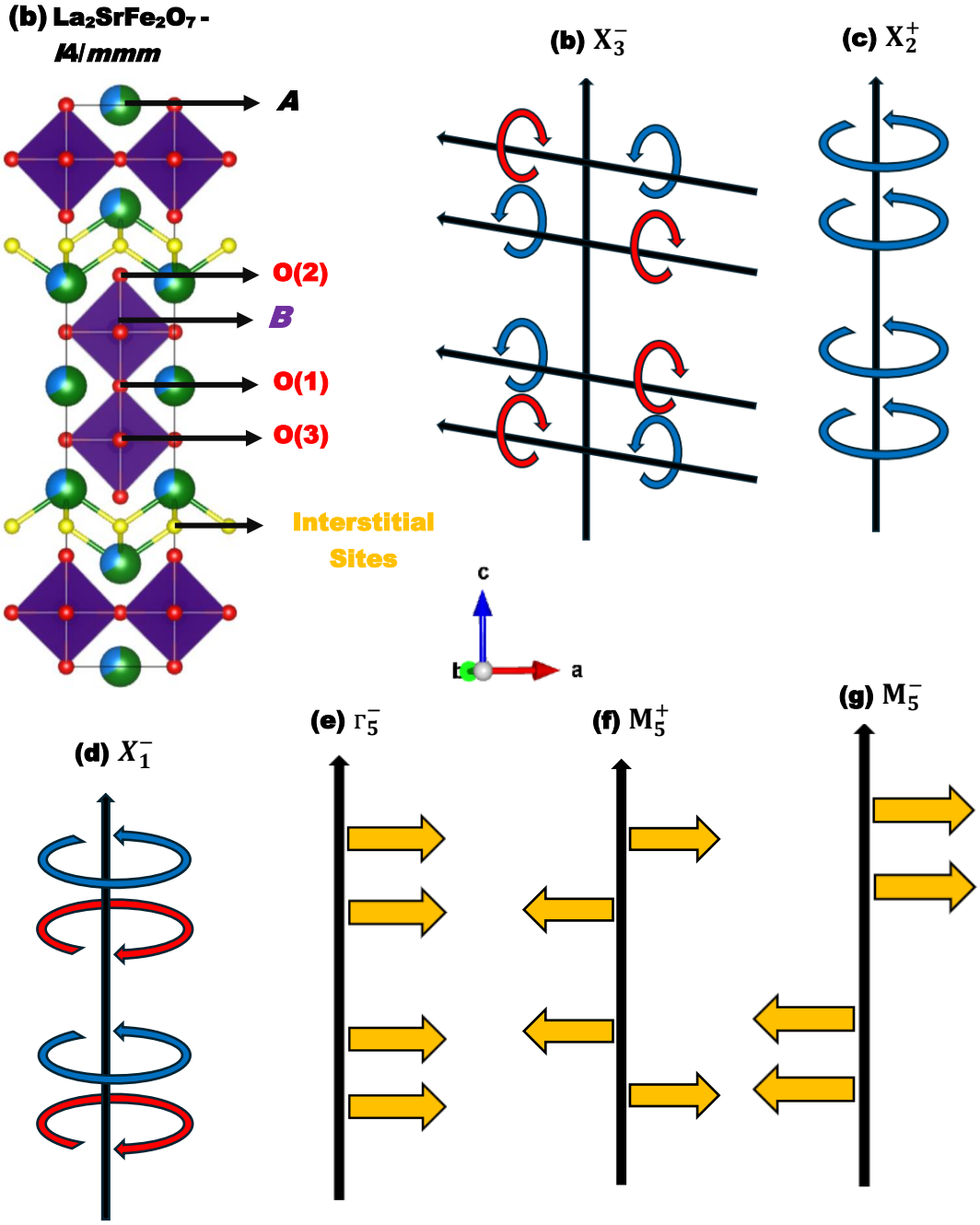

Figure 5.1: (a) High-symmetry tetragonal *I*4/*mmm* crystal structure of *n* = 2 $La_2SrFe_2O_7$ RP phase. Schematic illustration of (b) X_3^- in-plane octahedral rotation mode, (c), (d) X_2^+ and X_1^- out-of-plane octahedral rotation modes, (e) polar r_5^- displacive mode and (f), (g) antipolar M_5^+ and M_5^- displacive modes.

Figure 5.1 above shows the schematic illustration of the key displacive distortion modes observed in the *n* = 2 RP phases. The X_3^- mode corresponds to the in-plane octahedral tilts. The X_1^- (out-of-phase) and X_2^+ (in-phase) modes represent the out-of-plane octahedral rotations. The r_5^- mode describes the in-plane polar displacive distortions while M_5^+ and M_5^- are in anti-polar distortion modes.

5.2 Methods

5.2.1 Synthesis

The Ruddlesden-Popper phase $La_2SrFe_2O_7$ was synthesised by Dr Emma McCabe via the conventional solid-state reaction method. Stoichiometric amounts of high-purity La_2O_3, $SrCO_3$ and Fe_2O_3 were thoroughly ground together and heated at 1350 °C for 12 hours, followed by further heating at 1375 °C for 24 hours, with intermittent grinding to ensure homogeneity. Fluorination of $La_2SrFe_2O_7$ was first attempted using CuF_2(s) as the fluorinating agent. The reactions were carried at temperatures between 250 °C and 300 °C, with several 12-hour heating cycles and intermediate grinding. A single oxide-fluoride phase was obtained after heating with excess CuF_2(s) at 300 °C. However, CuO was observed as a byproduct.

To obtain phase-pure material, fluorination using a 10% F_2 / 90% N_2 gas mixture was done. This required harsher conditions: fluorination at 290 °C in flowing F_2 for 6 hours followed by static F_2 for an additional 12 hours. The resulting fine black powder was free from CuO contamination.

5.2.2 Analysis of Neutron Powder Diffraction (NPD) data

The NDP data were collected on the Polaris diffractometer by Dr Emma McCabe and Prof. C. Greaves, prior to the instrument upgrade. The data were analysed using the Rietveld method[10] in the Topas Academic software.[11, 12]

5.3 Results

5.3.1 Structural Characterisation of $La_2SrFe_2O_7F_2$

Rietveld refinements were carried out to fit the neutron powder diffraction data collected from a fluorinated sample of $La_2SrFe_2O_7$, henceforth referred to as $La_2SrFe_2O_7F_2$, with an aristotype *I*4*/mmm* model. The refinement profile shows that the peaks such as 4750, 4900, 5700, 7600, 9800, 145000 μs are not fitted by this model (**Figure 5.2**).

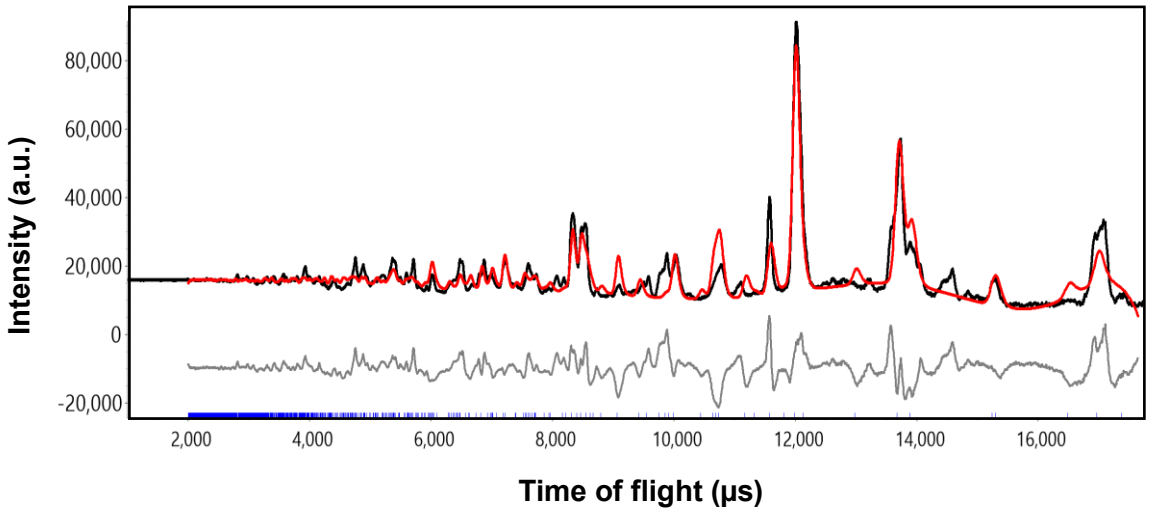

Figure 5.2: Rietveld refinement profile for $La_2SrFe_2O_7F_2$ refined in space group *I*4/*mmm*. The observed, calculated, and difference profiles are shown in black, red, and grey respectively).

Moreover, the model gave unreasonably high atomic displacement parameter (ADP) for the central equatorial oxygen site O(3) and apical oxygens O(1) and O(2). Allowing the ADPs to refine anisotropically suggested rotation of the BO_6 octahedra about the long axis as well as an in-plane axis. Therefore, models that allow the rotation of the octahedra about both the out-of-plane axis, described by X_1^- and X_2^+ modes, and in-plane axis, described by X_3^- mode, were considered. The lower symmetry models considered were *A*2$_1$*am* ($X_3^- + X_2^+ + \Gamma_5^-$), *Pnam* ($X_3^- + X_2^+ + M_5^-$), and *Pnab* ($X_3^- + X_1^- + M_5^+$). The space group setting for *Cmc*2$_1$, *Pnma* and *Pbcn* have been changed to *A*2$_1$*am, Pnam* and *Pnab* respectively to have long axis along *c*. We will be using these non-standard settings from here on. **Table 5.1** compares the R_{wp} values and number of parameters of the lower symmetry models with the parent *I*4/*mmm* model. Given the very similar neutron scattering cross sections of oxide and fluoride (O = 5.80(4) fm, F = 5.65(1) fm)[13] no attempt was made to differentiate between the two anions at this stage.

Table 5.1: Summary of R_{wp} values and number of parameters for the lower symmetry models compared with the parent *I*4/*mmm* model for $La_2SrFe_2O_7F_2$.

Model	R_{wp} (%)	Number of Parameters
Parent *I*4/*mmm*	14.62	23
X_3^- (a,0) *Amam*	10.99	45
X_3^- + r_5^- + X_2^+ (a,a|b;0) *A*2$_1$*am*	9.85	59
X_3^- + M_5^- + X_2^+ (a,0|0;b) *Pnam*	9.45	59
X_3^- + M_5^+ X_1^- (a;0|0;b) *Pnab*	10.45	51

Based on the data presented in the table above, the anti-polar *Pnam* (X_3^- + X_2^++ M_5^-) model is found to be most suitable for $La_2SrFe_2O_7F_2$ (**Figure 5.4**). This is consistent with the structure reported by R. Zhang et al. for fluorinated $La_3Ni_2O_7$ Ruddlesden-Popper phase.[7] Rietveld refinement profiles for the *Pnam* model are shown in **Figure 5.3**.

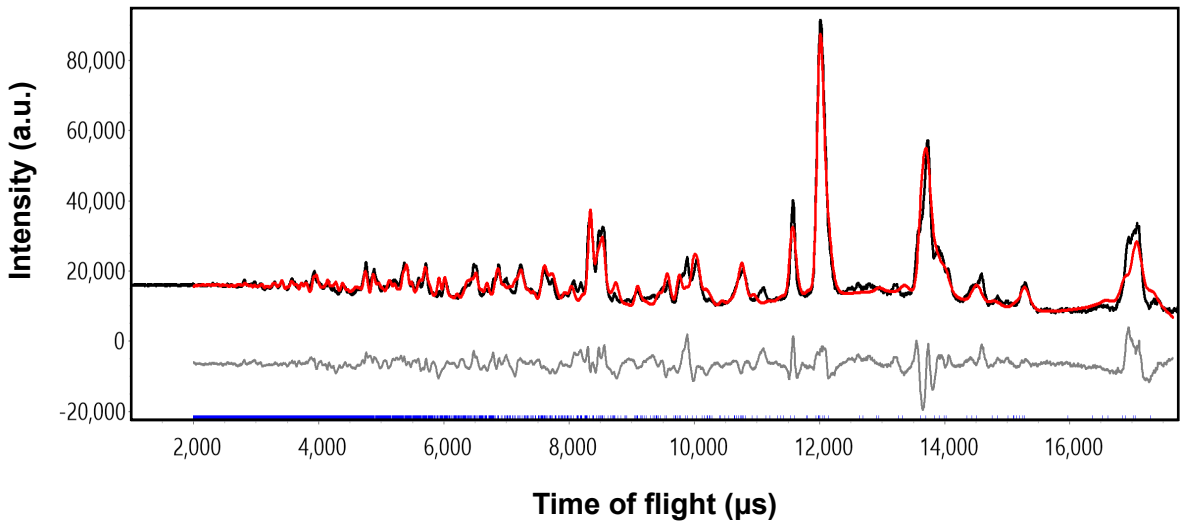

Figure 5.3: Rietveld refinement profile for $La_2SrFe_2O_7F_2$ refined in space group *Pnam*. The observed, calculated, and difference profiles are shown in black, red, and grey respectively).

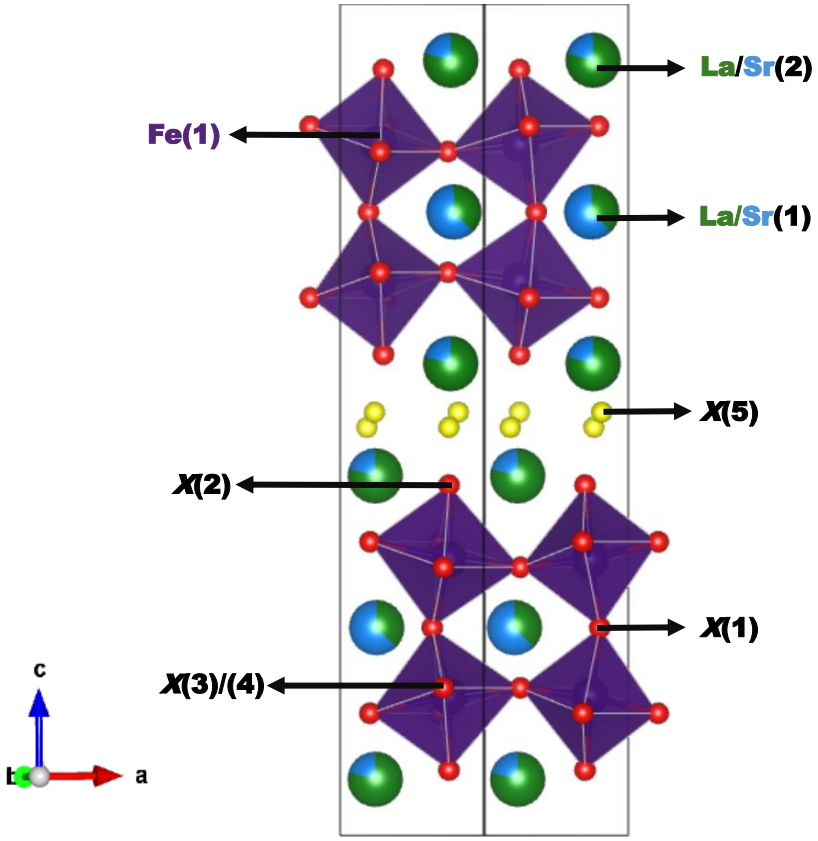

Figure 5.4: Crystal structure of *Pnam* model for $La_2SrFe_2O_7F_2$. La, Sr, Fe, O and F sites are shown in green, blue, purple, red, and yellow. FeX_6 octahedra are shown in purple.

The ADPs for the two La/Sr sites, 12-coordinated perovskite *A*-site (4*c*) and interlayer site (8*d*), were very high, prompting refinement of their occupancies (with constraints to maintain sample stoichiometry). The refinement results suggested a La:Sr distribution of 0.81(7):0.18(7) in the interlayer layer (8*d*) and 0.37(1):0.62(1) at the perovskite *A*-site (4*c*).

5.4 Discussion

The structure of $La_2SrFe_2O_7F_2$, determined using the NPD data, has an additional tetrahedral anion coordination site within the "rocksalt" layer. This distinguishes it from the parent $La_2SrFe_2O_7$ phase and is consistent with the structure observed in other topochemically fluorinated n = 2 Ruddlesden−Popper oxides.[14, 15] The larger Sr^{2+} cations preferentially occupy the larger 12-coordination site within the perovskite layers (4*c*) rather than the lower-coordinate 8*d* sites in the rocksalt layers.

As mentioned above, due to very similar X-ray and neutron scattering lengths of O^{2-} and F^-, the direct determination of the oxide/ fluoride distribution from diffraction data is not possible. However, it is possible to deduce the oxide/fluoride distributions using bond valence sums (BVS) as an indicator of which anion sites would most

favourably accommodate the fluorine atoms. **Table 5.2** shows the BVS for the five distinct anion sites in $La_2SrFe_2O_7F_2$ structure, calculated assuming as if each site is either occupied by oxide or fluoride ions.

Table 5.2 suggets that the apical anion site *X*(2) is occupied by fluoride ions. A similar anion distribution is observed in the structure of $Sr_3(Fe_{0.5}Ru_{0.5})_2O_{5.5}F_{3.5}$.[14] The BVS for *X*(3) suggests there could be partial occupancy of either fluoride or oxide ions, but bond lengths suggest that the site is occupied by oxide ions. The BVS for *X*(4) and *X*(5) anion sites suggest oxide ions occupancy.

The BVS for apical *X*(1) anion site is very high for both fluorine and oxide ion. This may indicate partial occupancy, static disorder or limitations in diffraction data quality. Further investigation using better quality data, or complementary characterisation methods example solid-state NMR might be necessary to resolve the true structure.

The refinement details and selected bond lengths are given in **Table 5.3** and **Table 5.4**.

Table 5.2: Anion bond valence sums for $La_2SrFe_2O_7F_2$.

$La_2SrFe_2O_7F_2$		
Anion	**BVS (F)**	**BVS (O)**
X(1)	1.910	2.611
X(2)	0.947	1.318
X(3)	1.337	1.810
X(4)	1.495	1.988
X(5)	1.270	1.915

Table 5.3: Structural parameters of $La_2SrFe_2O_7F_2$ from NPD data in space group *Pnam*. ADP values are constrained to be equal for all sites.

Space group: *Pnam* (No. 62). Cell parameters: *a* = 5.549(4) Å, *b* = 5.492(4) Å, *c* = 22.551(17) Å. R_{wp} = 9.45%, R_p = 6.39%, χ^2 = 2.75, 59 parameters.

Atom	Wyckoff Site	*x*	*y*	*z*	Occupancy	U_{iso} x 100 (Å^2)
La/Sr(1)	4*c*	0.769(4)	0.022(3)	0.25	0.37(1)/ 0.62(1)	0.69(8)
La/Sr(2)	8*d*	0.763(2)	0.006(2)	0.0675(2)	0.81(6)/ 0.18(7)	0.69(8)
Fe(1)	8*d*	0.745(2)	0.009(1)	0.833(2)	1	0.69(8)
O(1)	4*c*	0.778(4)	0.418(3)	0.25	1	0.69(8)
F(2)	8*d*	0.729(3)	0.028(2)	-0.079(4)	1	0.69(8)
O(3)	8*d*	-0.052(2)	0.738(3)	0.853(4)	1	0.69(8)
O(4)	8*d*	0.487(3)	0.234(4)	0.823(4)	1	0.69(8)
O(5)	8*d*	0.029(3)	0.789(3)	0.009(5)	1	0.69(8)

Table 5.4: Selected bond lengths and bond angles for $La_2SrFe_2O_7F_2$ from NPD data in space group *Pnam*.

Bond	Bond Length (Å)/Bond Angle (°)	Bond	Bond Length (Å)/Bond Angle (°)
Fe(1)-O(1)	1.932(7)	La/Sr(1)-O(4)	2.58(3), 2.65(3)
Fe(1)-F(2)	2.007(1)	La/Sr(2)-F(2)	2.64(1), 2.75(3), 2.84(3), 2.88(1)
Fe(1)-O(3)	1.92(1), 2.19(1)	La/Sr(2)-O(3)	2.49(1), 2.78(1)
Fe(1)-O(4)	1.91(3), 1.96(3)	La/Sr(2)-O(4)	3.13(1), 3.21(1)
La/Sr(1)-O(1)	2.18(3), 2.74(4), 2.82(4), 3.32(3)	La/Sr(2)-O(5)	2.31(1), 2.36(1), 2.46(1), 2.83(1)
		F(2)-O(1)-F(2)	162.2(6)
La/Sr(1)-O(3)	2.88(1), 3.10(1)	O(3)-O(4)-O(3)	159.6(4)

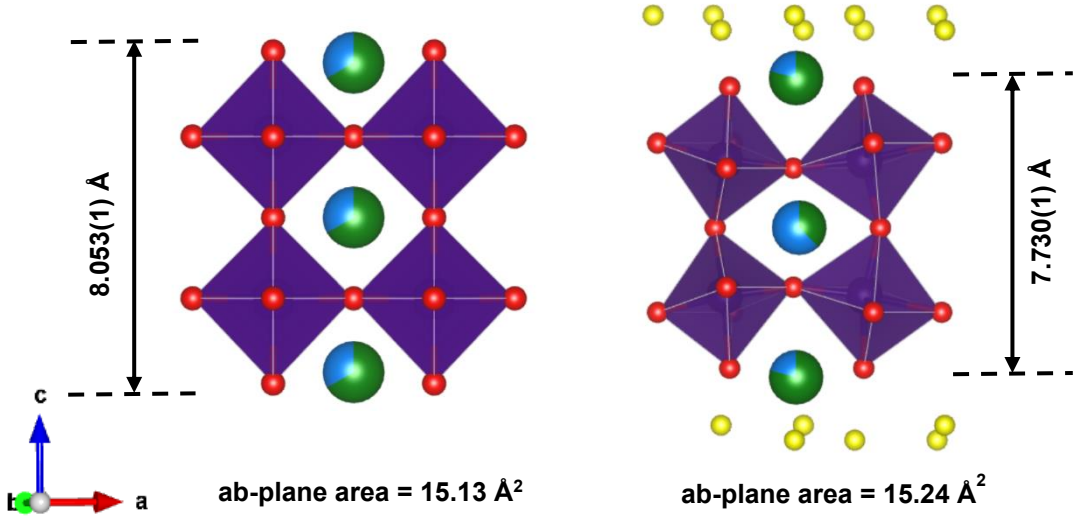

Figure 5.5: Fluorination of $La_2SrFe_2O_7F_2$ leads to a compression of the perovskite blocks, both parallel to the c axis and in the ab plane.

Inserting fluoride into $La_2SrFe_2O_7$ leads to the compression of the double perovskite layer presumably due to the Fe^{4+} cations. These d^4 cations are susceptible to Jahn-Teller distortions. While the *c* lattice parameter increases from 20.439(3) Å to 22.551(1) Å on fluorination, the *c* dimension of the double-perovskite blocks decreases from 8.053(1) Å to 7.730(1) Å, as shown in **Figure 5.5**. There is a small expansion in the *ab* plane as well, consistent with Jahn-Teller distortion.

As a result, the FeX_6 octahedra in the structure become more compressed along the *z*-axis, changing from a "tall and thin" shape to a "short and wide" shape. This leads to an expansion of the Fe-*X* equatorial bonds to allow the *A* cations to form strong interactions with both apical and equatorial anion sites, as well as the interstitial sites. If the octahedra were elongated along the axial direction, the *A* cations might not be able to form such strong interactions with both the equatorial and interstitial anions.

To fit these altered octahedra within the crystal framework, the structure responds by tilting and rotating FeX_6 octahedra about both in-plane (8.90(6)°) and out-of-plane (10.20(4)°) axis.

The insertion of fluoride into $La_2SrFe_2O_7$ structure results in the perovskite blocks adopting a $a^-a^-c^+$ tilt pattern. This distortion breaks the local inversion symmetry in each perovskite layer through coupled displacements of *A*-cations. However, despite breaking the local inversion symmetry, the overall structure is centrosymmetric. This is because the rotations about the long axis alternate

between the perovskite layers. As a result, the direction of the *A*-cation displacements is also opposite between adjacent perovskite layers. Thus, the structure is best described by the centrosymmetric space group *Pnam*, rather than the polar space group $A2_1am$.

5.5 Conclusion

In conclusion, this study shows that insertion of fluoride ions in the $n = 2$ $La_2SrFe_2O_7$ Ruddlesden-Popper phase leads to the rotation of octahedra about both in-plane and out-of-plane axes. The tilting and rotation of octahedra lead to a local breaking of inversion symmetry but due the displacement of *A*-cations in opposite directions in adjacent perovskite layers, the net polar displacement is zero. As a result, the structure adopts an antipolar centrosymmetric structure of *Pnam* space group.

This study reaffirms the previous reports that fluorination of the $n = 2$ RP phases enhances the tilting and twisting distortions in the structure.[1, 14, 16] This offers an alternate route, in addition to adjusting the tolerance factor by cation substitution, to tune the octahedral distortions in RP phases. If the formation of antiferroelectric phases can be suppressed, by either using particular bridging ligands[17, 18] which favour polar alignments and stabilise non-centrosymmetric structure or specific structure directing interactions between the oxide− fluoride anions and charge balancing cations[19] that maintain asymmetry, this structural tuning via fluorination could be particularly promising for designing functional materials, such as ferroelectrics.

1. R. Zhang, G. Read, F. Lang, T. Lancaster, S. J. Blundell and M. A. Hayward, *Inorganic chemistry*, 2016, **55**, 3169-3174.
2. L. Aikens, L. Gillie, R. Li and C. Greaves, *Journal of Materials Chemistry*, 2002, **12**, 264-267.
3. P. Slater and R. Gover, *Journal of Materials Chemistry*, 2002, **12**, 291-294.
4. C. Greaves and M. G. Francesconi, *Current Opinion in Solid State and Materials Science*, 1998, **3**, 132-136.
5. E. E. McCabe and C. Greaves, *Journal of Fluorine Chemistry*, 2007, **128**, 448-458.
6. A. T. Mulder, N. A. Benedek, J. M. Rondinelli and C. J. Fennie, *Advanced Functional Materials*, 2013, **23**, 4810-4820.
7. R. Zhang, M. S. Senn and M. A. Hayward, *Chemistry of Materials*, 2016, **28**, 8399-8406.
8. D. Samaras, A. Collomb and J. Joubert, *Journal of Solid State Chemistry*, 1973, **7**, 337-348.
9. I. B. Sharma and D. Singh, 1995.
10. H. M. Rietveld, *Applied Crystallography*, 1969, **2**, 65-71.
11. A. A. Coelho, *Coelho Software, Brisbane, Australia*, 2007.
12. A. Coelho, *Karlsruhe, Germany*, 2012.
13. V. F. Sears, *Neutron news*, 1992, **3**, 26-37.
14. F. D. Romero, P. A. Bingham, S. D. Forder and M. A. Hayward, *Inorganic chemistry*, 2013, **52**, 3388-3398.
15. T. Sivakumar and J. B. Wiley, *Materials Research Bulletin*, 2009, **44**, 74-77.
16. R. Li and C. Greaves, *Physical Review B*, 2000, **62**, 3811.
17. M.D. Donakowski, R. Gautier, J. H. Yeon, D. T. Moore, J. C. Nino, P. S. Halasyamani, K. R. Poeppelmeier, *Journal of the American Chemical Society*, 2012, 134, 7679.
18. R. Gautier, R. Gautier, K. B. Chang, K. R. Poeppelmeier, *Inorganic Chemistry*, 2015, 54, 1712.
19. M. R. Marvel, J. Lesage, J. Baek, P. S. Halasyamani, C. L. Stern, K. R. Poeppelmeier, *Journal of the American Chemical Society*, 2007, 129, 13963.

Chapter 6: Determining the Structure of Layered *A*-site Deficient Perovskites

6.1 Introduction

The *A*-site deficient perovskites with $Ln_{0.33}BO_3$ composition consist of partially occupied layers of *Ln*-site cations alternating with *Ln*-vacant layers along the *c*-axis leading to a doubling of the perovskite cell in this direction and BO_6 (*B* = Nb, Ta) octahedra that preserve the 3D connectivity of the *B* sublattice.[1-4] The ideal, high temperature aristotype structure is tetragonal of *P*4/*mmm* symmetry, as shown in **Figure 6.1(a)**.

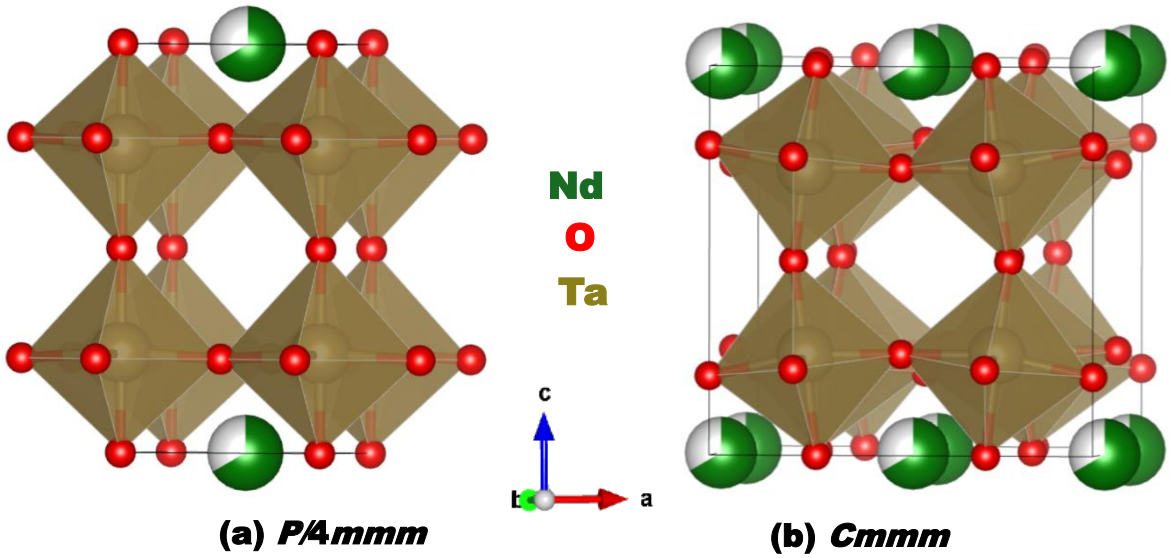

Figure 6.1: (a) High-symmetry tetragonal *P*4/*mmm* crystal structure of *A*-site deficient perovskites. (b) Crystal structure of *A*-site deficient $Nd_{0.33}TaO_3$ perovskite in *Cmmm* space group. Nd, Ta and O sites are shown in green, golden, and red. TaO_6 are shown in golden.

These materials are most commonly studied due to their ability to adopt polar structures[5, 6] and their layered nature makes them promising candidates for hybrid improper ferroelectricity. This has generated significant interest, as they offer a platform to investigate the competition between proper and hybrid improper ferroelectric mechanisms.

$Nd_{0.33}TaO_3$ crystallises in the orthorhombic *Cmmm* space group with $a^-b^0c^0$ tilts which is consistent with the structure reported by Q. Zhou et.al. (**Figure 6.1(b)**).[6] Building on earlier work by Nadiri,[7] who demonstrated the reductive intercalation of Li^+ into $Nd_{0.33}NbO_3$ results in the partial reduction of Nb^{5+} cations to Nb^{4+}, in this study, this approach is extended to the $Nd_{0.33}TaO_3$ system, intercalating monovalent cations Li^+, Na^+ and K^+ into the vacant *A*-site, thereby reducing Ta^{5+} cations to Ta^{4+}.

Symmetry analysis using ISODISTORT[8] mapped out the possible distortion modes expected for *A*-site ordered $A_{0.5}Nd_{0.33}TaO_3$ (*A* = Li, Na, K) perovskites (**Figure 6.2)**.

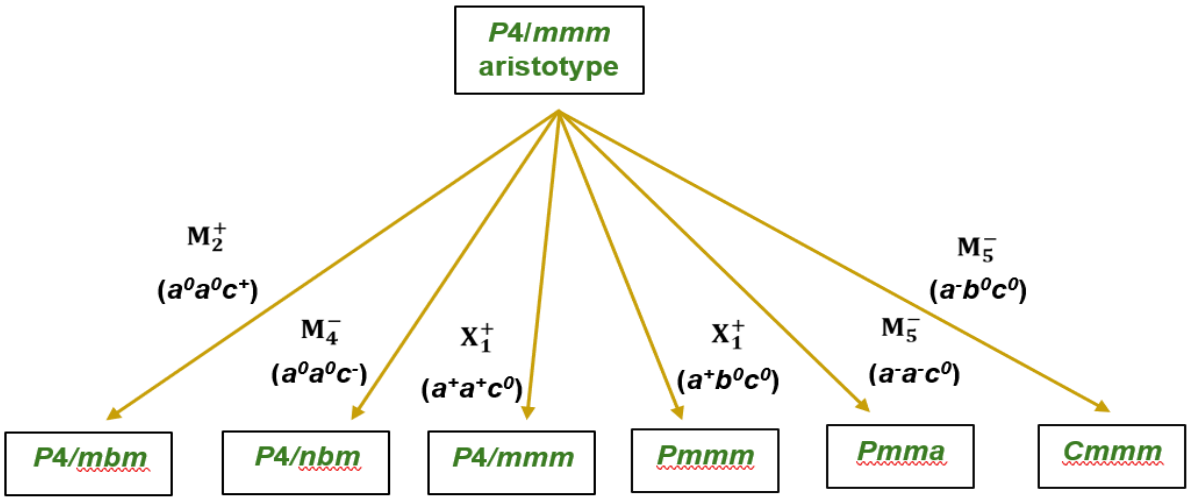

Figure 6.2: Symmetry analysis from ISODISTORT showing range of tilt distortions that $A_{0.5}Nd_{0.33}TaO_3$ (*A* = Li, Na, K) can undergo with respect to the *P*4/*mmm* space group.

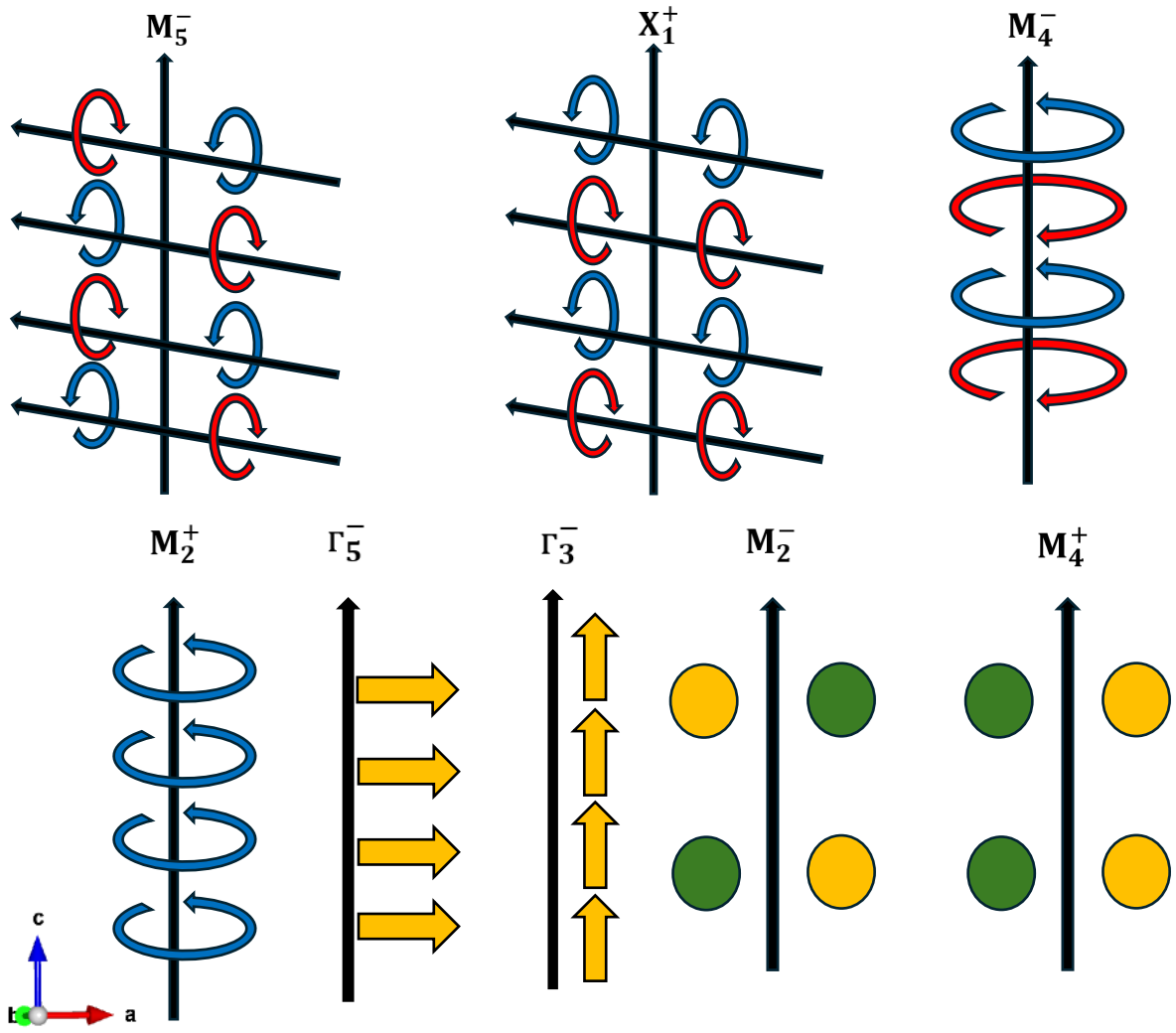

Figure 6.3: Schematic illustration of octahedral rotation modes, polar displacive modes and occupancy modes referred to in this chapter.

Figure 6.3 shows the schematic illustration of the key displacive and occupancy distortion modes observed in *A*-site ordered $A_{0.5}Nd_{0.33}TaO_3$ (*A* = Li, Na, K) perovskites. The M_5^- (out-of-phase) and X_1^+ (in-phase) modes correspond to in-plane octahedral tilts about in-plane axis. The M_4^- (out-of-phase) and M_2^+ (in-phase) modes represent the octahedral rotations about the long axis. The Γ_5^- and Γ_3^- modes describe polar displacive distortions in the in-plane and out-of-plane directions, respectively. The M_2^- is the occupancy mode showing checkerboard ordering of *B*-cation and the M_4^+ occupancy mode represents a checkerboard ordering within plane, but columns along *c*.

Given the known potential of these materials to adopt polar structures, this study aims to investigate whether adding Li^+, Na^+ and K^+ cations can effectively tune octahedral tilts and possible charge ordering thereby changing the structure and symmetry of the ground state. It has been proposed that combining octahedral rotations and *B*-site charge order might break inversion symmetry and provide an improper route to stabilise polar structures.[9] This makes *A*-site-deficient perovskites promising candidates for exploring ferroelectric mechanisms by both structural and electronic factors.

This study is a preliminary analysis based only on XRPD. To fully determine the structure of the materials under investigation, complementary techniques such as neutron powder diffraction (NPD), Solid-state NMR (ssNMR) and DFT calculations are necessary. Solid-state NMR studies are planned but were delayed due to difficulties with accessing the samples.

6.2 Methods

6.2.1 Synthesis

The precursor oxides were prepared by Dr Emma McCabe. Electrochemical intercalation of Li^+, Na^+ and K^+ cations was performed by Prof. Neeraj Sharma and his group, who also collected X-ray powder diffraction (XRPD) data on the resulting air-sensitive samples.

6.2.2 Analysis of XRPD data

The symmetry-adapted distortion mode approach was used to identify the distortions that give the most significant improvements to the fit. The XRPD data were analysed using the Rietveld method[10] in the Topas Academic software.[11, 12]

The samples were passed to Dr Karen Johnston for ssNMR measurements.

6.3 Results

6.3.1 Structural Characterisation of $Li_{0.5}Nd_{0.33}TaO_3$

Rietveld refinements were carried out to fit the XRPD data for $Li_{0.5}Nd_{0.33}TaO_3$ with an aristotype *P*4/*mmm* model. Rietveld refinement profile shows that the peaks between 46° and 47°, at 52° and at 77° 2θ are not fitted by the high symmetry model (**Figure 6.3**). Additional peaks observed at 43°, 50°, 74°, 90°, and 95° 2θ are from a copper substrate, which are consistently present across all three materials under investigation.

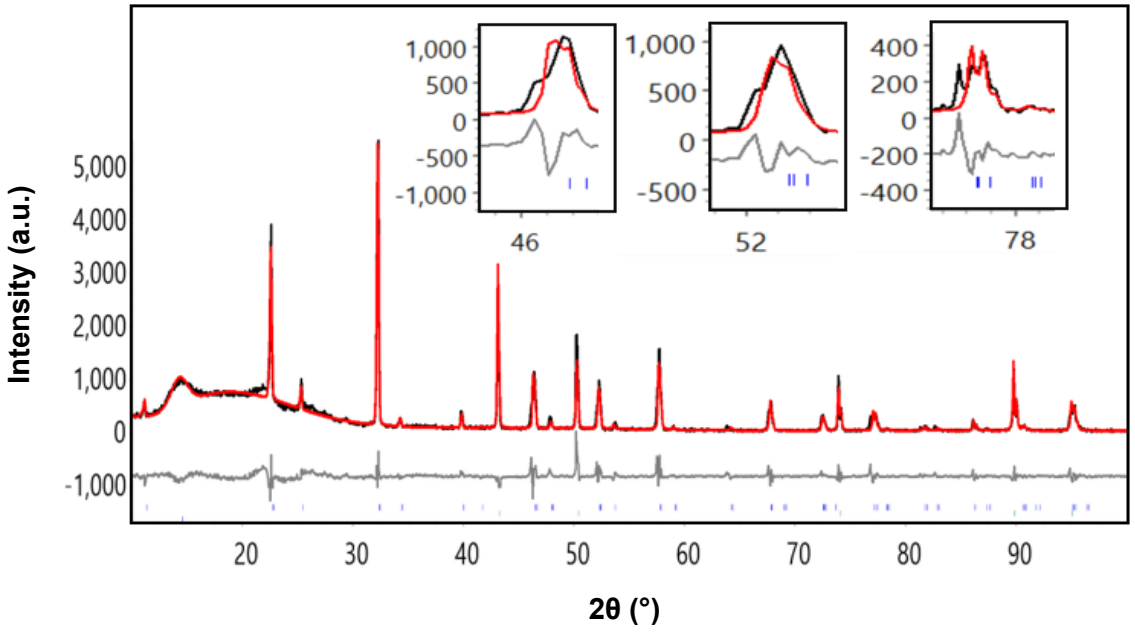

Figure 6.3: Rietveld refinement profile for $Li_{0.5}Nd_{0.33}TaO_3$ using XRPD data refined in space group *P*4/*mmm*. The observed, calculated, and difference profiles are shown in black, red, and grey respectively).

Mode inclusion analysis was carried out to understand possible distortions in the structure. The results from mode inclusion analysis show that the biggest improvement in the R_{wp} value is from the rotations about an in-plane axis described by M_5^-, as shown in **Figure 6.4**.

Refinement using the $2a_t \times 2a_t \times c$ model of *Cmmm* symmetry, corresponding to M_5^- octahedral tilts, gave R_{wp} = 13.12% (49 parameters). Compared to the ideal *P*4/*mmm* model with R_{wp} =16.11% (37 parameters), the *Cmmm* orthorhombic model shows a significant improvement in fit, particularly fitting the peak between 46° and 47°, at 52° and 77° 2θ (**Figure 6.5**).

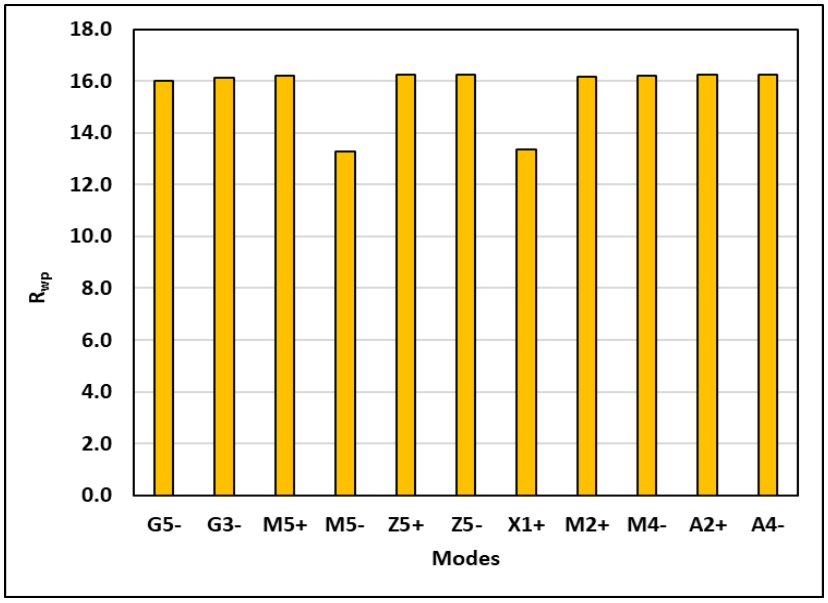

Figure 6.4: Results from mode inclusion analysis for $Li_{0.5}Nd_{0.33}TaO_3$ showing M_5^- mode gives the biggest improvement in the R_{wp} value.

In contrast, refinement using the $\sqrt{2}a_t \times \sqrt{2}a_t \times c$ model of *Pmam* (non-standard setting of *Pmma*) symmetry also corresponding to M_5^- rotations gave a higher R_{wp} of 15.13% (43 parameters) and did not fit the peak at 76.80° 2θ.

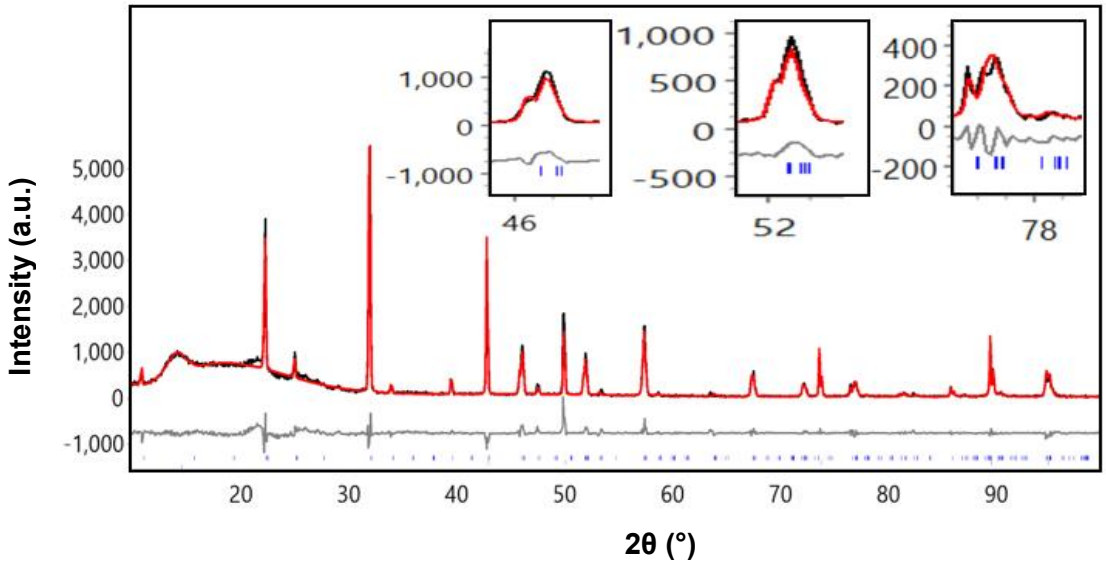

Figure 6.5: Rietveld refinement profile for $Li_{0.5}Nd_{0.33}TaO_3$ using XRPD data refined in space group *Cmmm*. The observed, calculated, and difference profiles are shown in black, red, and grey respectively).

Another round of mode inclusion analysis including M_5^- mode did not result in any further improvement in the R_{wp} value. Therefore, based on XRPD data, the M_5^- *Cmmm* best describes the structure of $Li_{0.5}Nd_{0.33}TaO_3$. The refinement details are given in **Table 6.1**. This is consistent with the structures reported for $Nd_{0.33}BO_3$ (B = Nb, Ta).[6, 13] $Li_xNd_{0.33}NbO_3$ has been reported to show octahedral tilts about both in-

plane axes[13] and similar tilts may be present in $Li_{0.5}Nd_{0.33}TaO_3$. However, no evidence for more complex structural models involving additional tilts was observed in our XRPD data. It is important to note that detecting the positions of light oxide sites is challenging using X-ray methods. This highlights the limitation of XRPD.

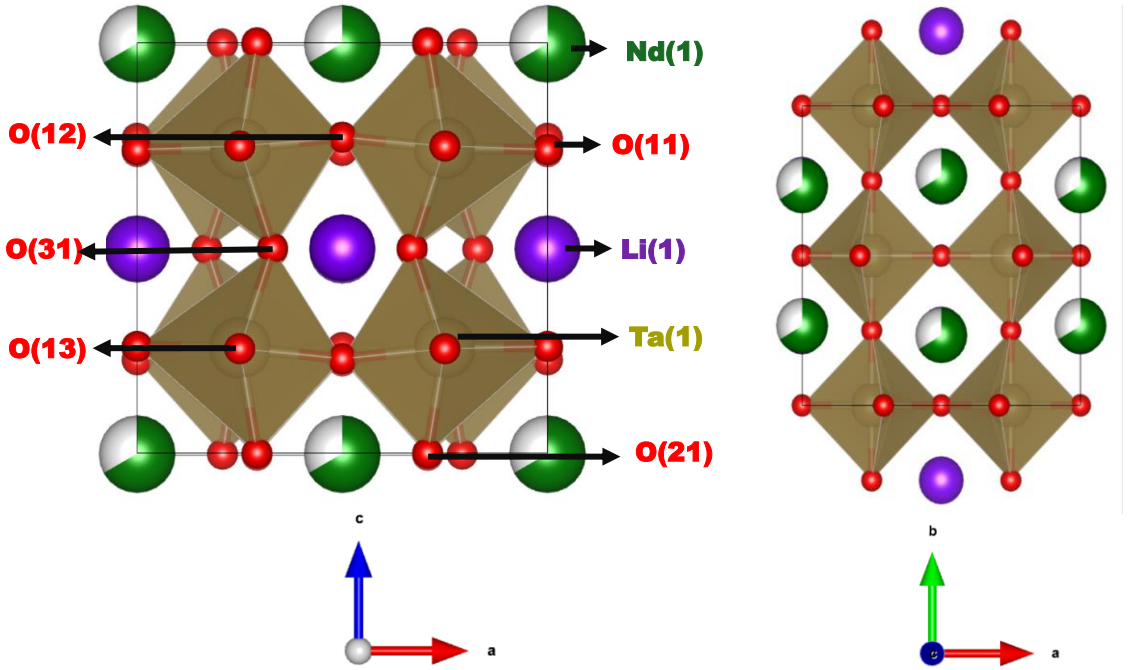

Figure 6.6: Crystal structure of M_5^- *Cmmm* model for $Li_{0.5}Nd_{0.33}TaO_3$. Li, Nd, Ta and O sites are shown in purple, green, golden, and red. TaO_6 are shown in golden.

Table 6.1: Structural parameters of $Li_{0.5}Nd_{0.33}TaO_3$ from XRPD data in space group *Cmmm.*

Space group: *Cmmm* (No. 65). Cell parameters: *a* = 7.7977(6) Å, *b* =7.7859 Å, *c* = 7.8309(5) (7) Å. R_{wp} = 13.12%, R_p = 9.56%, χ^2 = 4.28, 49 parameters.

Atom	Wyckoff Site	*x*	*y*	*z*	Occupancy	U_{iso} x 100 (Å^2)
Li(1)	4*j*	0	0.25	0.5	1	0.21(1)
Nd(1)	4*i*	0	0.266(3)	0	0.66	0.21(1)
Ta(1)	8*o*	0.749(1)	0	0.2568(7)	1	0.21(1)
O(11)	4*k*	0	0	0.26(3)	1	0.21(1)
O(12)	4*l*	0	0.5	0.23(3)	1	0.21(1)
O(13)	8*m*	0.25	0.25	0.747(1)	1	0.21(1)
O(21)	4*g*	0.708(1)	0	0	1	0.21(1)
O(31)	4*h*	0.670(1)	0	0.5	1	0.21(1)

6.3.2 Structural Characterisation of $Na_{0.5}Nd_{0.33}TaO_3$

Rietveld refinements were carried out to fit the XRPD data for $Na_{0.5}Nd_{0.33}TaO_3$ with an aristotype *P*4/*mmm* model. Rietveld refinement profile shows that the peaks between 46° and 47°, at 58° and at 77° 2θ are not fitted by the high symmetry model (**Figure 6.7**).

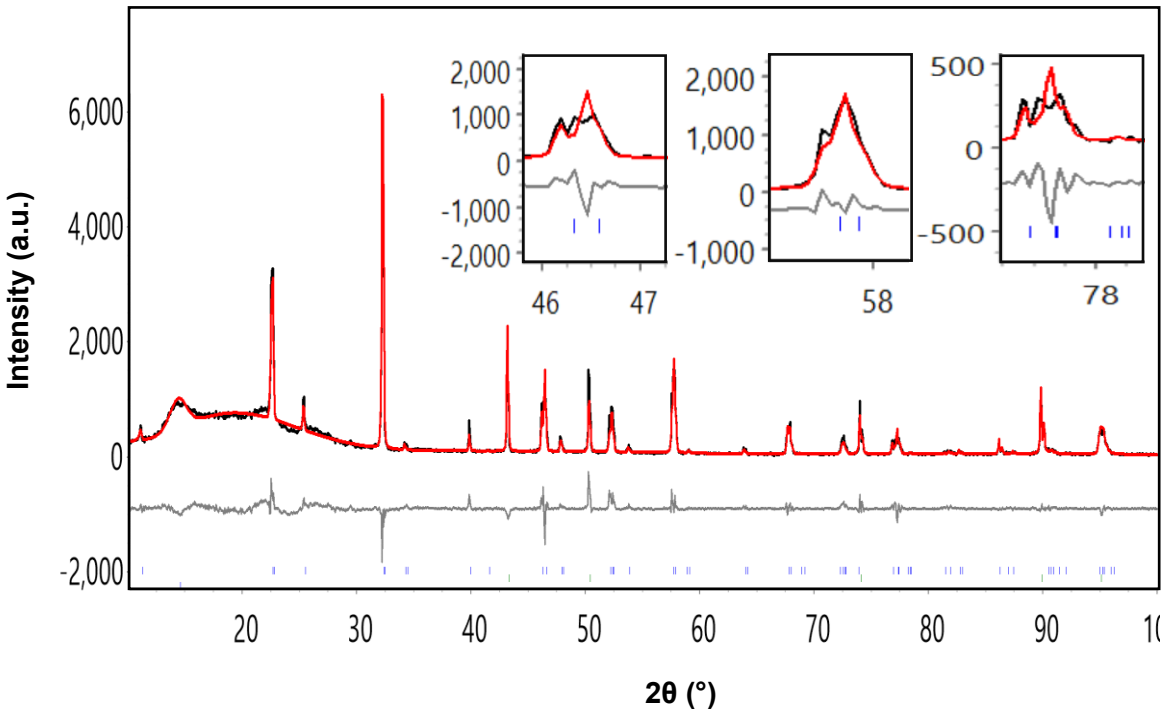

Figure 6.7: Rietveld refinement profile for $Na_{0.5}Nd_{0.33}TaO_3$ using XRPD data refined in space group *P*4/*mmm*. The observed, calculated, and difference profiles are shown in black, red, and grey respectively).

Similar to $Li_{0.5}Nd_{0.33}TaO_3$, mode inclusion analysis was carried out to investigate possible distortions in $Na_{0.5}Nd_{0.33}TaO_3$. The results similarly show that the biggest improvements in the R_{wp} value is from the rotations about an in-plane axis described by M_5^- (**Figure 6.8)**.

The *Cmmm* model, corresponding to M_5^- octahedral rotations gave R_{wp} = 11.96% (44 parameters). Compared to the ideal *P*4/*mmm* model with R_{wp} =14.48% (37 parameters), the *Cmmm* model shows a significant improvement in fit, particularly fitting the peak between 46° and 47°, at 58° and 77° 2θ (**Figure 6.9**).

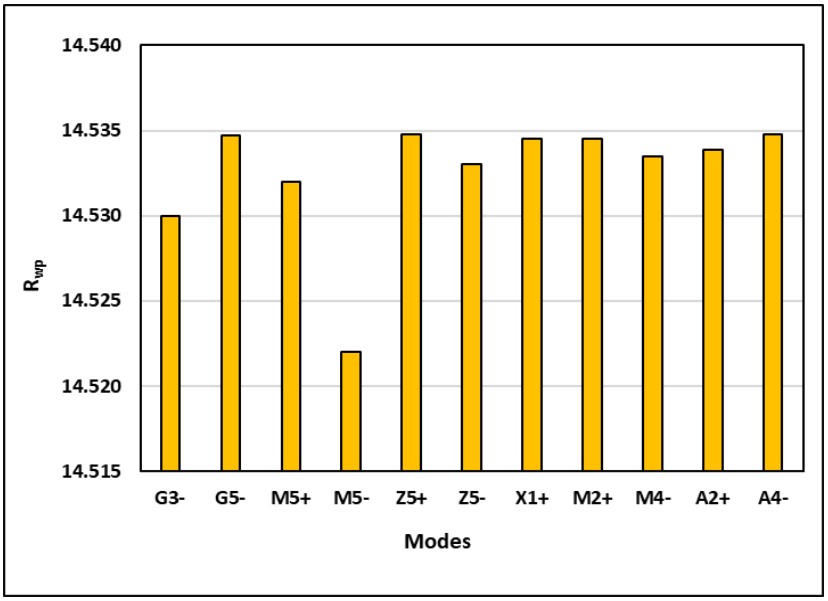

Figure 6.8: Results from mode inclusion analysis for $Na_{0.5}Nd_{0.33}TaO_3$ showing M_5^- mode gives the biggest improvement in the R_{wp} value.

Refinement using the *Pmam* (non-standard setting of *Pmma*) model also corresponding to M_5^- rotations gave a higher R_{wp} of 16.26% (43 parameters) and did not fit the peak between 46° and 47°, at 58° and 77° 2θ.

A second round of mode inclusion analysis including M_5^- mode did not result in any further improvement in the R_{wp} value. Therefore, based on XRPD data, the M_5^- *Cmmm* best describes the structure of $Na_{0.5}Nd_{0.33}TaO_3$. The refinement details are given in **Table 6.2**.

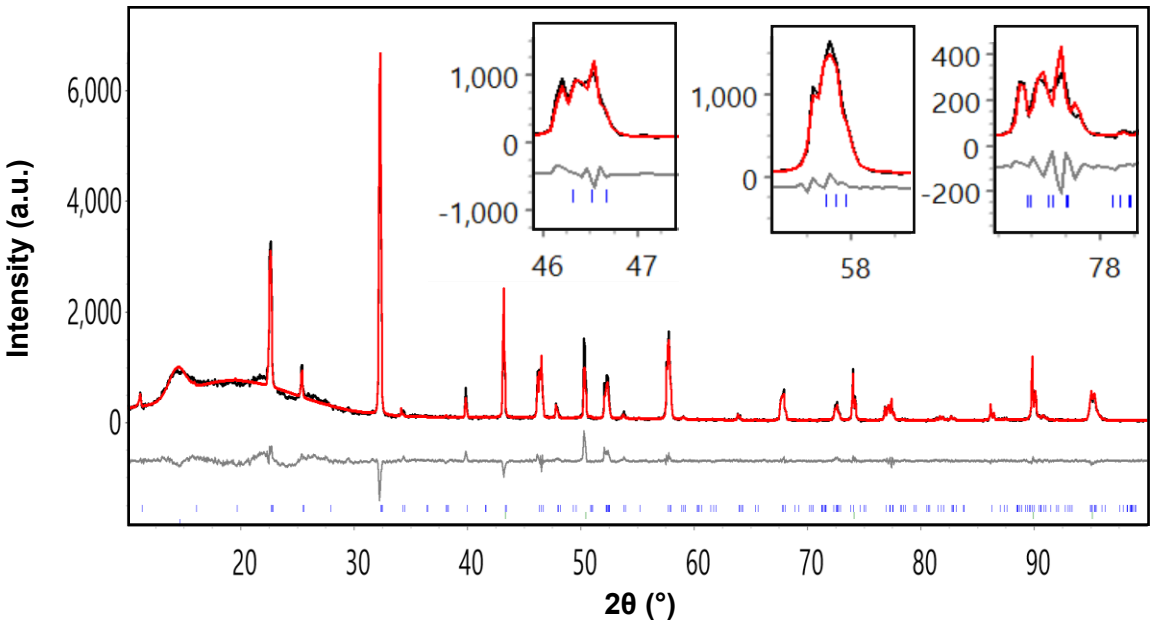

Figure 6.9: Rietveld refinement profile for $Na_{0.5}Nd_{0.33}TaO_3$ using XRPD data refined in space group *Cmmm*. The observed, calculated, and difference profiles are shown in black, red, and grey respectively).

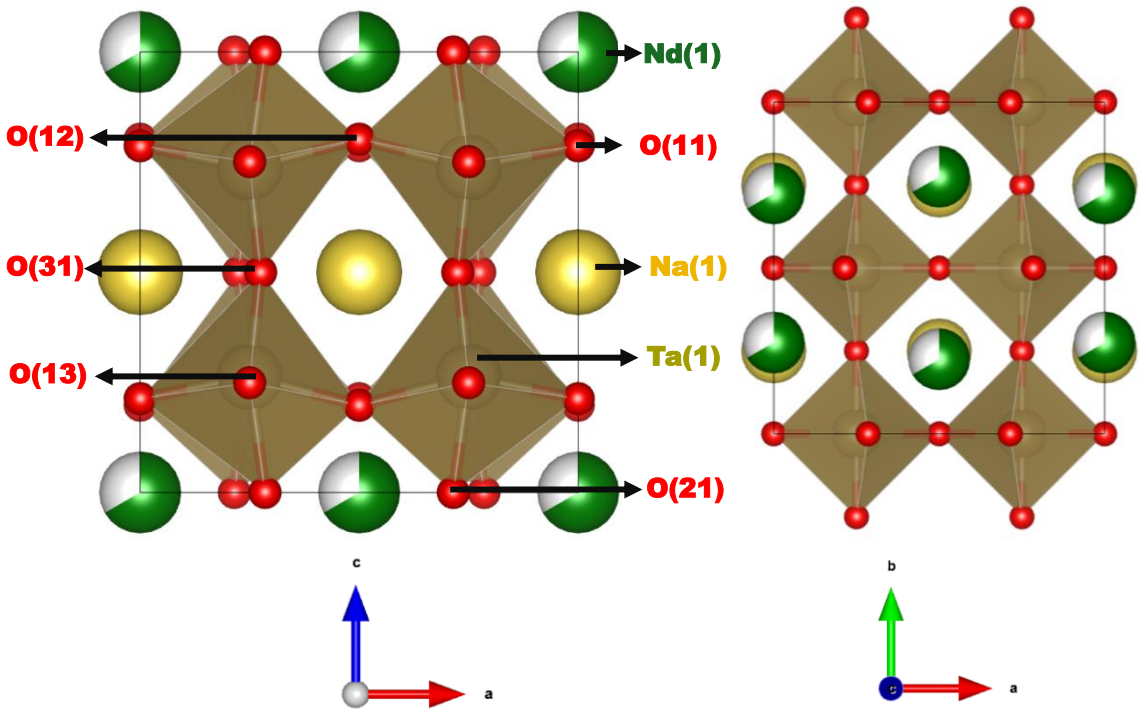

Figure 6.10: Crystal structure of M_5^- *Cmmm* model for $Na_{0.5}Nd_{0.33}TaO_3$. Na, Nd, Ta and O sites are shown in yellow, green, golden, and red. TaO_6 are shown in golden.

Table 6.2: Structural parameters of $Na_{0.5}Nd_{0.33}TaO_3$ from XRPD data in space group *Cmmm.*

Space group: *Cmmm* (No. 65). Cell parameters: *a* = 7.7780(4) Å, *b* = 7.8032(4) Å, *c* = 7.8343(4) Å. R_{wp} = 11.96%, R_p = 9.47%, χ^2 = 3.64, 44 parameters.

Atom	Wyckoff Site	*x*	*y*	*z*	Occupancy	U_{iso} x 100 (Å^2)
Na(1)	4*j*	0	0.25	0.5	1	0.67(9)
Nd(1)	4*i*	0	0.275(1)	0	0.66	0.67(9)
Ta(1)	8*o*	0.750(1)	0	0.2622(5)	1	0.67(9)
O(11)	4*k*	0	0	0.213(1)	1	0.67(9)
O(12)	4*l*	0	0.5	0.198(1)	1	0.67(9)
O(13)	8*m*	0.25	0.25	0.751(8)	1	0.67(9)
O(21)	4*g*	0.715(1)	0	0	1	0.67(9)
O(31)	4*h*	0.725(1)	0	0.5	1	0.67(9)

6.3.3 Structural Characterisation of $K_{0.5}Nd_{0.33}TaO_3$

Rietveld refinements were carried out to fit the XRPD data for $K_{0.5}Nd_{0.33}TaO_3$ with an aristotype *P*4/*mmm* model. Rietveld refinement profile shows that there is intensity mismatch and the peaks at 35°, between 46° and 47°, at 54°, 58°, 68° and 77° 2θ are not fitted by the high symmetry model (**Figure 6.11**).

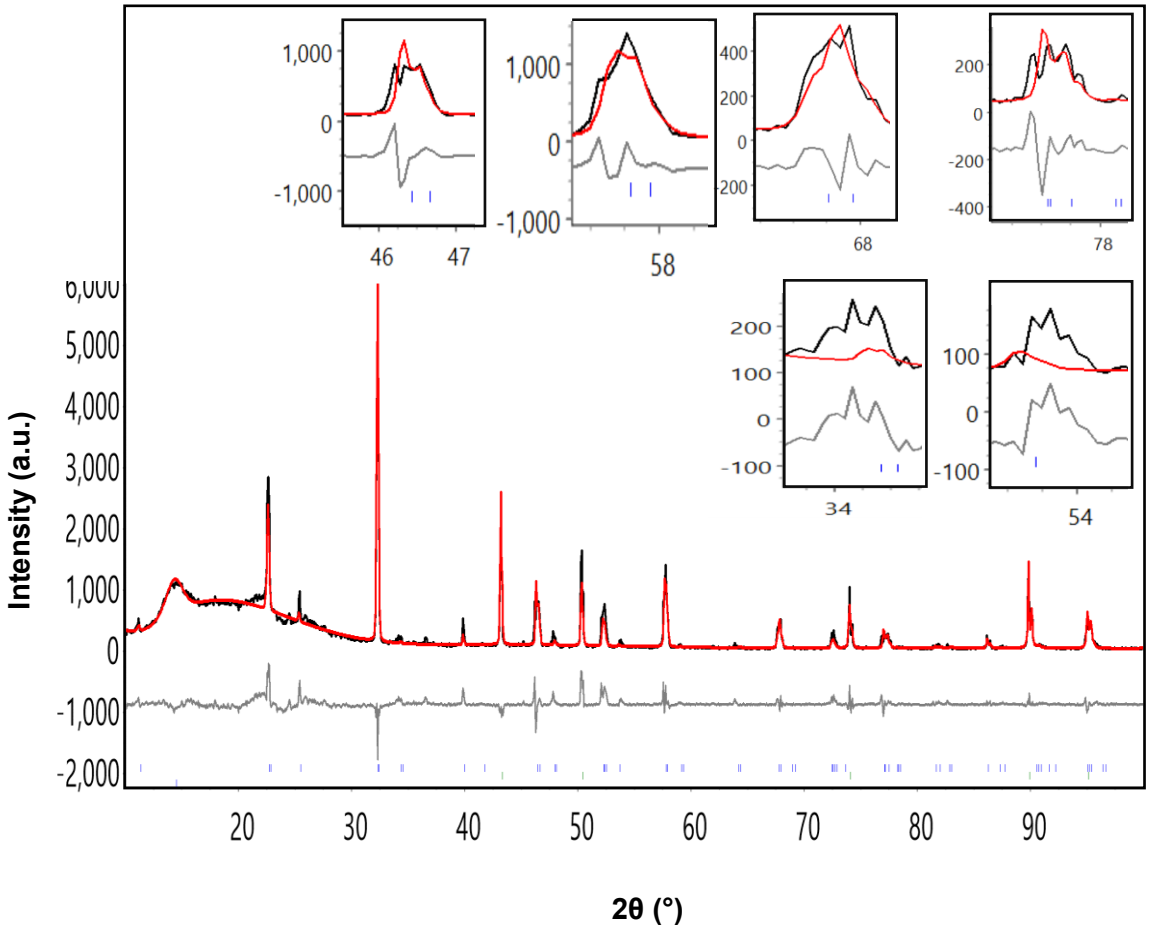

Figure 6.11: Rietveld refinement profile for $K_{0.5}Nd_{0.33}TaO_3$ using XRPD data refined in space group *P*4/*mmm*. The observed, calculated, and difference profiles are shown in black, red, and grey respectively).

Mode inclusion analysis showed that the biggest improvements in the R_{wp} value is from the Γ_5^- in-plane polar displacement (**Figure 6.12**). However, the Γ_5^- *Amm*2 model, similar to the parent *P*4/*mmm* model, failed to fit the above-mentioned peaks and the Γ_5^- *Pmm*2 model did not fit the peaks at 34° and 54° 2θ (**Figure 6.13**). A second round of mode inclusion analysis including Γ_5^- mode did not result in any further improvement in the R_{wp} value.

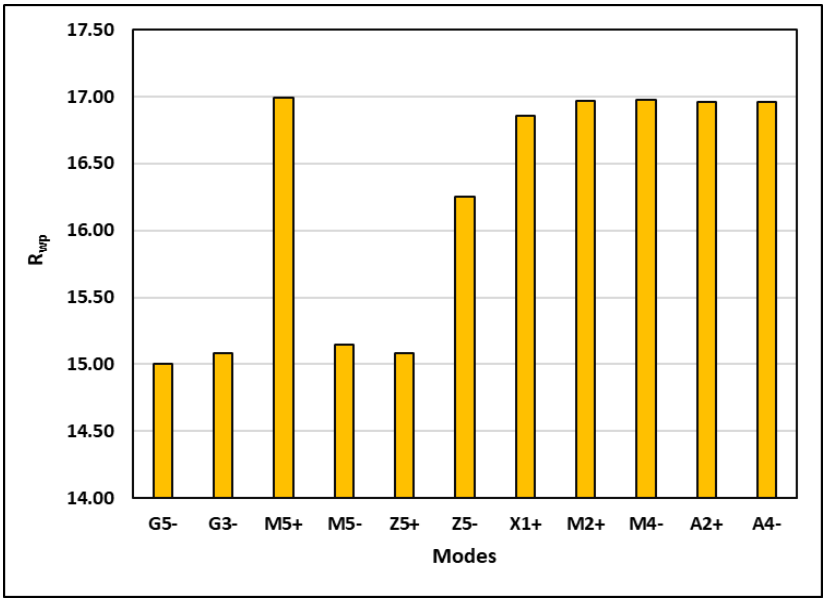

Figure 6.12: Results from mode inclusion analysis showing Γ_5^- mode gives the biggest improvement in the R_{wp} value.

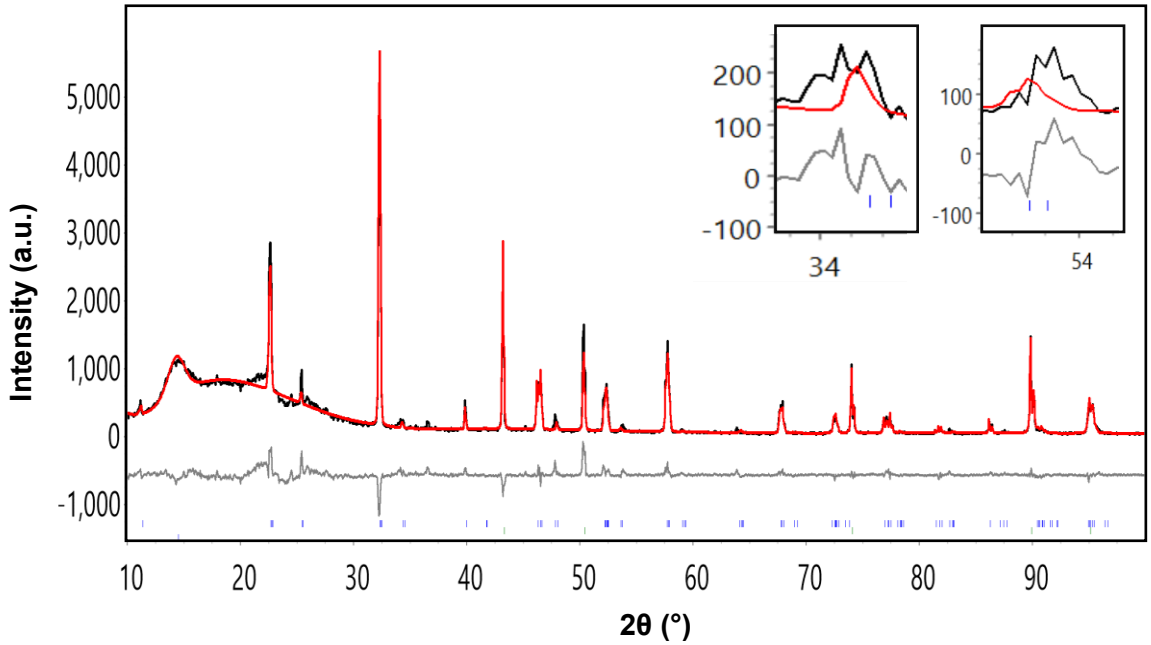

Figure 6.13: Rietveld refinement profile for $K_{0.5}Nd_{0.33}TaO_3$ using XRPD data refined in Γ_5^- *Pmm*2 space group. The observed, calculated, and difference profiles are shown in black, red, and grey respectively).

In addition, the M_5^- *Cmmm* model, previously tested $A_{0.5}Nd_{0.33}TaO_3$ (*A* = Li, Na), was also evaluated, but that also failed to fit the peaks at 35° and 55° 2θ (**Figure 6.14**). Another model - *Pmmm*, corresponding to X_1^+ in-plane octahedral rotations, was tested. However, it showed intensity mismatches and similarly did not fit the peaks at 35° and 55° 2θ.

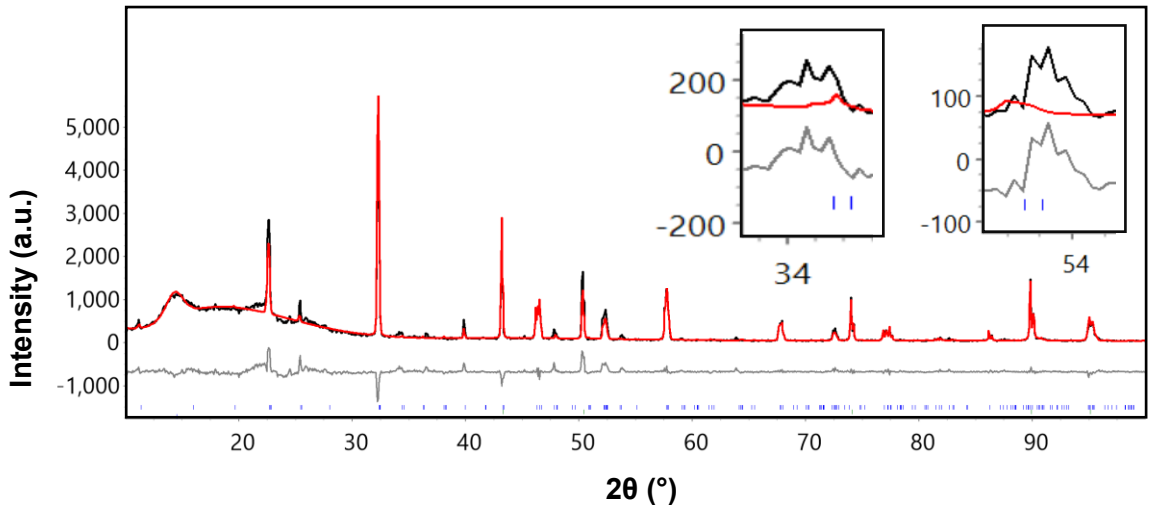

Figure 6.14: Rietveld refinement profile for $K_{0.5}Nd_{0.33}TaO_3$ using XRPD data refined in M_5^- *Cmmm* space group. The observed, calculated, and difference profiles are shown in black, red, and grey respectively).

To find a model capable of fitting all observed peaks, combinations of distortion modes were then investigated. Models combining Γ_5^- + M_5^- *Amm*2, *Pmc*2$_1$ and *Pmm*2 did not result in satisfactory fits.

Finally, models with X_1^+ mode (describing in-plane octahedral tilts) together with Γ_5^- were tested. Among them, the Γ_5^- + X_1^+ *Pm*2*m* (non-standard setting of *Pmm*2) model successfully fits all the peaks giving an R_{wp} = 11.97% with 52 parameters (**Figure 6.15**). Therefore, based on XRPD data, the Γ_5^- + X_1^+ *Pm*2*m* model best describes the structure of $K_{0.5}Nd_{0.33}TaO_3$. The refinement details are given in **Table 6.3**.

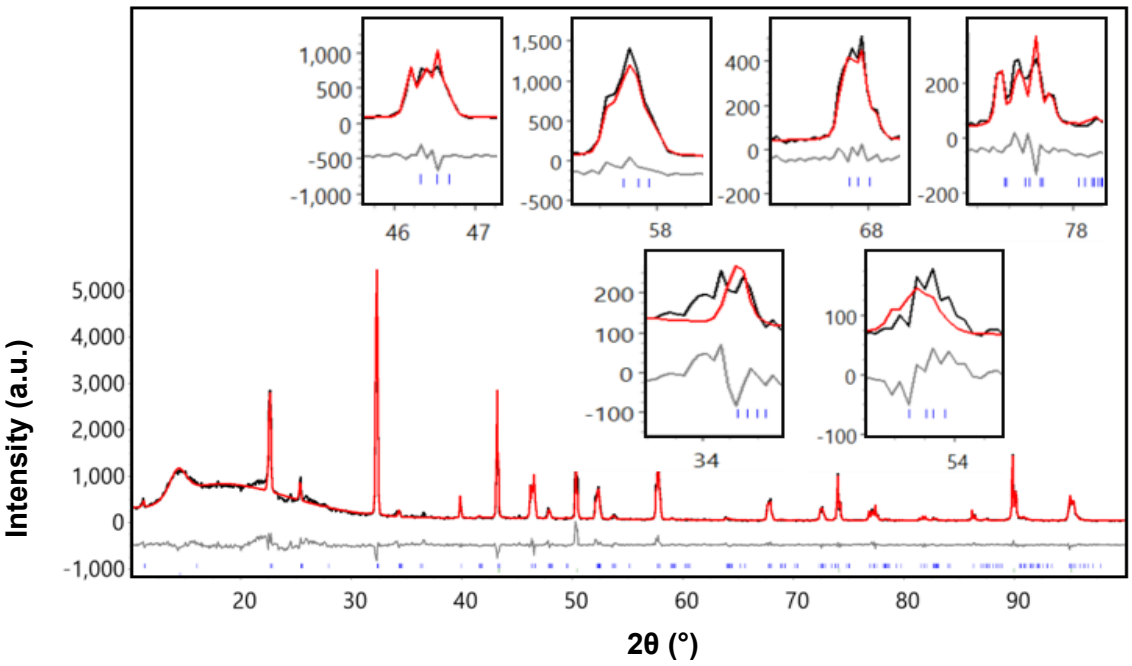

Figure 6.15: Rietveld refinement profile for $K_{0.5}Nd_{0.33}TaO_3$ using XRPD data refined in Γ_5^- + X_1^+ *Pm*2*m* space group. The observed, calculated, and difference profiles are shown in black, red, and grey respectively).

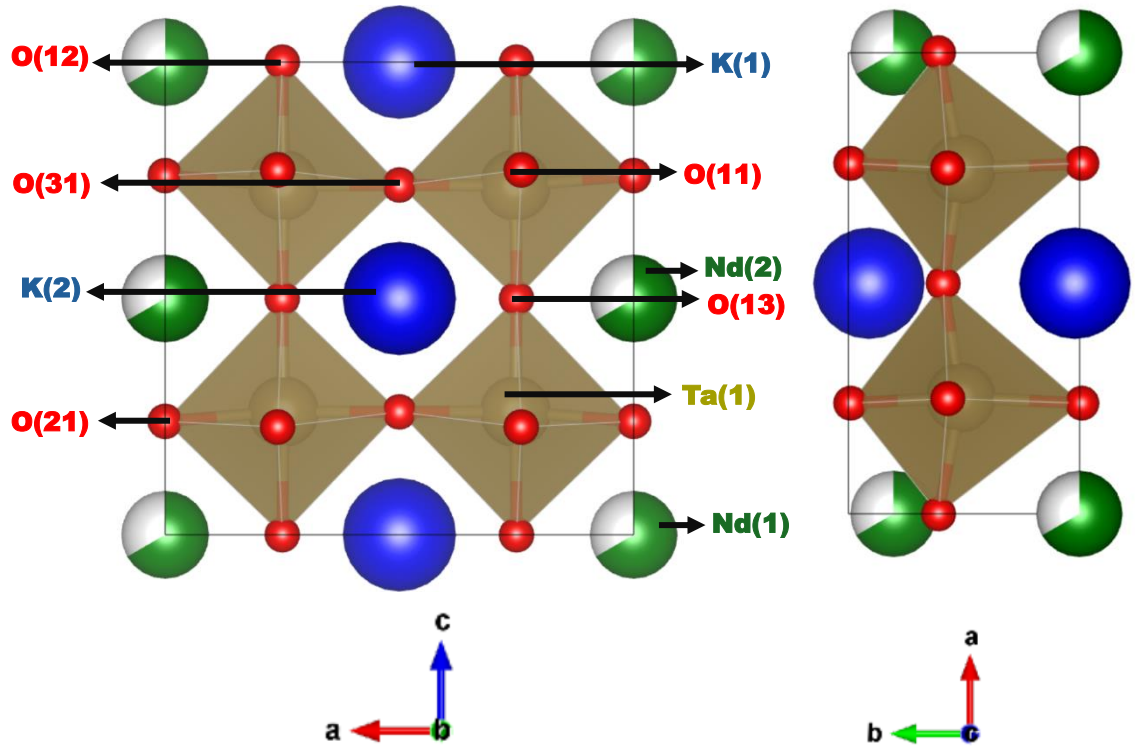

Figure 6.16: Crystal structure of $\Gamma_5^- + X_1^+$ *Pm*2*m* model for $K_{0.5}Nd_{0.33}TaO_3$. K, Nd, Ta and O sites are shown in pink, orange, golden, and red. TaO_6 are shown in golden.

Table 6.3: Structural parameters of $K_{0.5}Nd_{0.33}TaO_3$ from XRPD data in space group *Pm*2*m.*

Space group: *Pm*2*m* (No. 25). Cell parameters: *a* 7.7785(5) Å, *b* = 3.9012(3) Å, *c* = 7.8345(4) Å. R_{wp} = 12.71%, R_p = 6.13%, χ^2 = 4.28, 52 parameters.

Atom	Wyckoff Site	*x*	*y*	*z*	Occupancy	U_{iso} x 100 (Å^2)
K(1)	1*b*	0.5	0.02(3)	0	1	0.50(1)
K(2)	1*d*	0.5	-0.089(15)	0.5	1	0.50(1)
Nd(1)	1*a*	0	0.001(16)	0	0.66	0.50(1)
Nd(2)	1*c*	0	-0.195(8)	0.5	0.66	0.50(1)
Ta(1)	4*i*	0.252(1)	0.514(2)	0.260(1)	1	0.50(1)
O(11)	2*g*	0.24(2)	-0.01(4)	0.228(1)	1	0.50(1)
O(12)	2*h*	0.75(3)	0.57(5)	0	1	0.50(1)
O(13)	2*e*	0.75(3)	0.53(7)	0.5	1	0.50(1)
O(21)	2*f*	0	0.61(6)	0.24(3)	1	0.50(1)
O(31)	4*i*	0.5	0.59(6)	0.26(3)	1	0.50(1)

6.4 Discussion

This study is a preliminary analysis based only on XRPD. Due to the low x-ray scattering power of light atoms, accurately determining their positions is challenging. To fully determine the structure of the materials, complementary techniques are necessary. Neutron powder diffraction (NPD) will help in determining the position of light atoms and the distortions in the structure. In addition, ssNMR measurements will be done to distinguish between models identified by symmetry analysis in terms of Li sites. $A_{0.5}Nd_{0.33}NbO_3$ ssNMR data will help determine the number of Nb sites.

The structure of $Nd_{0.33}TaO_3$ is similar to $Nd_{0.33}NbO_3$ which consists of the layered ordering of Nd^{3+} cations and vacancies along the long axis.[4, 6] Monovalent cations namely Li^+, Na^+, and K^+ were introduced into the vacant *A*-sites to explore the balance between the proper and hybrid-improper mechanisms for polar behaviour in $A_{0.5}Nd_{0.33}TaO_3$ (*A* = Li, Na, K).

Preliminary X-ray powder diffraction (XRPD) data suggest that $K_{0.5}Nd_{0.33}TaO_3$ adopts a polar *Pm*2*m* structure, described by $\Gamma_5^- + X_1^+$, with K at 1*b* and 1*d* *A*-sites. In contrast, $Li_{0.5}Nd_{0.33}TaO_3$ and $Na_{0.5}Nd_{0.33}TaO_3$ crystallise in the centrosymmetric *Cmmm* space group, described by M_5^- mode. In these phases, Li^+ and Na^+ occupy the 4*j* *A*-sites respectively.

The unit cell volume of $Nd_{0.33}TaO_3$ is larger than $Na_{0.5}Nd_{0.33}TaO_3$ and $Li_{0.5}Nd_{0.33}TaO_3$. This is consistent with reduction of some Ta^{5+} to Ta^{4+} upon Li^+/Na^+ intercalation, which leads to reduction of unit cell volume. Notably, the decrease in the *a* unit cell parameter is more pronounced than in *b*, while the *c* parameter shows the smallest change. This suggests that the change in the structure to intercalation is not uniform.

Comparison of the XRPD-derived structures of $A_{0.5}Nd_{0.33}TaO_3$ (*A* = Li, Na) suggests a greater degree of octahedral tilting in the Li-containing phase compared to Na-containing phase. $Li_{0.5}Nd_{0.33}TaO_3$ is expected to have larger octahedral tilting due to a larger size mismatch between Nd^{3+} and Li^+ cations in alternating layers, which results in greater distortion in the TaO_6 framework.

Additionally, both the Li and Na phases exhibit quite distorted octahedra in the refined models, which may not be realistic. Insights from NPD data, which are more sensitive to light atoms, would be valuable for resolving the true structure of these materials.

XRPD is less sensitive to light Li and Na sites but can help detect the K sites. Preliminary analysis suggests that $K_{0.5}Nd_{0.33}TaO_3$ is the most distorted of the three compositions. One plausible explanation is the relatively large mismatch between the ionic radii of Nd^{3+} (1.27 Å) and K^+ (1.64 Å), compared to the smaller mismatches in the Na- and Li-based analogues. The XRPD analysis suggests that in small Li/Na cations octahedral tilting is alone sufficient to relieve the strain and optimise the bonding requirements in the structure. In contrast, the larger *A*-cation mismatch in $K_{0.5}Nd_{0.33}TaO_3$ requires additional structural distortions. The K^+ cation appears to be significantly displaced from the high symmetry site (1*b*) in a polar fashion. NPD together with XRPD will help accurately resolve the structure and understand the structure and composition relationship in these materials.

To further understand the local structure, particularly the number and symmetry of A^+ cation sites (*A* = Li, Na) and to assess the possibility of Ta^{5+}/Ta^{4+} charge ordering, lithium, sodium and niobium solid-state nuclear magnetic resonance (ssNMR) spectroscopy measurements are required to get insight into the local environments of these elements and cation distributions that are not accessible by diffraction techniques alone.

XRPD, NPD and ssNMR - all three techniques together will help construct a comprehensive picture of both the long-range and the local structure of $A_{0.5}Nd_{0.33}TaO_3$ (*A* = Li, Na, K) materials which will help us in understanding the mechanism of polar behaviour in them.

Symmetry analysis using ISODISTORT, suggest that M_5^- and X_1^+ in-plane octahedral tilts as well as M_2^+ and M_4^- out-of-plane octahedral tilts are possible in $A_{0.5}Nd_{0.33}TaO_3$ (*A* = Li, Na, K). The in-plane polarization, described by Γ_5^- mode, may originate either through a proper mechanism or can be induced through the combination of M_5^- and M_2^+ octahedral tilts by hybrid improper mechanism. Similarly, the out-of-plane polarization, described by Γ_3^- mode, can be proper or hybrid improper - induced by the combination of M_2^+ and M_4^- octahedral tilts.

A third potential mechanism of inducing ferroelectricity by charge ordering of *B* cation was also explored. In this case, Ta^{4+} and Ta^{5+} ions exhibit a checkerboard charge ordering pattern in *B*-cation layers. However, it was found that no combination of charge ordering, either M_2^- or M_4^+, with the allowed structural distortions results in sufficient symmetry breaking to permit out-of-plane polarization.

6.5 Conclusion

The structural investigation of *A*-site ordered $A_{0.5}Nd_{0.33}TaO_3$ phases shows that the structure undergoes a change when the vacancies in the structure are occupied by *A* = Li^+, Na^+ and K^+. XRPD analysis suggest that Li- and Na-containing phases adopt a non-polar *Cmmm* structure whereas $K_{0.5}Nd_{0.33}TaO_3$ adopts a more distorted (and possibly polar) structure. The study also highlights the limitations of XRPD.

From symmetry analysis it was found the polarization can be induced through geometric as well as electronic means. Although rocksalt Ta^{4+}/Ta^{5+} charge ordering was considered as a potential way of stabilising polar ground state, it does not produce sufficient symmetry breaking to support out-of-plane polar behaviour.

6.6 Future Work

To accurately determine the structure of $A_{0.5}Nd_{0.33}TaO_3$ (*A* = Li, Na, K) NPD is necessary, particularly for locating the position of light elements. Solid-state NMR would be able to aid in determining the local environments and symmetries of *A*-site and *B*-site cations within the structure. Second harmonic generation (SHG) measurements will help confirm if the materials are non-centrosymmetric. Density functional theory (DFT) calculations will help predict energetically favourable distortion modes and explore the interplay between octahedral tilts, polar displacements and polarization mechanisms.

Through a combined experimental and computational study, a more comprehensive understanding of structure - composition relationship in *A*-site deficient perovskite systems can be achieved which will help design new battery materials or ionic conductors.

1. H. Rooksby, E. White and S. Langston, *Journal of the American Ceramic Society*, 1965, **48**, 447-449.
2. B. J. Kennedy, C. J. Howard, Y. Kubota and K. Kato, *Journal of Solid State Chemistry*, 2004, **177**, 4552-4556.
3. F. Azough, R. Freer and B. Schaffer, *Journal of the American Ceramic Society*, 2010, **93**, 1237-1240.
4. P. Iyer and A. Smith, *Acta Crystallographica*, 1967, **23**, 740-746.
5. Z. Zhang, C. J. Howard, B. J. Kennedy, K. S. Knight and Q. Zhou, *Journal of Solid State Chemistry*, 2007, **180**, 1846-1851.
6. Q. Zhou, P. J. Saines, N. Sharma, J. Ting, B. J. Kennedy, Z. Zhang, R. L. Withers and K. S. Wallwork, *Chemistry of Materials*, 2008, **20**, 6666-6676.
7. A. NADIRI, G. LE FLEM and C. DELMAS, *Journal of solid state chemistry*, 1988, **73**, 338-347.
8. B. J. Campbell, H. T. Stokes, D. E. Tanner and D. M. Hatch, *Journal of Applied Crystallography*, 2006, **39**, 607-614.
9. R. Shankar PN, F. Orlandi, P. Manuel, W. Zhang, P. S. Halasyamani and A. Sundaresan, *Chemistry of Materials*, 2020, **32**, 5641-5649.
10. H. M. Rietveld, *Applied Crystallography*, 1969, **2**, 65-71.
11. A. A. Coelho, *Coelho Software, Brisbane, Australia*, 2007.
12. A. Coelho, *Karlsruhe, Germany*, 2012.
13. D. Beqiri, V. Cascos, J. Roberts-Watts, E. R. Clark, E. Bousquet, N. C. Bristowe and E. E. McCabe, *Chemical Communications*, 2019, **55**, 2609-2612.

Chapter 7: Conclusions and Future Work

Since the discovery of layered perovskites-related materials, the interest in them has continuously increased due to their promising properties such as ferroelectricity, ionic conductivity, ion exchange, photocatalysis.[1-4] This thesis focuses on experimental and computational investigations of layered perovskite-related materials namely Dion-Jacobson phases, Aurivillius phases and Ruddlesden-Popper phases to elucidate the structure-composition-property relationships in these materials in order to have a better understanding of these materials. A deeper understanding of these relationships is essential for developing optimised functional materials.

The structure-composition-property relationships of the n = 3 $A'A_2B_3O_{10}$ (A' = Rb, Cs; A = Ca, Sr, Ba; B = Nb, Ta) Dion-Jacobson phases were investigated. Ferroelectricity in these phases was found to originate from a proper mechanism rather than a hybrid improper mechanism. The study shows that as the size of the A-cation decreases, the tolerance factor decreases which leads to structural distortions such as tilting/rotations of octahedra about an in-plane, out-of-plane or both axes and polar/antipolar displacements of cations to satisfy the bonding requirements of the smaller A-cations.

The findings show that not only the geometric factors, but electronic factors also play a role in determining the structure of these materials. When the B-cation is changed from Nb^{5+} to Ta^{5+}, the in-plane polar displacements in the structure are reduced. This is due to the weaker SOJT effect of Ta^{5+} cation compared to Nb^{5+}. In addition to structural trends, the study also shows the dependence of bandgap on the size of A-cation such that as the size of A-cation decreases, the bandgap of the material increases.

To complement these results, future studies involving P-E hysteresis loop measurements would be valuable to confirm the ferroelectric behaviour of the polar phases.

Chapter 4 explores the structure-composition relationship in the n = 2 $Bi_2A_{0.5}La_{0.5}B_2O_9$ (A = Na, K; B = Nb, Ta) Aurivillius phases and $Li_2AB_2O_7$ (A = Ca, Sr, Ba; B = Nb, Ta) Ruddlesden-Popper phases. The study demonstrates a delicate competition between the polar and anti-polar states in these materials and suggests

how tuning the composition can tune the energy landscapes in these layered perovskite-related materials. The shallowest energy landscape is observed in the material which combines a large *A*-cation and *B*-cation with a weak SOJT effect.

The study further highlights the interplay between geometric and electronic factors in stabilising polar/antipolar phases in these materials. To build on these results, future studies such as second-harmonic generation (SHG) measurements would help confirm the polarity of the materials, while P-E hysteresis loop measurements would be valuable in verifying the ferroelectric nature of the polar structures. Additionally, exploring the substitution of Rb in place of K or Na may offer further insight into compositional tuning of the energy landscape.

The fluorination of the n = 2 $La_2SrFe_2O_7$ Ruddlesden-Popper phase has also been investigated in this thesis. The results show that inserting fluoride ions into $La_2SrFe_2O_7$ structure leads to tilting and rotation of FeX_6 octahedra. This results in the breaking of inversion symmetry but due the displacement of *A*-cations in opposite direction in adjacent perovskite layers, the net polar displacement is zero. As a result, $La_2SrFe_2O_7F_2$ adopts an antipolar centrosymmetric *Pnam* space group. This study demonstrates that topochemical fluorination of RP phases provides an alternative route, alongside cation substitution and tolerance factor tuning, for manipulating octahedral distortions in Ruddlesden-Popper phases to stabilise polar/antipolar structures.

For future work, it would be valuable to explore alternative synthetic methods, including more or less oxidising conditions, to assess whether this plays a role in the structures observed, or whether more crystalline phases could be obtained which would help with structural analysis. Additionally, techniques such as ^{19}F ssNMR could provide deeper insight into the local fluoride environments and their role in driving structural distortions.

Finally, a preliminary investigation on *A*-site deficient perovskites with $Nd_{0.33}TaO_3$ composition was conducted to explore how the structure evolves upon the insertion of monovalent cations Li^+, Na^+ and K^+ into the vacant *A*-site. Analysis of the XRPD data suggests that the Li- and Na-containing phases adopt a non-polar *Cmmm* structure whereas $K_{0.5}Nd_{0.33}TaO_3$ adopts a more distorted (and possibly polar) structure. The more distorted structure of $K_{0.5}Nd_{0.33}TaO_3$ is presumably due to the larger size mismatch between Nd^{3+} and K^+. A third potential mechanism of inducing ferroelectricity by charge ordering of *B*-cations was also explored. However, it was

found that no combination of charge ordering with allowed structural distortions results in sufficient symmetry breaking to allow out-of-plane polarization.

Future work will include NPD measurements to accurately determine the structure of $A_{0.5}Nd_{0.33}TaO_3$ (*A* = Li, Na, K). Solid-state NMR will help determine the local environments and symmetries of *A*-site and *B*-site cations within the structure. Second harmonic generation (SHG) measurements will be essential to verify the polarity of the materials. Density functional theory (DFT) calculations will be done to predict energetically favourable distortion modes and explore the interplay between octahedral tilts, polar displacements and polarization mechanisms. Magnetic measurements of the reduced samples - containing paramagnetic Ta^{4+} ions along with Nd^{3+} - may provide valuable information about magnetic behaviour and any relationship between structure and magnetic properties.

1. N. A. Benedek, J. M. Rondinelli, H. Djani, P. Ghosez and P. Lightfoot, *Dalton Transactions*, 2015, **44**, 10543-10558.
2. K. R. Kendall, C. Navas, J. K. Thomas and H.-C. zur Loye, *Chemistry of materials*, 1996, **8**, 642-649.
3. R. E. Schaak and T. E. Mallouk, *Chemistry of Materials*, 2002, **14**, 1455-1471.
4. I. A. Rodionov and I. A. Zvereva, *Russian Chemical Reviews*, 2016, **85**, 248.

Appendix 1

1.1 Results for $CsBa_2Nb_3O_{10}$

1.1.1 Lower symmetry Γ_5^- *Amm*2 model

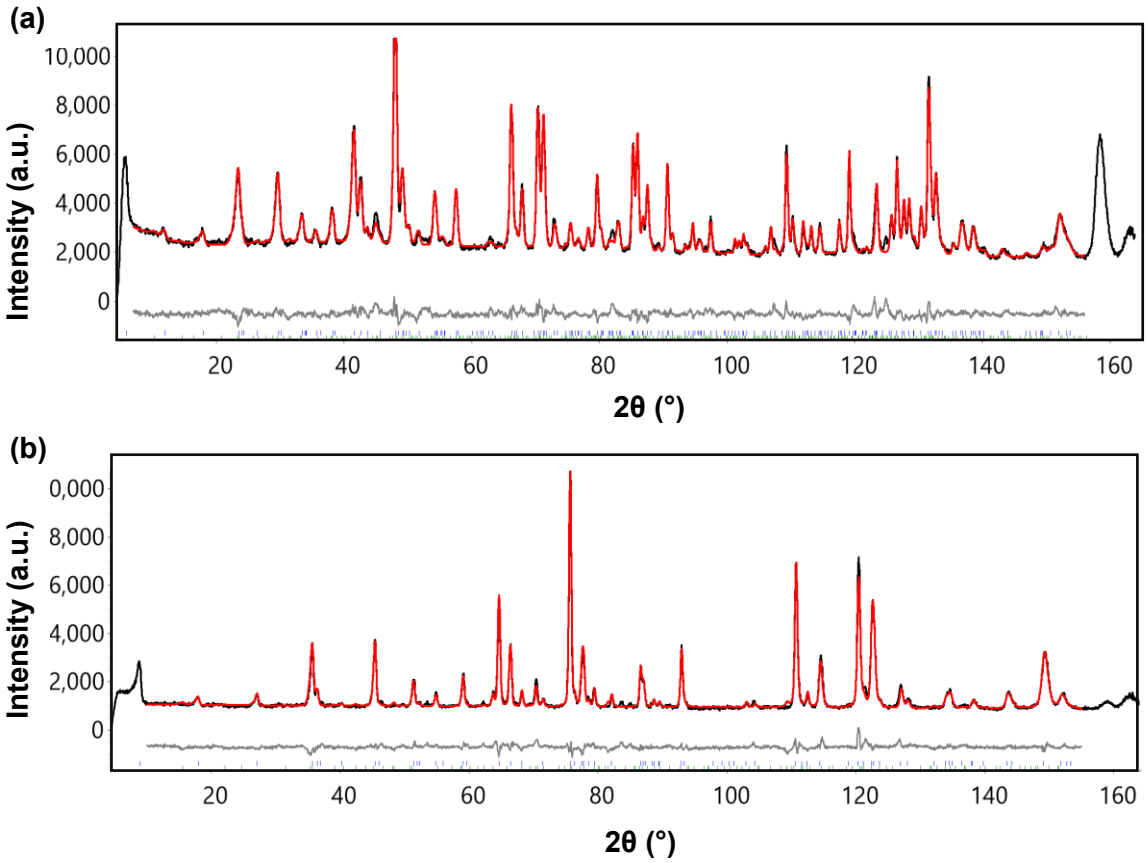

Figure 1.1: Rietveld refinement profiles from combined refinement using room-temperature (a) short wavelength (1.6218 Å) and (b) longer wavelength (2.4395 Å) NPD data for $CsBa_2Nb_3O_{10}$, refined in Γ_5^- *Amm*2 space group. The observed, calculated, and difference profiles shown in black, red, and grey respectively).

Table 1.1: Selected Bond Lengths and Bond Angles for $CsBa_2Nb_3O_{10}$ from combined refinement using room-temperature (a) short wavelength (1.6218 Å) and (b) longer wavelength (2.4395 Å) NPD data in space group *P4/mmm.*

Bond	Bond Length (Å)	Bond	Bond Length (Å)
Nb(1)-O(1)	1.98853(3)	Ba(1)-O(1)	2.988(3)
Nb(1)-O(2)	1.952(3)	Ba(1)-O(2)	2.8260(4)
Nb(2)-O(2)	2.553(4)	Ba(1)-O(3)	2.762(3)
Nb(2)-O(3)	2.0203(5)	Cs(1)-O(4)	3.2101(2)
Nb(2)-O(4)	1.741(4)		

1.2 Results for $CsSr_2Nb_3O_{10}$

Table 1.2: Selected Bond Lengths and Bond Angles for $CsSr_2Nb_3O_{10}$ from combined refinement using room-temperature (a) short wavelength (1.6218 Å) and (b) longer wavelength (2.4395 Å) NPD data in space group *P4/mbm.*

Bond	Bond Length (Å)/Bond Angle (°)	Bond	Bond Length (Å)/Bond Angle (°)
Nb(1)-O(11)	2.001(2)	Sr(1)-O(11)	2.709(2)
Nb(1)-O(21)	1.935(2)	Sr(1)-O(21)	2.780(3)
Nb(2)-O(21)	2.445(3)	Sr(1)-O(31)	2.599(2), 2.615(2)
Nb(2)-O(31)	1.998(1)	Cs(1)-O(41)	3.178(1)
Nb(2)-O(41)	1.764(3)	O(11)-O(11)-O(11)	155.27(1)

1.3 Results for $CsCa_2Nb_3O_{10}$

1.3.1 Rietveld refinement profile of *Pnam* model.

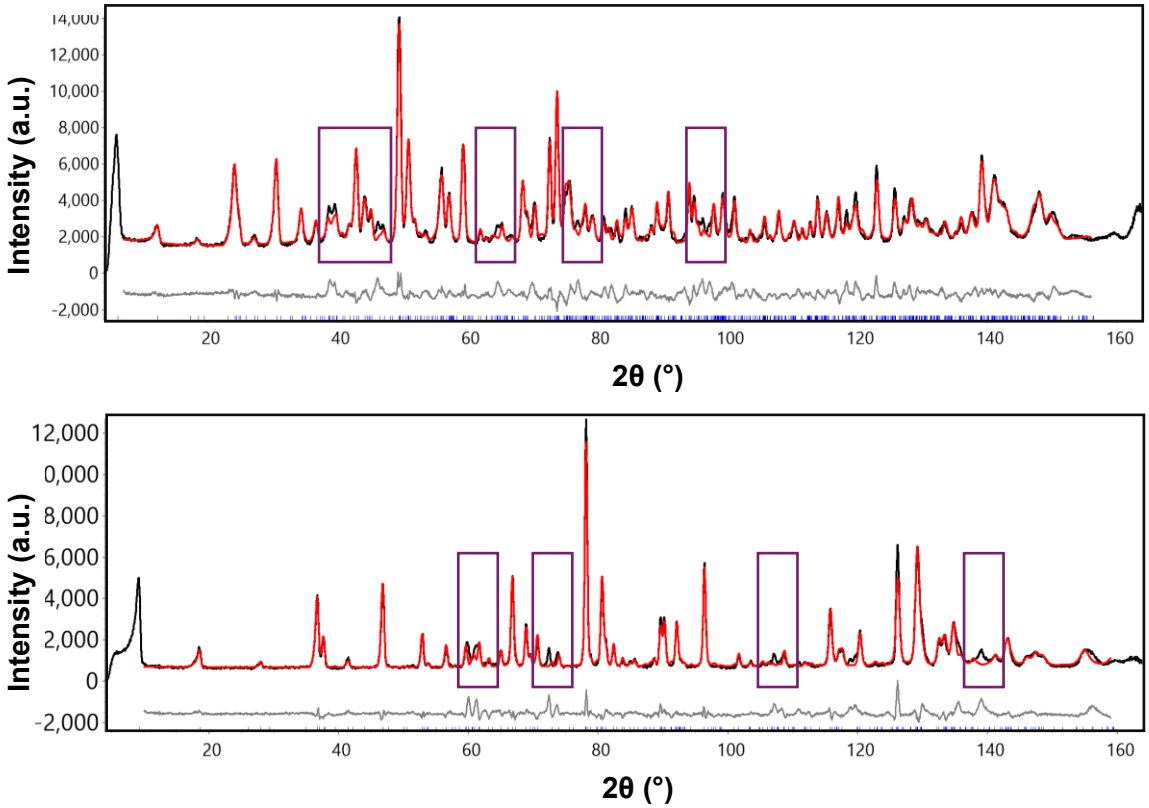

Figure 3.9: Rietveld refinement profiles from combined refinement using room-temperature (a) short wavelength (1.6218 **Å**) and (b) longer wavelength (2.4395 **Å**) NPD data for $CsCa_2Nb_3O_{10}$, refined in space group *Pnam*. The observed, calculated, and difference profiles shown in black, red, and grey respectively).

1.3.2 Selected mode amplitudes (Å) from refinement using room temperature NPD data for $CsCa_2Nb_3O_{10}$.

Mode	Amplitudes (Å)		
	Pmcn **(X_3^+ + A_5^+ (M_3^+))**	***P2₁cn*** **(X_3^+ + A_5^+ (M_3^+) + Γ_5^-)**	***Pm2₁n*** **(X_3^+ + A_5^+ (M_3^+) + Γ_5^-)**
M_3^+	0.61	0.60	0.49
X_3^+	0.74	0.75	0.75
A_5^+	0.71	0.68	0.69
Γ_5^-	-	0.32	0.21

1.3.3 Comparison of BVS between *Pna*2₁ and *Pmn*2₁ models for $CsCa_2B_3O_{10}$ (*B* = Nb, Ta).

$CsCa_2Nb_3O_{10}$	BVS		$CsCa_2Ta_3O_{10}$	BVS	
	Pna2₁	***Pmn2₁***		***Pna2₁***	***Pmn2₁***
Nb11	4.905	5.010	Ta11	5.609	5.160
Nb12	5.161	5.059	Ta12	4.797	5.208
Nb21	4.787	4.863	Ta21	5.110	4.917
Nb22	5.493	4.833	Ta22	4.973	5.011
Nb23	5.178	5.290	Ta23	5.703	4.995
Nb24	4.439	5.125	Ta24	4.828	5.183

Table 1.3: Selected bond lengths and bond angles for $CsCa_2Nb_3O_{10}$ from combined refinement using room-temperature (a) short wavelength (1.6218 Å) and (b) longer wavelength (2.4395 Å) NPD data in space group *Pm*2_1*n*.

Bond	Bond Length (Å)/Bond Angle (°)	Bond	Bond Length (Å)/Bond Angle (°)	Bond	Bond Length (Å)/Bond Angle (°)	Bond	Bond Length (Å)/Bond Angle (°)
Nb(11)-O(11)	2.07(3)	Nb(12)-O(11)	1.99(4)	Nb(21)-O(21)	2.18(1)	Nb(22)-O(22)	2.43(2)
Nb(11)-O(12)	1.86(3)	Nb(12)-O(12)	2.15(4)	Nb(21)-O(31)	1.94(3)	Nb(22)-O(31)	2.01(3)
Nb(11)-O(13)	1.98(1)	Nb(12)-O(14)	1.98(1)	Nb(21)-O(32)	2.08(3)	Nb(22)-O(32)	1.92(3)
Nb(11)-O(16)	2.08(1)	Nb(12)-O(15)	1.99(1)	Nb(21)-O(38)	1.99(1)	Nb(22)-O(37)	1.99(1)
Nb(11)-O(21)	2.13(1)	Nb(12)-O(22)	1.90(3)	Nb(21)-O(312)	1.94(1)	Nb(22)-O(311)	1.98(1)
Nb(11)-O(24)	1.84(2)	Nb(12)-O(23)	1.88(3)	Nb(21)-O(41)	1.87(3)	Nb(22)-O(42)	1.84(3)
Nb(23)-O(23)	2.56(2)	Nb(23)-O(36)	2.00(1)	Nb(24)-O(24)	2.41(2)	Nb(24)-O(35)	2.08(1)
Nb(23)-O(33)	2.01(4)	Nb(23)-O(310)	2.03(1)	Nb(24)-O(33)	1.97(3)	Nb(24)-O(39)	1.97(1)
Nb(23)-O(34)	1.95(4)	Nb(23)-O(43)	1.66(2)	Nb(24)-O(34)	2.05(3)	Nb(24)-O(44)	1.68(2)
Ca(11)-O(11)	3.51(3)	Ca(11)-O(15)	2.92(5)	Ca(11)-O(16)	2.39(5)	Ca(11)-O(21)	2.86(3)
Ca(11)-O(22)	2.18(3)	Ca(11)-O(31)	2.76(3)	Ca(11)-O(37)	2.75(4)	Ca(11)-O(38)	2.53(4)
Ca(12)-O(12)	2.49(3)	Ca(12)-O(16)	3.15(4)	Ca(12)-O(22)	3.02(3)	Ca(12)-O(37)	2.61(4)
Ca(12)-O(15)	3.73(4)	Ca(12)-O(21)	2.96(3)	Ca(12)-O(32)	2.38(3)	Ca(12)-O(38)	2.17(4)
Ca(13)-O(12)	3.48(3)	Ca(13)-O(14)	3.27(5)	Ca(13)-O(24)	2.78(3)	Ca(13)-O(35)	2.30(5)
Ca(13)-O(13)	2.50(5)	Ca(13)-O(23)	2.38(4)	Ca(13)-O(33)	2.71(3)	Ca(13)-O(36)	2.57(5)

Ca(14)-O(11)	2.31(3)	Ca(14)-O(14)	2.76(5)	Ca(14)-O(24)	3.31(4)	Ca(14)-O(35)	2.35(5)
Ca(14)-O(13)	2.75(5)	Ca(14)-O(23)	2.71(4)	Ca(14)-O(34)	2.52(3)	Ca(14)-O(36)	2.59(5)
Ca(15)-O(11)	2.93(4)	Ca(15)-O(14)	2.51(5)	Ca(15)-O(22)	2.73(3)	Ca(15)-O(311)	2.42(5)
Ca(15)-O(13)	3.38(4)	Ca(15)-O(21)	2.44(4)	Ca(15)-O(31)	2.60(3)	Ca(15)-O(312)	2.85(4)
Ca(16)-O(12)	3.00(3)	Ca(16)-O(14)	3.17(5)	Ca(16)-O(22)	3.46(4)	Ca(16)-O(311)	2.64(5)
Ca(16)-O(13)	3.01(4)	Ca(16)-O(21)	2.52(4)	Ca(16)-O(32)	2.44(3)	Ca(16)-O(312)	2.65(4)
Ca(17)-O(12)	3.03(3)	Ca(17)-O(16)	3.77(4)	Ca(17)-O(24)	2.44(4)	Ca(17)-O(39)	2.61(4)
Ca(17)-O(15)	2.94(4)	Ca(17)-O(23)	2.71(3)	Ca(17)-O(33)	2.74(3)	Ca(17)-O(310)	2.15(4)
Ca(18)-O(11)	2.94(3)	Ca(18)-O(16)	2.62(4)	Ca(18)-O(24)	2.73(4)	Ca(18)-O(39)	2.71(4)
Ca(18)-O(15)	2.35(4)	Ca(18)-O(23)	3.22(3)	Ca(18)-O(34)	2.36(3)	Ca(18)-O(310)	2.57(4)
Cs(11)-O(41)	2.97(3), 3.37(3)	Cs(12)-O(41)	3.00(3), 3.27(3)	Cs(13)-O(43)	3.17(3), 3.24(3)	Cs(14)-O(43)	3.16(3), 3.19(3)
Cs(11)-O(42)	3.12(3), 3.17(3)	Cs(12)-O(42)	3.01(3), 3.27(3)	Cs(13)-O(44)	2.99(3), 3.49(3)	Cs(14)-O(44)	3.04(3), 3.41(3)
O(11)-O(12)-O(11)	146.9(7)	O(42)-O(22)-O(23)	155.4(7)	O(21)-O(24)-O(44)	157.9(7)	O(34)-O(33)-O(34)	162.2(7)
O(14)-O(15)-O(14)	164(1)	O(22)-O(23)-O(43)	156.9(8)	O(11)-O(12)-O(11)	146.9(7)	O(310)-O(36)-O(310)	170.7(7)
O(13)-O(16)-O(13)	149.6(9)	O(41)-O(21)-O(24)	158.6(7)	O(31)-O(32)-O(31)	167.5(6)	O(39)-O(35)-O(39)	162.1(9)
O(15)-O(14)-O(15)	164(1)	O(41)-O(21)-O(24)	158.6(7)	O(42)-O(22)-O(23)	155.4(7)		
O(16)-O(13)-O(16)	149.6(9)	O(21)-O(24)-O(44)	157.9(7)	O(22)-O(23)-O(43)	156.9(8)		

1.4 Results for $CsCa_2Ta_3O_{10}$

Table 1.4: Selected bond lengths and bond angles for $CsCa_2Ta_3O_{10}$ using room-temperature longer wavelength (2.4395 Å) NPD data in space group *Pm*2$_1$*n*.

Bond	Bond Length (Å)/Bond Angle (°)	Bond	Bond Length (Å)/Bond Angle (°)	Bond	Bond Length (Å)/Bond Angle (°)	Bond	Bond Length (Å)/Bond Angle (°)
Ta(11)-O(11)	1.96(9)	Ta(12)-O(11)	1.99(4)	Ta(21)-O(21)	2.32(8)	Ta(22)-O(22)	2.42(8)
Ta(11)-O(12)	1.95(8)	Ta(12)-O(12)	2.1(1)	Ta(21)-O(31)	2.0(1)	Ta(22)-O(31)	2.00(1)
Ta(11)-O(13)	2.03(8)	Ta(12)-O(14)	2.03(7)	Ta(21)-O(32)	1.9(1)	Ta(22)-O(32)	1.981)
Ta(11)-O(16)	1.94(7)	Ta(12)-O(15)	1.99(7)	Ta(21)-O(38)	2.03(7)	Ta(22)-O(37)	2.00(7)
Ta(11)-O(21)	2.02(9)	Ta(12)-O(22)	1.87(9)	Ta(21)-O(312)	1.96(7)	Ta(22)-O(311)	1.98(7)
Ta(11)-O(24)	1.97(8)	Ta(12)-O(23)	1.88(8)	Ta(21)-O(41)	1.82(8)	Ta(22)-O(42)	1.79(8)
Ta(23)-O(23)	2.51(6)	Ta(23)-O(36)	1.98(7)	Ta(24)-O(24)	2.34(7)	Ta(24)-O(35)	2.11(8)
Ta(23)-O(33)	1.9(1)	Ta(23)-O(310)	2.02(7)	Ta(24)-O(33)	1.9(1)	Ta(24)-O(39)	1.97(7)
Ta(23)-O(34)	1.9(1)	Ta(23)-O(43)	1.80(7)	Ta(24)-O(34)	2.05(1)	Ta(24)-O(44)	1.73(8)
Ca(11)-O(11)	3.29(7)	Ca(11)-O(16)	2.7(1)	Ca(11)-O(22)	2.3(1)	Ca(11)-O(37)	2.7(1)
Ca(11)-O(15)	2.9(1)	Ca(11)-O(21)	2.8(1)	Ca(11)-O(31)	2.63(7)	Ca(11)-O(38)	2.5(1)
Ca(12)-O(12)	2.3(1)	Ca(12)-O(16)	3.15(4)	Ca(12)-O(22)	2.6(1)	Ca(12)-O(37)	2.4(1)
Ca(12)-O(15)	3.5(1)	Ca(12)-O(21)	3.1(1)	Ca(12)-O(32)	2.4(1)	Ca(12)-O(38)	2.4(1)

Ca(13)-O(12)	3.73(7)	Ca(13)-O(14)	3.7(1)	Ca(13)-O(24)	2.7(1)	Ca(13)-O(35)	2.0(1)
Ca(13)-O(13)	2.4(1)	Ca(13)-O(23)	2.4(1)	Ca(13)-O(33)	2.55(7)	Ca(13)-O(36)	2.5(1)
Ca(14)-O(11)	2.5(1)	Ca(14)-O(14)	2.8(1)	Ca(14)-O(24)	3.1(1)	Ca(14)-O(35)	2.3(1)
Ca(14)-O(13)	3.1(1)	Ca(14)-O(23)	2.7(1)	Ca(14)-O(34)	2.4(1)	Ca(14)-O(36)	2.3(1)
Ca(15)-O(11)	3.01(1)	Ca(15)-O(14)	2.3(1)	Ca(15)-O(22)	2.7(1)	Ca(15)-O(311)	2.2(1)
Ca(15)-O(13)	3.7(1)	Ca(15)-O(21)	2.5(1)	Ca(15)-O(31)	2.56(8)	Ca(15)-O(312)	2.8(1)
Ca(16)-O(12)	3.06(8)	Ca(16)-O(14)	3.04(1)	Ca(16)-O(22)	3.1(1)	Ca(16)-O(311)	2.5(1)
Ca(16)-O(13)	2.8(1)	Ca(16)-O(21)	2.6(1)	Ca(16)-O(32)	2.47(9)	Ca(16)-O(312)	2.6(1)
Ca(17)-O(12)	2.9(1)	Ca(17)-O(16)	3.1(1)	Ca(17)-O(24)	2.4(1)	Ca(17)-O(39)	2.6(1)
Ca(17)-O(15)	2.9(1)	Ca(17)-O(23)	2.8(1)	Ca(17)-O(33)	2.7(1)	Ca(17)-O(310)	2.2(1)
Ca(18)-O(11)	2.87(7)	Ca(18)-O(16)	2.8(1)	Ca(18)-O(24)	2.6(1)	Ca(18)-O(39)	2.7(1)
Ca(18)-O(15)	2.2(1)	Ca(18)-O(23)	3.4(1)	Ca(18)-O(34)	2.59(8)	Ca(18)-O(310)	2.6(1)
Cs(11)-O(41)	2.9(1), 3.3(1)	Cs(12)-O(41)	3.04(1), 3.2(1)	Cs(13)-O(43)	3.1(1), 3.3(1)	Cs(14)-O(43)	3.1(1), 3.3(1)
Cs(11)-O(42)	3.05(1), 3.2(1)	Cs(12)-O(42)	3.1(1), 3.1(1)	Cs(13)-O(44)	3.2(1)	Cs(14)-O(44)	3.0(1), 3.3(1)
O(11)-O(12)-O(11)	149(2)	O(42)-O(22)-O(23)	158(3)	O(21)-O(24)-O(44)	163(3)	O(34)-O(33)-O(34)	165.4(1)
O(14)-O(15)-O(14)	157(4)	O(22)-O(23)-O(43)	155(3)	O(11)-O(12)-O(11)	149(2)	O(310)-O(36)-O(310)	168(4)
O(13)-O(16)-O(13)	158(4)	O(41)-O(21)-O(24)	163(3)	O(31)-O(32)-O(31)	174(3)	O(39)-O(35)-O(39)	158(4)
O(15)-O(14)-O(15)	157(4)	O(41)-O(21)-O(24)	163(3)	O(42)-O(22)-O(23)	158(3)		
O(16)-O(13)-O(16)	158(4)	O(21)-O(24)-O(44)	163(3)	O(22)-O(23)-O(43)	155(3)		

1.4.1 Selected mode amplitudes (Å) from refinement using room temperature NPD data for $CsCa_2Ta_3O_{10}$.

Mode	Amplitudes (Å)		
	Pmcn **(X_3^+ + A_5^+ ($+M_3^+$))**	***P2₁cn*** **(X_3^+ + A_5^+ ($+M_3^+$) + Γ_5^-)**	***Pm2₁n*** **(X_3^+ + A_5^+ ($+M_3^+$) + Γ_5^-)**
M_3^+	0.59	0.38	0.45
X_3^+	0.58	0.62	0.61
A_5^+	0.72	0.71	0.70
Γ_5^-	-	0.38	0.39

1.5 Results for $RbSr_2Nb_3O_{10}$

Table 1.5: Selected Bond Lengths and Bond Angles for $RbSr_2Nb_3O_{10}$ from combined refinement using room-temperature (a) short wavelength (1.6218 Å) and (b) longer wavelength (2.4395 Å) NPD data in space group *P4/mbm.*

Bond	Bond Length (Å)/Bond Angle (°)	Bond	Bond Length (Å)/Bond Angle (°)
Nb(1)-O(11)	2.00(3)	Sr(1)-O(11)	2.693(3)
Nb(1)-O(21)	1.930(3)	Sr(1)-O(21)	2.7721(4)
Nb(2)-O(21)	2.461(3)	Sr(1)-O(31)	2.617(3)
Nb(2)-O(31)	1.989(1)	Rb(1)-O(41)	3.128(1)
Nb(2)-O(41)	1.761(4)	O(11)-O(11)-O(11)	153.83(1)

1.6 Results for $RbCa_2Nb_3O_{10}$

Table 1.6: Bond lengths and bond angles for $RbCa_2Nb_3O_{10}$ using room-temperature longer wavelength (2.4395 Å) NPD data in space group $P2_1$.

Bond	Bond Length (Å)/Bond Angle (°)	Bond	Bond Length (Å)/Bond Angle (°)	Bond	Bond Length (Å)/Bond Angle (°)	Bond	Bond Length (Å)/Bond Angle (°)
Nb(11)-O(11)	1.89(7)	Nb(21)-O(35)	1.9(1)	Nb(23)-O(38)	1.9(1)	Ca(11)-O(22)	2.4(1)
Nb(11)-O(12)	2.20(7)	Nb(21)-O(36)	2.0(1)	Nb(23)-O(43)	1.80(7)	Ca(11)-O(23)	2.6(1)
Nb(11)-O(13)	1.9(1), 2.0(1)	Nb(21)-O(41)	1.78(6)	Nb(24)-O(24)	2.51(7)	Ca(11)-O(24)	2.7(1)
Nb(11)-O(21)	1.83(7)	Nb(22)-O(22)	2.39(7)	Nb(24)-O(32)	1.89(6)	Ca(11)-O(31)	2.6(1)
Nb(11)-O(22)	1.95(7)	Nb(22)-O(32)	2.05(6)	Nb(24)-O(34)	2.00(7)	Ca(11)-O(32)	2.9(1)
Nb(12)-O(11)	2.11(7)	Nb(22)-O(34)	1.98(7)	Nb(24)-O(37)	2.0(1)	Ca(11)-O(35)	2.75(6)
Nb(12)-O(12)	1.95(7)	Nb(22)-O(35)	1.9(1)	Nb(24)-O(38)	1.9(1)	Ca(11)-O(37)	2.37(5)
Nb(12)-O(14)	1.9(1), 2.0(1)	Nb(22)-O(36)	2.0(1)	Nb(24)-O(44)	1.74(7)	Ca(12)-O(11)	3.6(1)
Nb(12)-O(23)	2.03(7)	Nb(22)-O(42)	1.71(7)	Ca(11)-O(11)	2.81(9)	Ca(12)-O(13)	2.54(6)
Nb(12)-O(24)	1.82(8)	Nb(23)-O(23)	2.38(7)	Ca(11)-O(12)	3.12(9)	Ca(12)-O(14)	3.19(5)
Nb(21)-O(21)	2.53(7)	Nb(23)-O(31)	2.10(7)	Ca(11)-O(13)	3.40(6)	Ca(12)-O(22)	2.6(1)
Nb(21)-O(31)	1.85(6)	Nb(23)-O(33)	1.93(7)	Ca(11)-O(14)	2.75(5)	Ca(12)-O(23)	2.3(1)
Nb(21)-O(33)	2.17(6)	Nb(23)-O(37)	1.9(1)	Ca(11)-O(21)	2.5(1)	Ca(12)-O(24)	2.4(1)

Ca(12)-O(31)	2.7(1)	Ca(13)-O(11)	2.9(1)	Ca(13)-O(21)	2.4(1)	Ca(13)-O(33)	2.3(1)
Ca(12)-O(32)	2.3(1)	Ca(13)-O(12)	2.7(1)	Ca(13)-O(22)	2.6(1)	Ca(13)-O(34)	2.6(1)
Ca(12)-O(36)	2.32(6)	Ca(13)-O(13)	2.63(6)	Ca(13)-O(23)	3.4(1)	Ca(13)-O(35)	2.67(6)
Ca(12)-O(38)	2.68(5)	Ca(13)-O(14)	2.62(5)	Ca(13)-O(24)	3.2(1)	Ca(13)-O(37)	2.74(5)
Ca(14)-O(11)	2.4(1)	Ca(14)-O(21)	3.2(1)	Ca(14)-O(33)	2.4(1)	Rb(11)-O(41)	2.85(9), 3.35(10)
Ca(14)-O(12)	2.2(1)	Ca(14)-O(22)	3.3(1)	Ca(14)-O(34)	2.3(1)	Rb(11)-O(42)	3.09(9), 3.2(1)
Ca(14)-O(13)	3.29(6)	Ca(14)-O(23)	2.7(1)	Ca(14)-O(36)	2.47(6)	Rb(11)-O(43)	3.0(1)
Ca(14)-O(14)	3.18(5)	Ca(14)-O(24)	2.5(1)	Ca(14)-O(38)	2.46(6)	Rb(11)-O(44)	3.0(1), 3.1(1)
Rb(12)-O(41)	3.01(9), 3.0(1)	O12-O11-O12	145(3)	O14-O14-O14	160.3(2)	O42-O22-O21	161(3)
Rb(12)-O(42)	3.00(9), 3.2(1)	O14-O14-O14	160.3(1)	O36-O35-O36	167.4(2)	O22-O21-O41	162(3)
Rb(12)-O(43)	3.2(1), 2.9(1)	O13-O13-O13	150(2)	O38-O37-O38	165.9(1)	O24-O23-O43	156(3)
Rb(12)-O(44)	3.4(1), 2.8(1)	O13-O13-O13	150(2)	O23-O24-O44	158(3)	O21-O22-O42	161(3)
O22-O21-O41	162(3)	O24-O23-O43	156(3)	O32-O34-O32	167(3)		
O44-O24-O23	158(3)	O31-O33-O31	164.1(2)	O12-O11-O12	145(3)		

1.6.1 Selected mode amplitudes (Å) from refinement using room temperature NPD data for $RbCa_2Nb_3O_{10}$.

Mode	Amplitudes (Å)		
	Pmmn (X_3^+ + ($+M_3^+$))	**P21/m (X_3^+ ($+M_3^+$) + M_5^+)**	**P21 (X_3^+ + ($+M_3^+$) + M_5^+ + Γ_5^-)**
M_3^+	0.60	0.57	0.53
X_3^+	0.88	0.76	0.77
M_5^+	-	0.67	0.64
Γ_5^-	-	-	0.26

1.7 Diffuse reflectance measurements on $CsCa_2Ta_3O_{10}$

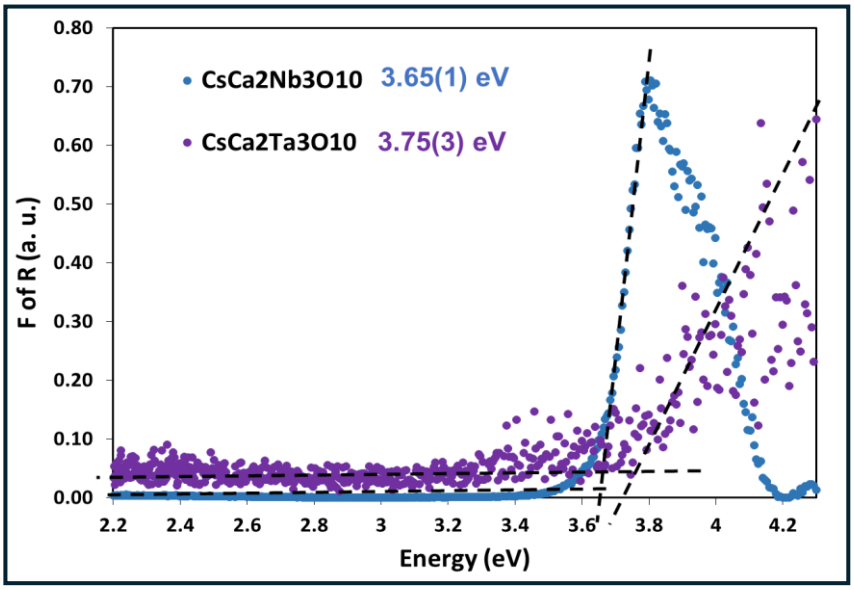

Figure 3.28: Diffuse reflectance spectra for $CsCa_2B_3O_{10}$ (B = Nb, Ta). The dotted lines indicate the band gap of the synthesized compounds. Data collected for $CsCa_2Ta_3O_{10}$ are not of high quality (possibly indicating low absorption coefficient) and do not allow the optical bandgap to be determined.

1.8 Results from DFT geometry optimisation calculations relative to high symmetry *P*4/*mmm* model (in meV per formula unit.)

Composition	***C*2*mm*** Γ_5^- **(a,a)**	***I*4/*mcm*** A_3^+ **(a)**	***P*4/*mbm*** M_3^+ **(a)**	***Icmm*** A_5^+ **(a,0)**	***Pbmn*** M_5^+ **(a,0)**	***Pmmn*** X_3^+ **(a,b) (with** M_3^+**)**	***Pmcn*** X_3^+ **(a,b) (with** M_3^+**) +** A_5^+	***P*2$_1$/*m*** X_3^+ **(a,b) (with** M_3^+**) +** M_5^+
$CsBa_2Nb_3O_{10}$	1.11	-11.4	-0.7	-0.1	3.4	-11.7		
$CsSr_2Nb_3O_{10}$	-0.1	-166.0	-166.3 **+** Γ_5^- **(*P*2$_1$*am*)** = -166.3	-24.3	-2.8	-167.4		
$CsCa_2Nb_3O_{10}$	-58.1	-398.9	-395.0	-443.1	-435.1	-556.6	-621.1 **+** Γ_5^- **(*P*2$_1$*cn*)** = -633.0 **+** Γ_5^- **(*Pm*2$_1$*n*)** = -632.7	
$CsCa_2Ta_3O_{10}$	-21.5	-368.3	-364.7	-404.1	-397.5	-496.6	-579.4 **+** Γ_5^- **(*P*2$_1$*cn*)** = -579.6 **+** Γ_5^- **(*Pm*2$_1$*n*)** = -574.0	
$RbCa_2Nb_3O_{10}$	-50.6	-424.0	-421.2	-467.3	-478.1	-566.1	-663.3	-682.7 **+** Γ_5^- **(*P*2$_1$)** = -688.0

Appendix 2

2.1 Results for $Bi_2Na_{0.5}La_{0.5}Nb_2O_9$

2.1.1 Rietveld refinement profile of *Pna*2_1 model.

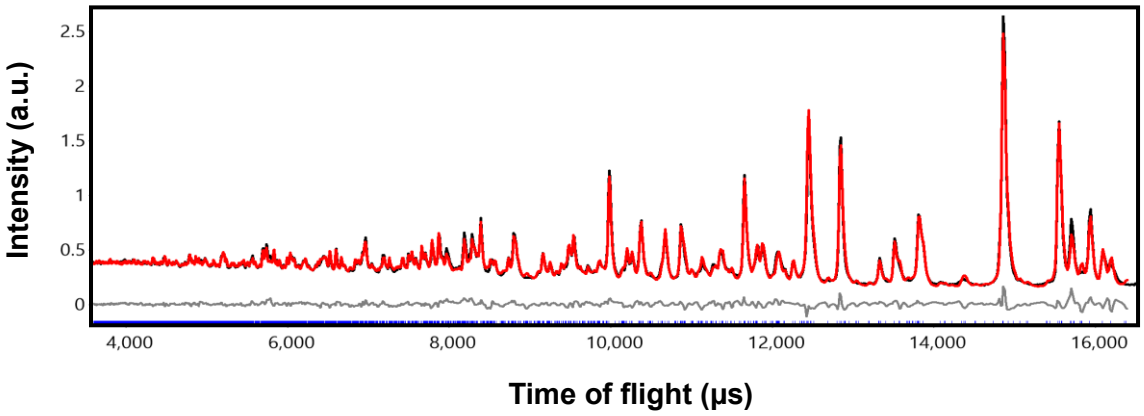

Figure 2.1: Rietveld refinement profile for highest resolution bank 6 data for $Bi_2Na_{0.5}La_{0.5}Nb_2O_9$, refined in space group *Pna*2_1. The observed, calculated, and difference profiles shown in black, red, and grey respectively).

2.1.2 Rietveld refinement profile of A21am for banks 1 through 5.

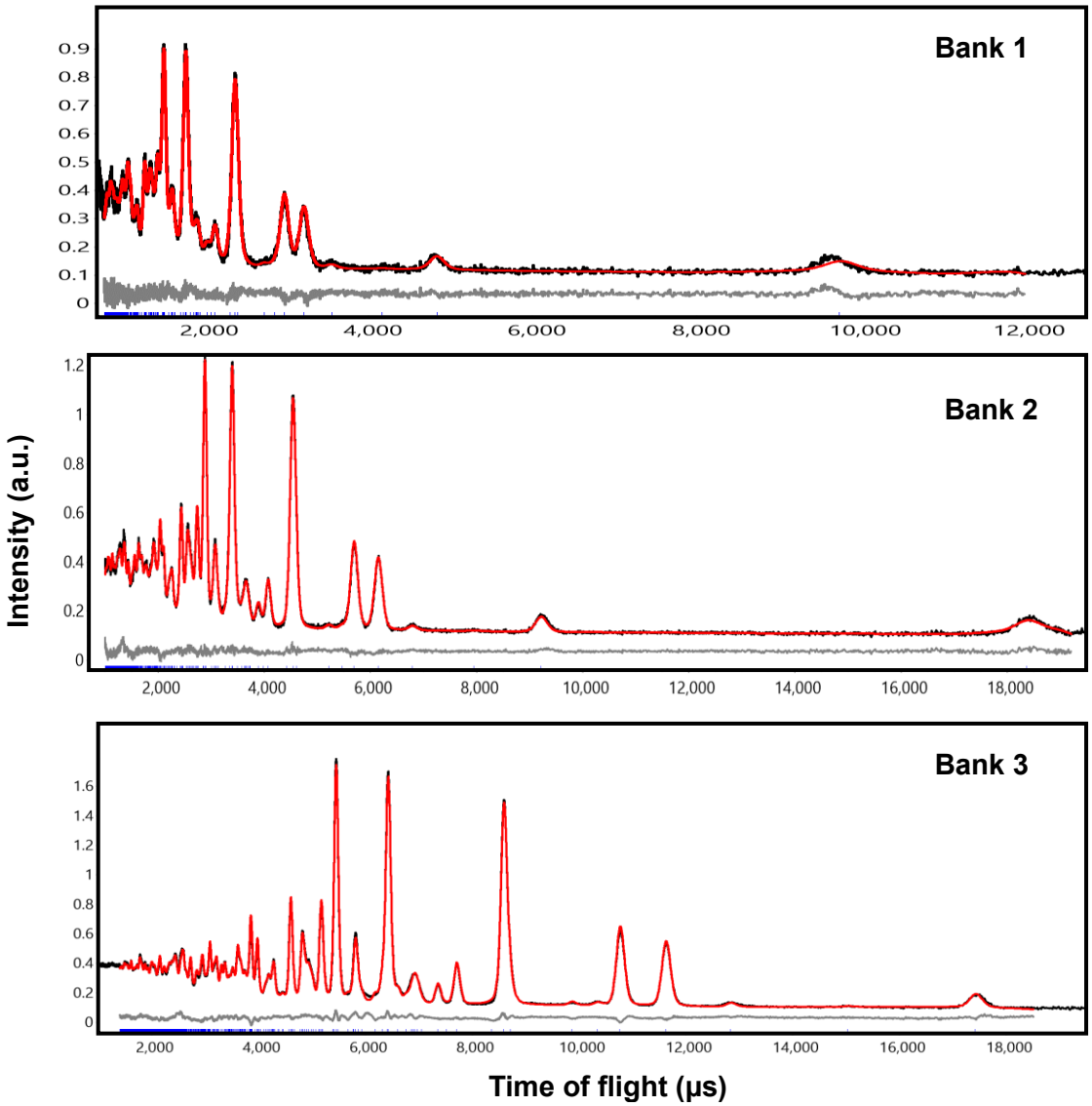

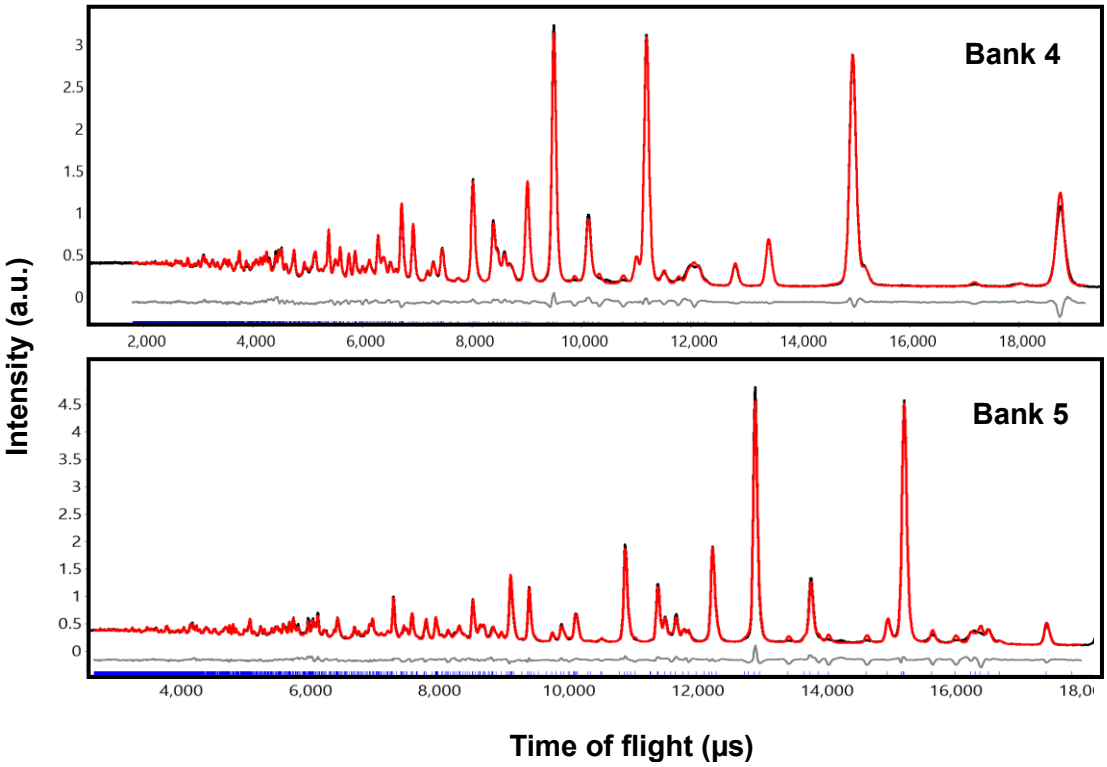

Figure 2.2: Rietveld refinement profiles for banks 1 through 5 for $Bi_2Na_{0.5}La_{0.5}Nb_2O_9$, refined in space group *A*2$_1$*am*. The observed, calculated, and difference profiles shown in black, red, and grey respectively).

2.1.3 Selected mode amplitudes (Å) from refinement using room temperature NPD data for $Bi_2Na_{0.5}La_{0.5}Nb_2O_9$.

Mode	**Amplitudes (Å)**		
	$\mathbf{X_3^- + M_5^+ + (X_1^-)}$ ***Pnab***	$\mathbf{X_3^- + M_5^- + (X_2^+)}$ ***Pnam***	$\mathbf{\Gamma_3^- + X_2^+ + X_3^-}$ ***Pna2$_1$***
M_5^-		0.31	0.25
X_2^+		0.51	0.50
X_3^-	0.65	0.65	0.56
M_5^+	0.30		0.19
X_1^-	0.50		0.25
Γ_3^-			0.29

2.2 Results for $Bi_2Na_{0.5}La_{0.5}Ta_2O_9$

2.2.1 Rietveld refinement profile of *Pna*2_1 model.

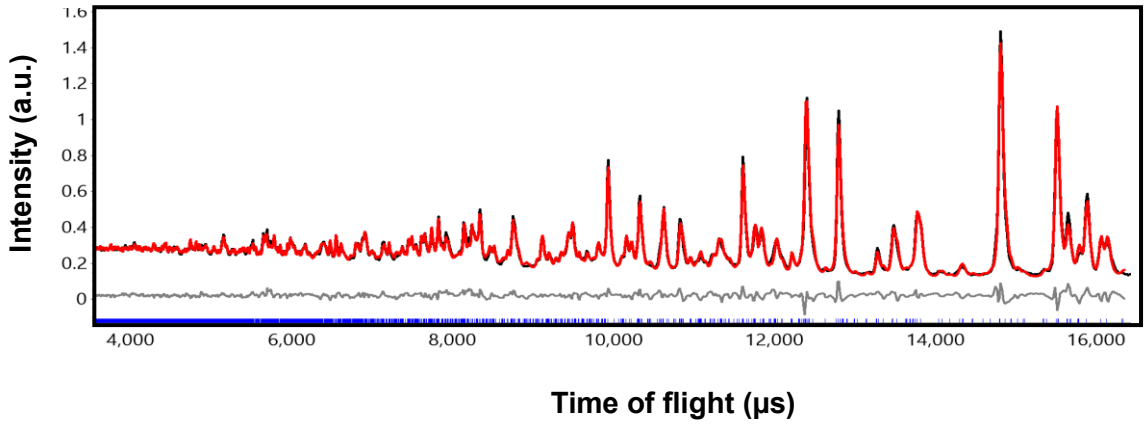

Figure 2.3: Rietveld refinement profile for highest resolution bank 6 data for $Bi_2Na_{0.5}La_{0.5}Ta_2O_9$, refined in space group *Pna*2_1. The observed, calculated, and difference profiles shown in black, red, and grey respectively).

2.2.2 Rietveld refinement profile of *A*2_1*am* model for banks 1 through 5.

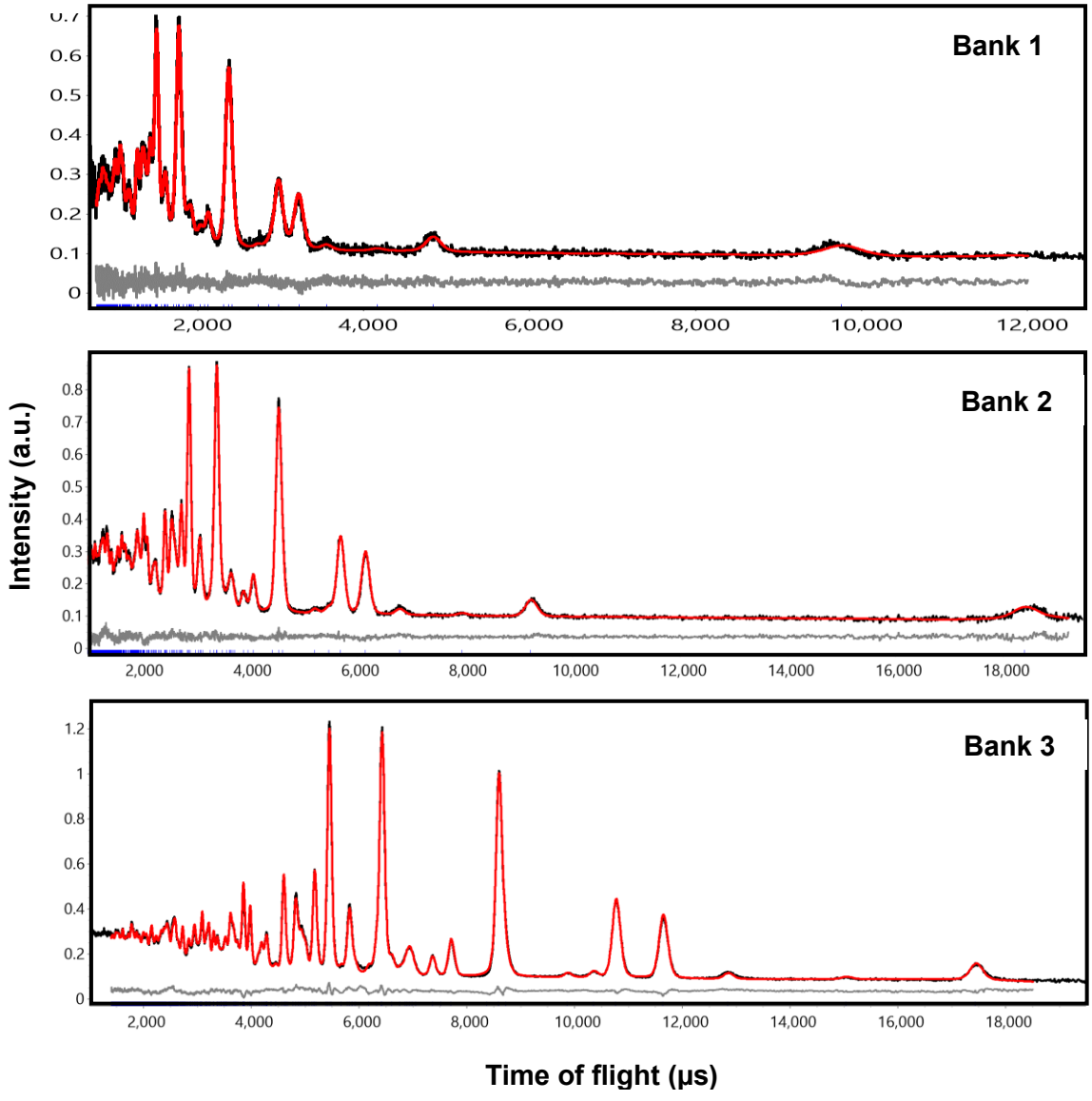

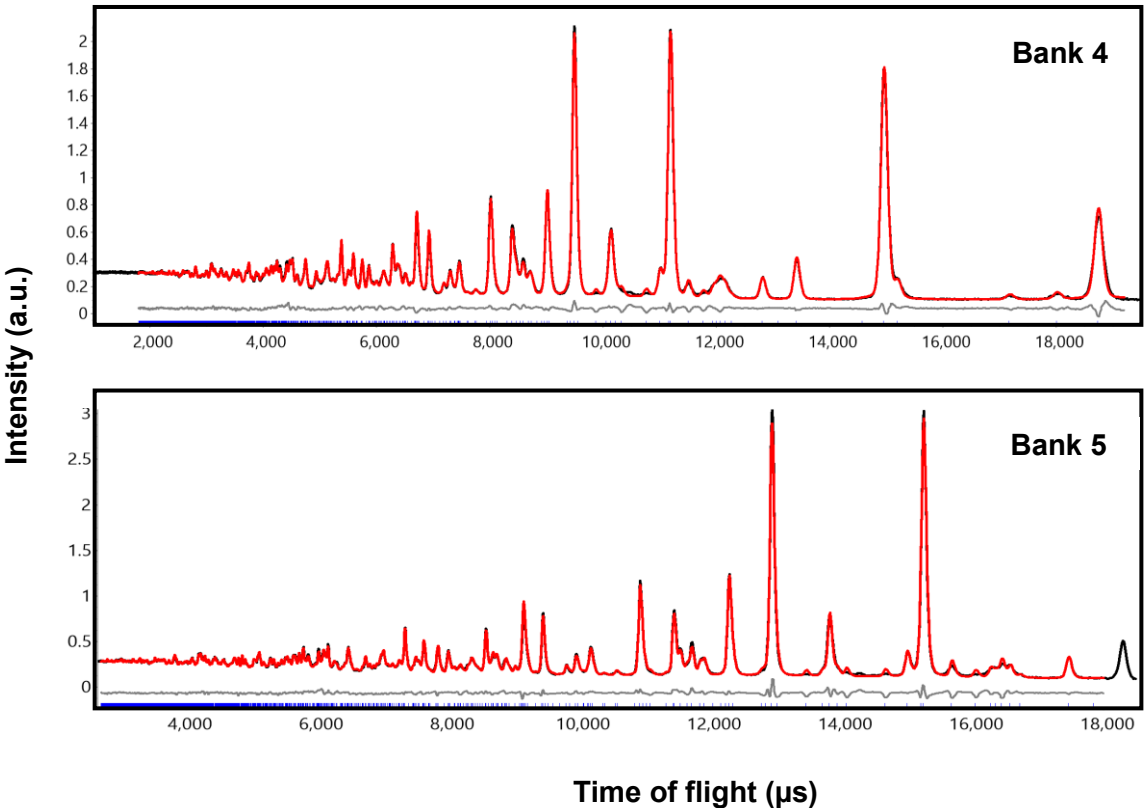

Figure 2.4: Rietveld refinement profiles for banks 1 through 5 for $Bi_2Na_{0.5}La_{0.5}Ta_2O_9$, refined in space group *A*2$_1$*am*. The observed, calculated, and difference profiles shown in black, red, and grey respectively).

2.2.3 Selected mode amplitudes (Å) from refinement using room temperature NPD data for $Bi_2Na_{0.5}La_{0.5}Ta_2O_9$.

Mode	**Amplitudes (Å)**		
	$X_3^- + M_5^+ + (X_1^-)$ ***Pnab***	$X_3^- + M_5^- + (X_2^+)$ ***Pnam***	$\Gamma_3^- + X_2^+ + X_3^-$ ***Pna2$_1$***
M_5^-		0.26	0.25
X_2^+		0.47	0.44
X_3^-	0.70	0.68	0.62
M_5^+	0.26		0.15
X_1^-	0.44		0.25
Γ_3^-			0.24

2.3 Results for $Bi_2K_{0.5}La_{0.5}Nb_2O_9$

2.3.1 Rietveld refinement profile of *Pnam* model.

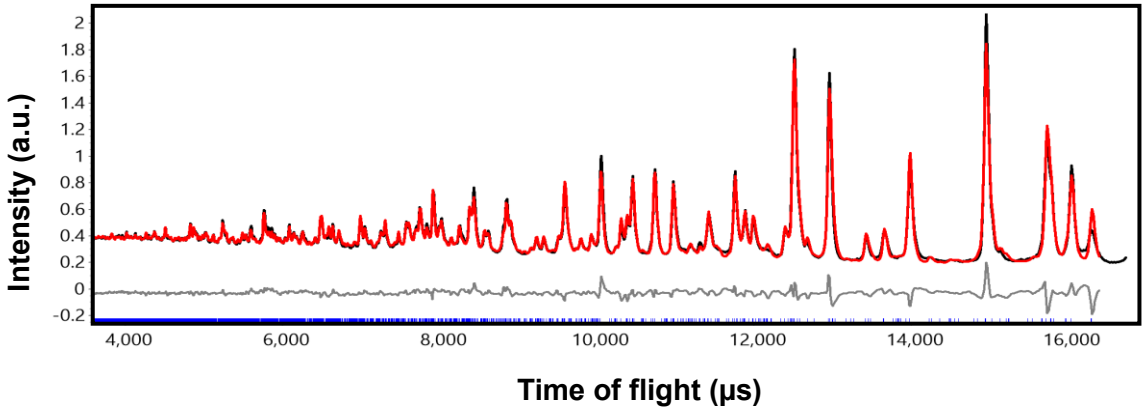

Figure 2.5: Rietveld refinement profile for highest resolution bank 6 data for $Bi_2K_{0.5}La_{0.5}Nb_2O_9$, refined in space group *Pnam*. The observed, calculated, and difference profiles shown in black, red, and grey respectively).

2.3.2 Rietveld refinement profile of *Pna*2_1 model.

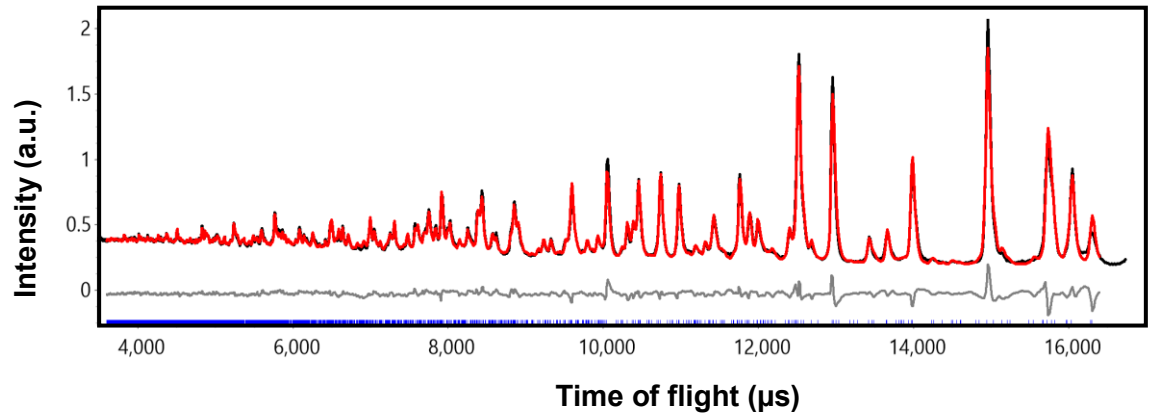

Figure 2.6: Rietveld refinement profile for highest resolution bank 6 data for $Bi_2K_{0.5}La_{0.5}Nb_2O_9$, refined in space group *Pna*2_1. The observed, calculated, and difference profiles shown in black, red, and grey respectively).

2.3.3 Rietveld refinement profile of *A*2_1*am* model for banks 1 through 5.

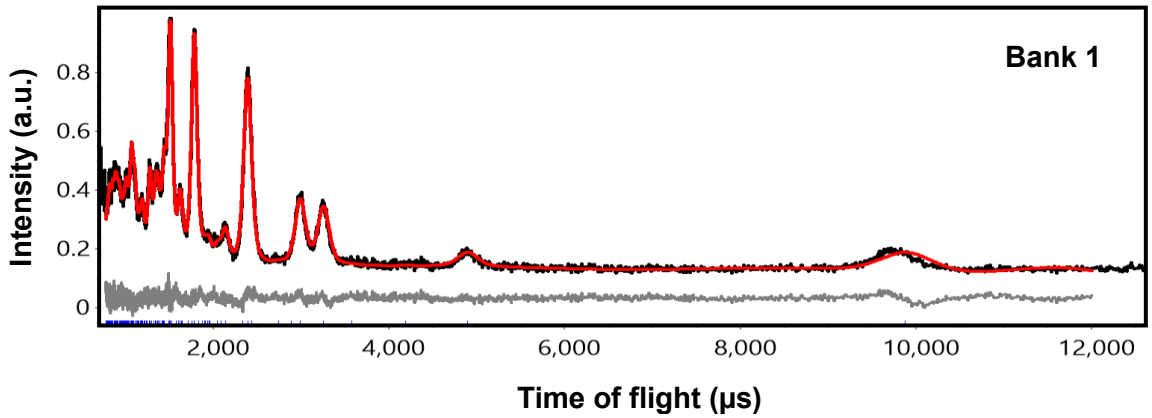

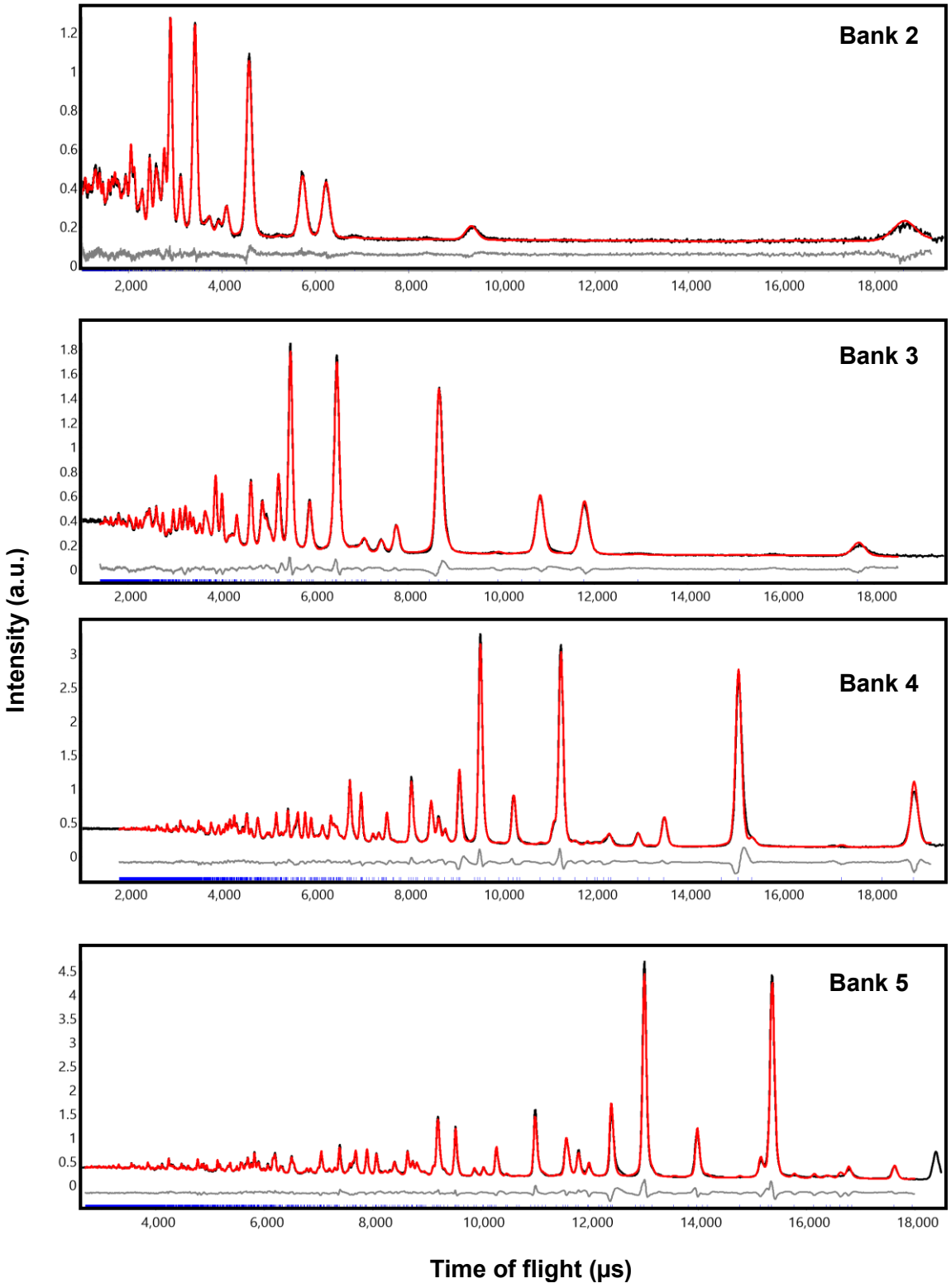

Figure 2.7: Rietveld refinement profiles for banks 1 through 5 for $Bi_2K_{0.5}La_{0.5}Nb_2O_9$, refined in space group $A2_1am$. The observed, calculated, and difference profiles shown in black, red, and grey respectively).

2.3.4 Selected mode amplitudes (Å) from refinement using room temperature NPD data for $Bi_2K_{0.5}La_{0.5}Nb_2O_9$.

Mode	Amplitudes (Å)		
	$X_3^- + M_5^+ + (X_1^-)$ ***Pnab***	$X_3^- + M_5^- + (X_2^+)$ ***Pnam***	$\Gamma_3^- + X_2^+ + X_3^-$ ***Pna2₁***
M_5^-		0.23	0.18
X_2^+		0.28	0.24
X_3^-	0.46	0.47	0.42
M_5^+	0.22		0.15
X_1^-	0.24		0.21
Γ_3^-			0.26

2.4 Results for $Bi_2K_{0.5}La_{0.5}Ta_2O_9$

2.4.1 Rietveld refinement profile of *Pnam* model.

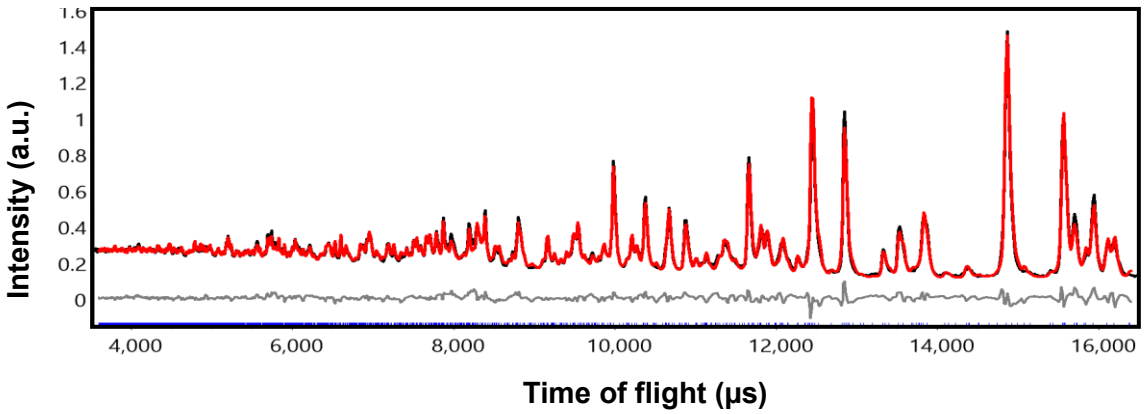

Figure 2.8: Rietveld refinement profile for highest resolution bank 6 data for $Bi_2K_{0.5}La_{0.5}Ta_2O_9$, refined in space group *Pnam*. The observed, calculated, and difference profiles shown in black, red, and grey respectively).

2.4.2 Rietveld refinement profile of *Pna*2$_1$ model.

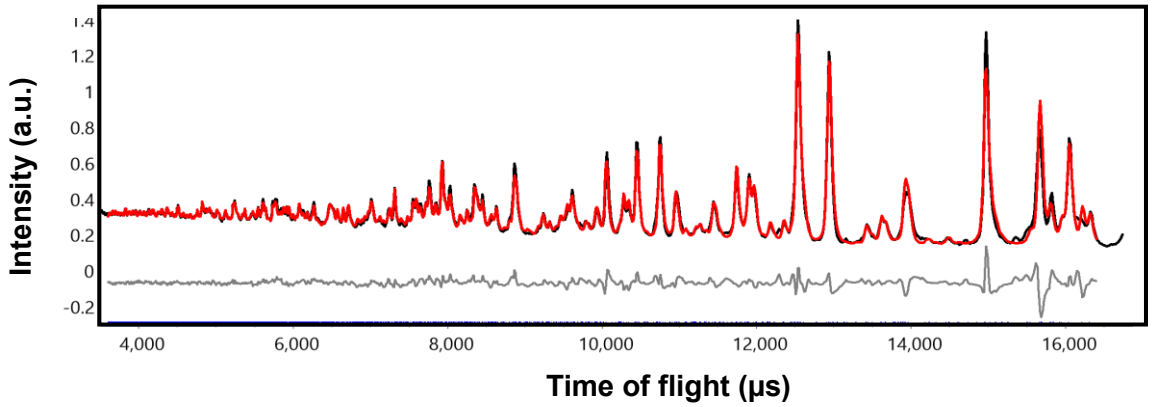

Figure 2.9: Rietveld refinement profile for highest resolution bank 6 data for $Bi_2K_{0.5}La_{0.5}Ta_2O_9$, refined in space group *Pna*2$_1$. The observed, calculated, and difference profiles shown in black, red, and grey respectively).

2.4.3 Rietveld refinement profile of *A*2$_1$*am* model for banks 1 through 5.

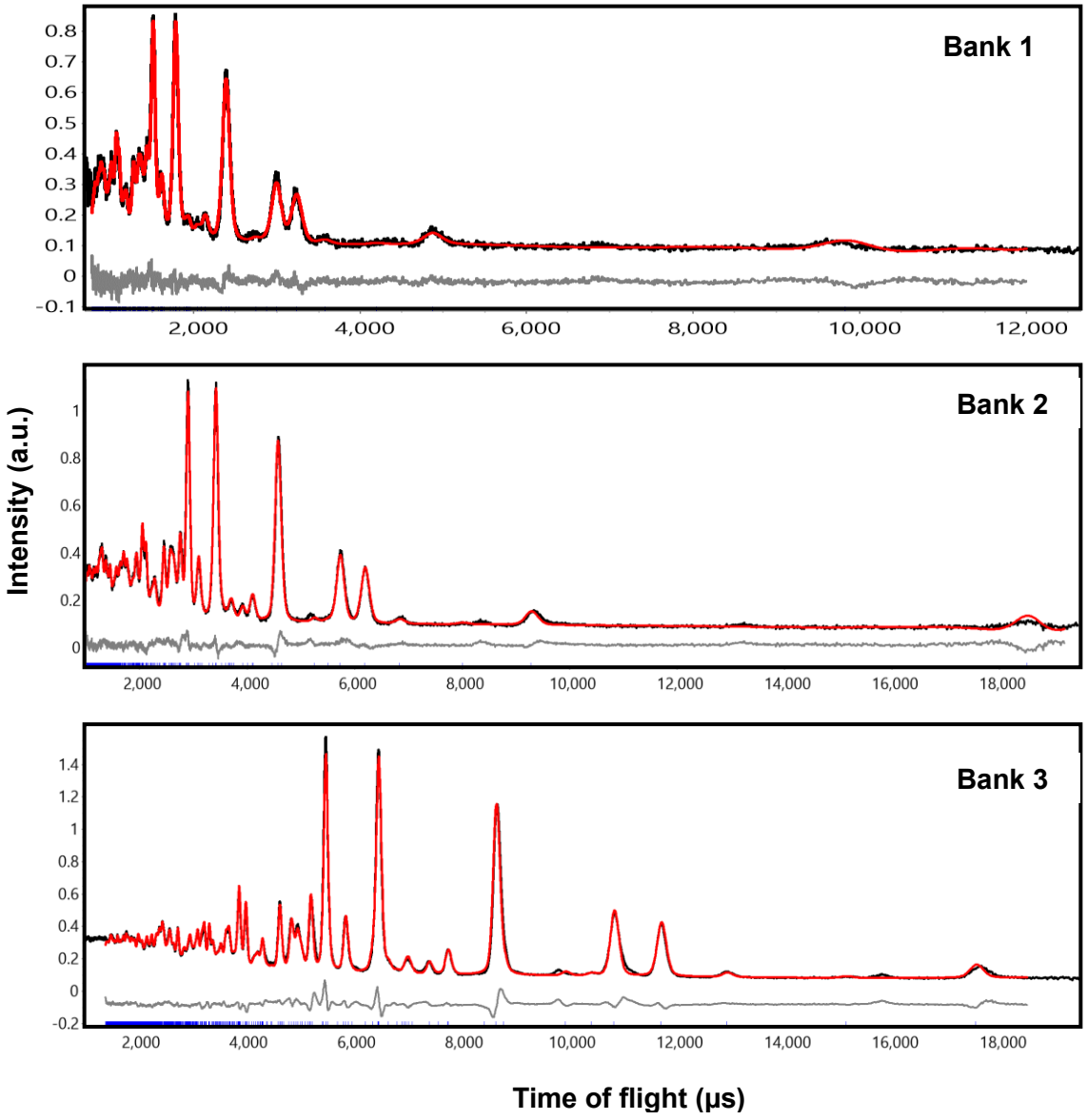

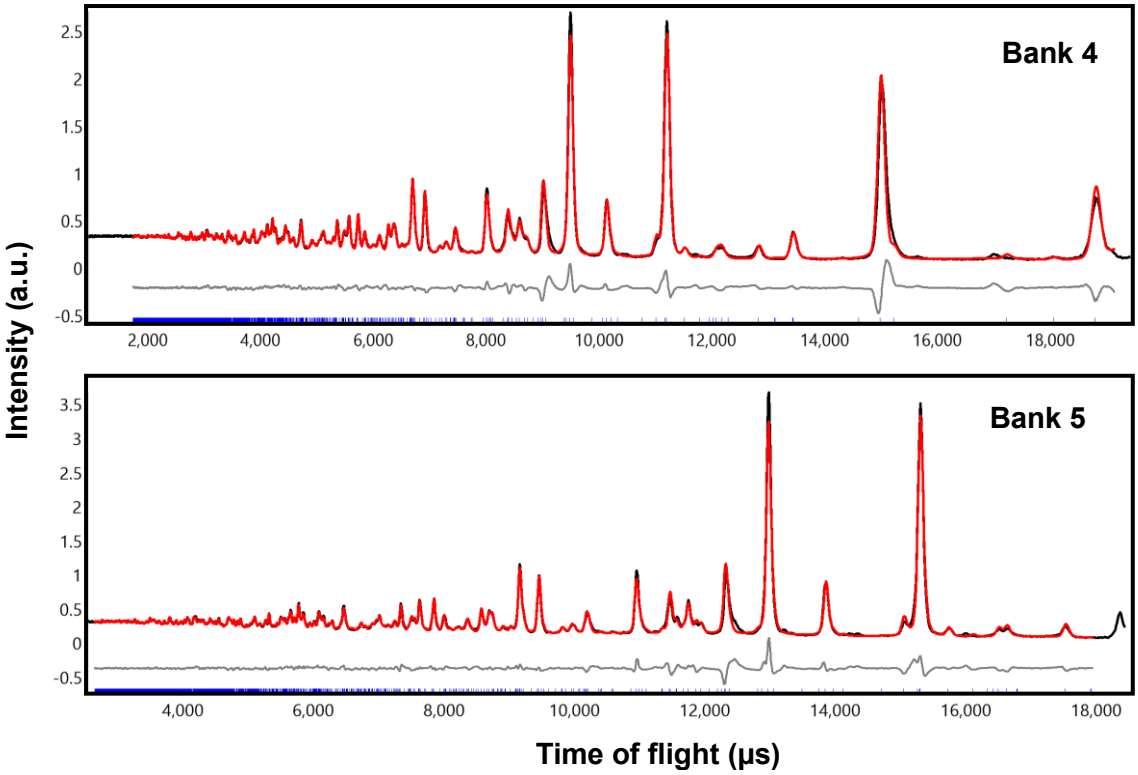

Figure 2.10: Rietveld refinement profiles for banks 1 through 5 for $Bi_2K_{0.5}La_{0.5}Ta_2O_9$, refined in space group $A2_1am$. The observed, calculated, and difference profiles shown in black, red, and grey respectively).

2.4.4 Selected mode amplitudes (Å) from refinement using room temperature NPD data for $Bi_2K_{0.5}La_{0.5}Ta_2O_9$.

Mode	**Amplitudes (Å)**		
	$\mathbf{X_3^-}$ **+** $\mathbf{M_5^+}$ **+** $\mathbf{(X_1^-)}$ ***Pnab***	$\mathbf{X_3^-}$ **+** $\mathbf{M_5^-}$ **+** $\mathbf{(X_2^+)}$ ***Pnam***	$\mathbf{\Gamma_3^-}$ **+** $\mathbf{X_2^+}$ **+** $\mathbf{X_3^-}$ ***Pna2₁***
M_5^-		0.25	0.21
X_2^+		0.13	0.08
X_3^-	0.60	0.59	0.60
M_5^+	0.17		0.13
X_1^-	0.11		0.02
Γ_3^-			0.24

2.5 Results from DFT geometry optimisation calculations relative to high symmetry *I*4/*mmm* model (in meV per formula unit).

Composition	M_5^- (a,0) *Cmcm*	M_5^+ (a,0) *Cmca*	Γ_5^- (a,a) *F2mm*	X_1^- (a;0) *Ccca*	X_2^+ (a;0) *Acam*	X_3^- (a;0) *Amam*	$X_3^- + M_5^+$ (X_1^-) *Pnab*	$X_3^- + \Gamma_5^-$ + (X_2^+) *A2₁am*	$X_3^- + M_5^-$ + (X_2^+) *Pnam*	$\Gamma_3^- + X_2^+$ + X_3^- *Pna2₁*
$Bi_2Na_{0.5}La_{0.5}Nb_2O_9$	-209.40	-138.40	-177.20	-90.40	-55.90	-303.20	-392.30	-465.60	-433.0	-433.10
$Bi_2Na_{0.5}La_{0.5}Ta_2O_9$	-113.30	-128.90	-144.20	-93.0	-50.40	-290.80	-368.60	-387.30	-363.10	-296.90
$Bi_2K_{0.5}La_{0.5}Nb_2O_9$	-143.0	-148.70	-172.50	-15.80	2.50	-218.0	-317.30	-364.80	-331.70	-329.80
$Bi_2K_{0.5}La_{0.5}Ta_2O_9$	-104.20	-135. 80	-140.30	-10.90	4.0	-217.70	-302.60	-310.10	-278.10	-217.50

Composition	M_5^- (a,0) *Cmcm*	Γ_5^- (a,a) *F2mm*	X_2^+ (a;0) *Acam*	X_3^- (a;0) *Amam*	$X_3^- + \Gamma_5^-$ + (X_2^+) *A2₁am*	$X_3^- + M_5^-$ (X_2^+) *Pnam*	$\Gamma_3^- + X_2^+$ + X_3^- *Pna2₁*
$Li_2CaNb_2O_7$	-70.88	-67.73	-81.65	-323.93	-434.58	-434.70	-435.00
$Li_2CaTa_2O_7$	-8.15	-6.98	-82.48	-294.88	-346.13	-353.28	-353.47
$Li_2SrNb_2O_7$	-14.02	-12.02	42.48	-58.15	-75.77	-77.25	-76.72
$Li_2SrTa_2O_7$	4.78	1.50	42.68	-37.73	-33.77	-36.25	-37.03
$Li_2BaNb_2O_7$	-26.70	-21.90	42.12	3.13	-23.68	-25.20	-25.67
$Li_2BaTa_2O_7$	0.15	0.67	41.95	-0.20	1.35	5.07	2.30

2.6 Selected mode amplitudes (Å) from DFT results for $Li_2SrNb_2O_7$.

Mode	Amplitudes (Å)		
	$X_3^- + \Gamma_5^- + (X_2^+)$ ***A2₁am***	$X_3^- + M_5^- + (X_2^+)$ ***Pnam***	$\Gamma_3^- + X_2^+ + X_3^-$ ***Pna2₁***
M_5^-		0.37	0.24
Γ_5^-	0.26		
X_2^+	0.10	0.12	0.09
X_3^-	0.66	0.66	0.67
M_5^+			0.01
X_1^-			0.01
Γ_3^-			0.01

2.7 Selected mode amplitudes (Å) from DFT results for $Li_2CaNb_2O_7$.

Mode	Amplitudes (Å)		
	$X_3^- + \Gamma_5^- + (X_2^+)$ ***A2₁am***	$X_3^- + M_5^- + (X_2^+)$ ***Pnam***	$\Gamma_3^- + X_2^+ + X_3^-$ ***Pna2₁***
M_5^-		0.56	0.44
Γ_5^-	0.44		
X_2^+	0.56	0.58	0.55
X_3^-	0.98	0.95	0.97
M_5^+			0.01
X_1^-			0.01
Γ_3^-			0.01

2.8 Selected mode amplitudes (Å) from DFT results for $Li_2CaTa_2O_7$.

Mode	Amplitudes (Å)		
	$X_3^- + \Gamma_5^- + (X_2^+)$ ***A2₁am***	$X_3^- + M_5^- + (X_2^+)$ ***Pnam***	$\Gamma_3^- + X_2^+ + X_3^-$ ***Pna2₁***
M_5^-		0.33	0.31
Γ_5^-	0.31		
X_2^+	0.50	0.55	0.55
X_3^-	0.95	0.93	0.94
M_5^+			0.03
X_1^-			0.06
Γ_3^-			0.02